Conductivity Coherence Factors in Superconductors

Olivier Klein

UNIVERSITY OF CALIFORNIA

Los Angeles

Conductivity Coherence Factors in Superconductors

A dissertation submitted in partial satisfaction of the

requirements for the degree Doctor of Philosophy

in Physics

by

Olivier Klein

1993

The dissertation of Olivier Klein is approved.

Sudip Chakravarty

Tatsuo Itoh

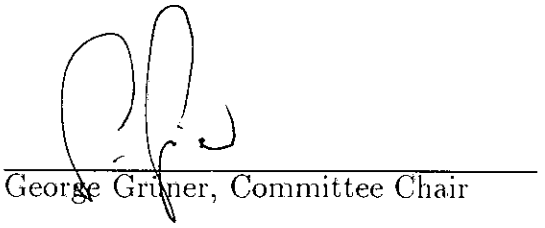

George Grüner, Committee Chair

University of California, Los Angeles

1993

Et s'il n'y avait pas la science?

Malheureux cloportes, bousouflés d'ingratitude aveugle et d'ignorance crasse, si y avait pas la science, combien d'entre nous pourraient profiter de leur cancer pendant plus de cinq ans? Et n'est-ce pas le triomphe absolu de la science que d'avoir permis qu'aujourd'hui, sur la seule decision d'un vieillard californien impuissant, ou d'un fossile ukrainien encore plus gâteux que l'autre, l'homme puisse en une seconde faire sauter quarante fois sa planète, sans bouger les oreilles!

Pierre Desproges, *textes de scènes.*

Contents

List of Figures

List of Tables

List of Symbols

In alphabetical order:

A^ν	:potential vector.
$A(\omega)$	:cavity absorption spectrum.
$\hat{a}^\dagger_{\mathbf{k},\sigma}$	:creation operator of Bloch-state ($\mathbf{k}$,σ).
$2a \geq 2b \geq 2c$	:sample dimensions.
$\alpha(T)$	:Pippard constant.
α_s/α_n	:absorption rate of the response function.
$\hat{\alpha}_e, \hat{\alpha}_m$	:electric and magnetic polarizability, $\mathbf{P} = \hat{\alpha}_e \mathcal{E}$.
b	:sample dimension.
β	:$1/k_B T$.
c	:sample dimension.
c_o	:speed of light.
χ_s	:electronic spin susceptibility.
χ_e, χ_m	:electric and magnetic susceptibility, $\mathbf{P} = \chi_e \mathbf{E}$.
(Δ)	:variation from the empty cavity measurement.
(Δ')	:variation from the $\hat{\sigma} \to \infty$ sample.
$\Delta\hat{\omega}/\omega_o$	:sample induced change of $\hat{\omega}$, $\Delta\hat{\omega}/\omega_o = -4\pi\gamma\hat{\alpha}$.
$\lim_{\lvert\hat{\sigma}\rvert\to\infty} \Delta\hat{\omega}/\omega_o{}_{\mathrm{E}}$	:metallic shift in the $\mathbf{E}$, $-\gamma/n$.
$\lim_{\lvert\hat{\sigma}\rvert\to\infty} \Delta\hat{\omega}/\omega_o{}_{\mathrm{B}}$	:metallic shift in the $\mathbf{H}$, $-\gamma/(n-1)$.
$\Delta f/f_o$	:frequency shift, $\Delta' f/f_o = \Delta f/f_o - \lim_{\lvert\hat{\sigma}\rvert\to\infty} \Delta\hat{\omega}/\omega_o$.
$\Delta\Gamma/2f_o$	:bandwidth change caused by the sample absorption.
$2\Delta(T)$	:single-particle gap.
Δ_1	:quasiparticle gap.
Δ_2	:quasiparticle life-time.
Δ_c	:cut-off energy in the gap, $\max(\hbar\omega, \Delta_2)$.
δ	: skin-depth, $\delta = 1/Im(\hat{k})$.
$\mathbf{E}$	:electric field, $\mathbf{E} = -\mathbf{q}\tilde{\Phi} - i\omega/c\mathbf{A}$.
$\mathbf{E} = \mathbf{E}_o\, e^{-i\hat{\omega}t}$	:time dependence convention (engineers use $j = -i$).
$\mathbf{E}$, $\mathbf{H}$, $\mathbf{B}$	:electric, magnetic and induction field inside the sample.
$\mathcal{E}$, $\mathcal{H}$	:external E and H field (far from the sample).
$E_{\mathbf{k}}$	:quasiparticle energy, $\sqrt{\Delta_{\mathbf{k}}{}^2 + \xi_{\mathbf{k}}{}^2}$.
e	:electron charge (positif).
$\hat{\epsilon} = \epsilon_1 + i\epsilon_2$	:permitivity, $\hat{\epsilon} = \epsilon_\infty + 4\pi i/\omega$.
ϵ_F	:fermi energy.
ϵ_1	:permitivity $\epsilon_1 = -4\pi\sigma_2/\omega$.
$\hat{\epsilon}_{eff} = \hat{\beta}\hat{\epsilon}$	:effective permitivity.
ϵ_∞	:high-frequency permitivity.

η :interference sign, ∓ 1 (case 1 and 2 respectively).
$F(\omega)$:phonon spectral density.
$f(E)$:fermi distribution, $(1+\exp[\beta E])^{-1}$.
f_o, Γ :characteristic frequency and bandwidth of the cavity.
$\hat{\Gamma}_{\mathbf{k}}$:quasiparticle vector.
$\hat{\gamma}^{\dagger}_{\mathbf{k},\sigma}$:quasiparticle creation operator.
γ :effective filling factor, $\gamma = \vartheta(V_s/V_c)$.
γ_e :electronic gyromagnetic ratio.
γ_n :nuclear gyromagnetic ratio.
$_e$ and $_h$:subscript used to differentiate electrons and holes.
$\hat{H}$:Hamiltonian of the ground-state.
$\hat{H}_i$:external probe Hamiltonian.
$\hat{H}_o$:hamiltonian of the unperturbed system.
$\hat{H}_n$:model hamiltonian of the quasiparticle gas.
$\mathbf{H}_{c1}$:lower critical field.
$\mathbf{H}_{c2}$:upper critical field.
$\mathbf{H}_e$:hyperfine field.
$\mathbf{H}_o$:external magnetic field.
h :Planck constant and $\hbar \equiv h/2\pi$.
$h.c.$:hermitian conjugate.
$\Im$:imaginary part.
$\mathbf{I}$:nuclear spin.
J :spin coupling.
J_μ :current density.
K_s :Knight shift.
$K_{\mu,\nu}$:Kernel of the electrodynamical response.
k_F :fermi wave-number.
$\hat{k} = \omega/c_o\sqrt{\hat{\epsilon}}$:wave number inside the sample.
κ :Coulomb coulping constant.
$\hat{\Lambda}_{\mathbf{k}}$:Bloch-state vector.
l_o, m_o, n_o, p_o :coherence factors.
L :averaged energy loss per cycle, $L = \omega_o <W>/Q$.
$_l$:as subscript, local limit.
$_L$:as subscript, London regim.
ℓ :mean-free-path, $\ell = v_F\tau$.
λ_L :London penetration depth, c/ω_p.
$\lambda(T)$:optical penetration depth.
λ_o :wavelength of light, $\lambda_o = c_o/\omega$.
$\mathbf{M}$, $\mathbf{P}$:magnetization and polarization inside the sample.
m :electron mass.
μ :chemical potential.
$\hat{\mu}$:permeability.
$\hat{\mu}_{eff} = \hat{\beta}\hat{\mu}$:effective permeability.
μ_e :bohr magneton.
N(0) :single-spin electron density of states at the Fermi energy.
$N_s(E)$:quasiparticle-state density.
n :depolarization factor, $\mathbf{E} = \mathcal{E} - 4\pi n\mathbf{P}$.

n_e :electron density.
n_n :normal fraction.
n_s :superfluid fraction.
$\hat{\omega} = \omega_o - i\omega_o/2Q$:complex resonance frequency.
ω :angular frequency of the electromagnetic radiation.
$\hbar\omega_e$:electronic Zeeman energy.
$\hbar\omega_n$:nuclear Zeeman energy.
ω_{ln} :average phonon frequency.
ω_n :nth matsubara frequency.
ω_p :plasma frequency, $\sqrt{4\pi ne^2/m}$
P :Gutzwiller projector.
$_P$:as subscript, Pippard regim.
Φ :electric potential.
Φ_o :magnetic fluxoid, $hc/2e$.
Q :quality factor of the cavity, $\Gamma = f_o/Q$.
$\mathbf{q}$:momentum of the light, $q = c_o/n\omega$.
$\Re$:real part.
R_s :surface resistance.
R_n :normal state surface resistance $R_s(Tc^+)$.
ρ :charge density.
$S(T)$:BCS parameter.
$\hat{\sigma}$:complex conductivity, $\hat{\sigma} = \sigma_1 + i\sigma_2$.
σ_1 :optical conductivity.
$\sigma_1{}^*$:height of the coherence peak $\sigma_1{}^* = \sigma_{1\max}$.
σ_n :normal state conductivity $\sigma_1(Tc^+)$.
T :temperature.
T^* :width of the coherence peak, $\sigma_1(T_c - T^*) = \sigma_n$.
T_1 :longitudinal nuclear spin relaxation rate.
T_c :transition temperature.
T_D :Debye temperature.
$t_{i,j}$:overlap integral between nearest neighbors.
τ :quasiparticle relaxation time.
θ_o :magic angle.
U :on-site Coulomb repulsion.
$\bar{\bar{U}}_{\mathbf{k}}$:Bogoliubov transformation.
$u_{\mathbf{k}}$ and $v_{\mathbf{k}}$:probability of an empty or filled Cooper pair.
V_s, V_c :volume of the sample and volume of the cavity.
$V_{\mathbf{k},\mathbf{l}}$:attractive potential between electron pairs.
v_F :fermi velocity.
ϑ :mode chraracteristic (appendix B).
$<W>$:averaged energy stored in the cavity.
X_s :surface reactance.
ξ :resonator constant, $\Delta\hat{\omega}/\omega_o - \lim_{|\hat{\sigma}|\to\infty} \Delta\hat{\omega}/\omega_o = \xi Z_s$.
$\xi_{\mathbf{k}}$:electron energy, $\hbar k^2/2m - \mu$.
ξ_o :BCS coherence length, $\pi\Delta(0)/\hbar v_F$.
$\xi(T)$:coherence length, $1/\xi(0) = 1/\ell + 1/\xi_o$.
Z :renormalization factor.
$Z_s = \sqrt{\hat{\mu}/\hat{\epsilon}}$:surface impedance, $Z_s = R_s - iX_s$.

Chapter 5:

σ_{ab}	:conductivity in the (ab)-plane.
σ_c	:conductivity along the c-axis.
x	:oxygen deficiency.

Chapter 6:

$\sigma_{\parallel}$	:conductivity in the (bc)-plane.
$\sigma_{\perp}$	:conductivity along the a-axis.

ACKNOWLEDGEMENTS

I owe an enormous debt of gratitude to my thesis advisor, Prof. George Grüner, who has provided me excellent opportunities to study physics. His insight, enthusiasm, encouragement and support, together with his great generosity, have made my years at UCLA an immense pleasure.

During this time, it has been my good fortune to learn from several of the leading researchers involved with the topic of this thesis. I am especially indebted to Prof. Károly Holczer, his insight and perseverance are greatly responsible for this work, he also taught me something new every time we talked and has always kept me on my feet, when I needed. I would also like to thank Prof. Henri Alloul, who welcomed me in his lab during Fall 91. My formative years were influenced by remarkable personality that have shown me the best side of our science, through their lectures, private discussions and exemplary conduct.

Special thanks are due to Prof. Stuart Brown, Prof. Tatsuo Itoh, Prof. Emily Carter and Prof. Sudip Chakravarty, for their participation in my oral committee.

I would also like to acknowledge Barakat Alavi, Dr. Anand Awasthi, Dr. Tamás Csiba, Dr. Leo Degiorgi, Dr. Larry Drabeck, Dr. Martin Dressel and Dr. Yong Kim for numerous semi-classical discussions and invaluable help in my work. I wish good success in their dissertation work to our new students Seth Bruder, Anthony Gopal and Andy Schwartz. A heartfelt thank-you is due to Dr. Steven Donovan and Dr. Marcos Lederman for their constant companionship, enduring encouragement during our years at UCLA and for thought-provoking questions and answers.

Personal thanks go to my parents for their support and encouragement and my dear friends David Senouf and Geoff Waring. My final thought goes to my fiancée Gretchen Schiller, I owe her everything.

VITA

February 17, 1965	Born, Versailles (France)
1985-1989	Ecole de Physique et Chimie, Paris (France)
July-December, 1987	Research Assistant, CERN, Geneva (Switzerland)
June 1989	Engineer Diploma, Physics, Ecole de Physique et Chimie, Paris (France)
1988-1992	University of California, Los Angeles
1988-1989	Teaching Assistant, Department of Physics, University of California, Los Angeles
December, 1989	Master of Science, Physics, University of California, Los Angeles
1990-1992	Research Assistant, Department of Physics, University of California, Los Angeles

PUBLICATIONS

K. Holczer, O. Klein, G. Grüner, Y. Yamachi, and F. Wudl, "The Electrodynamics of the Superconducting State of κ-(BEDT-TTF)$_2$Cu(NCS)$_2$", in *Organic Superconductors*, Eds. V.Z. Kresin and W.A. Little, (Plenum, New-York, 1991).

O. Klein, K. Holczer, G. Grüner, J.J. Chang, D. Scalapino, and F. Wudl, "Electrodynamics of the superconducting state of κ-(BEDT-TTF)$_2$Cu(NCS)$_2$", in *Synthetic Metals*, **41-43**, 2063, (1990).

K. Holczer, D. Quinlivan, O. Klein, and G. Grüner, "Temperature dependence and anisotropy of the penetration depth in κ-(BEDT-TTF)$_2$Cu(NCS)$_2$", in *Solid State Comm.*, **76**, 499, (1990).

O. Klein, K. Holczer, G. Grüner, J.J. Chang, and F. Wudl, "The Electrodynamics of the superconducting state of κ-(BEDT-TTF)$_2$Cu(NCS)$_2$", in *Phys. Rev. Lett.*, **66**, 655, (1991).

K. Holczer, O. Klein, and G. Grüner, "Observation of the Conductivity Coherence Peak in Superconducting Pb", in *Solid State Comm.*, **78**, 875, (1991).

K. Holczer, O. Klein, G. Grüner, J.D. Thompson, F. Diederich, and R.L. Whetten, "Critical Magnetic Fields in the Superconducting State of K_3C_{60}", in *Phys. Rev. Lett.*, **67**, 271, (1991).

K. Holczer, O. Klein, S.-M. Huang, R.B. Kaner, K.-J. Fu, R.L. Whetten, and F. Diederich, "Alkali-Fulleride Superconductors: Synthesis, Composition and Diamagnetic Shielding", in *Science*, **252**, 1154, (1991).

J.D. Thompson, G. Sparn, K. Holczer, O. Klein, G. Grüner, F. Diederich, R.B. Kaner, and R.L. Whetten, "Characterisation of Superconducting Fullerenes", in *Oxide Superconductivity*, (Plenum, New York, 1992).

O. Klein, K. Holczer, G. Grüner, and G.A. Emelchenko, "Conductivity Coherence Peak in $YBa_2Cu_3O_7$", in *J. de Phys. I* (Paris), **2**, 517, (1992).

O. Klein, K. Holczer, and G. Grüner, "Reply to the comments by M.L. Horbach, W. van Saarloos, and D.A. Huse, *Phys. Rev. Lett.*, **67**, 3464 (1991); and H.K. Olsson and R.H. Koch, *Phys. Rev. Lett.*, **68**, 2406 (1992)", in *Phys. Rev. Lett.*, **68**, 2407, (1992).

O. Klein, G. Grüner, S.-M. Huang, J.B. Wiley, and R.B. Kaner, "Electrical Resistivity of K_3C_{60}", in *Phys. Rev. B*, **46**, 11247, (1992).

H. Alloul, A. Mahajan, H. Casalta, and O. Klein, "^{89}Y NMR Study of the Anisotropy of the Static and Dynamic Susceptibility in $YBa_2Cu_3O_{6+x}$", in *Phys. Rev. Lett.*, **70**, 1171, (1993).

O. Klein, S. Donovan, M. Dressel, K. Holczer, and G. Grüner, "Microwave Cavity Perturbation Techniques, Part I: Principia", to be published in *J. Appl. Phys.*, (1993).

S. Donovan, O. Klein, M. Dressel, K. Holczer, and G. Grüner, "Microwave Cavity Perturbation Techniques, Part II: Experimental Scheme", to be published in *J. Appl. Phys.*, (1993).

M. Dressel, S. Donovan, O. Klein, K. Holczer, and G. Grüner, "Microwave Cavity Perturbation Techniques, Part III: Results", to be published in *J. Appl. Phys.*, (1993).

K. Holczer, O. Klein, H. Alloul, Y. Yoshinari, F. Hippert, S.-M. Huang, R.B. Kaner, and R.L. Whetten, "Non-Korringa ^{13}C Nuclear Relaxation in the Normal State of K_3C_{60} Superconductor", to be published, (1993).

M. Dressel, L. Degiorgi, O. Klein, and G. Grüner, "The Electrodynamics of Organic Superconductors", Santa Fe Conference Proceedings, (1993).

ABSTRACT

Conductivity Coherence Factors in Superconductors

Olivier Klein

Department of Physics, University of California, Los Angeles, Los Angeles, California 90024

(Received March, 15 1993)

In all textbooks, the microscopic mechanism of superconductivity is described as an attractive interaction between pairs of electrons which are bound together by lattice polarization forces. The recent discovery of materials which superconduct at unexpectedly high temperatures, raised some doubts on the general validity of this picture. Our prospect was to study their electrodynamic excitation spectrum in the microwave frequency range (0.1 to 10 cm^{-1}), where the photon energy is of the same scale as the attractive interaction responsible for the pairing mechanism. In particular we were interested by coherence effect, a characteristic peak that appears in the temperature dependence of the optical conductivity and is a consequence of the peculiar pairing symmetry. By developing a novel detection scheme, we have measured for the first time the conductivity coherence peak on conventional superconductors: Nb and Pb. Then, we have broaden our study to new classes of two-dimensional compounds including organic metals and the cuprates. For all those materials, the inferred pair symmetry was found to be invariant under time reversal, in full agreement with that proposed in the original model.

Chapter 1

Introduction

In principle an ideal Fermi-gas cannot undergo a phase transition, but if one allows a weak interaction to exist between the fermions, then it can condense when cooled below a sufficiently low temperature, T_c. Remarkable examples of such systems can be found in the electron gas of some metals and various types of condensed phases have been observed: superconductivity, Charge-Density-Wave (CDW) or Spin-Density-Wave (SDW) states. The former one is certainly the most well-known because of its super-properties (e.g. zero dc-electrical resistance, perfect diamagnetism, etc...). All those ground-state share the same microscopic mechanism, pair of electrons at the fermi surface form bound states which effectively behave as bosons and thus undergo Bose condensation leading to a macroscopic quantum state.

The physical properties of those condensed phases are related to their particular excitation spectrum. Remarkably, the qualitative response behavior to any external perturbation can be inferred from the symmetry of the pairing solely: those are the so-called coherence factors. The external probe used in this research is a transverse electromagnetic wave and the measured response function is the optical conductivity. Results in Nuclear Magnetic Resonance (NMR) will be mentioned too.

1.1 Pairing theory of superconductivity

1.1.1 Experimental evidence

Several experimental observations have indeed shown that the microscopic mechanism of superconductivity involves electron-pairs. The skeptical reader will find below a review of the most relevant ones.

Flux quantization

One consequence of the long range phase coherence in a superconductor is the quantization of the magnetic flux in a macroscopic superconducting ring. The phenomenon is analogous to the Aharonov-Bohm effect, but involves an electron pair ($2e$) rather than a single particle (as in mesoscopic systems). The value of the quantum fluxoid Φ_0 (inferred from the contour integral of the potential vector $\mathbf{A}$ around the ring) in a superconductor is half smaller that expected for unpaired electrons

$$\frac{2e}{c}\oint \mathbf{A}dl = 2\pi\hbar n, \tag{1.1.1a}$$

$$\Phi_n = n\left(\frac{hc_o}{2e}\right), \tag{1.1.1b}$$

where e is the electron charge, h the Planck constant and c_o the speed of light.

Later experiments by B.S. Daever [52] confirmed the result and gave the first experimental evidence of the pairing mechanism.

Tunneling experiment

D.B. Josephson suggested in 1962 [101], that it should be possible for an electron pair to tunnel between two superconductors separated by a thin isolating junction. The effect was confirmed experimentally a year later by J.M. Rowell [15]. The pair-tunneling current depends only on the phase difference between the two ground-state wave-functions on both sides of the junction, and this phase oscillates at a rf-frequency $2e/\hbar$ [76] when the junction is biased by a dc-potential V. It leads to an oscillating tunneling current of the form:

$$I = I_c \sin\left(\frac{2e}{\hbar}Vt + \Phi_0\right). \tag{1.1.2}$$

Mesoscopic grains

A recent experiment by M. Tinkham [191] has shown an even-odd parity effect of transport properties through tunnelling junctions in a mesoscopic superconducting grain of Al. In this case, they observe a 2e-periodicity in the I-V characteristic with respect to the gate-induced charge.

1.1.2 BCS theory

The general microscopic theory of superconductivity was developed by Bardeen, Cooper and Schrieffer (BCS) in 1957 [19, 20]. The fundamental aspect of the model was to state that, in the presence of an attractive interaction, electrons in the neighborhood of the fermi surface condense into a new ground-state formed of electron-pairs with equal and opposite momentum and opposite spin components called Cooper pair: $(\mathbf{k}, \uparrow)$ and $(-\mathbf{k}, \downarrow)$ Bloch states. The attraction between the electrons in a pair can in principle be due to any suitable kind of interaction that overcomes the Coulomb repulsion. The energy required to break a pair is $\Delta(0)$. The discovery that for many superconductors T_c depends on the isotopic mass [165], showed that for those compounds the attractive interaction is mediated by lattice distortions (phonons) . In this case, the transition temperature scales as the Debye temperature (T_D). Early, it was anticipated that other mechanism could also lead to the same pairing, but so far conclusive examples have not been found. Although the BCS theory was developed for superconductivity, its principle is general enough to apply for every type of pairing (for example CDW and SDW order).

It is assumed that the reader is already familiar with the microscopic BCS theory, later the discussion will be centered around the consequences of the pairing mechanism solely. For further details, there are several well-known textbooks that review the subjects, in part written by Schrieffer [178], de Gennes [51] or Tinkham [188], the later will be the referenced introduction and in particular the notation convention adopted throughout this report is identical: all the equations will be given in cgs units and the experimental values will be quoted in SI units (as it is the adopted custom among experimentalists), the conversion from one system to another is explained in Jackson [97].

The remaining of the section will be devoted to review the principal results of the original theory, the purpose is to define all the fundamental parameters that will be used extensively later.

One of the main characteristics of the condensed phase is that the quasiparticle excitation spectrum has an energy gap $2\Delta(0)$ at zero temperature. In the BCS model, this gap is isotropic and independent of the $\mathbf{k}$ direction. The model also simplifies the interaction between the fermions to a simple two-square-well form. A cut-off energy ($\hbar\omega_c = k_B T_D$) fixes the neighborhood of the fermi-level affected by the attractive interaction. $N(0)$ is defined as the single-spin electron density at the fermi energy and V represents the interaction energy between the electrons. In the weak coupling limit or $VN(0) \to 0$, the amplitude of the gap takes the limiting form:

$$\Delta(0) \sim 2\hbar\omega_c e^{-1/N(0)V}. \tag{1.1.3}$$

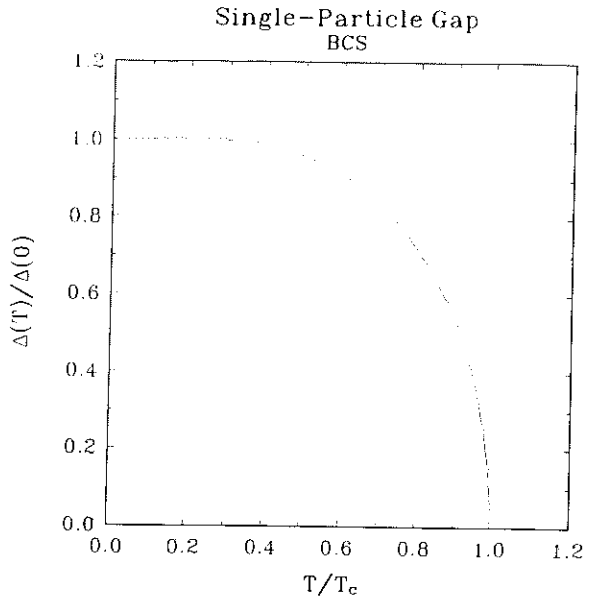

Fig. [1.1]: Temperature dependence of the single particle gap for a BCS superconductor.

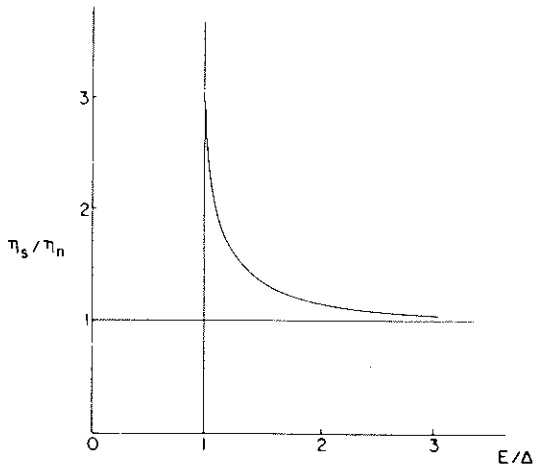

Fig. [1.2]: Energy dependence of the quasiparticle density of states for a BCS superconductor.

The transition temperature can be then estimated from the gap value:

$$2\Delta(0) = 3.528 k_B T_c. \tag{1.1.4}$$

The temperature dependence of $\Delta(T)$ is inferred from the gap equation

$$1 = VN(0)\int_0^{\hbar\omega_c} du \frac{\tanh\left(\sqrt{u^2+\Delta^2(T)}/2k_BT\right)}{\sqrt{u^2+\Delta^2(T)}}, \tag{1.1.5}$$

and the corresponding variation is represented in Fig. [1.1].

The optical properties (the penetration depth λ and the electromagnetic coherence-length ξ) are in general interdependent quantities and both vary with temperature and impurity concentration. To avoid confusion, the adopted custom is to express all variables in terms of a few simple constants that are defined simply from the intrinsic properties. Those are the zero temperature values of λ and ξ in the London limit:

$$\lambda_L = \frac{c_o}{\omega_P}, \tag{1.1.6}$$

and:

$$\xi_o = \frac{\hbar v_F}{\pi\Delta(0)}. \tag{1.1.7}$$

v_F is the fermi velocity and ω_P is the plasma frequency

$$\omega_P{}^2 = \frac{4\pi n_e e^2}{m}. \tag{1.1.8}$$

n_e is the electron density and m the electron mass.

1.1.3 Super-complete BCS Hamiltonian

The model discussed in this section, illustrates the general ground-state properties of a superconductor. As discussed earlier, in this model fermions have a weak attraction to form Cooper pairs, if their kinetic energy lies in an interval $\hbar\omega_c$ on either side of the fermi surface. In the mean field approximation, the hamiltonian simplifies to the following form:

$$\hat{H} = \sum_{\mathbf{k},\sigma} \frac{\hbar^2 k^2}{2m} \hat{a}^\dagger_{\mathbf{k},\sigma} \hat{a}_{\mathbf{k},\sigma} + \sum_{\mathbf{k},\mathbf{l}} V_{\mathbf{k},\mathbf{l}} < \hat{a}_{\mathbf{l}\uparrow} \hat{a}_{-\mathbf{l}\downarrow} > \hat{a}^\dagger_{\mathbf{k}\uparrow} \hat{a}^\dagger_{-\mathbf{k}\downarrow} \quad + \quad h.c. \tag{1.1.9}$$

The $<>$ brackets represents the thermal average:

$$< \hat{a}_{\mathbf{l}\uparrow} \hat{a}_{-\mathbf{l}\downarrow} > \quad = \quad \mathrm{Tr}\ \hat{\rho} \hat{a}_{\mathbf{l}\uparrow} \hat{a}_{-\mathbf{l}\downarrow}, \tag{1.1.10}$$

where $\hat{\rho}$ is the density operator:

$$\hat{\rho} = \frac{e^{-\beta(\hat{H}-\mu\hat{N})}}{\mathrm{Tr}\ e^{-\beta(\hat{H}-\mu\hat{N})}}, \tag{1.1.11}$$

$\hat{N}$ the number operator, μ the chemical potential and $\beta = 1/k_B T$. It is useful to rewrite the hamiltonian in the more concise form:

$$\hat{H}' = \hat{H} - \mu\hat{N} = \sum_{\mathbf{k}} \hat{\Lambda}^\dagger_{\mathbf{k}} \bar{\bar{\mathcal{E}}}_{\mathbf{k}} \hat{\Lambda}_{\mathbf{k}}, \tag{1.1.12}$$

with

$$\hat{\Lambda}_{\mathbf{k}} \quad = \quad \begin{pmatrix} \hat{a}_{\mathbf{k}\uparrow} \\ \hat{a}^\dagger_{-\mathbf{k}\downarrow} \end{pmatrix}, \tag{1.1.13}$$

and

$$\bar{\bar{\mathcal{E}}}_{\mathbf{k}} \quad = \quad \begin{pmatrix} \xi_{\mathbf{k}} & \Delta_{\mathbf{k}} \\ \Delta^\dagger_{\mathbf{k}} & -\xi_{\mathbf{k}} \end{pmatrix}. \tag{1.1.14}$$

$\Delta^\dagger_{\mathbf{k}}$ is the hermitian conjugate. The matrix elements are simply

$$\xi_{\mathbf{k}} \quad = \quad \left(\frac{\hbar^2 k^2}{2m} - \mu \right), \tag{1.1.15a}$$

$$\Delta_{\mathbf{k}} \quad = \quad \sum_{\mathbf{l}} V_{\mathbf{k},\mathbf{l}} < \hat{a}_{\mathbf{l}\uparrow} \hat{a}_{-\mathbf{l}\downarrow} > . \tag{1.1.15b}$$

The hamiltonian in Eq. (1.1.12) can be diagonalized by means of a unitary transformation, suggested by Bogoliubov in 1958 [28]

$$\hat{\Gamma}_{\mathbf{k}} = \bar{\bar{U}}_{\mathbf{k}} \hat{\Lambda}_{\mathbf{k}} \quad \text{where} \quad \bar{\bar{U}}_{\mathbf{k}} = \begin{pmatrix} u^*_{\mathbf{k}} & v_{\mathbf{k}} \\ -v^*_{\mathbf{k}} & u_{\mathbf{k}} \end{pmatrix}, \tag{1.1.16}$$

with the constraint $|u_{\mathbf{k}}|^2 + |v_{\mathbf{k}}|^2 = 1$.

The new vector $\hat{\Gamma}_{\mathbf{k}}$ represents the single particle excitation of the ground-state (the quasiparticles) and they obey Fermi anti-commutation rules:

$$\hat{\Gamma}_{\mathbf{k}} = \begin{pmatrix} \hat{\gamma}_{\mathbf{k},0} \\ \hat{\gamma}^{\dagger}_{\mathbf{k},1} \end{pmatrix}. \tag{1.1.17}$$

The eigenvalues are:

$$E_{\mathbf{k}} = \sqrt{{\Delta_{\mathbf{k}}}^2 + {\xi_{\mathbf{k}}}^2}, \tag{1.1.18}$$

and they define the quasiparticle energies.

The symmetry of the ground-state is defined by the operation that interchanges the components of the quasiparticle vectorial notation ($\hat{\Gamma}_{\mathbf{k}}$). The resulting degeneracy of the complete base-set is reflected in the dimensionality of the vector. In this case, the ground-state is time-reversal invariant and doubly degenerate (Kramers degeneracy).

It can be shown that the excitation-state density for the condensed phase is of the form:

$$N_s(E_{\mathbf{k}}) = N(0)\Re\left(\frac{E_{\mathbf{k}}}{\sqrt{{E_{\mathbf{k}}}^2 - {\Delta_{\mathbf{k}}}^2}}\right). \tag{1.1.19}$$

In the BCS theory the $V_{\mathbf{k},\mathbf{l}}$ interaction takes the two-square-well form:

$$V_{\mathbf{k},\mathbf{l}} = \begin{cases} -V & \text{if } |\xi_{\mathbf{k}}| \text{ and } |\xi_{\mathbf{l}}| \leq \hbar\omega_c, \\ 0 & \text{otherwise.} \end{cases} \tag{1.1.20}$$

Then the single-particle gap is a scalar, $\Delta(0)$. The zero temperature quasiparticle density of states follows the curve sketched in Fig. [1.2]: there are no states below a gap edge $\Delta(0)$ at which point there is a singularity.

1.2 Coherence effects in a BCS superconductor

One striking feature of superconductors is that the absorption rate of such external probes as sound or rf-electromagnetic waves, have a very different qualitative behavior in spite of the fact they couple to the same excitations. In all cases the probe-energy is well below the gap value and the momentum transfer is small compared to k_F: the absorption processes are dominated by the unpaired electrons (quasiparticles) that scatter to higher kinetic energy states.

1.2.1 Experimental results

This section gives a partial list of some few external probes that satisfy the constraint sketched above. The temperature dependence of their respective absorption rate is reported.

Ultrasonic attenuation

An acoustic wave modulates the position of the ions in the lattice creating a longitudinal electric field $\mathbf{D}(\mathbf{q},\omega) = \mathbf{E} + 4\pi\mathbf{P}$ that couples to the charged carriers. In the case of longitudinal acoustic waves, only the normal electrons participate in the absorption process. The rate is given by $\mathbf{D}^2/2\Im(\epsilon)$, where $\epsilon(\mathbf{q},\omega)$ is the complex dielectric constant. The sound wave velocity in a metal is of the order of $u = 10^5$ cm sec^{-1}, much smaller than the fermi velocity $v_F = 10^7$ cm sec^{-1} hence the wave vector $\mathbf{q}$ of the acoustic wave is

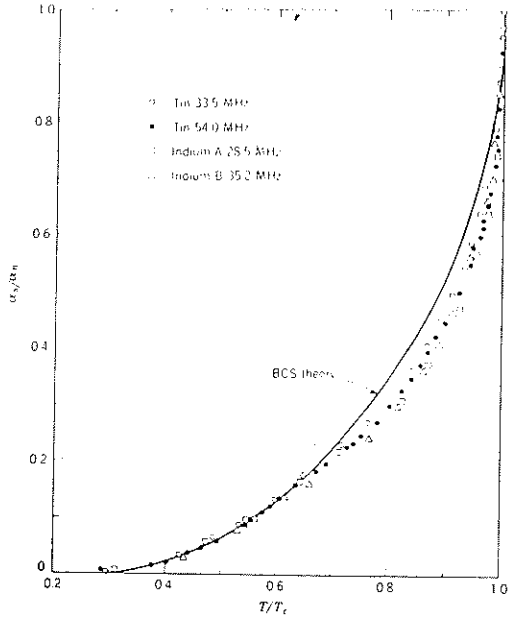

Fig. [1.3]: Temperature dependence of the ultrasonic attenuation in tin and indium, after Ref. [144].

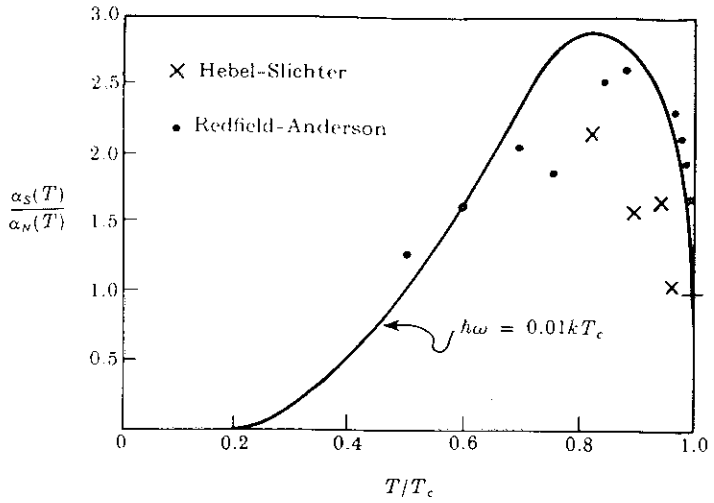

Fig. [1.4]: Temperature dependence of the nuclear spin relaxation rate in aluminium, after Ref. [85].

small and given by:

$$\hbar u q = \hbar \omega. \tag{1.2.1}$$

where $f = \omega/2\pi$ is the frequency of the wave, typically 100 MHz (or 5×10^{-4} meV), much smaller than a typical pair breaking energy 1 meV.

Fig. [1.3] displays the acoustic attenuation of longitudinal sound waves in tin and indium [144]. The rapid decrease in the attenuation coefficient as the temperature is lowered is due in part to the decreasing number of excitations available to absorb the phonons, but another effect must come to play and outweigh the increasing density of states.

Nuclear magnetic resonance

The longitudinal nuclear magnetization of a solid relaxes along its equilibrium axis with a characteristic time constant, T_1 called the spin-lattice relaxation time (the relaxation rate is defined as the inverse of T_1). This relaxation process is dissipative and for metals, the released energy goes to the electronic degree of freedom through the contact interaction (usually the dominant term). The electronic excitation is of the order of the electronic Zeeman energy because it involves an electron spin flip. For a superconductor in a 2 Tesla magnetic field, the dissipation quanta is typically 2×10^{-1} meV.

Fig. [1.4] shows the temperature dependence of the nuclear spin relaxation rate as measured by Hebel and Slichter on aluminium [85]. One striking feature is that the relaxation rate increases below T_c before decreasing at low temperature. In this case the increasing density of states dominates near T_c while at low temperature the statistical factor (decrease in the number of quasiparticles) outweighs the former effect.

Electromagnetic absorption

If one conducts optical experiments in a similar energy window as the previous experiments and follows the double constraints that the photon energy be much smaller than the gap but larger than thermal processes (otherwise thermal noise screens the optical effect), then the spectral range implied are mm-waves. To our knowledge there are no experiments that have yet measured $\sigma_1(T)$ of superconductors at microwave frequencies because of technical difficulties.

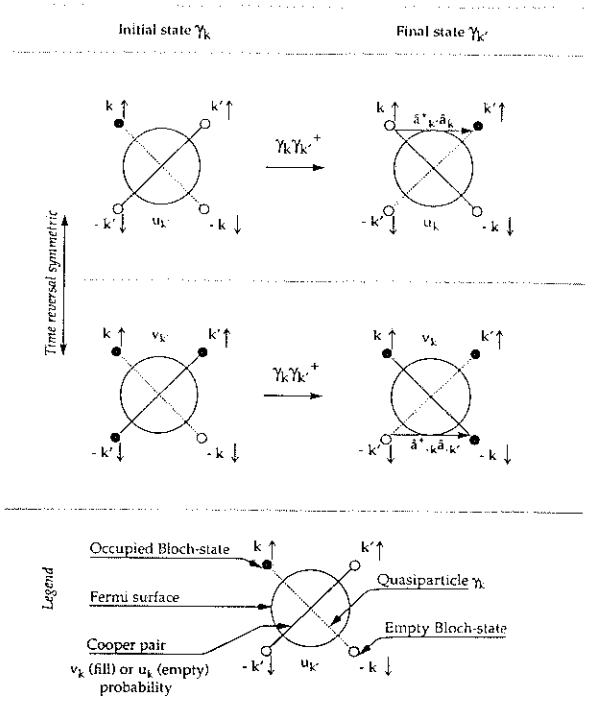

Fig. [1.5]: Illustration of coherence factors: in the first row, a quasiparticle (unpaired electron) in $(\mathbf{k},\uparrow)$ scatters to $(\mathbf{k}',\uparrow)$: $\gamma^{\dagger}_{\mathbf{k}'}\gamma_{\mathbf{k}}$. The second row shows the *same* event factorized by a *different* (time reversed) Bloch-state process $(\hat{a}^{\dagger}_{-\mathbf{k}}\hat{a}_{-\mathbf{k}'})$.

Conclusion

Obviously a factor has been left out in the derivation to account for the discrepancy between those experiments. Next, one will see that the left out term (the coherence factor) is intimately related to the symmetry of the pairing.

1.2.2 Coherence factors

The differences between those previous experimental results find a natural explanation in the pairing mechanism. In calculating the matrix elements between the quasiparticles in a superconductors, one has to take into account that the ground-state is occupied by pairs. There is not a one to one correspondence between a given quasiparticle scattering and its associated Bloch-state process, but rather all the different channels that belong to the same symmetry-class (symmetry of the pairing) factorize to the same quasiparticle scatter. Now, when the matrix elements are squared, those degenerate events will interact coherently if the different matrix elements of the probe differ at most by a phase factor for the particular pairing symmetry, in which case the effect gives rise to interference effects which would be completely absent in the normal-state (independent summation). For the particular case of (BCS) superconductors, the ground-state is invariant under time-reversal and *two* (original and its time-reversed) Bloch-state processes interact. The sign of the interference (whether they add constructively or destructively) depends only on the interaction symmetry. The situation is best seen by means of a little bit of algebra.

Lets assume that the external probe is of the form

$$\hat{H}_i = \sum_{\mathbf{k},\mathbf{k}',\sigma,\sigma'} < \mathbf{k}',\sigma'|\hat{H}_i|\mathbf{k},\sigma > \hat{a}^{\dagger}_{\mathbf{k}',\sigma'}\hat{a}_{\mathbf{k},\sigma}. \tag{1.2.2}$$

The constraints imposed on the probe are $|k-k'| \ll k_F$ and $|k^2/2m - k'^2/2m| \ll \hbar\omega_c$. Using simple linear algebra argument, it can be shown from Eq. (1.1.16) that $\hat{a}^{\dagger}_{\mathbf{k}',\sigma'}\hat{a}_{\mathbf{k},\sigma}$ and its time-reversal symmetric

$\hat{a}_{-\mathbf{k}',-\sigma'}\hat{a}^{\dagger}_{-\mathbf{k},-\sigma}$ connects the same quasiparticle states. In the particular case where $\sigma' = \sigma$ then:

$$\begin{aligned}\hat{a}^{\dagger}_{\mathbf{k}'\uparrow}\hat{a}_{\mathbf{k}\uparrow} = \quad & +v^{*}_{\mathbf{k}'}v_{\mathbf{k}}\hat{\gamma}_{\mathbf{k}',1}\hat{\gamma}^{\dagger}_{\mathbf{k},1} + u^{*}_{\mathbf{k}'}u_{\mathbf{k}}\hat{\gamma}^{\dagger}_{\mathbf{k}',0}\hat{\gamma}_{\mathbf{k},0} \\ & -v^{*}_{\mathbf{k}'}u_{\mathbf{k}}\hat{\gamma}_{\mathbf{k}',1}\hat{\gamma}_{\mathbf{k},0} - u^{*}_{\mathbf{k}'}v_{\mathbf{k}}\hat{\gamma}^{\dagger}_{\mathbf{k}',0}\hat{\gamma}^{\dagger}_{\mathbf{k},1}, \qquad (1.2.3a)\\ \hat{a}^{\dagger}_{-\mathbf{k}\downarrow}\hat{a}_{-\mathbf{k}'\downarrow} = \quad & -u^{*}_{\mathbf{k}}u_{\mathbf{k}'}\hat{\gamma}_{\mathbf{k}',1}\hat{\gamma}^{\dagger}_{\mathbf{k},1} - v^{*}_{\mathbf{k}}v_{\mathbf{k}'}\hat{\gamma}^{\dagger}_{\mathbf{k}',0}\hat{\gamma}_{\mathbf{k},0} \\ & -v^{*}_{\mathbf{k}}u_{\mathbf{k}'}\hat{\gamma}_{\mathbf{k}',1}\hat{\gamma}_{\mathbf{k},0} - u^{*}_{\mathbf{k}}v_{\mathbf{k}'}\hat{\gamma}^{\dagger}_{\mathbf{k}',0}\hat{\gamma}^{\dagger}_{\mathbf{k},1}. \qquad (1.2.3b)\end{aligned}$$

Notice that the last two terms in the two equations are irrelevant for probing energies below the gap, as they refer to pair breaking process. After summing all the independent possibilities, the coefficients in front of the $\hat{\gamma}^{\dagger}_{i}\hat{\gamma}_{i}$ (with $i = 0, 1$) are proportional to:

$$\left(u^{*}_{\mathbf{k}'}u_{\mathbf{k}} + \eta v^{*}_{\mathbf{k}'}v_{\mathbf{k}}\right). \qquad (1.2.4)$$

with $\eta = \pm 1$ depending on the probe symmetry. Those coefficients are the so-called coherence factors and two cases appears:

1. $\eta = -1$, the interference is destructive (case 1).
2. $\eta = +1$, the interference is constructive (case 2).

When the spin is a conserved quantity of the interaction (the case above), η is defined by the equality:

$$< -\mathbf{k}, -\sigma|\hat{H}_i| - \mathbf{k}', -\sigma > \quad \equiv \quad -\eta < \mathbf{k}', \sigma|\hat{H}_i|\mathbf{k}, \sigma > . \qquad (1.2.5)$$

If the absorption process involves an electron-spin flip, then the interference sign has to be defined by:

$$< -\mathbf{k}, -\sigma|\hat{H}_i| - \mathbf{k}', \sigma > \quad \equiv \quad +\eta < \mathbf{k}', -\sigma|\hat{H}_i|\mathbf{k}, \sigma > . \qquad (1.2.6)$$

For the case where the probe energy is above the gap, the absorption is dominated by the $\hat{\gamma}^{\dagger}_{i}\hat{\gamma}^{\dagger}_{|i-1|}$ (with $i = 0, 1$) and the coefficient in front are:

$$\left(u^{*}_{\mathbf{k}'}v_{\mathbf{k}} - \eta v^{*}_{\mathbf{k}'}u_{\mathbf{k}}\right), \qquad (1.2.7)$$

with η defined by Eqs. (1.2.5) and (1.2.6). Notice that the middle-sign is inverted.

In Schrieffer's notation [178] the different coherence factors are labeled as:

$$\begin{aligned} l_o(\mathbf{k}, \mathbf{k}') = \quad & u^{\star}_{\mathbf{k}}u_{\mathbf{k}'} + v_{\mathbf{k}}v^{\star}_{\mathbf{k}'} \quad \text{or } h.c., \qquad (1.2.8a)\\ m_o(\mathbf{k}, \mathbf{k}') = \quad & u^{\star}_{\mathbf{k}}u_{\mathbf{k}'} - v_{\mathbf{k}}v^{\star}_{\mathbf{k}'} \quad \text{or } h.c., \qquad (1.2.8b)\\ n_o(\mathbf{k}, \mathbf{k}') = \quad & u^{\star}_{\mathbf{k}}v_{\mathbf{k}'} + v_{\mathbf{k}}u^{\star}_{\mathbf{k}'} \quad \text{or } h.c., \qquad (1.2.8c)\\ p_o(\mathbf{k}, \mathbf{k}') = \quad & u^{\star}_{\mathbf{k}}v_{\mathbf{k}'} - v_{\mathbf{k}}u^{\star}_{\mathbf{k}'} \quad \text{or } h.c. \qquad (1.2.8d)\end{aligned}$$

The factors that apply to the probes mentioned above are derived next.

Ultrasonic attenuation

For sound waves, the ultrasonic attenuation has the form:

$$\hat{H}_i = \alpha \sum_{\mathbf{k},\mathbf{k}',\sigma} \hat{a}^{\dagger}_{\mathbf{k}',\sigma}\hat{a}_{\mathbf{k},\sigma}, \qquad (1.2.9)$$

with α a scalar. The spin is conserved, therefore the sign is given by Eq. (1.2.5). Because α is constant, $\eta = -1$ and case 1 applies. A word of caution: in the case of transverse waves, several mechanisms for absorption are important, some of which are case 1 and some case 2.

Electromagnetic absorption

For electromagnetic waves, the absorption hamiltonian is:

$$\hat{H}_i = \frac{-e\hbar}{2mc} \sum_{\mathbf{k},\mathbf{k}',\sigma} \mathbf{A}(\mathbf{k}-\mathbf{k}').(\mathbf{k}+\mathbf{k}')\hat{a}^{\dagger}_{\mathbf{k}',\sigma}\hat{a}_{\mathbf{k},\sigma}. \tag{1.2.10}$$

Here again, the spin is conserved, thus Eq. (1.2.5) gives the relevant sign. The interaction depends on the momentum direction of the electron (odd for time reversal symmetry) $\eta = +1$: case 2 applies.

Nuclear magnetic resonance

For nuclear spin relaxation, the absorption hamiltonian is of the form:

$$\hat{H}_i = \alpha \sum_{\mathbf{k},\mathbf{k}',\sigma} \hat{a}^{\dagger}_{-\mathbf{k}',-\sigma}\hat{a}_{\mathbf{k},\sigma}. \tag{1.2.11}$$

with α, the contact interaction (a scalar). NMR relaxation flips the spin of the electron (σ'=$-\sigma$) and Eq. (1.2.6) defines the phase sign $\eta = +1$, case 2 applies.

1.2.3 Absorption rate

Temperature dependence

The coherence factors can be expressed in terms of quasiparticle energies and gap value; using Tinkham's results [188]:

$$(u^{\star}_{\mathbf{k}}u_{\mathbf{k}'} + \eta v_{\mathbf{k}}v^{\star}_{\mathbf{k}'}) = \frac{1}{2}\left(1 + \frac{\xi_{\mathbf{k}}\xi_{\mathbf{k}'}}{E_{\mathbf{k}}E_{\mathbf{k}'}} + \eta\frac{\Delta^2}{E_{\mathbf{k}}E_{\mathbf{k}'}}\right). \tag{1.2.12}$$

When summed over the k values, the middle term disappears:

$$F(E,E') = \frac{1}{2}\left(1 + \eta\frac{\Delta^2}{EE'}\right) \sim \begin{cases} 0 & \text{if } \eta = -1, \\ 1 & \text{if } \eta = +1. \end{cases} \tag{1.2.13}$$

To derive an expression for the absorption rate, one starts from the Fermi golden rule:

$$\alpha_s = \int |M|^2 F(E, E+\hbar\omega) N_s(E) N_s(E+\hbar\omega) \left\{f(E) - f(E+\hbar\omega)\right\} dE \tag{1.2.14}$$

where $|M|^2$ is the matrix transition, $\hbar\omega$ the probing energy and:

$$N_s(E) = 1/\sqrt{E^2-\Delta^2} \quad \text{is the density of states,} \tag{1.2.15a}$$

$$f(E) = 1/[1+\exp(\beta E)] \quad \text{is the Fermi distribution.} \tag{1.2.15b}$$

Defining α_n as the value of α_s at T_c:

$$\frac{\alpha_s}{\alpha_n} = \frac{1}{\hbar\omega}\int_{-\infty}^{\infty} \frac{\left|E(E+\hbar\omega)+\eta\Delta^2\right|\left[f(E)-f(E+\hbar\omega)\right]}{\sqrt{E^2-\Delta^2}\sqrt{(E+\hbar\omega)^2-\Delta^2}} dE. \tag{1.2.16}$$

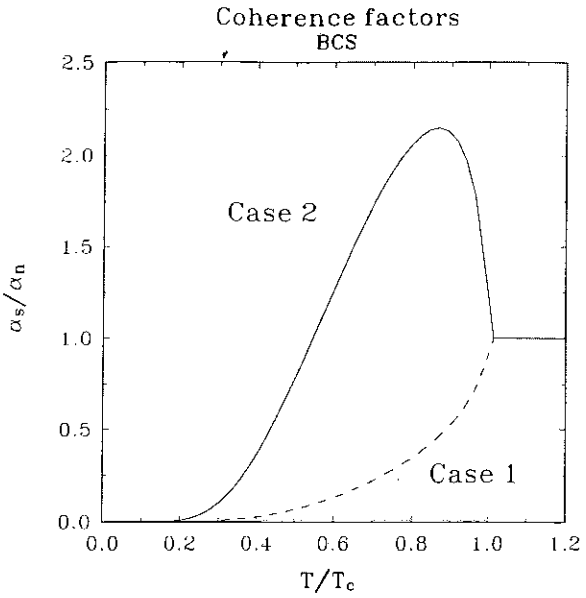

Fig. [1.6]: Temperature dependence of the low frequency absorption rate for case 1 and 2 coherence factors. Case 1 applies for ultrasonic attenuation while case 2 describes electromagnetic absorption or nuclear relaxation.

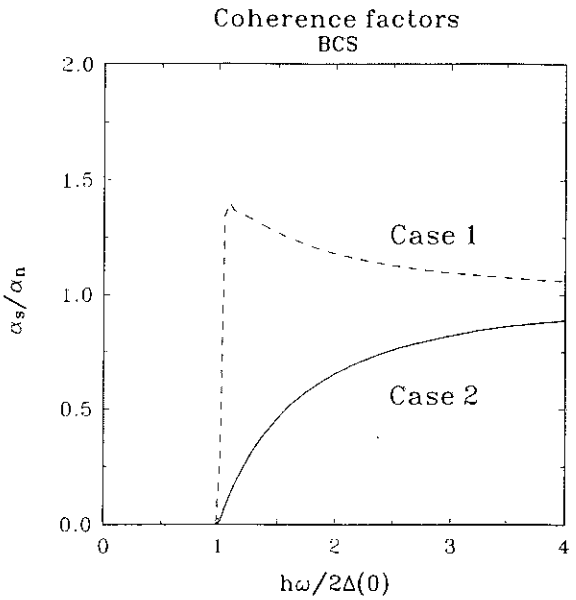

Fig. [1.7]: Frequency dependence of the T=0 absorption rate for case 1 and 2 coherence factors.

It is understood that the regions $|E|$ or $|E+\hbar\omega| < \Delta$ are excluded from the integration. Using Eq. (1.2.16), the temperature dependence of the absorption rate is plotted in Fig. [1.6] for both case 1 and 2.

- Case 1: One observes a rapid decrease of the simple functional form:

$$\frac{\alpha_s}{\alpha_n} = 2f(\Delta). \tag{1.2.17}$$

- Case 2: The integral diverges logarithmically and a cut-off energy of ($\Delta_c = 0.02\Delta$ in the figure) has to be introduced in order to prevent the integral from diverging. This cut-off was interpreted originally as a level broadening in the density of states due to some anisotropy of the gap (later on it will be shown that $\Delta_c = \hbar\omega$). One often uses the approximate form given below to fit the experimental results:

$$\frac{\alpha_s}{\alpha_n} = 2f(\Delta)\left[1 + \frac{\Delta}{k_B T}(1 - f(\Delta))\ln\left(\frac{2\Delta}{\Delta_c}\right)\right]. \tag{1.2.18}$$

In summary, the interference is constructive for nuclear spin relaxation and optical conductivity and leads to a peak in the temperature dependence of their absorption rate, below T_c. The interference is destructive for ultrasonic attenuation and leads to an exponential decrease.

Spectrum

The excitation spectrum is of primordial interest as it gives all the physical properties of the condensed phase. At zero temperature there are no thermally excited quasiparticles, and the absorption rate is null at probing energy below 2Δ. At $\hbar\omega \geq 2\Delta$, pair breaking processes are allowed and the absorption rate is non-zero. Notice that in this last case, the n_o and p_o coherence factors are introduced. It can be shown that the normalized rate takes the form:

$$\frac{\alpha_s}{\alpha_n} = \frac{1}{\hbar\omega}\int_{\Delta-\hbar\omega}^{-\Delta} \frac{|E(E+\hbar\omega) + \eta\Delta^2|}{\sqrt{E^2-\Delta^2}\sqrt{(E+\hbar\omega)^2-\Delta^2}} dE. \tag{1.2.19}$$

Pairing	Ultrasonic attenuation	Electromagnetic absorption	Nuclear spin relaxation
SS	1	2	2
CDW	2	"1"	x
SDW	2	"1"	2
TS	2	2	x
A	1	1	2
B	2	2	2

Pairing:
SS: $(\mathbf{k},\uparrow)_e \leftrightarrow (-\mathbf{k},\downarrow)_e$
CDW: $(\mathbf{k},\uparrow)_e \leftrightarrow (-\mathbf{k},\uparrow)_h$
SDW: $(\mathbf{k},\uparrow)_e \leftrightarrow (-\mathbf{k},\downarrow)_h$
TS: $(\mathbf{k},\uparrow)_e \leftrightarrow (-\mathbf{k},\uparrow)_e$
Case A: $(\mathbf{k},\uparrow)_e \leftrightarrow (\mathbf{k},\downarrow)_e$
Case B: $(\mathbf{k},\uparrow)_e \leftrightarrow (\mathbf{k},\downarrow)_h$

Table 1.1: Coherence factors for various pairing at $\hbar\omega < 2\Delta(0)$. Case 1 (destructive interference) induces a rapid decrease in the temperature dependence of the absorption rate and no Goldstone mode in the spectrum. Case 2 (constructive interference) creates a peak in the temperature dependence of the absorption rate and a collective mode in the spectrum.

Fig. [1.7] displays the spectrum of the absorption relaxation rate for both case 1 and 2 coherence factors.

Any first order (linear) approximation on the response-function of a physical system (causal) is constraint to the sum-rule. This theorem stipules that the total integral of the response-function over the full spectrum is a conserved quantity and proportional to the total number of particles:

$$\int_0^\infty \frac{\alpha_s(\omega)}{\alpha_n} d\omega \propto N. \tag{1.2.20}$$

It has been shown that the absorption rate vanishes at frequencies below 2Δ, while being finite in the normal state. To satisfy the sum rule principle, the 'missing area' must be displaced to some other range of the T=0 spectrum. The fundamental difference between the two coherence factors is that for case 1, this 'missing area' is shifted above 2Δ while for case 2 it disappears in the superfluid response (goldstone mode). For electromagnetism the missing spectral weight goes in a dirac peak that builds up at $\omega = 0$: it is this collective mode that is responsible for the Meisner effect (the infinite dc-conductivity is a consequence of the missing spectral weight scenario). In remark, the mode can very well be shifted to finite frequency as it is the observed case in other examples. In conclusion, the condensed phase does not couple to the external perturbation for case 1.

1.3 Other pairing symmetry

The work shown in the previous section can be extended to any other type of pairing mechanism. For example one can used the same tools to grind through the CDW ground state. The author is not aware of any similar analogy in the literature. The CDW state couples an electron and an hole of opposite spin at the antipode of the fermi surface: $(\mathbf{k},\uparrow)_e$ and $(-\mathbf{k},\uparrow)_h$. Other pairing symmetry include:

1. SDW, coupling an electron $(\mathbf{k},\uparrow)_e$ to a hole $(-\mathbf{k},\downarrow)_h$ of same spin.

2. TS (triplet superconductivity), coupling two electrons of same spin but opposite momentum $(\mathbf{k},\uparrow)_e$ and $(-\mathbf{k},\uparrow)_e$ (never observed).

3. Other exotic combinations are two electrons of same momentum and opposite spin $(\mathbf{k},\uparrow)_e$ and $(\mathbf{k},\downarrow)_e$ (case A),

4. or an electron and a hole of same spin and momentum $(\mathbf{k},\uparrow)_e$ and $(\mathbf{k},\downarrow)_h$ that interact (case B).

N.B: The notation used, follows the long tradition of physicists fruitful imaginations, that have lead to the labeling of the difference coherence cases.

1.3.1 Charge Density Waves

In the CDW phase the electrons and holes pair, if their momentum difference is equal to $\mathbf{Q}$ the ordering wave vector. The orientation of $\mathbf{Q}$ indicates a preferential crystallographic axis, consistent with the fact that those transitions are usually observed in one-dimensional metals (very anisotropic already in their normal-state). It will be assumed that $\mathbf{Q} = 2k_F$. The starting point of the discussion is again the mean-field Hamiltonian:

$$\hat{H} = \sum_{\mathbf{k},\sigma} \frac{\hbar^2 k^2}{2m} \hat{a}^\dagger_{\mathbf{k},\sigma} \hat{a}_{\mathbf{k},\sigma} - I \sum_{\mathbf{k},\mathbf{l}} < \hat{a}^\dagger_{\mathbf{l}\uparrow} \hat{a}_{\mathbf{l}-\mathbf{Q}\uparrow} > \hat{a}^\dagger_{\mathbf{k}\downarrow} \hat{a}_{\mathbf{k}-\mathbf{Q}\downarrow} \quad + \quad h.c. \tag{1.3.1}$$

It is convenient to define right and left-going electrons:

$$\hat{c}_{\mathbf{k},0} = \hat{a}_{\mathbf{k}+\mathbf{k}_F\uparrow}; \quad \hat{c}^\dagger_{\mathbf{k},1} = \hat{a}_{\mathbf{k}-\mathbf{k}_F\uparrow}; \quad |k| \ll k_F. \tag{1.3.2}$$

A careful reader will notice that our definition does not conserve the total number of particles, the difficulty was omitted intentionally as it does not affect the end result, but complicate greatly the discussion. An exact definition can be found in Schrieffer's textbook page 52 [178]. Defining a vector:

$$\hat{\Lambda}_{\mathbf{k}} \quad = \quad \begin{pmatrix} \hat{c}_{\mathbf{k},0} \\ \hat{c}^\dagger_{\mathbf{k},1} \end{pmatrix}, \tag{1.3.3}$$

one note that the system is invariant under Galilean boost of $\mathbf{Q}$ momentum.

In the discussion, we will neglect umklapp scattering, where a right-going electron scatters to a left-going one. For probing energies below the gap, the coefficient in front of the $\hat{\gamma}^\dagger_i \hat{\gamma}_i$ (with $i = 1, 0$) is:

$$\left(u^*_{\mathbf{k}'} u_{\mathbf{k}} + \eta v^*_{\mathbf{k}'} v_{\mathbf{k}} \right), \tag{1.3.4}$$

where η is defined by:

$$< \mathbf{k}', 1 | \hat{H}_i | \mathbf{k}, 1 > \quad \equiv \quad +\eta < \mathbf{k}', 0 | \hat{H}_i | \mathbf{k}, 0 > . \tag{1.3.5}$$

Notice that the sign in front of η in Eq. (1.3.5) differs from the earlier result derived for superconductors, Eq. (1.2.5).

Ultrasonic attenuation

The coupling term is a scalar, the η factor in Eq. (1.3.5) is equal to $+1$, or case 2 coherence factor. The result is in agreement with neutrons experiment, where the goldstone mode [66] appears in the phonon spectrum (Kohn anomaly [47]) predicted only for case 2.

Electromagnetic absorption

The electromagnetic hamiltonian is not symmetric under Galilean boost of momentum $\mathbf{Q}$.

$$< \mathbf{k}', \sigma | \hat{H}_i | \mathbf{k}, \sigma > \quad = \quad \frac{-e\hbar}{2mc} \mathbf{A}(\mathbf{k} - \mathbf{k}').(\mathbf{k} + \mathbf{k}' \pm \mathbf{Q}). \tag{1.3.6}$$

But the ground-state condensation occurs only in the neighborhood of the fermi surface, and the electrons affected have a momentum distribution $\delta\mathbf{k}$ of the order $\Delta(0)/v_F$ around $\mathbf{k}_F$. As a first approximation one can only retain the leading term in the expansion in powers of (Δ/ϵ_F):

$$< \mathbf{k}', 1 | \hat{H}_i | \mathbf{k}, 1 > \quad \sim \quad \frac{-e\hbar}{2mc} \sum_{\mathbf{k},\mathbf{k}',\sigma} \mathbf{A}(\mathbf{k} - \mathbf{k}').(-\mathbf{Q}), \tag{1.3.7a}$$

$$< \mathbf{k}', 0 | \hat{H}_i | \mathbf{k}, 0 > \quad \sim \quad \frac{-e\hbar}{2mc} \sum_{\mathbf{k},\mathbf{k}',\sigma} \mathbf{A}(\mathbf{k} - \mathbf{k}').(+\mathbf{Q}). \tag{1.3.7b}$$

The η factor in Eq. (1.3.4) is -1 and one recognizes case 1 coherence factor or a zero dc-conductivity. The approximation above can lead to the presence of a re-normalized collective mode in the spectrum whose dressed mass depends on the ratio Δ/ϵ_F.

Conclusion

One can play a similar game, with other types of pairing. The reader will not be bored by repeating the analysis once more. The coherence factors corresponding to other pairing under various external probes are just listed in Table [1.1]. For SDW, the mean field hamiltonian is of the form:

$$\hat{H} = \sum_{\mathbf{k},\sigma} \frac{\hbar^2 k^2}{2m} \hat{a}^\dagger_{\mathbf{k},\sigma} \hat{a}_{\mathbf{k},\sigma} - I \sum_{\mathbf{k},\mathbf{l}} < \hat{a}^\dagger_{\mathbf{l}\uparrow} \hat{a}_{\mathbf{l}-\mathbf{Q}\downarrow} > \hat{a}^\dagger_{\mathbf{k}\downarrow} \hat{a}_{\mathbf{k}-\mathbf{Q}\uparrow} \quad + \quad h.c. \tag{1.3.8}$$

For TS, the mean field hamiltonian is of the form:

$$\hat{H} = \sum_{\mathbf{k},\sigma} \frac{\hbar^2 k^2}{2m} \hat{a}^\dagger_{\mathbf{k},\sigma} \hat{a}_{\mathbf{k},\sigma} - I \sum_{\mathbf{k},\mathbf{l}} < \hat{a}_{\mathbf{l}\uparrow} \hat{a}_{-\mathbf{l}\uparrow} > \hat{a}^\dagger_{\mathbf{k}\downarrow} \hat{a}^\dagger_{-\mathbf{k}\downarrow} \quad + \quad h.c. \tag{1.3.9}$$

1.3.2 Unconventional pairing

In the BCS model, the gap value $\Delta(T)$ depends on one parameter: the temperature. Several variations from this simple assumption have been attempted: for example, the gap can depend on the quasiparticle energy too $\Delta(T, E)$ and the consequences are referred as strong coupling effects (the problem will be studied in the next chapter). Also, the broken symmetry of the condensed phase can change: for a BCS superconductor, the gap is isotropic and the broken symmetry is the U(1) local gauge (in group theory notation), but the gap can also be k-dependent and follow some non-trivial representation, like 'd-wave' pairing:

$$\Delta_{\mathbf{k}} = \Delta(0) Y_{21}(\hat{k}), \tag{1.3.10}$$

where $Y_{2\pm1}(\hat{k}) = 2\hat{k}_z(\hat{k}_x \pm i\hat{k}_y)$ are the orbital harmonics. The 'd-wave' pairing symmetry (a candidate for the cuprates) posses two lines of nodes around the fermi surface, Fig. [1.8]. In order to understand the consequences of such an assumption, it is necessary to go back to the Landau description of phase transitions. (If the reader is unfamiliar with this formalism, a good introduction can be found in the

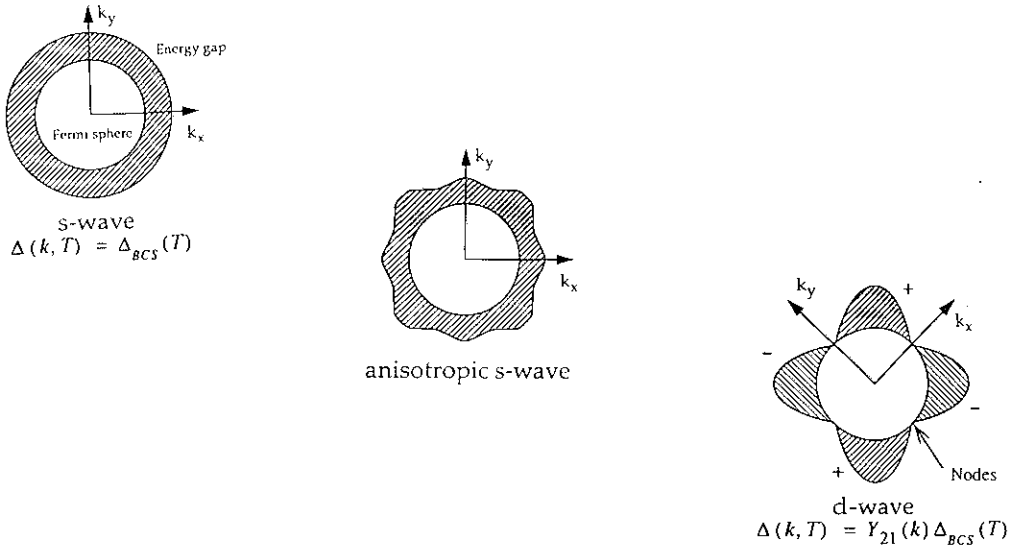

Fig. [1.8]: Schematic illustration of various gap symmetry, the shaded area is the single particle gap that enclosed the fermi sphere. The 'd-wave' pairing has a gap-symmetry in the k-momentum space described by the spherical harmonics $Y_{\ell=2,m}$: notice the alternating sign of each lob and the two line of nodes that crosses in the perpendicular direction.

Landau and Lifshitz Vol. 5 [120].) It has been shown by Gor'kov [69] that the order parameter is equal to the superfluid fraction, related to the gap value ($\propto \Delta$ for $T \ll T_c$ but $\propto \Delta^2$ for $T \sim T_c$). Depending on the broken-symmetry the order parameter can have multiple components: in the BCS model, the order parameter is a complex number (two components: an amplitude and a phase). Each degree of freedom has a collective excitation associated (or a Goldstone mode [67]) and one of those mode couples to electromagnetism. Superconductors are charged fluids with long range order: among the two goldstone modes of the BCS model, one is massive and corresponds to the amplitude modulation of the order parameter. This mode responds at the plasma frequency (for clean metals) because of its coupling with the charge density [28]. It can couple to non-massive modes of an external probe (like transverse fields in electromagnetism) and make those fields become massive (Anderson-Higgs mechanism [13, 86]). In this case, the mode is responsible for the Meisner effect. For lower pairing symmetry, the complex order parameter has other components: it can be as rich as 18 with the five components of the 'd-wave' [87] leading to a complicated phase-diagram.

In the literature several authors have treated the problem of the temperature dependence of the absorption rate for various pairing symmetry. The findings are that the size of the coherence peak decreases with decreasing symmetry as it increases the number of nodes (line or point) in the gap (the nuclear spin relaxation was computed by Hasegawa for anisotropic pairing [81]). Concerning the absorption spectrum, some of the new components of the order parameter couple to the interaction and lead to collective modes [88, 90, 89] that appear as new resonance lines in the spectrum. Those ideas have been principally developed for heavy-fermions superconductors [180].

Chapter 2

Electrodynamics of the Superconducting State

Nothing original is presented in this chapter, the theory was developed more than a decade ago and a complete introduction can be found in Tinkham [188]. In most textbooks however, the presentation of this material is fairly confusing because of the many limiting cases that lead to simplified expressions. Our aim is to write a concise guide (not a complete review) on the area of applicability of several models and focus on the characteristics of the coherence peak.

2.1 Kernel

This chapter studies the current response J_μ of a superconductor irradiated by a transverse electromagnetic field of the form $\exp(i\mathbf{qr} - i\omega t)$. The field, defined by its potential vector A^ν, is viewed as a weak perturbation of the system and only the first order term (linear) in the expansion is retained. We define the Kernel $K_{\mu\nu}$ as the impulse-response in the momentum space:

$$J_\mu(\mathbf{q},\omega) = -\frac{c_o}{4\pi} K_{\mu\nu}(\mathbf{q},\omega) A^\nu. \tag{2.1.1}$$

The metric convention used is $x^\mu = \{x^0, x^1, x^2, x^3\} = \{t, x, y, z\}$ where $x_\mu = g_{\mu,\nu} x^\nu$ with $1 = g_{00} = -g_{11} = -g_{22} = -g_{33}$. The q-dependence of K allows responses which are non-localized (the current at one position may be determined by the field elsewhere). Equivalently the propagator describes the current-current correlation function (fluctuation-dissipation theorem).

2.1.1 Transverse field

As a first step, we found it useful to recall the formulas that describe electromagnetism in solids. One is the current density operator in a superconductor [178]:

$$\begin{aligned} \hat{J}_\mu(\mathbf{q},\omega) &= \frac{e\hbar}{2mV_s} \sum_{\mathbf{k},\sigma} \hat{a}^\dagger_{\mathbf{k},\sigma} \hat{a}_{\mathbf{k}+\mathbf{q},\sigma} (2\mathbf{k}+\mathbf{q}) \\ &\quad - \frac{e^2}{mc_o V_s} A_\mu(\mathbf{q},\omega) \sum_{\mathbf{k},\sigma} \hat{a}^\dagger_{\mathbf{k},\sigma} \hat{a}_{\mathbf{k},\sigma}, \end{aligned} \tag{2.1.2}$$

where V_s is the sample volume. The expression is derived from the momentum operator $(-ih\nabla - e\mathbf{A}/c)$. The current density divides in two parts, the paramagnetic (first term), and diamagnetic current (second term). For the normal fraction of electrons both terms cancel out, while for the superfluid part, the

diamagnetic current dominates (as long as the transverse part of **A** is used) and this gives the London formula. For longitudinal excitations ($\nabla.\mathbf{A} \neq 0$) the paramagnetic current cancels the gauge potential ('diamagnetic') as required by invariance.

The hamiltonian for light absorption is given by Eq. (1.2.10):

$$\hat{H}_i = \frac{-e\hbar}{2mc_o} \sum_{\mathbf{k},\mathbf{k}',\sigma} \mathbf{A}(\mathbf{k}-\mathbf{k}').(\mathbf{k}+\mathbf{k}')\hat{a}^{\dagger}_{\mathbf{k}',\sigma}\hat{a}_{\mathbf{k},\sigma}. \tag{2.1.3}$$

The aim is to compute the expectation value of **J** as a function of **A**. The bold font indicates a vector in cartesian coordinates ($i = 1, 2, 3$), while the operator and the expectation value differ by the hat symbol:

$$\mathbf{J}(\mathbf{q},\omega) = < \hat{\mathbf{J}}(\mathbf{q},\omega) > . \tag{2.1.4}$$

The <> brackets denotes thermal average, as in Eq. (1.1.10).

The expression for **J** is given by the fluctuation-dissipation theorem:

$$\mathbf{J}(\mathbf{q},\omega) \;=\; \lim_{\tau\to\infty} \frac{-i}{\hbar} \int_0^{+\infty} dt \left\langle \left[\hat{\mathbf{J}}^{(H)}(t), \hat{H}_i \right] \right\rangle e^{i\omega t - t/\tau}, \tag{2.1.5}$$

where τ is artificially introduced in the computation to eliminate any non-vanishing contributions to the integrand at large time scales. Physically it represents the time decay of the transport properties due to scattering mechanisms. This expression has the analytical properties of a causal function (Cauchy's theorem [97]) and the Kernel expression follows from the solution of Eq. (2.1.5). The observable $\hat{O}^{(H)}(t)$ is the Heisenberg representation of the Schrödinger operator $\hat{O}$:

$$\hat{O}^{(H)}(t) \equiv e^{iHt}\hat{O}e^{-iHt}. \tag{2.1.6}$$

If one splits the hamiltonian H of the system in two parts: $\hat{H}_o$ the hamiltonian of the unperturbed superconductor (that does not contain time explicitly) and the additional part due to the electromagnetic excitation $\hat{H}_i$:

$$\hat{H} = \hat{H}_o + \hat{H}_i \exp^{-i\omega t}, \tag{2.1.7}$$

then it is tempting to replace $\hat{H}_o$ by the known effective Hamiltonian that accounts for the thermodynamic properties:

$$\hat{H}_n = \sum_{\mathbf{k},\sigma} E_{\mathbf{k}} \hat{\gamma}^{\dagger}_{\mathbf{k},\sigma}\hat{\gamma}_{\mathbf{k},\sigma}. \tag{2.1.8}$$

$\hat{H}_n$ is determined solely by the (temperature dependent) fraction of normal electrons and $E_{\mathbf{k}}$ is their respective energy as defined in Eq. (1.1.18). The difference $\hat{H}_o - \hat{H}_n$ is negligible for all phenomena, however $\hat{H}_n$ is inappropriate for longitudinal excitations as the operator does not conserve the charge quantity and the substitution leads to the more general problem of gauge invariance.

For transverse waves:

$$\hat{H}_o \sim \hat{H}_n, \tag{2.1.9}$$

and the computation of the current density Eq. (2.1.5) can be performed [169].

After some algebra, one obtains the expression:

$$\begin{aligned}
\mathbf{J}(\mathbf{q},\omega) &= \frac{1}{V_s c_o}\left(\frac{e\hbar}{2m}^2\right)\sum_{\mathbf{k}} 2\mathrm{k}[\mathbf{A}(\mathbf{q},\omega).2\mathrm{k}] \\
&\times\left[\left(\frac{1}{E_{\mathbf{k}}+E_{\mathbf{k+q}}-\hbar\omega-i\hbar/\tau}+\frac{1}{E_{\mathbf{k}}+E_{\mathbf{k+q}}+\hbar\omega+i\hbar/\tau}\right)\right. \\
&\times[1-f(E_{\mathbf{k}})-f(E_{\mathbf{k+q}})](u_{\mathbf{k}}v^{\star}_{\mathbf{k+q}}-v_{\mathbf{k}}u^{\star}_{\mathbf{k+q}})^2 \\
&+\left(\frac{1}{-E_{\mathbf{k}}+E_{\mathbf{k+q}}-\hbar\omega-i\hbar/\tau}+\frac{1}{-E_{\mathbf{k}}+E_{\mathbf{k+q}}+\hbar\omega+i\hbar/\tau}\right) \\
&\times\left.[f(E_{\mathbf{k}})-f(E_{\mathbf{k+q}})](u_{\mathbf{k}}u^{\star}_{\mathbf{k+q}}+v^{\star}_{\mathbf{k}}v_{\mathbf{k+q}})^2\right] \\
&-\frac{ne^2}{mc_o}\mathbf{A}(\mathbf{q},\omega). \qquad (2.1.10)
\end{aligned}$$

One recognizes the two coherence factors $p_o^2(\mathbf{k},\mathbf{k}+\mathbf{q})$ and $l_o^2(\mathrm{k},\mathrm{k}+\mathbf{q})$ (case 2) defined in Eq. (1.2.8d).

When the limit $\mathbf{q}$ tends to zero, Eq. (2.1.10) simplifies to:

$$\mathbf{J} = -(\text{positive constant})\mathbf{A}, \qquad (2.1.11)$$

which is precisely the criterion for the Meissner effect.

2.1.2 Longitudinal field

Similarly, one computes the interaction of a longitudinal electric field (defined by its scalar potential Φ) on a charge density $\rho(\mathbf{q},\omega)$ and the result is:

$$\begin{aligned}
\rho(\mathbf{q},\omega) &= -\frac{e^2}{V_s}\sum_{\mathbf{k}}\Phi(\mathbf{q},\omega) \\
&\times\left[\left(\frac{1}{E_{\mathbf{k}}+E_{\mathbf{k+q}}-\hbar\omega-i\hbar/\tau}+\frac{1}{E_{\mathbf{k}}+E_{\mathbf{k+q}}+\hbar\omega+i\hbar/\tau}\right)\right. \\
&\times[1-f(E_{\mathbf{k}})-f(E_{\mathbf{k+q}})](u_{\mathbf{k}}v^{\star}_{\mathbf{k+q}}+v_{\mathbf{k}}u^{\star}_{\mathbf{k+q}})^2 \\
&+\left(\frac{1}{-E_{\mathbf{k}}+E_{\mathbf{k+q}}-\hbar\omega-i\hbar/\tau}+\frac{1}{-E_{\mathbf{k}}+E_{\mathbf{k+q}}+\hbar\omega+i\hbar/\tau}\right) \\
&\times\left.[f(E_{\mathbf{k}})-f(E_{\mathbf{k+q}})](u_{\mathbf{k}}u^{\star}_{\mathbf{k+q}}-v^{\star}_{\mathbf{k}}v_{\mathbf{k+q}})^2\right]. \qquad (2.1.12)
\end{aligned}$$

It is the same expression as Eq. (2.1.10) but with the m_o^2 and n_o^2 coherence factors. This expression is not gauge invariant and the approximation used in Eq. (2.1.9) is not always good. The domain of validity of Eq. (2.1.12) is when the following inequality is satisfied:

$$\hbar\omega \ll \hbar v_F q \ll 2\Delta. \qquad (2.1.13)$$

That corresponds to the already encountered case of longitudinal acoustic waves attenuation.

2.1.3 Gauge invariance

So far, the derivation has been based solely on the quasiparticle response, but this simplification leads to unphysical results such as non-conservation of the charge quantity. This problem is linked to the early

criticism of the BCS theory: for longitudinal fields, the current density carried by a quasiparticle is no longer equal to the charge carried by the wave-packet multiplied by the velocity. A complete derivation based on a gauge invariant Hamiltonian was first performed by G. Rickayzen in 1958 [168].

2.2 Microwave properties

The remaining discussion reviews the electrodynamic properties of a superconductor under a transverse wave excitation.

2.2.1 Complex conductivity

The complex conductivity in the Fourier space is defined as the ratio of the current density to the electric driving field:

$$\frac{\mathbf{J}(\mathbf{q},\omega)}{\mathbf{E}} \equiv \hat{\sigma} = \sigma_1 + i\sigma_2. \tag{2.2.1}$$

It includes both an ohmic and eddy current term.

In the London gauge ($\phi = 0$), there is a simple relation between the Kernel, defined in Eq. (2.1.1), and the conductivity:

$$\hat{\sigma}(\mathbf{q},\omega) = -\frac{{c_o}^2}{4\pi i\omega} K(\mathbf{q},\omega). \tag{2.2.2}$$

Light probes, in general, average electrodynamic response over several lattice sites (the wavelength is larger than the lattice constant), thus for most metals, the local ($\mathbf{q} = 0$) response is dominant. However, in very clean conductors, the length scale can be regulated by some other intrinsic parameter such as the mean-free-path, ℓ, or the coherence length, $\xi(0)$. A careful treatment of those various cases will be done in what follows.

2.2.2 Mattis-Bardeen

A first limit of Eq. (2.1.10) was investigated by Mattis and Bardeen in 1958 [135]. When $\tau \to \infty$ the equation simplifies to:

$$\frac{\hat{\sigma}}{\sigma_n} = \frac{2}{\omega}\int_{\Delta}^{\infty}[f(u) - f(u+\omega)]g(u)du + \frac{1}{\omega}\int_{\Delta-\omega}^{\Delta}[1 - 2f(u+\omega)]g(u)du, \tag{2.2.3}$$

where

$$\begin{aligned}
g(u) &= (u^2 + \Delta^2 + \omega u)/u_1 u_2, \qquad \text{where} \begin{cases} u_1 = \mathrm{sgn}(u)\sqrt{u^2-\Delta^2} & |u| > \Delta \\ \quad = -i\sqrt{\Delta^2 - u^2} & |u| < \Delta \end{cases} \\
& \qquad\qquad\quad u_2 = \sqrt{(u+\omega)^2 - \Delta^2} \\
f(u) &= 1/[1 + \exp(u/T)], \\
\omega &\equiv \hbar\omega,\ T \equiv k_B T \text{ and } \Delta \equiv \text{BCS gap.}
\end{aligned}$$

From this expression, one derives the corresponding spectrum of the conductivity at zero temperature:

$$\frac{\sigma_1}{\sigma_n} = \left[1 + \frac{2\Delta(0)}{\hbar\omega}\right]E(k) - \frac{4\Delta(0)}{\hbar\omega}K(k), \tag{2.2.4a}$$

$$\frac{\sigma_2}{\sigma_n} = \frac{1}{2}\left[1 + \frac{2\Delta(0)}{\hbar\omega}\right]E(k') - \frac{1}{2}\left[1 - \frac{2\Delta(0)}{\hbar\omega}\right]K(k'), \tag{2.2.4b}$$

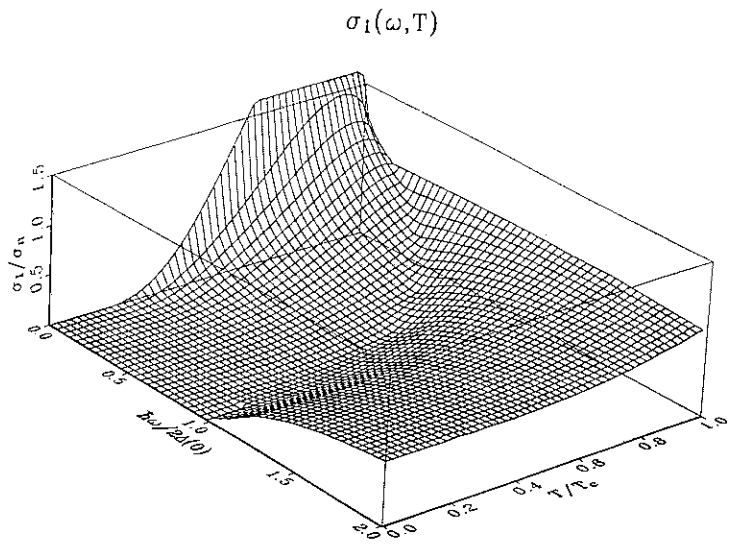

Fig. [2.1]: Temperature and frequency dependence of the conductivity $\sigma_1(T,\omega)$ as evaluated from the Mattis-Bardeen expression, Eq. (2.2.3). The coherence peak exists only at low frequencies $\hbar\omega/2\Delta(0) < .1$. The local minimum is the energy gap.

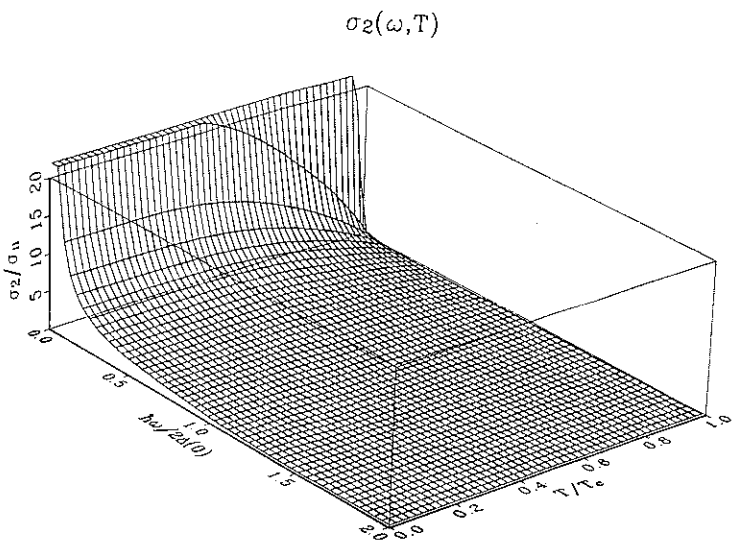

Fig. [2.2]: $\sigma_2(T,\omega)$ as evaluated from the Mattis-Bardeen expression, Eq. (2.2.3). σ_2 diverges as $1/\omega$ below the gap and saturates in temperature to $\pi\Delta(0)/\hbar\omega$.

where E and K are the complete elliptic integrals and:

$$k' = \sqrt{1-k^2}, \tag{2.2.5a}$$

$$k = \left|\frac{2\Delta(0)-\hbar\omega}{2\Delta(0)+\hbar\omega}\right|. \tag{2.2.5b}$$

Figs. [2.1] and [2.2] summarize the temperature and frequency dependence of σ_1 and σ_2 respectively as derived from Eq. (2.2.3). It reproduces the behavior predicted for case 2 coherence factors (Figs. [1.6] and [1.7]) inferred from symmetry argument only. $\sigma_1(T)$ shows a peak just below T_c at low frequency. The height of the peak goes as:

$$\frac{\sigma_1{}^*}{\sigma_n} \sim \log\left(\frac{2\Delta(0)}{\hbar\omega}\right), \tag{2.2.6}$$

where $\sigma_1{}^*/\sigma_n \equiv (\sigma_1/\sigma_n)_{\max}$. The peak has completely disappeared for $\hbar\omega \geq \Delta/5$ (well before 2Δ). In conclusion, a photon energy below the single particle gap is not a sufficient condition to observe the coherence peak. The width of the peak is slightly frequency dependent and its qualitative behavior will be discussed later (the dependence is shown in Fig. [2.10] for $\ell/\pi\xi(0) = 0.1$). $\sigma_1(T)/\sigma_n$ can be approximated by the following algebraic formula:

$$\frac{\sigma_1(T)}{\sigma_n} \sim 2f[\Delta(T)]\left\{1+\frac{\Delta(T)}{k_BT}[1-f(\Delta(T))]\ln\left[\frac{2\Delta(T)}{\hbar\omega}\right]\right\}. \tag{2.2.7}$$

This expression is identical to Eq. (1.2.18), where $\Delta_c = \hbar\omega$.

On the other hand, σ_2/σ_n is related to the gap parameter through the expression:

$$\frac{\sigma_2(T)}{\sigma_n} \sim \frac{\pi\Delta(T)}{\hbar\omega}\tanh\left[\frac{\Delta(T)}{2k_BT}\right]. \tag{2.2.8}$$

As mentioned at the beginning, Mattis-Bardeen uses the approximation that ($\tau \gg \hbar/\Delta > \lambda/v_F$) to

simplify the algebra. S.B. Nam [145] however, showed that the definition domain of those equations is more general and the formulas are also valid for dirty superconductors when $\tau \rightarrow 0$ (all those different regimes are defined later).

2.2.3 Surface impedance

In the microwave range, one measures the surface impedance. This parameter is meaningful only in the limit where the field decays to zero well inside the sample. The field is screened from the interior if the light penetrates on a length scale smaller than the sample dimensions. This length scale is defined by wavevector inside the material:

$$\delta \equiv \frac{1}{\Im(\hat{k})}, \tag{2.2.9}$$

and an expression for $\hat{k}$ is derived from the eddy-current equation (Ampère's law):

$$\hat{k}^2 = \frac{i4\pi\hat{\sigma}\omega}{c_o^2}. \tag{2.2.10}$$

The length scale δ is the skin-depth for a metal and the penetration depth for a superconductor. It is assumed that the surface is flat at the scale of δ.

The surface impedance is a complex number:

$$Z_s = R_s \ - iX_s, \tag{2.2.11}$$

where R_s is the surface resistance and X_s is the surface reactance. The surface impedance is defined [119] as the ratio of the electric and magnetic strength at the surface of the metal:

$$Z_s \equiv \frac{\mathbf{E}_{||}}{\mathbf{H}_{||}} = \frac{\mathbf{E}_{||}}{\int_0^\infty \mathbf{J}_{||} dz}, \tag{2.2.12}$$

where $\mathbf{E}_{||}$ and $\mathbf{H}_{||}$ are the electric and magnetic fields respectively, in the plane of the surface, and z is measured normal to the surface. For an isotropic media the two fields are orthogonal. We use a definition that is unitless and normalized by the impedance of the vacuum $Z_o = 4\pi/c_o = 377\Omega$.

2.2.4 Specular and diffuse scattering

In order to relate Z_s to the Kernel defined in Eq. (2.1.1), one has to deal with another difficulty, that is the behavior of the electrons at the boundary of the metal. There are two cases that have been studied:

- Diffuse scattering, where it is assumed that the electrons lose their drift velocity when they reach the surface (the charged-particle $\mathbf{q}$ vanishes at the boundary) and

$$Z_s(\omega) \ = \ 4\pi^2 i\omega \left(\int_0^\infty \ln[1 + K(\mathbf{q},\omega)/q^2] dq \right)^{-1}. \tag{2.2.13a}$$

- Specular scattering, where it is assumed that the electron is reflected at the surface, this limit is equivalent to the assumption of periodic boundary conditions in the Fourier space:

$$Z_s(\omega) \ = \ 8i\omega \int_0^\infty \frac{dq}{q^2 + K(\mathbf{q},\omega)/4\pi}. \tag{2.2.13b}$$

Despite the fact that the two expressions have very different forms, the end results only differ slightly by a constant prefactor in the anomalous regime (defined later), where the gradient of the field is so small that one has to correct for effects within the q length-scale. It is important to note that the relation between the surface impedance and complex conductivity is not a constant one, but is dependent on several parameters to be discussed shortly.

2.3 Various regimes

The electrodynamic response has different form depending how the three length scales (ℓ, ξ_o, λ_L) compare to each other.

2.3.1 local and anomalous regime

For classical metals the relation between the current and the field is a *local* one, i.e. that the current density at one point in the conductor depends on the field at that position only (Ohm's law). This condition presupposes that the electron mean-free-path (ℓ) is small compared with the distances over which the field varies (the skin-depth δ). In this case the field decays exponentially as it penetrates in the sample. Then, the surface impedance is simply equal to the complex refractive index $\sqrt{\hat{\epsilon}}$ where $\hat{\epsilon} = 4\pi i\hat{\sigma}/\omega$:

$$Z_s = \sqrt{\frac{\omega}{4\pi i(\sigma_1 + i\sigma_2)}}, \tag{2.3.1}$$

This definition is *independent* of the surface geometry. A development of the previous expression gives:

$$R_s = \sqrt{\frac{\omega}{4\pi}} \frac{1}{\sqrt{{\sigma_1}^2 + {\sigma_2}^2}} \sqrt{\frac{-\sigma_2 + \sqrt{{\sigma_1}^2 + {\sigma_2}^2}}{2}}, \tag{2.3.2a}$$

and

$$X_s = \sqrt{\frac{\omega}{4\pi}} \frac{1}{\sqrt{{\sigma_1}^2 + {\sigma_2}^2}} \sqrt{\frac{+\sigma_2 + \sqrt{{\sigma_1}^2 + {\sigma_2}^2}}{2}}. \tag{2.3.2b}$$

It is assumed that the permeability $\mu \sim 1$, usually the case for metals [119]. For a good metal $\sigma_1 \gg \sigma_2$ in the mm-wave range, the classical skin-depth of Eq. (2.2.10) is defined:

$$\delta_o = \frac{c_o}{\sqrt{2\pi\omega\sigma_1}}. \tag{2.3.3}$$

In this regime the surface impedance has the simple form:

$$R_s = X_s = \frac{\omega}{c_o}\frac{\delta_o}{2}. \tag{2.3.4}$$

In the superconducting phase $\sigma_2 \gg \sigma_1$ and $1/\Im(\hat{k})$ is called the penetration depth:

$$\lambda = \frac{c_o}{\sqrt{4\pi\omega\sigma_2}}. \tag{2.3.5}$$

In this regime, the surface impedance tends to the value:

$$R_s \sim 0 \text{ and } X_s = \frac{\omega}{c_o}\lambda. \tag{2.3.6}$$

The former equation assumes that the frequency is low enough that electromagnetic oscillations within the mean-free-path can be neglected. The simplest model that accounts for scattering time is the Drude model:

$$\hat{\sigma} = \frac{n_e e^2 \tau}{m} \frac{1}{1 - i\omega\tau}. \tag{2.3.7}$$

The model studied above corresponds to the regime where $\omega\tau < 1$ (Hagen-Rubens), and $\sigma_o = \sigma(\omega = 0)$. Another limit is when $\omega\tau > 1$, the relaxation regime. Using Eq. (2.3.2a) one computes the surface resistance:

$$R_s \sim \frac{1}{4\sqrt{\pi\sigma_o\tau}} = \frac{1}{2\omega_p\tau}, \tag{2.3.8}$$

and $X_s \sim 2\omega\tau R_s$. The skin-depth, defined by Eq. (2.2.10), has the form:

$$\delta = \delta_o \sqrt{\frac{\omega\tau}{2}}. \tag{2.3.9}$$

A complete list of all the correction factors for a Drude metal is in Table [2.1].

The opposite limiting case is when $\delta \ll \ell$ and the classical theory is no longer valid [162] (the wave propagation is not exponential). This limit is called the *anomalous regime* and all the equations derived above have to be modified. The exact solution is elaborate [164] and a simplified picture is to suppose that only a fraction $\alpha\delta/\ell$ of the electrons are effective in the conductivity ($\sigma_1 = \alpha\sigma_o\delta/\ell$). If we solve Eq. (2.3.3) self-consistently the skin-depth is:

$$\delta^3 = \frac{c_o^2 \ell}{2\pi\alpha\sigma_o\omega}. \tag{2.3.10}$$

The factor α was computed by Reuter and Sondheimer in 1948 [164]. For specular scattering, $\alpha = 3^{11/2}\pi/128 \sim 10$ and for diffuse scattering $\alpha = 4\pi/\sqrt{3} \sim 7$. The expression for the surface resistance follows:

$$R_s = \frac{2\pi\omega}{c_o^2} \left(\frac{c_o^2 \ell}{2\pi\alpha\sigma_1\omega} \right)^{1/3}, \tag{2.3.11a}$$

and

$$X_s = \sqrt{3} R_s. \tag{2.3.11b}$$

In summary the relation between the conductivity and the surface impedance is not universal, in the local regime ($\omega\tau < 1$):

$$\frac{Z_s}{R_n} = \sqrt{2} \left(\frac{i\hat{\sigma}}{\sigma_n} \right)^{-1/2}, \tag{2.3.12a}$$

while in the anomalous regime:

$$\frac{Z_s}{R_n} = 2 \left(-\frac{\hat{\sigma}}{\sigma_n} \right)^{-1/3}. \tag{2.3.12b}$$

	Hagen-Rubens regime $x < 1$	Relaxation regime $x > 1$
$R_s = \frac{\omega}{c_o}\frac{\delta_o}{2}\times$	$(1 - \frac{x}{2} + \frac{x^2}{8} + O[x^3])$	$(\frac{1}{\sqrt{2x}} - \frac{1}{2(2x)^{5/2}} + O[x^{-9/2}])$
$X_s = \frac{\omega}{c_o}\frac{\delta_o}{2}\times$	$(1 + \frac{x}{2} + \frac{x^2}{8} + O[x^3])$	$(\sqrt{2x} + \frac{1}{2(2x)^{3/2}} + O[x^{-7/2}])$
$\frac{X_s}{R_s} =$	$(1 + x + \frac{x^2}{2} + O[x^3])$	$(2x + \frac{1}{2x} - \frac{1}{8x^3} + O[x^{-5}])$
$\delta = \delta_o\times$	$(1 - \frac{x}{2} + \frac{5x^2}{8} + O[x^3])$	$(\sqrt{\frac{x}{2}} + \frac{3}{2(2x)^{3/2}} + O[x^{-7/2}])$

Drude metal:

$\sigma = \frac{n_e e^2 \tau}{m}\frac{1}{1-i\omega\tau}$

$x = \omega\tau$

$\sigma_o = \sigma(\omega = 0)$

$\delta_o = c_o/(2\pi\omega\sigma_o)^{1/2}$

Table 2.1: Correction factor for the electrodynamic properties of a Drude metal in the local regime.

The subscript n, indicates the normal-state value, or the value just above the transition temperature T_c. The dc-value of the conductivity differs between the two regimes. In the local limit σ_n is given by:

$$\sigma_o = \frac{{\omega_p}^2}{4\pi}\tau, \tag{2.3.13}$$

while in the anomalous regime:

$$\sigma_o = \frac{3\pi}{4qv_F\tau}. \tag{2.3.14}$$

In the superconducting phase $\sigma_2 \gg \sigma_1$, the local expression above simplifies to:

$$\frac{Z_s}{R_n} \sim \sqrt{\frac{2\sigma_n}{\sigma_2}}\left(\frac{\sigma_1}{2\sigma_2} - i\right). \tag{2.3.15a}$$

Using Eqs. (2.2.7) and (2.2.8), we derive the important relation that $R_s \propto \omega^2$ below T_c. In contrast, in the anomalous regime the surface impedance of a superconductor is approximately:

$$\frac{Z_s}{R_n} \sim 2\left(\frac{\sigma_n}{\sigma_2}\right)^{1/3}\left(\frac{\sigma_1}{3\sigma_2} - i\right). \tag{2.3.15b}$$

2.3.2 London limit and Pippard limit

The electromagnetic response of a superconductor is dictated by three parameters: the mean-free-path, ℓ, the coherence lenght, ξ, and the pentration depth, λ. The expressions for ξ and λ differs depending on the

particular regime. The coherence length $\xi(T)$ is defined by

$$\lim_{q\to\infty} \frac{qK(q,0)}{K(0,0)} \equiv \frac{3\pi}{4\xi(T)}, \tag{2.3.16a}$$

it represents the mean distance between electrons of a Cooper pair. In the normal-state, the former equation defines also the mean-free-path. The penetration depth gives the length-scale of the magnetic field decay in a superconductor, it was defined by Eq. (2.2.9) or for specular scattering:

$$\lambda(T) \equiv \frac{2}{\pi}\int_0^\infty \frac{dq}{q^2 + K(\mathbf{q},\omega)/4\pi}. \tag{2.3.16b}$$

The values of ξ and λ will be expressed in terms of two material dependent quantities, that were defined on page 3, it was ξ_o, the BCS coherence length of Eq. (1.1.7) and λ_L, the London penetration depth.

A superconductor may be classified as being in one of the three domains:

- *The local regime* is characterized by the condition $\ell < \xi(0)$. The limit in which $\ell/\xi(0) \to 0$ is called the *dirty limit.*

When non-local effects are important, $\ell/\xi(0) \to \infty$ (or *clean limit*), it is necessary to introduce:

- *The Pippard regime* or *anomalous regime*, is that in which $\ell > \xi(0)$ and $\xi(0) > \lambda$. This is the regime of type I superconductors.

- *The London regime* is that in which $\ell > \xi(0)$ and $\xi(0) < \lambda$. This is the regime of type II superconductors.

In Fig. [2.3] one can find a schematic definition of those limits, expressed with the three length-scales (ξ_o, ℓ, λ_L). The figure would have looked different if drawn in terms of $\xi(0)$ and λ: two shares of the pie would have disappeared. It is now worth pointing out that among the six domains that define all the permutations possible, only three regimes need to be distinguished for the analysis (local, Pippard and London).

S.B. Nam showed that $\hat{\sigma}/\sigma_n$ was equal both in the Pippard and local limits [145] (but the surface impedance value is different as the relation between Z_s and $\hat{\sigma}$ changes, Fig. [2.4]). The domain of validity for the Mattis-Bardeen expression is then all of the shaded area in Fig. [2.4].

2.3.3 $K(\mathbf{q})|_{\omega=0}$

The zero-frequency limit of the Kernel describes the penetration depth. The q-dependence of the Kernel is represented in Fig. [2.5] for different regimes. At zero-temperature, $\xi(0) \to 0$ in both the local and London limits: for both cases the q-dependence of the Kernel is negligible (scales as $1/\xi(0)$) and K is dominated by the $\mathbf{q} = 0$ part:

$$K(\mathbf{q}, \omega = 0) \sim K(0,0). \tag{2.3.17}$$

Notice however that the $K(0,0)$ value differs between the two limits, but the surface impedance expression (specular and diffuse) is identical.

On the other hand, in the Pippard limit $\xi(0) \to \infty$; the $q = \infty$ behavior of the Kernel determines the integrand of Eq. (2.2.13a). At large q, the Kernel K(q) varies as $1/q$:

$$K(\mathbf{q}) = \frac{3\pi}{4}\frac{1}{\lambda(0)^2\xi(0)}\frac{1}{q}. \tag{2.3.18}$$

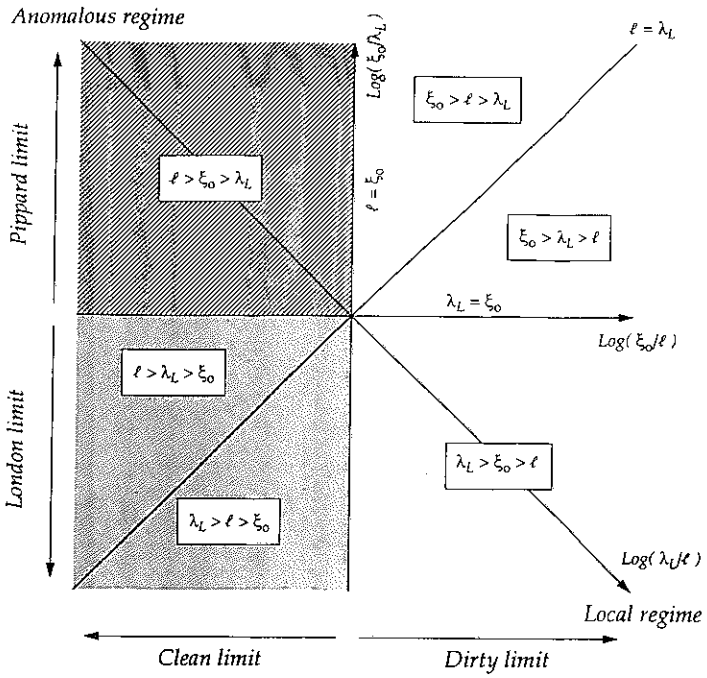

Fig. [2.3]: Schematic representation of the definition domain for the local, London and Pippard limit.

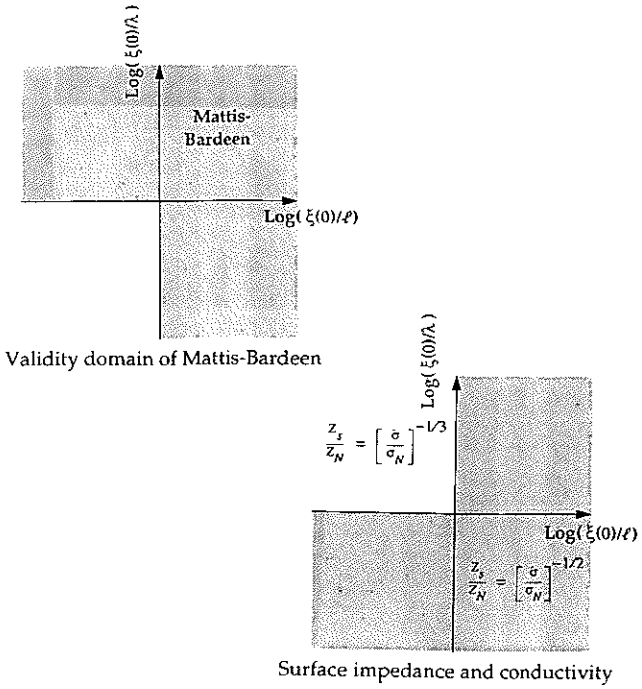

Fig. [2.4]: Schematic representation of the validity domain of the Mattis Bardeen expression.

As mentioned above, the conductivity value is identical in the Pippard and local regime but the penetration-depth value differs as it depends on the q-integrated value of the conductivity. The temperature dependence of the penetration depth $\lambda(T)$ is regulated by the parameter S defined as:

$$S(T) = \frac{\Delta(T)}{\Delta(0)} \tanh \frac{\Delta(T)}{2k_B T}. \tag{2.3.19}$$

Using Eq. (2.3.5) in the local limit [145]:

$$\frac{\lambda_L}{\lambda_l(T)} = \sqrt{\frac{\ell}{\xi_o} S(T)}, \tag{2.3.20}$$

or can be expressed equivalently [178]:

$$\frac{\sigma_2}{\sigma_n} = \frac{\pi \Delta(T)}{\hbar \omega} \tanh \frac{\Delta(T)}{2k_B T}. \tag{2.3.21}$$

In the anomalous regime (diffuse scattering):

$$\frac{\lambda_L}{\lambda_P(T)} = \left[\frac{3\pi^2}{4} \frac{\lambda_L}{\xi_o} S(T) \right]^{1/3}. \tag{2.3.22}$$

The different results are represented in Fig. [2.6].

Only the London limit has not been covered yet by the discussion. In this regime, the temperature dependence of the penetration-depth is given by the Yosida function [199], with behavior similar to that observed in spin-susceptibility. The purpose of the next part is then to study the crossover from the local to the London limit, where by definition:

$$\left[\frac{\lambda_l(T)}{\lambda_L(T)} \right]^2 = \frac{\xi(T)}{\ell}. \tag{2.3.23}$$

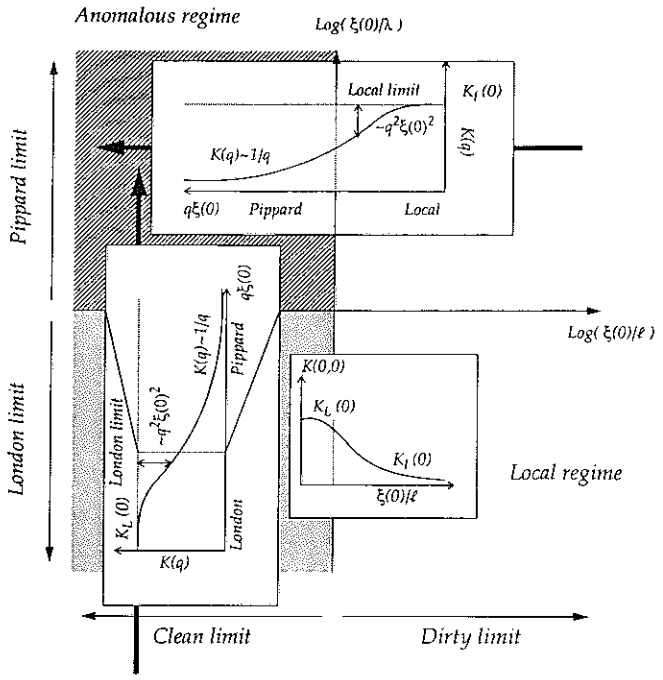

Fig. [2.5]: Schematic representation of the q-dependence of the Kernel at $\omega = 0$, notice that both the London and local limit are dominated by the $q = 0$ value, while the Pippard measure the $\mathbf{q} = \infty$ domain.

2.3.4 $K(\omega)|_{\mathbf{q}=0}$, impurity effect

The temperature dependence of the coherence length follows from the expression:

$$\frac{1}{\xi(T)} = \frac{1}{\ell} + \frac{\alpha(T)}{\xi_o}, \tag{2.3.24}$$

where the value of $\alpha(T)$ is derived from the Far-Grover sum-rule [188]. The function $\alpha(T)$ decreases monotonically from $\alpha(T = T_c) = 1.33$ to $\alpha(T = 0) = 1$.

As we know already, the spectrum of $\sigma_1(\omega)$ is a conserved quantity and its weight is fixed by the plasma frequency:

$$\int_0^\infty \sigma_1(\omega) d\omega = \frac{\omega_p^2}{8}. \tag{2.3.25}$$

The conductivity obeys case 2 coherence factors and the missing area A in the spectrum of a superconductor at zero-temperature, creates a Dirac δ function (the goldstone mode) at $\omega = 0$ that represents the electromagnetic response of the superfluid fraction (Meisner effect). The Kramers-Kronig relation implies that:

$$\sigma_2 = \frac{2A}{4\pi\omega} = \frac{c_o^2}{4\pi\omega}\frac{1}{\lambda(T)^2}. \tag{2.3.26}$$

The formula for the penetration depth is then simply related to this missing spectral weight:

$$\lambda(T) = \frac{c_o}{\sqrt{8A}}. \tag{2.3.27}$$

It is clear from the Fig. [2.7] that A depends on the value of the scattering rate $1/\tau$. The figure uses the Drude model to explain the impurity dependence of the electrodynamics.

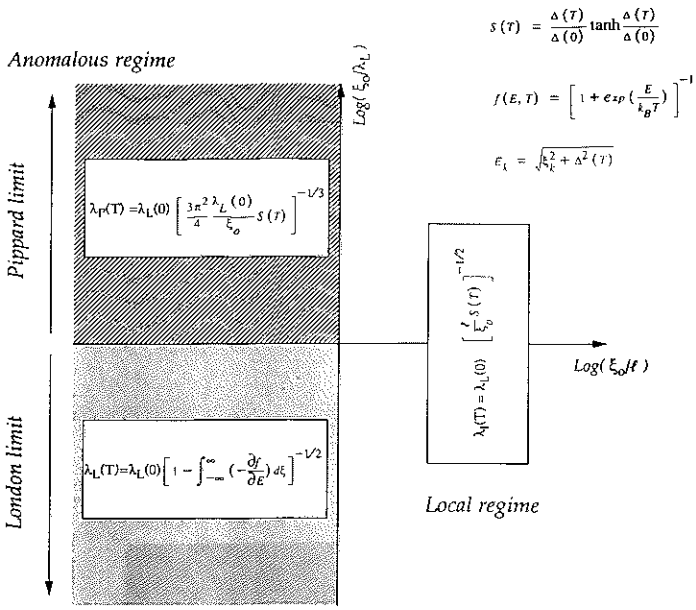

Fig. [2.6]: Expression of the temperature dependence of the penetration depth $\lambda(T)$ in different regimes. The result is shown in the inset.

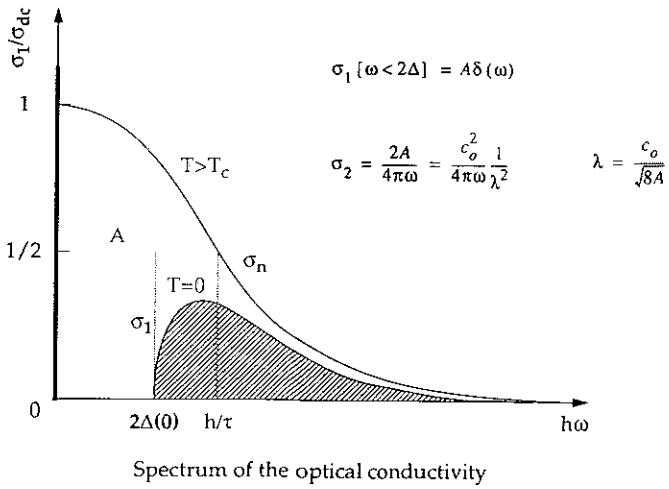

Fig. [2.7]: Schematic representation of the spectrum of the optical conductivity σ_1 both in the normal ($T > T_c$) and superconducting state ($T = 0$) for a Drude metal, the electrodynamics properties of the condensate are determined by the missing spectral weight A that depends on how $1/\tau$ compares with Δ.

1. For $\ell/\pi\xi(0) > 1$ or $\hbar/\tau < \Delta(0)$, the London limit:

$$A = \frac{\omega_p^2}{8} \quad \text{and} \quad \lambda_L(0) = \lambda_L, \tag{2.3.28}$$

$$\sigma_2 = \frac{\omega_p^2}{4\pi\omega} \quad \text{or} \quad \frac{\sigma_2(0)}{\sigma_n} = \frac{1}{\omega\tau}. \tag{2.3.29}$$

2. For $\ell/\pi\xi(0) < 1$ or $\hbar/\tau < \Delta(0)$, the local limit:

$$A = \frac{\pi^2}{2}\frac{\Delta(0)\sigma_n}{\hbar} \quad \text{and} \quad \lambda_l(0) = \lambda_L\sqrt{\frac{\xi_o}{\ell}}, \tag{2.3.30}$$

$$\frac{\sigma_2(0)}{\sigma_n} = \frac{\pi\Delta(0)}{\hbar\omega}. \tag{2.3.31}$$

A complete mapping of the height and width of the coherence peak, going from the local to London limit was done through computer simulations and the result is plotted in Figs. [2.9] and [2.10]. The Mattis-Bardeen result is recovered for small mean-free-path. The obtained values are identical to the predicted results of Chang and Scalapino [43].

Another question then rises: how does the shape (width and height) of the coherence peak change if the scattering rate $1/\tau$ varies with temperature? The dominant effect is the temperature dependence of the normalization parameter ($\sigma_n \propto \tau$) and in general $\sigma_n(T < T_c)$ is not easily accessible (one can drive the sample normal by applying a magnetic field above H_{c2}, but then one has to solve other associated problems, like magnetoresistance effects etc...). The experimental data is usually only divided by the measured value of σ_1 just above T_c, without taking account of the change of the σ_n value below T_c. The theoretical fit however can include any arbitrary $\tau(T)$ function and some examples are shown in Figs. [2.11] and [2.12]. In the two figures the change of $\tau(T)$ in Eq. (2.1.10) was also taken into account as a second order effect. The main conclusion is that the shape (width and height) is not very sensitive to the temperature variation

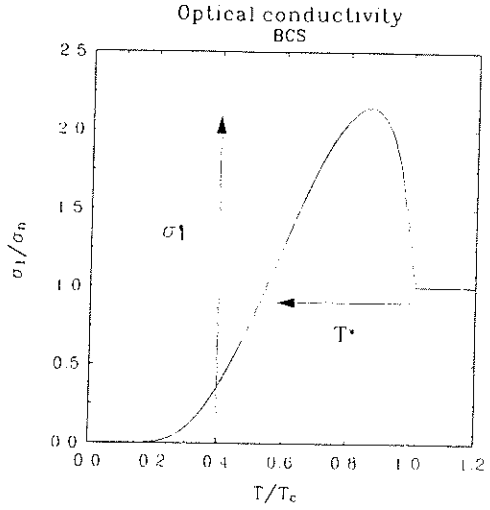

Fig. [2.8]: Characterisation of the coherence peak height $\sigma_1{}^*$ and width T^* in reduced units.

of $\tau(T)$ and a linear temperature dependence, $\tau(T_c)/\tau(T) = (T/T_c)^\alpha$ with α=1, has almost the same shape as the direct BCS result (α=0). One need some drastic variation ($\alpha > 3$) to change the shape apreciably, and this affects primarily the width of the peak.

2.4 Strong coupling

One of the fundamental assumptions of the BCS model is that the attractive pseudo-potential between electrons can be approximated by a two-square-well form. More elaborate solution have been attempted by taking into account the retarded nature of the interaction between the electrons (life-time effect are introduced through an imaginary component in the gap, $\Delta = \Delta_1 + i\Delta_2$). Those effects are important for materials with large coupling constants. In the model, the gap depends on the quasiparticle energy (ω) and the form of $\Delta(\omega, T)$ fits the exact electron-boson (phonon) spectral density $\alpha^2F(\omega)$ of the element. The Coulomb coupling constant κ is:

$$\kappa = 2\int_0^\infty d\omega\alpha^2\frac{F(\omega)}{\omega}. \tag{2.4.1}$$

The equivalent of the cut-off frequency introduced by BCS, is the average boson (phonon) frequency:

$$\omega_{ln} = \exp\left(\frac{2}{\kappa}\int_0^\infty \ln(\omega)\frac{\alpha^2F(\omega)}{\omega}d\omega\right). \tag{2.4.2}$$

In this case the Eq. (1.2.18) developed by BCS is replaced by

$$\frac{2\Delta(0)}{k_BT_c} = 3.53\left[1 + 12.5\left(\frac{T_c}{\omega_{ln}}\right)^2\ln\left(\frac{T_c}{\omega_{ln}}\right)\right], \tag{2.4.3}$$

which is a simplified form of the Allen-Dynes equation [6]. Strong coupling modified the density of states divergence:

$$\frac{N_s(\omega)}{N_n(\omega)} = \Re\left(\frac{\omega}{\sqrt{\omega^2 - \Delta^2(\omega)}}\right) \tag{2.4.4}$$

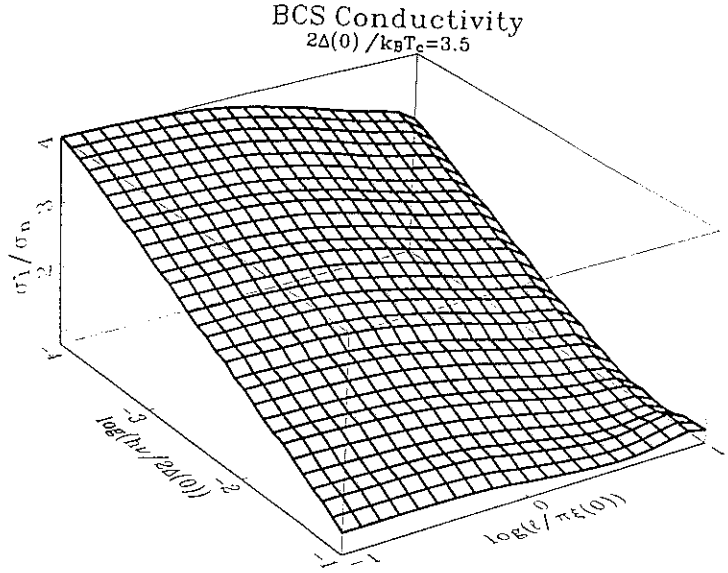

Fig. [2.9]: Mean-free-path and frequency dependence of the height of the coherence peak at the cross-over between the London and local regime. The quantity $\sigma_1{}^*$ is defined in Fig. [2.8].

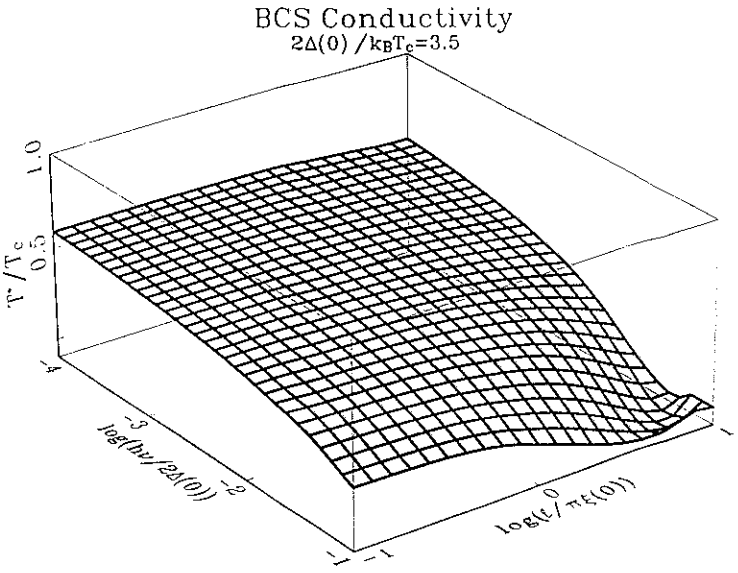

Fig. [2.10]: Mean-free-path and frequency dependence of the width of the coherence peak.

The gap edge is defined by the equation $\Delta_1 = \Delta(\omega = \Delta_1, T)$. The important conclusion is that strong coupling attenuates the singularity in the excitation density of states [7] and thus decreases the size of the coherence peak [62, 133]. An evaluation of the effect can be obtained by replacing $\Delta_1 = \Delta_{BCS}(T)$ and $\Delta_2 = \Delta_c$ in Eq. (1.2.18). For completeness, it is useful to recall Fibich's result [60] for Al:

$$\frac{\Delta_2(T)}{\Delta(0)} = -1.5 \times 10^{-2} \left[\frac{\Delta(0)}{\Delta(T)}\right]^{1/3} \left(\frac{T}{T_c}\right)^{8/3}. \tag{2.4.5}$$

In the London limit, the effect is more subtle and requires a knowledge of the renormalization factor Z(ω):

$$Z(i\omega_n) = 1 + \frac{\pi T}{\omega_n} \sum_m \kappa(i\omega_m - i\omega_n) \frac{\omega_m}{\sqrt{\omega^2{}_m + \Delta^2(i\omega_m)}}, \tag{2.4.6}$$

which depends on the impurity and coupling constants. The notation used the nth Matsubara frequency $\omega_n = \pi k_B T(2n-1)$ that simplifies thermally averaged expressions:

$$\sum_{n=-\infty}^{\infty} F(i\omega_n) = \frac{i}{2\pi k_B T} \int_C \frac{F(\omega)}{\exp(\omega/k_B T) + 1}. \tag{2.4.7}$$

The end result was derived by S.B. Nam [146] in 1967, in the London limit the surface impedance of strong coupling superconductors is

$$\frac{\omega}{c_o} Z_s = \left(\frac{4}{3}\pi N(0) e^2 {v_F}^2 T \sum_{n=1}^{\infty} \frac{\Delta^2(i\omega_n)}{Z(i\omega_n)[\omega_n^2 + \Delta^2(i\omega_n)]^{3/2}}\right)^{-1/2}, \tag{2.4.8}$$

to compare with the local limit expression:

$$\frac{\omega}{c_o} Z_s(T) = \left(\frac{8}{3}\pi N(0) e^2 {v_F}^2 \tau T \sum_{n=1}^{\infty} \frac{\Delta^2(i\omega_n)}{\omega_n^2 + \Delta^2(i\omega_n)}\right)^{-1/2}. \tag{2.4.9}$$

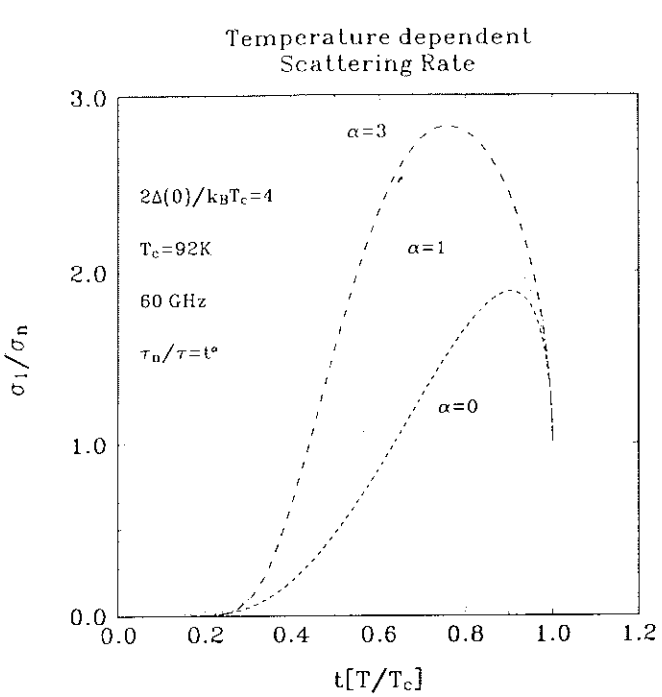

Fig. [2.11]: Change of the coherence peak shape for a temperature dependent scattering rate that follows various power laws, with $\hbar/\tau(T_c) = \Delta$ or $\ell/\pi\xi_o = 1$.

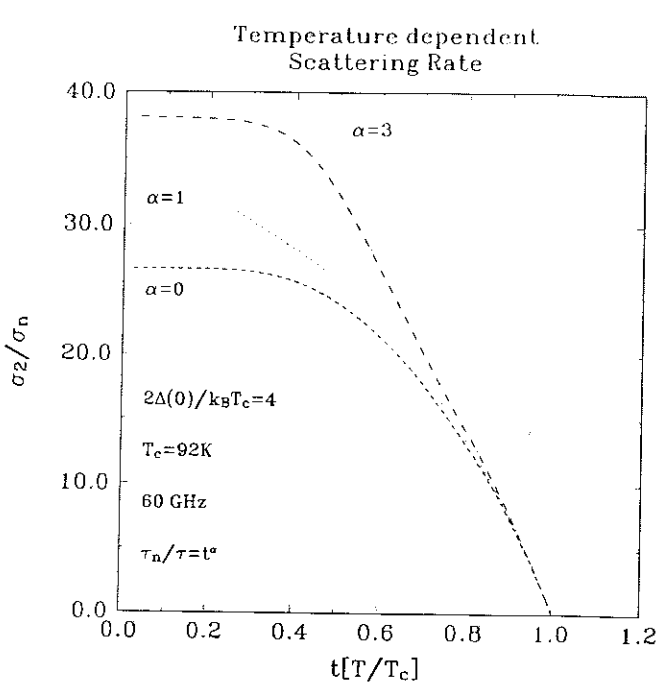

Fig. [2.12]: Change of the $\sigma_2(T)$ using the same parameters as in Fig. [2.11].

Strong coupling also affects the width of the coherence peak. As the gap value gets larger, the opening of the single particle gap gets faster, $\partial\Delta/\partial T$ increases near T_c. It implies that as the coupling constant increases, the temperature scale shrinks near T_c and this decreases the width of the peak in σ_1. This situation is best seen in Figs. [2.13] and [2.14], where the coupling value is changed while keeping BCS formalism intact.

2.5 Nuclear Magnetic Resonance

We shall review very briefly the basic properties of NMR in superconductors. Full details of this subject can be found in various references [181, 196]. Nuclear moments are extremely weak compared to any other energy scales in a metal. For example, the nuclear dipole interaction is of the order of $1\mu K$ at 1 Tesla and the nuclear Zeeman spliting is three orders of magnitude smaller than the electronic splitting. The aim is to measure the nuclear susceptibility by the use of resonant technique. In a metal, the nuclear moment is coupled to the electronic degrees of freedom through the hyperfine interaction, that has three different terms:

1. the contact term of purely quantic origin; it represents the finite probability for an electron to be located at the nucleus position. The contact term is non-zero for s-electrons solely. Usually electrons in complete shells do not contribute to this effect (unless there is core polarization). Also, for most metals, the contact term is the dominant interaction between the nucleus and its electrons.

2. the dipolar term, that is the interaction between the nuclear dipole and the electronic one. This term vanishes for any nucleus with a cubically symmetric electron cloud.

3. the orbital term; that is, the finite magnetic field at the nucleus created by the motion of the electrons around it. This term vanishes for most transition elements, as the orbital moment is quenched (or averaged to zero) through crystal distortion (Jahn-Teller or crystal field effects).

To investigate the electronic degrees of freedom, one can measure three different parameters:

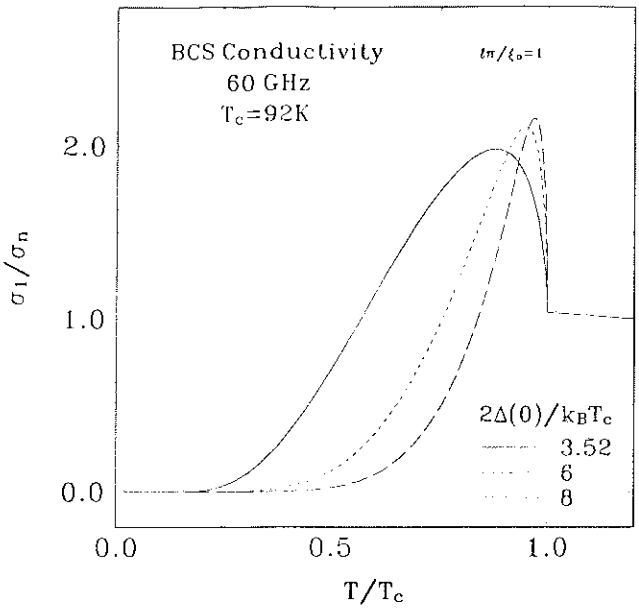

Fig. [2.13]: Temperature dependence of σ_1 for various value of the coupling constant but keeping the BCS formalism. The width of the coherence peak scales with how fast the single particle gap opens with decreasing temperature.

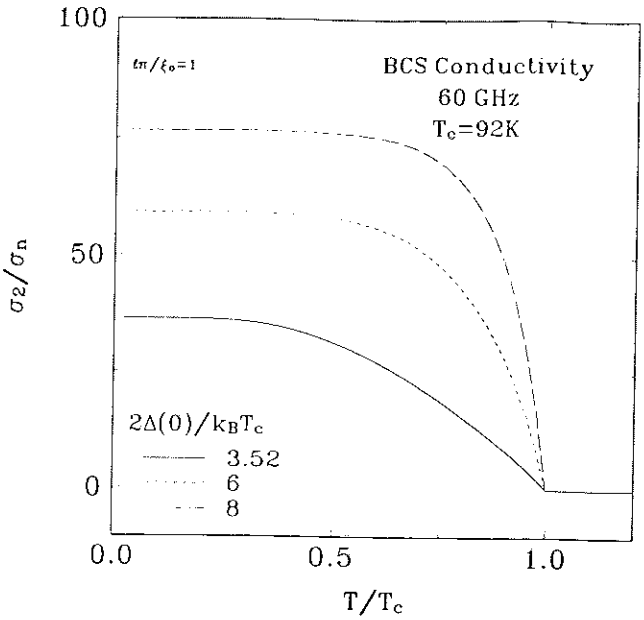

Fig. [2.14]: Temperature dependence of σ_2 for various value of the coupling constant but keeping the BCS formalism. The low temperature limit depends on the ratio $\pi\Delta(0)/\hbar\omega$.

2.5.1 Frequency shift

The resonance line position depends on the local magnetic field at the nucleus. A shift in the resonance implies that, at the nucleus position, the externally applied field is partially enhanced (or screened) by the static field created by the electrons. In metals, the resonance frequency is usually shifted to a higher value, independently of the temperature: the dominant effect is then the contact interaction and the shift is called the Knight shift, K_s. The magnitude of K_s is proportional to the spin susceptibility.

It can be shown that the spin susceptibility of a superconductor is given by the expression:

$$\begin{aligned}\chi_s(\mathbf{q},\omega) &= -2{\mu_e}^2 \sum_{\mathbf{k}} \\ &+ \left[\left(\frac{1}{E_{\mathbf{k}} + E_{\mathbf{k+q}} - \hbar\omega - i\hbar/\tau} + \frac{1}{E_{\mathbf{k}} + E_{\mathbf{k+q}} + \hbar\omega + i\hbar/\tau}\right)\right. \\ &\times [1 - f(E_{\mathbf{k}}) - f(E_{\mathbf{k+q}})](u_{\mathbf{k}} v^{\star}_{\mathbf{k+q}} - v_{\mathbf{k}} u^{\star}_{\mathbf{k+q}})^2 \\ &+ \left(\frac{1}{-E_{\mathbf{k}} + E_{\mathbf{k+q}} - \hbar\omega - i\hbar/\tau} + \frac{1}{-E_{\mathbf{k}} + E_{\mathbf{k+q}} + \hbar\omega + i\hbar/\tau}\right) \\ &\left. \times [f(E_{\mathbf{k}}) - f(E_{\mathbf{k+q}})](u_{\mathbf{k}} u^{\star}_{\mathbf{k+q}} + v^{\star}_{\mathbf{k}} v_{\mathbf{k+q}})^2\right], \end{aligned} \tag{2.5.1}$$

where we recognize the same expression as for the complex conductivity, with the usual coherence factors (cf. Eq. (2.1.10)). The qualitative $\mathbf{q}$ dependence of this function is shown in Fig. [2.15] at low temperatures. The temperature dependence of the spin susceptibility for a uniform field was calculated by Yosida in 1958 [199] (cf. Fig. [2.16]).

$$\chi_s(\mathbf{q}=0) = -2{\mu_e}^2 \sum_{\mathbf{k}} \frac{\partial f_{\mathbf{k}}}{\partial E_{\mathbf{k}}}. \tag{2.5.2}$$

The theory predicts that the shift decreases to zero at T=OK, while experimental results have always observed a finite susceptibility at low temperature. The reason for this discrepancy is still unclear today

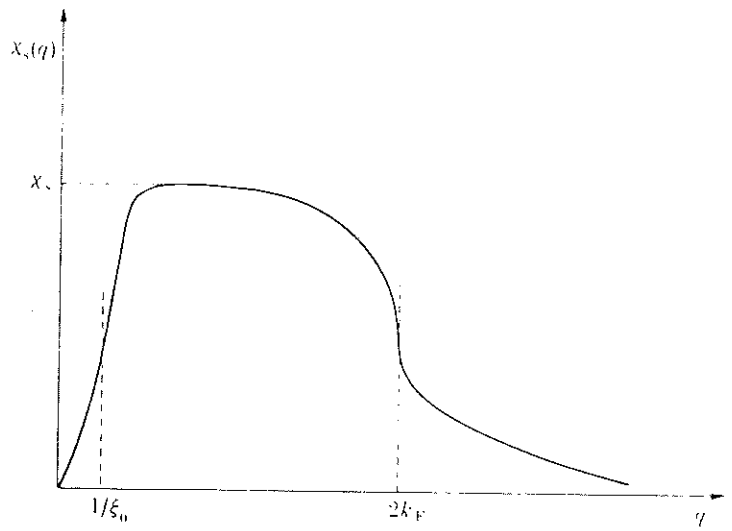

Fig. [2.15]: q-dependence of the electronic susceptibility for a superconductor at zero temperature, after Ref. [196]. In practice $\chi_s(0,T)$ (Yosida function) saturates to a finite value at $T = 0$, in disagreement with the model.

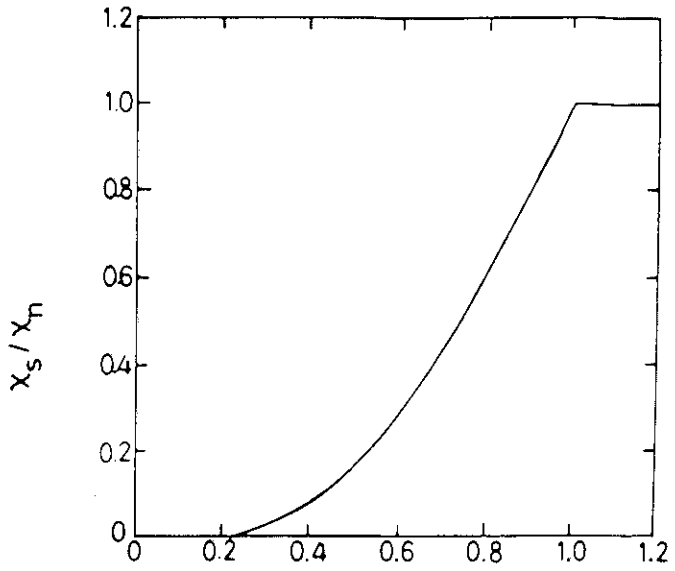

Fig. [2.16]: Temperature dependence of the electronic spin susceptibility, after Yosida (1958) [199].

[1] and several mechanism like orbital paramagnetism, surfacic spin-orbit coupling have been suggested. A good discussion on this matter can been found in Schrieffer's book [178] between pages 245-248. Notice also that performing nuclear magnetic resonance in bulk samples, whose dimensions are larger than the penetration depth, leads to spurious effects caused by the screening of the magnetic field from the inside of the sample and contribute, in particular, to a shift of the resonance.

2.5.2 Linewidth

The resonance line has a characteristic width, Γ, because usually a given nucleus at various crystal sites is effected by a slightly different magnetic field. An obvious cause of this distribution is inhomogeneities in the crystal: it then represents the intrinsic resolution threshold. Also, a type II superconductor, in an applied magnetic field whose magnitude lies between the lower and upper critical field, developes a mixed state formed by an array of magnetic vortices, causing an increase in the linewidth. Another common cause of the line broadening is that the nuclear energy levels have a finite width, proportional to the life time of the nucleus (or relaxation time, T_1). This result is a direct consequence of the Heisenberg uncertainty theorem:

$$\Gamma = \frac{\hbar}{T_1}. \tag{2.5.3}$$

The last main contribution for line broadening is the dipolar interaction between nuclei. This effect cancels out for sites of cubic symmetry. For other sites of lower symmetry, the effect can be averaged out by spinning the sample at a particular angle θ_o (the magic angle) from the static field where:

$$1 - 3\cos^2\theta_o = 0. \tag{2.5.4}$$

2.5.3 Nuclear spin relaxation time

An introduction was already given page 6. As mentioned, for most metals the dominant term in the hyperfine coupling is the contact interaction. In this case, there is a simple relation between the nuclear

spin relaxation time (T_1) and the frequency shift K_s, and it is called the Korringa law:

$$T_1 T K_s^2 = \frac{\hbar}{4\pi k_B}\left(\frac{\gamma_e}{\gamma_n}\right)^2. \tag{2.5.5}$$

The expression for the interaction is:

$$\begin{aligned}\hat{H}_i &= \sum_{\mathbf{k},\mathbf{k}'} |\psi(0)|^2 \Big[I_z(\hat{a}^\dagger_{\mathbf{k}'\uparrow}\hat{a}_{\mathbf{k}\uparrow} - \hat{a}^\dagger_{\mathbf{k}'\downarrow}\hat{a}_{\mathbf{k}\downarrow}) \\ &\quad + I_+\hat{a}^\dagger_{\mathbf{k}'\downarrow}\hat{a}_{\mathbf{k}\uparrow} + I_-\hat{a}^\dagger_{\mathbf{k}'\uparrow}\hat{a}_{\mathbf{k}\downarrow}\Big],\end{aligned} \tag{2.5.6}$$

where $|\psi(0)|^2$ is the probability of the Bloch function at the nuclear site, and I_z is the nuclear spin ($I_\pm \equiv I_x \pm iI_y$).

The height of the peak depends on the magnetic field. The equivalent of the photon energy is the *electronic* Zeeman energy and the cut-off energy of Eq. (1.2.18) is $\hbar\omega_e$. Another effect is the finite lifetime of elementary excitations. A last possibility, is a distribution in the magnitude of the gap [12]. This suggestion was advanced as an explanation accounting for the experimental findings on Al [85]. However, an experiment on indium with different degrees of purity showed later unambiguously that this is negligible [39].

A type II superconductor ($\xi < \lambda$) in an external field falling between the lower and upper critical field limits, is in a mixed state made of vortices that are arranged in a two dimensional array of triangular symmetry. The inside of the filament is normal on a length scale $\xi(T)$, while the surrounding superfluid screens out the magnetic field on a length scale $\lambda(T)$. As mentioned before, this mixed phase broadens the resonance line (the shape depends on the array structure). The excitation spectrum depends strongly on the value of the mean-free-path ℓ and how it compares with the coherence length $\xi(T)$. Again the net effect is to change the shape of the density of state spectrum and, in particular, to remove the singularity at the gap value. Also, because there are normal electrons inside the vortex core, the relaxation is not homogeneous: at low temperature normal electrons relax faster than the few remaining quasiparticles in the superfluid region. A non-exponential behavior is then observed, and people use a stretch exponential fit to extract T_1. Some other tricks are used to homogenize the relaxation, the principle being to move around the vortices array and obtain a spatial average. The techniques include rotating the sample with respect to the applied field or adding a large low frequency magnetic field modulation to the static field. Other methods are field cycling techniques, that are suitable for very slow relaxation process. The principle is to magnetize the sample with a strong static field and then remove the sample at a constant temperature and study the decay in the absence of any externally applied field. The size of the coherence peak is directly affected by the value of the magnitude of the static field, the higher the field, the bigger the cut-off Zeeman energy and the smaller the height of the peak; the sensitivity of the technique goes as the square of the magnetization. Field cycling techniques are the best compromise of sensitivity vs. signal.

Chapter 3

Experimental Techniques

The techniques used to measure the electrodynamic response of solids divide in different categories depending on how the wavelength compares to the sample size. In the short and long wavelength limit, a same device can cover a wide frequency range, but spectroscopy in the intermediate regime (1 cm^{-1} to 10 cm^{-1}) practically necessitates a set of instruments for each frequency as light diffracts with most laboratory sized objects. This incomplete frequency coverage can be partially compensated by the use of resonant techniques and narrow band detection schemes to achieve a higher relative sensitivity.

3.1 Resonant cavities

3.1.1 Bandwidth and characteristic frequency

Above a lower cut-off frequency, a cavity can sustain many standing-wave modes and near each resonant frequency, the power absorption spectrum has a Lorentzian shape [97]:

$$A(\omega) = \frac{1}{4(\omega - \omega_o)^2 + (2\pi\Gamma)^2}, \tag{3.1.1}$$

where $f_o = \omega_o/2\pi$ is the center frequency and Γ is the bandwidth or full frequency width at half-maximum. Both f_o and Γ are the two characteristics of the resonator. We often refer to another redundant parameter, the quality factor Q of the cavity, define as:

$$Q \equiv \frac{f_o}{\Gamma} = \frac{\omega_o <W>}{L}, \tag{3.1.2}$$

where $<W>$ is the time-averaged energy stored in the cavity and L the energy loss per cycle. The Lorentzian shape spectrum can be simply formulated by the use of a complex resonance frequency:

$$\hat{\omega} \equiv \omega_o - i\frac{\omega_o}{2Q}, \tag{3.1.3}$$

where all fields have a time dependence of the form $e^{-i\omega t}$.

3.1.2 Quality factor

There are two main loss mechanisms in the cavity: ohmic and radiative (losses through the coupling holes), and they both contribute in an additive way:

$$\frac{1}{Q_\ell} = \frac{1}{Q_\Omega} + \frac{1}{Q_r}, \tag{3.1.4}$$

f_o GHz	Q @ 300 K	d mm	h mm	V_c mm^3
7.5	20,000	57.28	38.19	98,411
9.2	25,000	43.90	39.20	59,334
12	15,000	35.8	23.87	24,027
35	13,000	12.44	7.90	960.2
60	7,500	7.15	4.77	191.5
100	7,000	4.21	2.81	39.1
150	4,000	2.86	1.91	12.3

Table 3.1: The resonant frequency f_o, quality factor Q, diameter d, height h and volume V_c for each of our cavities in the micro and millimeter wave spectral range.

where Q_ℓ represents the total loss (loaded cavity), Q_Ω the Ohmic loss in the walls of the resonator (sample included), Q_r represents the radiative losses.

Q_Ω is proportional to the ratio of the volume occupied by the fields to the volume of the conductor into which the fields penetrate [97] :

$$Q_u = \frac{V_c}{S\delta}. \tag{3.1.5}$$

The sensitivity of a measurement is proportional to the resonator Q, so the highest possible quality factor is desired. As indicated by Eq. (3.1.5), maximizing the volume to surface area ratio, generally increases the cavity Q. This fact together with some other mechanical constraints (a sphere is difficult to tool) has led to the widespread use of both cylindrical and rectangular cavities. The sensitivity is also proportional to the sample to cavity volume ratio, the sample filling factor. A simpler analysis requires the fields to be constant over the length of the sample and lower order modes are generally used.

All our cavities are made of Oxygen Free Copper (OFC), with walls anneal for 48h at 200°C, acid etch and then manually polished down to 0.3 μm, and the obtained Q has a typical value of approximately 10^4 in transmission.

3.1.3 TE_{011} mode

These cavities are made of copper and consist of an annular cavity body on which two flat endplates can be mechanically attached with screws. The field distributions within the cavity are shown in Figs. [3.1,3.2]. In this mode only circumferential currents flow, both in the cylindrical walls and endplates, making both the field distribution and Q virtually independent of the quality of the contact between the body-walls and the removable endplate, as no current flows between them. This allows one to open the cavity to introduce the sample without a subsequent degradation of the Q. Unfortunately, this mode is also degenerate with the TM_{111} mode. As the two modes have different field distributions, the degeneracy can be removed by slightly modifying the shape of the resonator at a position of an anti-node of the undesired mode. In our case, the mode splitting is accomplished by cutting small grooves at both the top and bottom edges of the cavity body as shown in Fig. [3.3]. The grooves are at an anti-node position for the TM mode but at a node for the TE mode. The net effect is that the TM mode sees an effectively larger cavity and its resonance is shifted to lower frequencies.

The diameter, d, to height, h, ratio of the cavity should be chosen carefully in order to both optimize the Q of the TE_{011} mode (maximum with d/h near 1) while also minimizing the density of modes near the desired resonance frequency. We have chosen a ratio $d/h \sim 1.50$ for most of our cavities, as it represents a good compromise. In Table [3.1] we present the cavity sizes we use at each frequency.

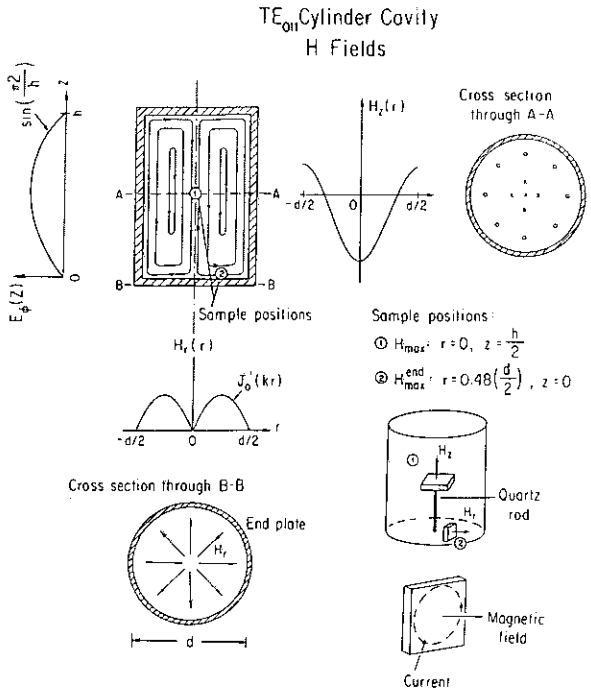

Fig. [3.1]: Magnetic field lines inside a cylindrical cavity resonating in the TE_{011} mode. Both the maximum magnetic field in the cavity H_{max}, position 1, and on the endplate H^{end}_{max}, position 2, are indicated on the Figure.

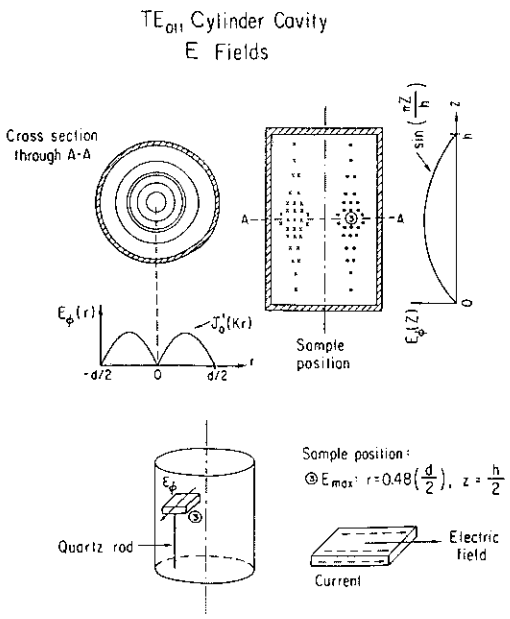

Fig. [3.2]: Electric field lines inside a cylindrical cavity resonating in the TE_{011} mode. The position of the maximum electric field E_{max}, position 3, is also indicated on the Figure.

3.1.4 Coupling holes

The excitation of a particular mode is done through a coupling device that connects a similar field pattern in both the waveguide and the cavity. It has been found experimentally that coupling through a small hole in the cavity wall (at the magnetic field anti-node) is much *less* temperature dependent than coupling to the cavity with a wire antenna. For the TE_{011} mode, we use a coupling through the top plate (for practical purpose) and the hole is located at 48% of the radius of the cavity (from the cavity center) and at the center of the connecting waveguide as shown on Fig. [3.4]. We use a 0.010" thick OFC copper coupling plate. Care must be taken not to bend it, and the plate is flush against the waveguide in order to avoid cross-talk that will distort the resonance.

As mentioned earlier the highest Q is desired, that implies that one coupling hole with the minimum diameter (undercoupled) should be favored. Unfortunately working with one coupling hole (i.e. in the reflection mode) gives rise to an undesirable effect: as the frequency is changed, some large distortions in the base-line occurs, due to the formation of standing waves in the wave-guide. In practice, the use of reflection cavities is limited to frequencies less than 20 GHz. Above this threshold, we are forced to use the resonator in the transmission mode, where two coupling holes are drill. The main advantage is that an uni-directional isolator can be inserted in the output wave-guide to prevent the formation of interference. This improvement is paid by lowering the total Q of the cavity.

3.2 Amplitude technique

3.2.1 Principles

Conventional techniques measure f_o and Γ by sweeping the source frequency over a sufficiently wide frequency window to cover the full absorption spectrum of the resonator and fit the transmitted power with a Lorentzian. A more precise way of measuring both of them is to use a narrow bandwidth source (bandwidth smaller than Γ) that operates at the central frequency of the *cavity*: f_o is then the frequency

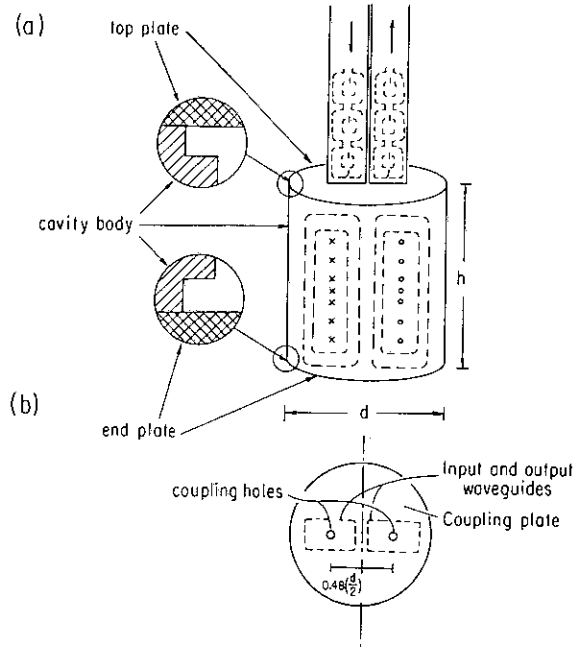

Fig. [3.3]: Sideview of a TE_{011} cavity coupled via the magnetic field, shown with the dashed lines. In addition, the grooves in the cavity walls which split the degenerate TE_{011} and TM_{111} modes, shifting the TM_{111} mode to lower frequencies while leaving the TE_{011} mode undisturbed are illustrated.

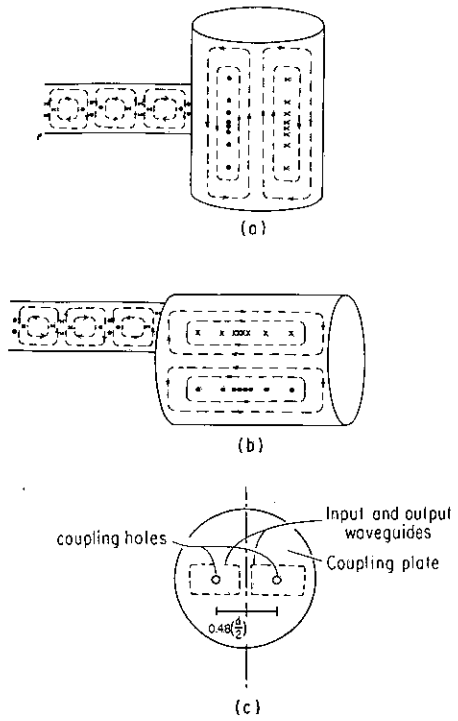

Fig. [3.4]: Cavity top plate used in a transmission configuration. The two coupling holes are centered about the position of maximum magnetic field on the endplate, a distance 0.48 a from the center. The waveguide is attached such that the coupling holes are also at the maximum magnetic field of the waveguide.

of the emitter and the bandwidth of the cavity is related to the power transmitted through the resonator. The coupling of the source frequency F to f_o is achieved by modulating the source frequency around F (a schematic is displayed in Fig. [3.5]); a detection of the in-phase amplitude of the transmitted signal at the modulation frequency, will measure the derivative of the cavity absorption spectrum, and be proportional to the error $\epsilon = (F\text{-}f_o)$ at first order. ϵ is then fed-back into the source to create an automatic restoring signal that assure the stability of the system. This type of feed-back automatism is similar to the AFC (Automatic Frequency Control) used in ESR.

3.2.2 Bandwidth evaluation

In the amplitude method one measures both f_o and the transmitted power at f_o, $A(f_o)$. From Eq. (3.1.1), $A(f_o)$ is simply related to the bandwidth by the following relation:

$$A(f_o) = \alpha\Gamma^{-2}. \tag{3.2.1}$$

Notice that for narrow bandwidth resonator, it is more appropriate to measure $A(f_o)$ than Γ. To measure the amplitude, we chop the power emitted by the source and use an other phase-sensitive detection to analyze the signal transmitted. The chopping frequency is 3 orders of magnitude higher than the frequency of modulation to avoid mixing contributions induced by higher order non-linearities.

In Fig. [3.7] we show the measured width together with $1/\sqrt{A}$ over a broad temperature range. This good overall agreement implies that the absorption line has a Lorentzian shape. As shown earlier, the quantity of interest is $\Delta\Gamma$ which, using Eq. (3.2.1), is related to the measured values of A_s by

$$\Delta\Gamma \;=\; \Gamma_s - \Gamma_o = \left(\frac{\alpha_s}{\sqrt{A_s}} - \frac{\alpha_o}{\sqrt{A_o}}\right), \tag{3.2.2}$$

where α_s and α_o are the proportionality constants with the sample in and out of the cavity respectively.

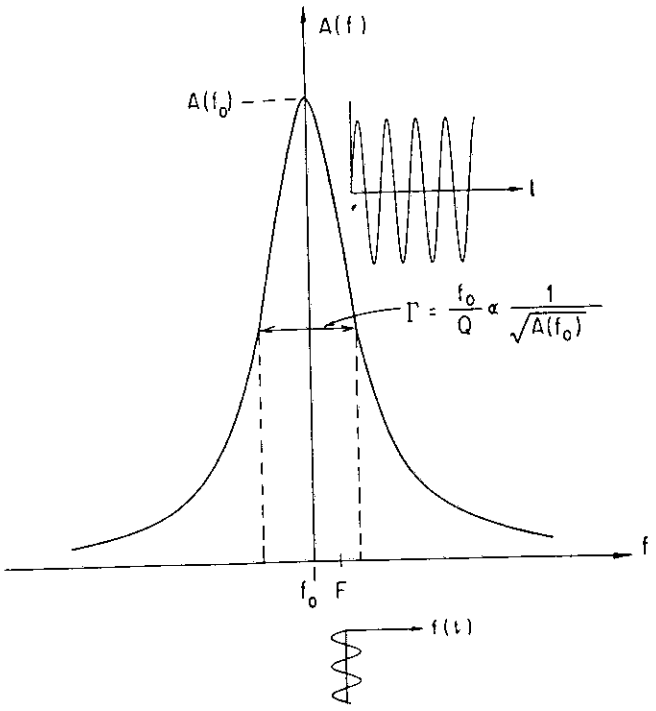

Fig. [3.5]: Principle of the novel detection scheme: a modulation frequency $f(t)$ ($|f| \ll \Gamma$) is superimposed to the central frequency F of the source. The in-phase component of the detected signal is proportional to the difference (F-f_o). This difference is fed back to the source in order to lock F at f_o. By measuring accurately F (with a frequency counter) and the amplitude of the signal at f_o: $A(f_o)$, we can deduce both f_o and Γ.

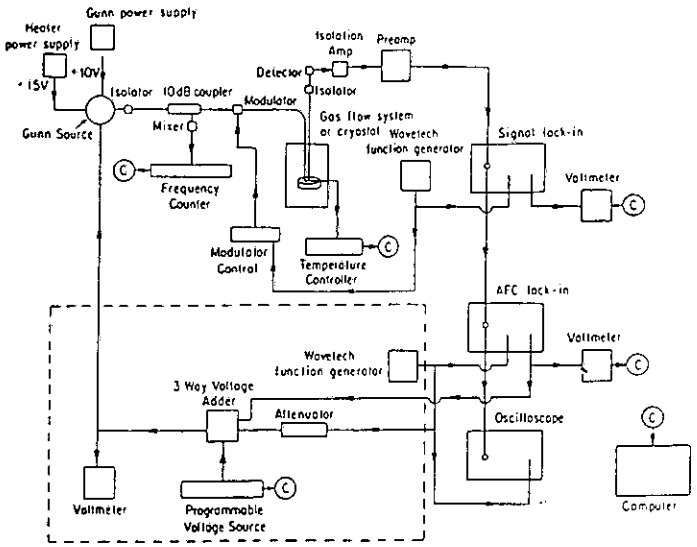

Fig. [3.6]: Experimental setup for the amplitude measurement technique. This configuration is for a varactor tuned Gunn oscillator. If an Impatt source is used then the dashed box is replaced by an HP 8350B mainframe.

We have found that both α_s and α_o are virtually temperature independent over a broad temperature range and they are also unchanged by the introduction of the sample into the cavity. Thus, within the experimental accuracy, $\alpha_s = \alpha_o$, and Eq. (3.2.2) can be rewritten in the form

$$\Delta\Gamma \;=\; \Gamma_s - \Gamma_o = \alpha\left(\frac{1}{\sqrt{A_s}} - \frac{1}{\sqrt{A_o}}\right), \tag{3.2.3}$$

where α is the proportionality constant. α is determined by measuring both the width and the amplitude at *one* temperature. The fact that α is independent of both time and temperature has been checked experimentally on the scales needed for the experimental studies (T < 100 K and t < 48 hours). The independence of α implies the following:

1. The coupling of the cavity is essentially unchanged over a broad temperature range.

2. The power of the source is constant over the time scale of days and that it is independent of frequency over a frequency range of approximately 10 MHz.

3. The coupling constant is independent of the introduction of the sample into the cavity. This implies that the field distribution is not drastically changed once the sample is introduced.

These experimental facts are only true over a limited range of sample size.

It should be noted that the amplitude of the transmitted signal is very sensitive to any absorption or radiative process and care must be used to ensure the reproducibility of the measurement. In particular, when the cavity is opened to remove the sample one must consider the reproducibility of the following factors: quantity of exchange gas, liquid He levels, and the waveguide flange connections.

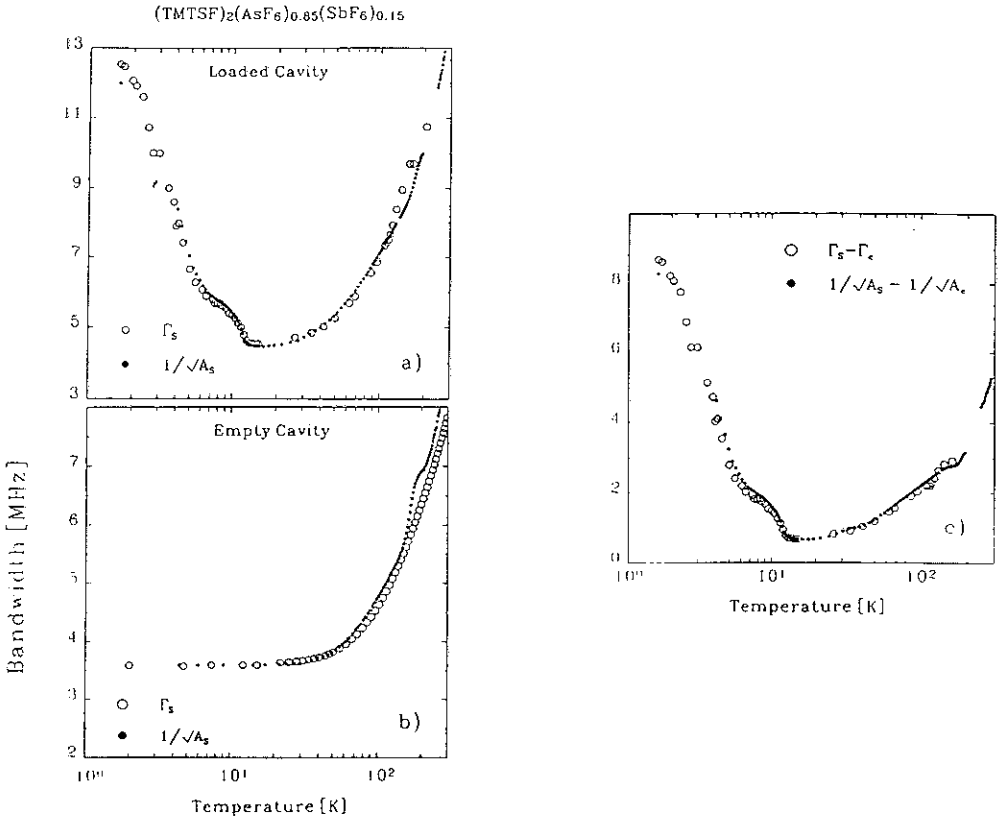

Fig. [3.7]: Comparison of the temperature dependence of the bandwidth measured both by the conventional method (open circles) and the amplitude technique (filled circle) with a sample of $(TMTSF)_2AsF_6$ at 60 GHz using the perturbation technique. In a) the cavity is empty, in b) a sample is loaded, and c) is the difference between a) and b).

3.2.3 Experimental set-up

In this setup (shown in Fig. [3.6] the microwave power is directed toward the cavity in a rectangular waveguide through a ferrite isolator. A 10 dB coupler is attached to a broad band mixer, which in turn is connected to a microwave frequency counter EIP 578B. The counter is capable of reading frequencies up to 110 GHz. By averaging the measurement a 100 times, we can evaluate the central frequency of the source with an accuracy better than 10 ppm. Next we put a modulator, that chops the microwave power at a frequency of 100 kHz. After the cavity, the microwave pass through another ferrite isolator before reaching the Schottky barrier diode detector, sensitive to the micro-wave power transmitted.

Typically the source is either a Gunn diode (35, 100 GHz) or an Impatt source (60, 100, 150 GHz). These are low noise and low power devices (less than 100 mW) that are readily available. In either case, the central frequency of the source is assigned by a dc voltage V linearly related to F up to a very good degree of accuracy, enabling us to change F by step lower than 1ppm. The total frequency of the source F_s is the sum of the central frequency F, modulated by a time dependent signal f(t):

$$F_s = F + f(t) \tag{3.2.4}$$

The modulation of the frequency $f(t)$ about F has a sawtooth form with a period of typically 10 ms (100 Hz) and an amplitude less than 1% of the resonator bandwidth. The detected signal is amplified and analyzed with a phase-sensitive detector PAR 5204 whose reference arm is the 100 Hz sweep signal.

The dc-output of the lock-in is then added (with a variable gain) to V. A computer aided program correct constantly F as to minimize the fed back voltage. The microwave source that we have used in the present report is wether an Impatt source at 60 GHz driven by an HP 8350B sweep oscillator or a Gunn diode at 35 and 100 GHz. In the case of the Impatt source, the driving voltage (dc + modulation) is already built in the HP sweep oscillator. For other frequencies, the 35 and 110 GHz, a Wavetek power supply generates the saw-tooth modulation, the dc being controlled by an IEEE interfaced dc power supply (HP 6632A). Another phase-sensitive detector PAR 5204 is used to measure the amplitude of the power transmitted at f_o and its reference is the chopping frequency of the modulator.

3.3 Perturbation of boundary conditions

Most techniques using resonant cavities, measure the influence of a foreign body on the characteristics of the resonator. The idea is that the boundary conditions at the walls (partially fixed by the specimen) decides the field structure in the resonator, on which depends f_o and Γ. A direct evaluation of the complex conductivity $\hat{\sigma} = \sigma_1 + i\sigma_2$ necessitates the measurement of two independent variables. In fact, the second parameter is also conjugate of the first through the Kramers-Kronig relations, and its evaluation is possible if one variable has been measured on a wide spectrum. The technique described, measure at the same time to a high accuracy the *both* characteristics f_o and Γ, enabling a direct evaluation of $\hat{\sigma}$.

3.3.1 Definitions

There are many ways to equivalently express the response function of the system to an electromagnetic probe. Since they ease analogies with the static case, they will be used extensively in the following and it is therefore useful to review them briefly. The complex permittivity is defined as:

$$\hat{\epsilon} = \epsilon_1 + i\epsilon_2 = \epsilon_\infty + 4\pi i\frac{\hat{\sigma}}{\hat{\omega}}, \tag{3.3.1}$$

where ϵ_∞ is the permittivity due to the high frequency response (preferentially single out). It defines a complex refractive index $\sqrt{\hat{\epsilon}}$ and a complex wavevector inside the medium:

$$\hat{k} = \frac{\omega}{c_o}\sqrt{\hat{\epsilon}}. \tag{3.3.2}$$

The skin-depth δ is the characteristic wavelength inside the compound $\delta = 1/\Im(\hat{k})$. The complex susceptibility is related to the dielectric constant through the relation:

$$\chi_e \equiv \frac{\hat{\epsilon} - 1}{4\pi}. \tag{3.3.3}$$

In the case of magnetic materials, a complex permeability $\hat{\mu}$ is used. The magnetic susceptibility is defined as:

$$\chi_m \equiv \frac{\hat{\mu} - 1}{4\pi}. \tag{3.3.4}$$

The susceptibility represents the generalized (first order) response of the system to an external perturbation, and both [120] the real and imaginary part are related through the Kramers-Kronig relation [97].

3.3.2 Depolarization factor

It is important to separate effects of independent origin: the properties of the compound from the sample dimension or its geometry. A trivial factor is the volume of the sample (assuming that the material is

isotropic and homogenous [137]). The remaining term can be factored by a subtle use of the linearity of Maxwell's equations: a sample in an externally applied field (the field far from the sample surface, denoted by calligraphic letters) possesses a local field (or field in the sample, written in capital letters) that can be expressed as the sum of the applied field plus a correction field (the depolarization field) proportional to the former. The correction factor is both proportional to the susceptibility χ of the compound and a geometrical part, n, the depolarization factor, a 3×3 matrix and rank one tensor defined as follows:

$$\mathbf{E} = \mathcal{E} - 4\pi n\mathbf{P} \quad \text{in the electric field,} \tag{3.3.5a}$$

$$\mathbf{H} = \mathcal{H} - 4\pi n\mathbf{M} \quad \text{in the magnetic field.} \tag{3.3.5b}$$

$\mathbf{P}$ and $\mathbf{M}$ are the polarization or magnetization of the sample, respectively; they are both the product of the susceptibility times the local field:

$$\mathbf{P} = \chi_e \mathbf{E}, \tag{3.3.6a}$$

$$\mathbf{M} = \chi_m \mathbf{H}. \tag{3.3.6b}$$

This definition of the susceptibility must not be confused with the polarizability $\hat{\alpha}$ defined by:

$$\mathbf{P} = \hat{\alpha}_e \mathcal{E}, \tag{3.3.7a}$$

$$\mathbf{M} = \hat{\alpha}_m \mathcal{H}. \tag{3.3.7b}$$

Both are related through the Clausius-Mosotti relations [97]. In general the depolarization field is spatially dependent. However for ellipsoidal shaped samples a uniform external field produces a uniform depolarization field inside the specimen [97] (the demagnetizing field for non-ellipsoidal bodies was studied by R.I. Joseph and E. Schlömann [100]).

A useful relationship exist among the matrix elements of the depolarization tensor: in its principal basis the trace is equal to the unity: $(n_x + n_y + n_z = 1)$. Osborn [155] calculated in 1945 the depolarization factor of a general ellipsoid. Let a, b and c be the sample dimension along the three cartesian axes x, y and z respectively, with the assumption $a \geq b \geq c \geq 0$. The formulas for the different factors are:

$$n_x = \frac{\cos\phi\cos\theta}{k^2\sin^3\theta}\left[F(k,\theta) - E(k,\theta)\right], \tag{3.3.8a}$$

$$n_y = \frac{\cos\phi\cos\theta}{k^2(1-k^2)\sin^3\theta}\left[E(k,\theta) - (1-k^2)F(k,\theta) - \frac{k^2\sin\theta\cos\theta}{\cos\phi}\right], \tag{3.3.8b}$$

$$n_z = \frac{\cos\phi\cos\theta}{(1-k^2)\sin^3\theta}\left[\frac{\sin\theta\cos\phi}{\cos\theta} - E(k,\theta)\right], \tag{3.3.8c}$$

where

$$\cos\phi = b/a, \quad (0 \leq \phi \leq \frac{\pi}{2}), \tag{3.3.9a}$$

$$\cos\theta = c/a, \quad (0 \leq \theta \leq \frac{\pi}{2}), \tag{3.3.9b}$$

$$k = \sin\phi/\sin\theta. \tag{3.3.9c}$$

$F(k,\theta)$ and $E(k,\theta)$ are the elliptic integrals of the first and second kind: k the modulus and θ the amplitude. The values obtained for degenerate shapes are listed in appendix A.

3.3.3 Polarizability

The principle of the technique is to measure separately the characteristics of a cavity, first empty (o) and then after loading it with a small sample (s). The variation induced is

$$\Delta\hat{\omega} = \hat{\omega}_s - \hat{\omega}_o. \tag{3.3.10}$$

If the change $\Delta\hat{\omega}$ is adiabatic, then the product of the period and the time averaged energy stored is invariant [160] (Boltzmann- Ehrenfest theorem [33]):

$$\frac{<W>}{\hat{\omega}} = \text{constant}. \tag{3.3.11}$$

This implies that

$$\frac{\Delta <W>}{<W>} = \frac{\Delta\hat{\omega}}{\hat{\omega}} \sim \frac{f_s - f_o}{f_o} - \frac{i}{2}\left(\frac{1}{Q_s} - \frac{1}{Q_o}\right), \tag{3.3.12a}$$

$$<W> = \frac{1}{16\pi}\int_{V_c}(|\mathcal{E}(\mathbf{r})|^2 + |\mathcal{H}(\mathbf{r})|^2)dv, \tag{3.3.12b}$$

$$\Delta <W> = -\frac{1}{4}\int_{V_s}(\mathbf{P}\cdot\mathcal{E}^* + \mathbf{M}\cdot\mathcal{H}^*)dv. \tag{3.3.12c}$$

In our definition, Δ is the variation caused by the introduction of a foreign body in the resonating structure: Δf is the frequency shift and $\Delta\Gamma$ is the sample absorption. By convention, when the $(\mathbf{r})$ dependence is omitted, then the implied value is the sample position.

If we put the sample in the antinode of the electric field ($\mathcal{H} = 0$), then

$$\mathbf{P} = \hat{\alpha}_e\mathcal{E}, \tag{3.3.13}$$

$$\frac{\Delta\hat{\omega}}{\omega} = -\frac{\hat{\alpha}_e}{4}V_s\frac{|\mathcal{E}|^2}{<W>} = -4\pi\gamma\hat{\alpha}_e. \tag{3.3.14}$$

where $\hat{\alpha}_e$ is the polarizability of the sample and γ is a constant that depends only on the resonance mode of the cavity:

$$\gamma = \frac{|\mathcal{E}|^2}{16\pi <W>}V_s = \frac{V_s}{V_c}\frac{|\mathcal{E}|^2}{2<|\mathcal{E}|^2>}, \tag{3.3.15a}$$

$$<|\mathcal{E}|^2> = \frac{1}{V_c}\int_{V_c}|\mathcal{E}(\mathbf{r})|^2 dv. \tag{3.3.15b}$$

The values of the constant γ are given in the appendix B for the TE_{011} mode. We define ϑ, the mode constant. For the electric field configuartion (position 3):

$$\vartheta = \frac{|\mathcal{E}|^2}{2<|\mathcal{E}|^2>}. \tag{3.3.16}$$

If the sample is in the antinode of the magnetic field, Eqs.(3.3.13)- (3.3.15b) will be identical except $\mathcal{E}$ will be replaced with $\mathcal{H}$ and $\mathbf{P}$ with $\mathbf{M}$.

In conclusion, the absorption of electromagnetic waves by small particles is proportional to the polarizability of the sample:

$$\frac{\Delta\hat{\omega}}{\omega} = -4\pi\gamma\hat{\alpha}. \tag{3.3.17}$$

3.3.4 Limiting cases

In this section, the polarizability will be derived in a few limiting cases. The general solution for a sphere will be given later.

$\hat{k}a \ll 1$

For low conductivity compound, we have $a \ll \delta$, the so-called depolarization regime ($2a$ is the sample dimension). In the regime where $\epsilon_2 < (1-n)/n + \epsilon_1$, the magnetic polarizability is negligible compared to the electric. In the electric field anti-node, the field inside the sample is:

$$\mathbf{E} = \frac{\mathcal{E}}{1 + n(\hat{\epsilon} - 1)}, \tag{3.3.18}$$

where n is the depolarization factor along the external field direction. Replacing the value in Eq. (3.3.7a), one get an expression for the polarizability:

$$\hat{\alpha}_e = \frac{1}{4\pi} \frac{\hat{\epsilon} - 1}{1 + n(\hat{\epsilon} - 1)}. \tag{3.3.19}$$

The measured parameters are thus:

$$\frac{1}{2}\left(\frac{1}{Q_s} - \frac{1}{Q_o}\right) = \gamma \frac{\epsilon_2}{[1 + n(\epsilon_1 - 1)]^2 + (n\epsilon_2)^2}, \tag{3.3.20a}$$

$$\frac{f_s - f_o}{f_o} = -\gamma \frac{(\epsilon_1 - 1)[1 + n(\epsilon_1 - 1)] + n{\epsilon_2}^2}{[1 + n(\epsilon_1 - 1)]^2 + (n\epsilon_2)^2}. \tag{3.3.20b}$$

This relation was pointed out by Buranov and Shchegolev in 1971 [37].

If $\epsilon_2 > (1-n)/n + \epsilon_1$, the electric part of the absorption becomes small and the magnetic absorption may be important. In the limit $|\hat{\epsilon}| \gg 1$:

$$\hat{\alpha}_e = \frac{1}{4\pi n}\left(1 - \frac{1}{n\hat{\epsilon}} + \frac{1-n}{(n\hat{\epsilon})^2} + 0\left[\frac{1}{\hat{\epsilon}}\right]^3\right). \tag{3.3.21}$$

Implying:

$$\frac{1}{2}\left(\frac{1}{Q_s} - \frac{1}{Q_o}\right) = \gamma \frac{\epsilon_2}{|n\hat{\epsilon}|^2} + 0\left[\frac{1}{\hat{\epsilon}}\right]^2, \tag{3.3.22a}$$

$$\frac{f_s - f_o}{f_o} = \frac{-\gamma}{n} + \gamma \frac{\epsilon_1}{|n\hat{\epsilon}|^2} + 0\left[\frac{1}{\hat{\epsilon}}\right]^2. \tag{3.3.22b}$$

For $\hat{k}a \ll 1$ the magnetic polarizability is computed from the same expression as Eq. (3.3.19), where the permittivity constant $\hat{\epsilon}$ is replaced by its permeability $\hat{\mu}$. A non-magnetic metal has a dc-permeability $\mu_{dc} = 1$, and the high-frequency correction value goes as $(\hat{k}a)^2$:

$$\frac{\hat{\mu}}{\mu_{dc}} \sim \left(1 + \frac{(\hat{k}a)^2}{\alpha}\right), \tag{3.3.23}$$

where α is a geometrical constant: $\alpha = 10$ for a sphere or $\hat{\alpha}_m = 1/40\pi(\hat{k}a)^2$.

$\hat{k}a \gg 1$

When the conductivity increase further, the skin-depth δ becomes smaller than the sample dimension $2a$ (the skin-depth regime). Then the absorption is given by the time averaged energy flux of the Poynting vector through the surface of the metal:

$$<\mathbf{S}> = \frac{c_o}{8\pi}\mathbf{E}_{||} \times \mathbf{H}_{||}^{\star} = -\frac{c_o}{8\pi} Z_s |\mathbf{H}_{||}|^2 \hat{n}, \tag{3.3.24}$$

where $\mathbf{E}_{||}$ and $\mathbf{H}_{||}$ are the electric and magnetic field respectively, in the plane of the surface and $\hat{n}$ is a unit vector along the outward normal to the surface. For a good conductor, $\mathbf{E}_{||}$ and $\mathbf{H}_{\perp} \to 0$, while $\mathbf{E}_{\perp}$ or $\mathbf{H}_{||}$ are proportional to the external electric and magnetic field respectively (the factor depends solely on the sample geometry). In both cases, the loss is caused by the induced eddy-currents of an effective surface current density:

$$\mathbf{K}_{||} = \frac{c_o}{4\pi} \hat{n} \times \mathbf{H}_{||}. \tag{3.3.25}$$

The current is proportional to the external field, independently of the sample conductivity (current-driven excitation) and the loss is thus proportional to Z_s in all cases. As shown in Eq. (3.3.12a), the energy dissipated in the sample is responsible for the variation of the complex frequency of the resonator. If we refer to the perturbation $\Delta\hat{\omega}$ (the variation caused by the introduction of the sample in the empty cavity), we have to include a *real* additive constant, $\lim_{|\hat{\sigma}|\to\infty} \Delta\hat{\omega}/\omega_o$, that represents the shift of the resonance frequency caused by the excluded volume of the field when the body tends to the perfect conductor limit. This offset is called the metallic shift and depends on the volume of the sample, its geometry and its position in the resonator. For a sample in the skin-depth regime, $\Delta\hat{\omega}$ is thus simply related to the surface impedance:

$$\frac{\Delta\hat{\omega}}{\omega_o} = \xi Z_s + \lim_{|\hat{\sigma}|\to\infty} \frac{\Delta\hat{\omega}}{\omega_o}. \tag{3.3.26}$$

The proportionality constant ξ, depends on the geometry of the surface and its dimension: it is called the resonator constant. For easier handling, we define a new variation:

$$\frac{\Delta'\hat{\omega}}{\omega_o} \equiv \xi Z_s, \tag{3.3.27}$$

where $\Delta'\hat{\omega}/\omega_o$ is the theoretical change in $\hat{\omega}$ measured from the notional perfect conducting state of the sample, where the penetration depth is zero (i.e. the same body is a loss-free object in the skin-depth regime: $Z_s = 0$ or $|\hat{\sigma}| \to \infty$).

This implies that:

$$\Delta'\Gamma = \Delta\Gamma, \tag{3.3.28a}$$

$$\Delta' f = \Delta f - \lim_{|\hat{\sigma}|\to\infty} \Delta f. \tag{3.3.28b}$$

$\Delta' f$ will be called the perfect conductor frequency shift.

3.3.5 Endplate technique

If the sample dimensions exceed the cavity diameter, the endplate can be replaced by the sample, as illustrated in Fig. [3.8]. This is the so-called endplate technique and certain other restrictions apply:

- The conductivity of the sample should be large enough that the cavity Q is not significantly altered by radiation losses through the endplate. This requires the skin depth to be less than the sample

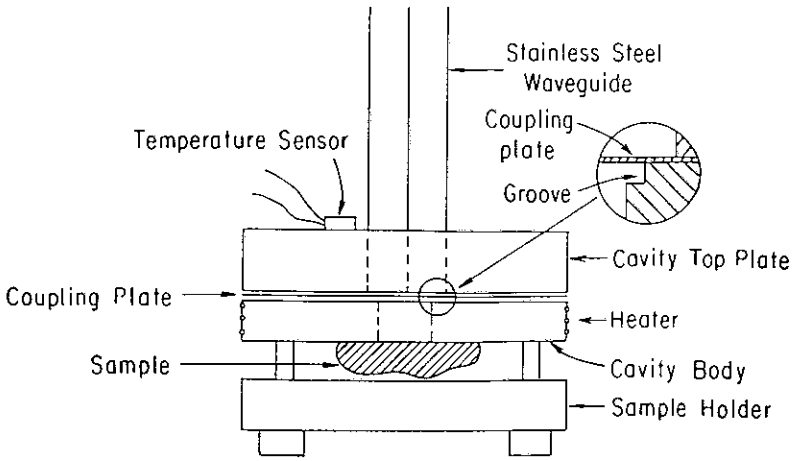

Fig. [3.8]: Diagram of the setup used for the end-plate measurement of the surface impedance. The end-plate has been replaced by the sample under investigation.

thickness. It should be noted that some corrections for radiation leakage are possible, but one must include the effects of a substrate or any other material near the cavity endplate [54].

- As a circumferential current is induced in the cavity endplate, the sample should be nearly isotropic in the plane of the endplate (i.e at least a two-dimensional (2D) conductor). As the in-plane anisotropy is increased, the field distribution inside the cavity is expected to change, which would also change the cavity Q and all the corrections required are not well understood at this point. However, materials with a mild in-plane anisotropy, like the High T_c Superconductors, where the in plane anisotropy is 2-5, have given results in the endplate technique which are consistent with measurements made in other ways [108, 53].

- The sample has to be flat over a distance of the cavity diameter.

- In addition, the surface of the sample should be smooth down to the length scale of the skin-depth (or penetration depth).

As can be seen in Fig. [3.1], only the radial component of the magnetic field is non-zero at the cavity endplate and hence circumferential currents flow in the plane of the endplate (ϕ direction). In this case, the in-plane conductivity is measured and, unless the sample is large enough to polish several perpendicular faces, the anisotropy cannot be extracted.

3.3.6 Perturbation technique

If the sample dimension is much smaller than the wavelength, one can introduce the sample inside the cavity at the antinode of either the electric or magnetic field. The position of both the maximum magnetic, H_{max}, and electric, E_{max}, fields are shown in Figs. [3.1,3.2] for a cavity in the TE_{011} mode. There are several important points to note:

- The direction of current flow within the sample differs at the electric or magnetic antinode, and this permits a direct measurement of the loss along a selected direction. This is particularly important in strongly anisotropic conductors, such as the quasi-one-dimensional (1d) charge and spin density wave (CDW and SDW) compounds [74].

- Unlike with the endplate technique, there are no inherent limitations on the range of sample conductivity which can be measured. Ultimately, the range of sample conductivity which can be extracted depends only on the sensitivity of the measurement and is determined by such factors as: the sample shape, size, location, the cavity Q and the resonance frequency. Typically, measurements can be made over a range covering more than 6 orders of magnitude in conductivity.

With both the endplate and perturbation techniques, the cavity must be opened to introduce the sample and this is usually accomplished by removing the endplate. To position the sample in either E_{max} or H_{max}, a small quartz rod (diameter 0.20 mm and height $h/2$) is glued to the endplate at the appropriate location (see Figs. [3.1,3.2)]. The quartz rod does not significantly alter the cavity Q but does shift the resonance frequency slightly. The resonant frequency is extremely sensitive to the cavity volume and it has been found that the endplate cannot be removed and replaced in such a way that the resonance frequency is not shifted. The shift is due to the mechanical nature with which the endplate is fastened to the bottom of the cavity and in the 60 GHz cavity a non-reproducible shift of $\pm$ 2 MHz is typical, corresponding to an irreproduciblity in the cavity height of $\pm$ 0.5μm. We will come back to this problem later, where we will explain how in certain cases this frequency offset can be determined.

E field In the electric field anti-node, position 3 on Fig. [3.2], the current flow is only along the field direction, in the ϕ direction. If the maximum sample dimension is much less than the field radius of curvature, one can directly measure the conductivity along any desired direction by properly orienting the sample. It should be noted that the depolarization factor is generally different for each sample orientation and thus the sensitivity is not the same for measurements made in each direction.

H field In the magnetic field anti-node, the inductive eddy current flows in a plane perpendicular to the field and the in-plane conductivity is measured. However, unlike with the endplate technique, the sample can be easily rotated to determine the conductivity in any desired plane. Depending on the sample geometry and anisotropy ratio in the plane, one may be able to extract the conductivity along a particular direction.

An additional drawback of this cavity perturbation technique stems from the difficulty to accurately orient the sample atop a thin quartz rod. In the magnetic field this problem can be eased by placing the sample in the position of the magnetic field maximum on the endplate H_{max}^{end}, indicated as position 2 on Fig. [3.1]. In this case the sample rests on the cavity endplate and can be easily manipulated. There are two important facts concerning measuring in H_{max}^{end}:

- In a TE_{011} mode, the magnetic field at this position is smaller by a factor of 4.18 h/d, decreasing the sensitivity of the measurement. With $h/d = 0.67$, the field is smaller by a factor of 2.8 and the sensitivity is reduced by a factor of almost 8.

- A conducting sample on the endplate alters the field distribution in the vicinity of the sample. This in turn changes the current distribution on the endplate and causing a slight change in the loaded Q, which does *not* originate from a loss in the sample.

Normally, we are well above the sensitivity limit and a big advantage is realized by the comparative ease with which the sample can be manipulated on the endplate. Furthermore, experiments on superconducting samples have given an upper bound on the loss due to the endplate current redistribution and for small volume filling factors (typically 10^{-4} or less) this effect is negligible. It is for these reasons that the endplate is the usual sample location for our magnetic field measurements.

We measure usually the perturbation in two separate runs, one with the sample and one without it (in the case of the end-plate technique, we just replace the sample by a wall made of copper). But at low frequency (10 GHz), it is possible to introduce a mechanism for rotating the sample in and out of the

cavity, thus eliminating the need to disassemble the cavity in order to measure the change in parameters. This is practically impossible above 35 GHz, due to the small size of the cavity.

3.4 Data analysis

3.4.1 Width

The analysis required to determine the width change when the sample is inserted inside the cavity is trivial. In this case one simply takes the difference of the measured widths with the sample in and out. However, for the endplate technique, one does not measure the perturbation due to the sample, but rather the difference in the measured width between the sample and copper endplates. In order to extract the surface resistance of the sample one of several procedures must be followed. The frequency of resonance f_o and the half-width Γ are measured as a function of the temperature in two separate runs one before and one after the replacement of the copper endplate by the sample.

$$\Delta\Gamma = \Gamma_s - \Gamma_{Cu} = \alpha\left(\frac{1}{\sqrt{A_s}} - \frac{1}{\sqrt{A_{Cu}}}\right), \tag{3.4.1}$$

$$\Delta f = f_s - f_{Cu}. \tag{3.4.2}$$

The difference is related to Z_s the surface impedance of the sample through the relation:

$$\frac{\Delta f}{f_o} + i\frac{\Delta\Gamma}{2f_o} = \frac{\Delta\hat{\omega}}{\omega_o} = \xi(Z_s - Z_{Cu}), \tag{3.4.3}$$

where ξZ_{Cu} is the loss of the copper endplate only and ξ is the resonator constant, given by

$$\xi = \frac{-ic_o^3\pi^2}{h^3\omega^3}. \tag{3.4.4}$$

The loss due to the copper endplate can be determined with three different methods:

1. If the temperature is not too low then the surface impedance of copper can easily be obtained by assuming a simple Drude metal in the Hagen-Rubens limit. However, at low temperatures, the mean-free-path exceeds the skin depth (the anomalous regime) and this simple expression is no longer valid. In this case, the mean-free-path is required in order to find Z_s.

2. One can calculate the ratio of the losses due to the copper endplate compared with the total losses at all the other surfaces in the cavity. This ratio is independent of the surface impedance. For a cylindrical cavity operating in the TE_{011} mode with a d/h ratio of 1.5, 39% of the wall losses occur on the endplate. If the assumption is made that all of the loses in the cavity occur at the walls of the cavity (i.e. neglecting coupling and radiation losses) then using Eq.(3.4.3) together with:

   $$\xi Z_{Cu} = .39\hat{\omega}_{Cu}, \tag{3.4.5a}$$

   gives

   $$\hat{\omega}_s - .61\hat{\omega}_{Cu} = \xi Z_s, \tag{3.4.5b}$$

   where the superscripts s and e refer to the sample in and empty measurements respectively.

3. If a superconducting endplate of Nb is used then at low temperatures no temperature dependence is seen in the width. At this point one can assume that all the losses are coming from the copper walls. A second measurement with the copper endplate gives the additional losses due to this endplate.

From our experience, the third method is the most reliable. A typical value for copper at 100 GHz and 4.2 K is $R_s \sim 30m\Omega/377\Omega \sim 7.96 \times 10^{-5}$.

3.4.2 Frequency

As mentioned previously, if the endplate is removed the frequency shift f_s - f_{Cu} can be measured only up to a numerical additive constant f_a. In other words, while $\Delta\Gamma$ can be evaluated (as reassembling does not change the loss), only $f_s - f_{Cu} + f_a$ can be measured with f_a unknown. f_a can be determined in either of the following two cases:

1. If the sample is a simple metal then it can be shown that

$$\frac{R_s}{X_s} = \left(\frac{-x + \sqrt{1+x^2}}{+x + \sqrt{1+x^2}}\right)^{1/2}, \tag{3.4.6}$$

   where $x = \omega\tau$. In the so-called Hagen-Rubens limit, $x \ll 1$ and $R_s = X_s$. Thus, from the measured R_s, X_s can be determined and this is related to the frequency shift. Thus, in this limit the frequency offset can be determined.

2. The sample is in a superconducting state of known penetration depth λ. In this case $\sigma_2 \gg \sigma_1$, $R_s \sim 0$, and $X_s = \omega\lambda/c_o$ and again, from a known value of X_s one can extract the frequency offset.

If none of these conditions can be fulfilled, it is not possible to isolate the part of the measured frequency shift due to the sample.

3.4.3 Sensitivity

The electromagnetic response of the sample in the microwave cavity can be evaluated from four experimentally accessible parameters: the frequency shift Δf, the change in bandwidth $\Delta\Gamma$, the measurement frequency f_0 and the temperature T.

Temperature

In all our experiments the temperature is measured with a calibrated silicon diode attached to the outside of the copper cavity wall and is read with an error less than 0.05 K. During the data acquisition the temperature is stabilized by a temperature controller driving a heater. The high heat capacity of the copper cavity guarantees a large time constant and we usually observe a stability of 0.1 K per data point. In order to stay close to equilibrium the temperature is changed very slowly (0.1 to 0.2 K per minute). The sample always has the same temperature as the copper cavity, because either it is put directly on the cavity endplate or, if the sample is placed on top of an insulating post or tray, radiation and exchange gas provide sufficient thermal contact. For the endplate technique the direct thermal link additionally guarantees the proper temperature. This has been checked with measurements of the transition temperature $\hat{\tau}$ in a wide variety of superconducting materials. It has also been checked that the microwave power we used has no heating effect.

The main error of the absolute value of the conductivity measured by microwave cavities lies in the estimation of the geometrical factor n and γ. Furthermore there are additional errors due to the uncertainty in measuring the frequency shift and the change in the quality factor. In the following paragraphs the accuracy and sensitivity of the frequency and width measurement are both discussed.

Frequency

The main advantage of the amplitude method is that the frequency can be directly measured by a frequency counter. The oscillator frequency is modulated around the peak at 100 Hz to detect the maximum by a

	T = 300 K		T = 4 K	
	width	amplitude	width	amplitude
$\Delta f/f_0$	5×10^{-6}	5×10^{-7}	1×10^{-6}	1×10^{-7}
$\Delta\Gamma/2f_0$	1×10^{-7}	1×10^{-7}	5×10^{-8}	5×10^{-8}

Table 3.2: The measurement errors of the frequency shift $\Delta f/f_0$ and of the change in bandwidth $\Delta\Gamma/2f_0$ for the amplitude and width method.

lock-in amplifier. This sweep amplitude depends on the sharpness of the resonance, i.e. the Q of the cavity, and is typically less than 1 % of the width. Due to the microwave source the center frequency can not be adjusted better than 10 kHz, except for 35 GHz where we reach a 1 kHz stability. The uncertainty, however, is mainly governed by the noise of the source and the stability of the cavity. After averaging the frequency typically one hundred times we achieve an overall accuracy in frequency measurement of $\pm$ 10 kHz and better. The stability of the source and temperature drift of the cavity prevents the use of a time constant larger than 30 s. As soon as the quality of the cavity decreases due to losses in the sample the error of the frequency measurement increased; in order to lock on a broad maximum, the amplitude of the sweep has to be enlarged. This reduces the frequency accuracy up to two orders of magnitude. On the other hand, the higher Q at low temperatures allows more accurate measurements. The frequency shift Δf for the 60 GHz-cavity can be measured within 20 kHz and therefore $\delta(\Delta f/f_0) = 5 \times 10^{-7}$. This is almost one order of magnitude better than the width method. As mentioned above, a temperature independent, but unknown frequency offset (of up to $\pm$ 2 MHz) has to be added, because the cavity's endplate must be removed between measuring the loaded and unloaded cavity.

Bandwidth

In order to measure the amplitude of the transmitted signal with a larger sensitivity, we modulate the microwave power with a frequency of 10 kHz, and the transmitted signal was phase sensitively amplified. The sensitivity limit is reached with a cavity Q below 100. The major problem of broader resonances is, that it was more and more difficult to control the center frequency. Increasing the frequency sweep results in larger error of the amplitude measurement. The accuracy of the evaluation of $\Delta\Gamma$ is given by the reproducibility of two consecutive runs. The endplate removal does not change the quality within the sensitivity of our measurements. It turns out, that care has to be taken to keep the same experimental procedure because the transmitted signal is sensitive to the cooling and warming rate, particularly the attenuation of the waveguides inside the cryostat is temperature dependent. The temperature dependent change of the coupling due to thermal expansion of the holes has a minor influence. We experimentally estimate a sensitivity in the change of bandwidths $\Delta\Gamma/2f_0$ to 1×10^{-7} and better. This is comparable to the width technique. The estimated uncertainties in our measurements at 300 K and at 4 K, respectively, are compiled in Table [3.2] for both techniques, assuming small losses in the sample.

3.4.4 Sample orientation

The value of the loss can depend strongly on the orientation of the sample with respect to the field. In a simplistic way, the enhancement of the depolarization filed (n) follows the radii of curvature of the surface. Meaning that a needle edge will have a small n, while a flat surface will have a n approaching unity.

Restraining our study to cases where the local field is null ($\mathbf{E} = \mathbf{H} = 0$), the optimum orientation of the sample depends on the type of field:

- In the $\mathcal{E}$ field, the sample acquires a polarization Eq. (3.3.5a):

$$\mathbf{P} = \frac{\mathcal{E}}{4\pi n}, \tag{3.4.7a}$$

  in the limit $|\hat{\epsilon}| \to \infty$, which corresponds whether to a good dielectric or a good conductor. An optimum geometry is thus a needle-shaped sample pointing along the direction of the electric field ($n \to 0$), the so-called edge-effect.

- In the $\mathcal{H}$ field, the sample acquires a magnetization Eq. (3.3.5b):

$$\mathbf{M} = \frac{\mathcal{H}}{4\pi(n-1)}, \tag{3.4.7b}$$

  in the limit $|\hat{\sigma}| \to \infty$ or $|\hat{\mu}_{eff}| \to 0$, corresponding to a perfect diamagnetic material. The best geometry is a flat surface sample oriented perpendicularly to the magnetic field direction, such that $(1-n) \to 0$.

3.5 Evaluation of the complex conductivity

Several authors have studied the problem previously: Champlin and Krongard [42] together with Brodwin and Parsons [34] solved the problem exactly for a sphere placed in either the maximum of the magnetic or electric field; Buranov and Shchegolev [37] for a prolate spheroid in the electric field maximum when the electromagnetic radiation penetrates uniformly within the sample (depolarization regime); Cohen [45] together with work by Ong [152] for a prolate spheroid in the electric field maximum, when the electromagnetic wave penetrates within the sample a distance which is smaller than the minimum sample dimension (skin-depth regime). To our knowledge, no general study has been made for a uniaxial spheroid in the maximum of the magnetic field, nor for an oblate spheroid in the electric field maximum. We intend to present a complete solution table for these geometries.

3.5.1 Helmholtz equation

The aim is to compute the polarizability of an arbitrary shaped sample. In order to get an analytical formula, one has to solve a system of Helmholtz differential equations [97]:

$$\nabla^2\mathbf{E}(\mathbf{r}) = 0 \quad \mathbf{r} \text{ outside the sample,} \tag{3.5.1a}$$

$$\nabla^2\mathbf{E}(\mathbf{r}) + \hat{k}^2\mathbf{E}(\mathbf{r}) = 0 \quad \mathbf{r} \text{ inside the sample.} \tag{3.5.1b}$$

$\hat{k}$ is the wave vector defined in Eq. (3.3.2) (the same equations apply in the $\mathbf{H}$ field).

The lowest sample shape symmetry, that has a solution independent of $\mathbf{r}$ is the treatment of the perturbation caused by an ellipsoidal body; the ellipsoidal coordinates are the most general form of separable coordinates for the Laplace equation (Eq. (3.5.1b)). In this system the differential equation is called the Lamé equation, and the solutions are the ellipsoidal harmonics [144, 31]. The ellipsoidal coordinates are related to the cartesian dimension through the elliptic function of the first and second kind [155]. Solving the problem for an ellipsoid is appealing because of its generality, but the solution is elaborate (it cannot be expressed in term of classical algebraic functions) and no new concepts are involved. Thus, for didactic purpose, we will first look at the simplest case: a spherical sample [119, 42, 34] and later we will explain how to extend the result to a spheroid (an ellipsoid with a symmetry axis).

3.5.2 The Sphere

We are looking for a solution of the Helmholtz equation that depends only on the external field $\mathcal{E}$ or $\mathcal{H}$.

We will solve first the problem of a sphere in a magnetic field. Following Landau [119], for the field inside the sample, we look for a solution of the form $\mathbf{A} = \beta\nabla \times (s\mathcal{H})$, where $\mathbf{A}$ is the vector potential (polar) and $\mathbf{H} = \nabla \times \mathbf{A}$ is the magnetic field. s is the spherically symmetrical solution of the scalar equation $\nabla^2 s + \hat{k}^2 s = 0$ and β is a constant which depends on the boundary conditions. The only solution (finite at $r = 0$) of this differential equation is the zeroth order spherical Bessel function, $s = j_o(\hat{k}r)$. The solution of the differential equation (Laplace) exterior to the sample gives an external field $\mathbf{H}$ sum of the applied field $\mathcal{H}$ plus the induced dipole field $\hat{\alpha}\mathcal{H}$. By matching the boundary conditions, we compute the polarizability $\hat{\alpha}$ of the specimen:

$$\hat{\alpha} = \frac{1}{4\pi}\frac{n}{n-1}\left(1 - \frac{xj_1(x)}{n\partial[xj_1(x)]/\partial x}\right)_{x=\hat{k}a}, \tag{3.5.2}$$

where $n = 1/3$ is the depolarization factor of a sphere, $-j_1(x)/2 = j_o'(x)$ is the first derivative of the zeroth order spherical Bessel function and a is the radius of the sphere.

In the case of the electric field excitation, inside the sample, we search for a solution of the form $\phi = -\beta\nabla.(s\mathcal{E})$ where $\mathbf{E} = -\nabla(\phi)$ and ϕ is the electric potential.

Because the both cases (electric and magnetic field excitation) are related, it is useful to write the solution in a more general way. This can be achieved by defining an effective permeability $\hat{\mu}$ or an effective permittivity $\hat{\epsilon}$:

$$\hat{\mu}_{eff} = \hat{\beta}\hat{\mu}, \tag{3.5.3a}$$

$$\hat{\epsilon}_{eff} = \hat{\beta}\hat{\epsilon}, \tag{3.5.3b}$$

where $\hat{\beta}$ is given by the same expression for the two cases:

$$\hat{\beta} = -2\left(\frac{-(\hat{k}a)\cos(\hat{k}a) + \sin(\hat{k}a)}{-(\hat{k}a)\cos(\hat{k}a) + \sin(\hat{k}a) - (\hat{k}a)^2\sin(\hat{k}a)}\right). \tag{3.5.4}$$

One can use the Clausius-Mosotti [97] equation to get the polarization and the magnetization from the permittivity and permeability response with

$$\mathbf{P} = \frac{3}{4\pi}\frac{\hat{\epsilon}_{eff} - 1}{\hat{\epsilon}_{eff} + 2}\mathcal{E} = \hat{\alpha}_e\mathcal{E}, \tag{3.5.5a}$$

and

$$\mathbf{M} = \frac{3}{4\pi}\frac{\hat{\mu}_{eff} - 1}{\hat{\mu}_{eff} + 2}\mathcal{H} = \hat{\alpha}_m\mathcal{H}. \tag{3.5.5b}$$

From the resulting value of $\hat{\alpha}$ plugged into Eq. (3.3.14), we obtain the relation between $\hat{\epsilon}$ (or $\hat{\sigma}$) and $\Delta\hat{\omega}$. An abstract is found in appendix C. Notice that a non-trivial result is obtained in the magnetic field: a non-magnetic sample has a non-zero high-frequency magnetic polarizability that depends on the conductivity of the material.

The value of $\hat{\beta}$ takes some simple limiting value when $|\hat{k}a| \ll 1$ or $\gg 1$:

$$\lim_{\hat{k}a\to 0}\hat{\beta} = 1 + \frac{1}{10}(\hat{k}a)^2 + \frac{9}{700}(\hat{k}a)^4 + O[\hat{k}a]^6, \tag{3.5.6a}$$

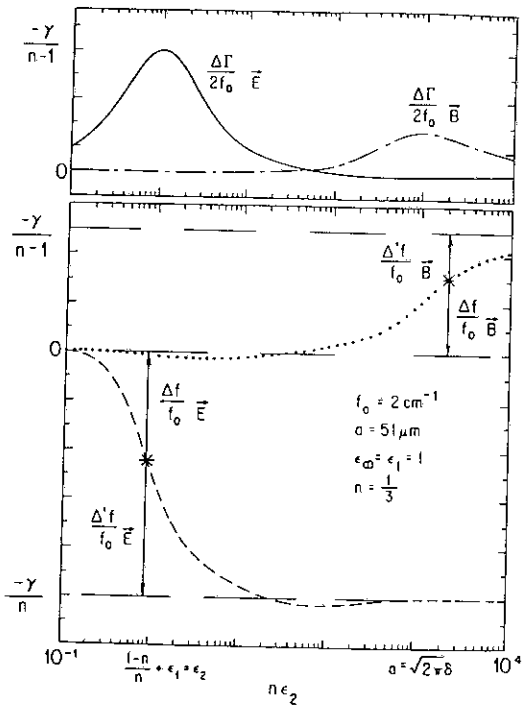

Fig. [3.9]: σ_1 dependence of $\Delta\hat{\omega}/\omega_o$ for a sphere of radius a = 51 μm in the electric field and magnetic field maxima (σ_2 is held constant). Δf is the frequency shift, and $\Delta' f$ is the perfect conductor frequency shift (cf. page 45). The metallic shift ($\lim_{|\hat{\sigma}|\to\infty} \Delta\hat{\omega}/\omega_o$) is equal to γ/n in the **E** field and $\gamma/(n-1)$ in the **B** field.

$$\lim_{\hat{k}a\to\infty} \hat{\beta} \;=\; \frac{2i}{\hat{k}a}. \tag{3.5.6b}$$

3.5.3 Sphere in the E

Following this procedure we have computed $\Delta'\hat{\omega}/\omega_o = \Delta' f/f_o + \mathrm{i}\ \Delta'\Gamma/2f_o$ for a sphere in the electric field as a function of $n\epsilon_2$ ($n = 1/3$ for a sphere), with ϵ_1 held constant. We have displayed on Fig. [3.9] the results, and we observe that:

a. the absorption, $\Delta\Gamma$, peaks when $\epsilon_1 = \epsilon_2 + 1 - 1/n$.

b. the metallic shift ($\lim_{|\hat{\sigma}|\to\infty} \Delta\hat{\omega}/\omega_o$) is equal to $-\gamma/n$ (note the sign).

c. the shift $\Delta' f/f_o$ (cf. page 45) changes sign and becomes negative in the skin-depth regime.

On Fig. [3.10] we have plotted on a logarithmic scale the same figure, to highlight that in the skin-depth regime $\Delta\Gamma$ and $\Delta' f$ are simply proportional to the surface impedance. We have also shown the dependence of the absolute value of the perfect conductor frequency shift ($\Delta' f/f_o$): on this plot $\Delta' f/f_o$ changes sign at the position of the logarithmic divergence. We have normalized the parameters to the metallic shift (γ/n). In the electric field maxima, we observe three independent regimes, each characterized by a different power law dependence of the loss $\Delta\Gamma$ versus σ_1:

1. $\epsilon_2 < \epsilon_1/n$, this is the insulator side of the depolarization regime (where n is the depolarization factor). In this range, $\Delta\Gamma/2f_o \propto \sigma_1$ and the frequency shift saturates to a constant approximately zero in the case of a metal ($\Delta f/f_o \sim 0$).

2. $\epsilon_1/n < \epsilon_2 < 4\pi(c_o/\omega a)^2$, this is the metallic side of the depolarization regime, where the skin-depth ($\delta = c_o/\omega\sqrt{2/\epsilon_2}$) is bigger than the radius of the sphere (a) but with the restriction $\sigma_1 > (\omega/4\pi)\epsilon_1/n$.

In this regime $\Delta\Gamma/2f_o \propto 1/\sigma_1$ and the frequency shift goes asymptotically to the metallic shift from below.

3. $4\pi(c_o/\omega a)^2 < \epsilon_2$, this is the skin-depth regime, where the fields do not penetrate throughout the sample. In this regime, $\Delta\Gamma/2f_o \sim -\Delta' f/f_o \propto 1/\sqrt{\sigma_1}$ as shown on the Fig. 3.10, thus showing that in this regime $\Delta'\hat{\omega}/\omega_o = \xi Z_s$ as predicted by Eq. (3.3.27). In order to calculate the resonator constant, ξ, we can use Eqs. (3.3.14) and (3.5.5a)

$$\frac{\Delta\hat{\omega}}{\omega_o} = -\frac{\gamma}{n}\,\frac{\hat{\epsilon}_{eff}-1}{\hat{\epsilon}_{eff}+2}, \tag{3.5.7}$$

where $n = 1/3$ for a sphere. Using the fact that as $\lim_{\sigma_1\to\infty}\hat{\beta} = 2i/\hat{k}a$

$$\lim_{\sigma_1\to\infty}\frac{\Delta\hat{\omega}}{\omega_o} \sim -\frac{\gamma}{n}\left(1+\frac{i\hat{k}a}{2n\hat{\epsilon}}\right), \tag{3.5.8}$$

Comparing this result to Eq. (3.3.27), we find the value of the resonator constant for a sphere in the electric field maximum.

$$\xi = \frac{-i\gamma}{n^2}\left(\frac{\omega a}{2c_o}\right) = -\frac{9}{2}\,i\gamma\,\frac{\omega a}{c_o}. \tag{3.5.9}$$

3.5.4 Sphere in the H

Using the same procedure as in the previous case, we have computed $\Delta'\hat{\omega}/\omega_o$ induced by a sphere in the maximum of the magnetic field, we observe from Fig. [3.9] several differences with the electric field maximum result:

a. the absorption, $\Delta\Gamma$, peaks when $\delta/a = \sqrt{2\pi}$.

b. the metallic shift ($\lim_{|\hat{\sigma}|\to\infty}\Delta\hat{\omega}/\omega_o$) is positive and equal to $-\gamma/(n-1)$ (the difference of sign can be explained by noticing that for a metal in the electric field the finite frequency polarizability is positive while in the magnetic field it is negative).

c. the frequency shift $\Delta f/f_o$ changes sign and becomes positive in the skin-depth regime.

As for the electric field, we have plotted the absolute value of the results on a logarithmic scale, Fig. [3.11], and we show that in the magnetic maximum case there are only two independent regimes:

1. $4\pi(c_o/\omega a)^2 > \epsilon_2$, this is again the depolarization regime, where the magnetic field penetrates throughout the sample. We observe that $\Delta\Gamma/2f_o \propto \sigma_1$ and the frequency shift Δf saturates to a constant approximately zero for a metal (Δf negative).

2. $4\pi(c_o/\omega a)^2 < \epsilon_2$, this is again the skin-depth regime, where the magnetic field is expelled from the sample (diamagnetism). As with the electric field in this regime, $\Delta\Gamma/2f_o = -\Delta' f/f_o \propto 1/\sqrt{\sigma_1}$. In this regime $\Delta'\hat{\omega}/\omega_o$ is proportional to the surface impedance, cf. Eq. (3.3.27). To compute the proportionality constant (resonator constant) we follow the same procedure as for the electric field:

$$\lim_{\sigma_1\to\infty}\frac{\Delta\hat{\omega}}{\omega_o} \sim -\frac{\gamma}{n-1}\left(1+\frac{2i}{\hat{k}a(n-1)}\right). \tag{3.5.10}$$

In the magnetic field, the resonator constant of a sphere is,

$$\xi = \frac{-i\gamma}{(n-1)^2}\left(\frac{2c_o}{\omega a}\right) = -\frac{9}{2}\,i\gamma\,\frac{c_o}{\omega a}. \tag{3.5.11}$$

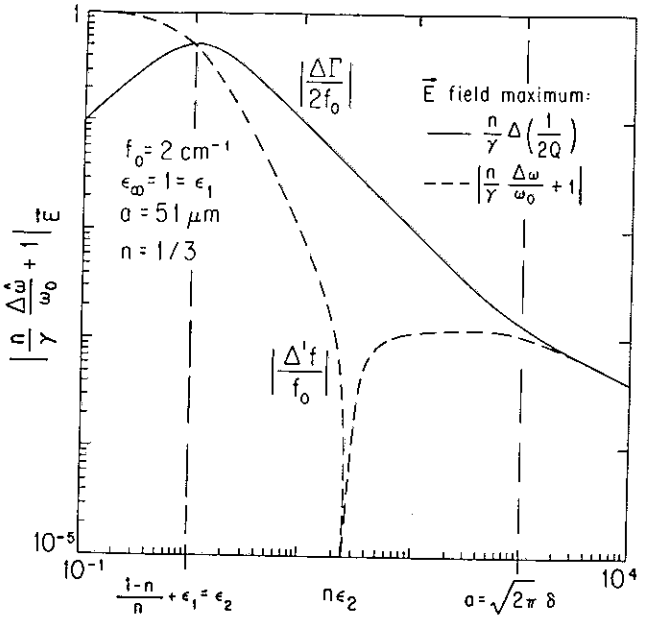

Fig. [3.10]: The σ_1 dependence of the absolute value of $\Delta\Gamma$ and $\Delta' f$ for a sphere of radius a= $51\mu m$ in the electric field maximum at f = $2cm^{-1}$ with $\epsilon_1 = 1$. We observe 3 distinct regimes, each characterized by a different power law dependence of the loss $\Delta\Gamma$. In the skin-depth regime $\Delta\Gamma = -\Delta' f \propto \sqrt{1/\sigma_1}$ and thus $\Delta'\hat{\omega}/\omega_o$ is simply proportional to the surface impedance. The frequency shift $\Delta f/f_o$ is always negative, but the perfect conductor frequency shift $\Delta' f/f_o = \Delta f/f_o + \gamma/n$ changes sign for $n\epsilon_2 > 20$ (to become negative) and equals zero at the point of negative divergence.

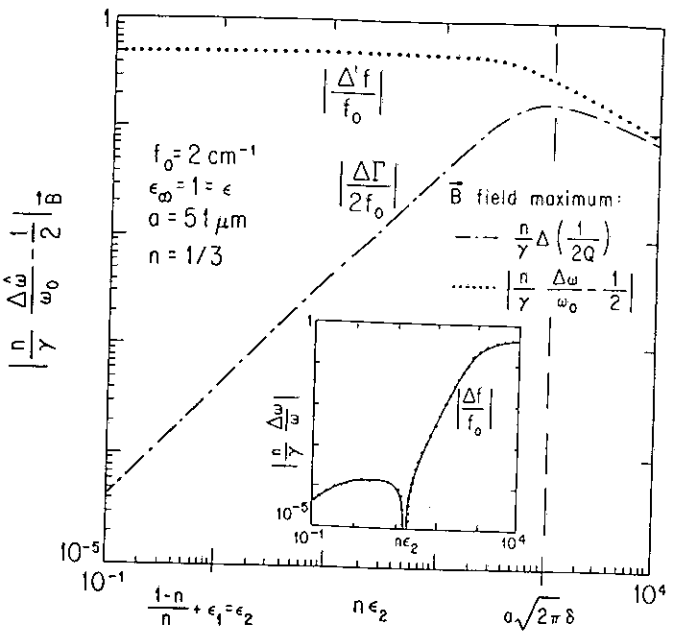

Fig. [3.11]: The σ_1 dependence of the absolute value of $\Delta\Gamma$ and $\Delta' f$ for a sphere of radius a= $51\mu m$ in the magnetic field maximum at f = $2cm^{-1}$ with $\epsilon_1 = 1$. In the insert we show the dependence of the frequency shift $\Delta f/f_o$. We observe 2 distinct regimes, each characterized by a different power law dependence of the loss $\Delta\Gamma$. In the skin-depth regime $\Delta\Gamma = -\Delta' f \propto \sqrt{1/\sigma_1}$ and $\Delta'\hat{\omega}/\omega_o$ is simply proportional to the surface impedance. The perfect conductor frequency shift $\Delta' f/f_o$ is always negative, but the frequency shift $\Delta f/f_o$ = $\Delta' f/f_o$ - $\gamma/(n-1)$ changes sign for $n\epsilon_2 > 20$ (to become positive) and equals zero at the point of negative divergence on the insert.

In the insert we have plotted $\Delta f/f_o$ to show the change of sign of the frequency shift. We have assumed that the permeability of the material is 1 (generally the case for a metal [119]).

3.5.5 Spherical approximation

A more insightful way to look at the problem, is to first remark that the Clausius-Mosotti expression was conceived as a first order approximation of the polarizability for a spherically symmetric system. In an attempt to define an expression relating the permittivity and the polarizability for an ellipsoid, we define a generalized Clausius-Mosotti expression:

$$\hat{\alpha}_e = \frac{1}{4\pi n}\frac{\hat{\epsilon}_{eff} - \alpha_1}{\hat{\epsilon}_{eff} + \alpha_2}, \tag{3.5.12}$$

where the effective values are defined by the same formulas as in Eq. (3.5.3b). A similar expression was already encountered in the limit $\hat{k}a \ll 1$ by Eq. (3.3.18). The previous definition is compatible with the former result if:

$$\alpha_1 = 1, \tag{3.5.13a}$$

$$\alpha_2 = \frac{1-n}{n}. \tag{3.5.13b}$$

We thus obtain the following expressions:

$$\hat{\alpha}_e = \frac{1}{4\pi}\frac{\hat{\beta}\hat{\epsilon}-1}{n(\hat{\beta}\hat{\epsilon}-1)+1}, \tag{3.5.14a}$$

$$\hat{\alpha}_m = \frac{1}{4\pi}\frac{\hat{\beta}\hat{\mu}-1}{n(\hat{\beta}\hat{\mu}-1)+1}. \tag{3.5.14b}$$

$\hat{\beta}$ is a priori given by the same expression for the two cases. Notice that for most metals in the magnetic field $\hat{\mu}=1$.

In the other limit $\hat{k}a \gg 1$, $\hat{\beta} \propto (\hat{k}a)^{-1}$ and the effective permittivity $\hat{\epsilon}_{eff} \to \infty$. Thus the induced variation of the cavity characteristics in the electric field is:

$$\frac{\Delta\hat{\omega}}{\omega_o} = -\frac{\gamma}{n} + \frac{\gamma}{n^2}\frac{1}{\hat{\epsilon}_{eff}}, \tag{3.5.15}$$

using a first order expansion in power of $1/\hat{\epsilon}_{eff}$ of the previous expression. On the other hand $\hat{\mu}_{eff} \to 0$, and in the magnetic field:

$$\frac{\Delta\hat{\omega}}{\omega_o} = \frac{\gamma}{1-n} + \frac{\gamma}{(1-n)^2}\hat{\mu}_{eff}. \tag{3.5.16}$$

The values of $\lim_{\sigma_1\to\infty}\hat{\beta}$ are computed in Table [3.3] for different spheroids in the limit $a \gg b$. The results are expressed in terms of a normalized resonator constant, value expected for an imaginary sphere inclosing the sample (radius a). More explicitly, in the case of the electric field, we obtain:

$$\frac{\Delta\hat{\omega}}{\omega_o} = -\frac{\gamma}{n} + \frac{\gamma}{n^2}\frac{\omega a}{2c_o}(-i)Z_{eff}, \tag{3.5.17a}$$

$$Z_{eff} = \frac{\xi}{\xi_{sphere}}Z_s. \tag{3.5.17b}$$

And in the magnetic field:

$$\frac{\Delta\hat{\omega}}{\omega_o} = \frac{\gamma}{1-n} + \frac{\gamma}{(1-n)^2}\frac{2c_o}{\omega a}(-i)Z_{eff}. \tag{3.5.18}$$

3.5.6 Ellipsoid in the E (skin-depth regime)

To our knowledge, the relationship between $\hat{\sigma}$ and $\Delta\hat{\omega}/\omega_o$ for a general shape has never been calculated. Moreover, the resonator constant ξ of a spheroid (ellipsoid with one symmetry axis) is known in one case solely: a prolate spheroid in the electric field maximum, with the field along the symmetry axes. The computation was performed by Cohen and Ong in 1975 [45, 152]. For a prolate spheroid ($a > b = c$) of eccentricity $e = \sqrt{1-(b/a)^2}$ with $a \gg b$ they obtain

$$\Im\left(\frac{\Delta\hat{\omega}}{\omega_o}\right) = \Im(\xi Z_s), \tag{3.5.19a}$$

where

$$\xi = -i\frac{9\pi}{2^5}\frac{\gamma}{n^2}\left(\frac{\omega b}{2c_o}\right), \tag{3.5.19b}$$

and n is the depolarization factor along the field.

We have completed the work by computing the resonator constants of a prolate and oblate spheroid in

Resonator Constant			
	ξ/ξ_{sphere}	Electric Field	Magnetic Field
Prolate Spheroid	Field $\parallel \hat{z}$	$(3^2\pi/2^5)\ b/a$	$(3\pi/2^3)\ a/b$
	Field $\perp \hat{z}$	$(3\pi^3/2^6)\ b/a$	$(3\pi/2^4)\ a/b$
Oblate Spheroid	Field $\parallel \hat{z}$	$(3/2^3)\ a/b$	$(3/2)\ b/a\ \ln(a/b)$
	Field $\perp \hat{z}$	$(3^2/2^3)\ b/a\ \ln(a/b)$	$(3/2^2)\ a/b$
Sphere	ξ_{sphere}	$-i\gamma/n^2\ \ [\omega a/2c_o]$	$-i\gamma/(n-1)^2\ \ [2c_o/\omega a]$

Table 3.3: Resonator constant of a spheroid for different orientation in the **E** and **H** field, where $2a > 2b$ are the sample dimensions (the values are computed in the limit $a \gg b$), c_o is the speed of light, n is the depolarization factor, ξ_{sphere} is the resonator constant of the equivalent sphere inclosing the sample (radius a), $\hat{z}$ is the direction of the spheroid symmetry axis and the field is either parallel or perpendicular to this axis.

both the electric and magnetic field for all possible orientations. The results are listed in Table [3.3]. The details of the algebra are shown for one example in appendix D.

3.5.7 Ellipsoid in the H (skin-depth regime)

The exact resonator constant of a prolate spheroid placed at the anti-node of the magnetic field is derived in the appendix. In the limit $a \gg b$ (i.e. needle shaped sample) one finds

$$\xi = \frac{-3i\gamma c_o \pi}{4b\omega(n-1)^2}. \tag{3.5.20}$$

A comparison can be made of the loss obtained when the sample is placed at the maximum of the electric field maximum to the loss for the magnetic field. For a prolate spheroid in the limit $a \gg b$ where the bulk of the currents run along the a axis ($\mathbf{E}\|\hat{a}$ and $\mathbf{H} \perp \hat{a}$) one finds

$$\rho = \frac{\Delta\left(\frac{1}{2Q}\right)_{\mathbf{B}}}{\Delta\left(\frac{1}{2Q}\right)_{\mathbf{E}}} = \frac{2}{3}\frac{{n_\parallel}^2}{(1-n_\perp)^2}\left(\frac{2c_o}{\omega b}\right)^2, \tag{3.5.21}$$

where $n_\parallel$ and $n_\perp$ are the depolarization factors parallel and perpendicular to $\hat{a}$ respectively. Typical values are $a = 575\ \mu$m, $b = 50\ \mu$m, and $f = \omega/2\pi = 60 \times 10^9 sec^{-1}$. Using these values of a and b one finds [155] $n_\parallel = .0164$, $n_\perp = .4918$, and $\rho = .71$. As ρ depends on the geometry of the sample, one can increase the relative sensitivity of the measurement by choosing the appropriate configuration.

In summary, we have described the experimental technique used in this study and established a relationship between the intrinsic conductivity $\hat{\sigma} = \sigma_1 + i\sigma_2$ and the parameters experimentally accessible with the cavity perturbation technique: the frequency shift $\Delta f$and the bandwidth $\Delta\Gamma$. We have computed explicitly the result for a sphere and compared it with the calculation of the surface impedance. In the

skin-depth regime, we have carried out the computation for both a prolate an oblate spheroid at the electric and magnetic field maximum.

Chapter 4

Experiments on conventional superconductors

The motivation for a new measurement on the electrodynamics of a conventional superconductor was two-fold. First, it was necessary to test the sensitivity of our new amplitude technique and for that we needed compounds that had optical properties already extensively studied. Second, nobody has ever observed the conductivity coherence peak: although this feature was expected, its observation represented a technological challenge. The materials selected were Nb and Pb, since they were readily available in the lab with a T_c large enough ($\sim$ 10 K) to be studied in their superconducting phase with an ^{4}He cryogenic system.

4.1 Historical survey

Our discussion will start with a brief account of the extensive work done by our predecessors.

4.1.1 Optical properties

The first experiments on the electrodynamic properties of superconductors were done by M. Tinkham twenty years ago [65]. He and Richards investigated extensively the far-infrared properties of several metallic elements In, Sn, Hg, Ta, V, Pb and Nb [167]. His results were the first optical evidence that a single particle gap exists in the excitation spectrum of a superconductor. The technology developed was remarkable for the time as the frequency window investigated was the lower end of the Far Infra-Red spectrum (10 – 200 cm^{-1}). Even nowadays, very few experimental group still explore this difficult spectral range. The observation by Palmer and Tinkham of the shallow increase of the conductivity at the gap edge proved that σ_1 was indeed governed by case 2 coherence factors [159] (Fig. [1.7]): the spectrum of $\sigma_1(\omega)$ was in good agreement with the Mattis-Bardeen expression [135]. The Pb in particular was the center of a detailed study [65], some apparent structure in the spectrum at 17 cm^{-1} was attracting much of the attention [64] as it could indicate the presence of unpredicted goldstone modes. Later experiments showed that the effect was in fact spurious [55]. In 1957, millimeter-wave experiments (2 – 200 cm^{-1}) were performed by Glover and Tinkham on thin-films of Pb using transmission techniques [96]. The extracted complex frequency was compared with the new BCS theory (mentioned in the paper as a footnote) and the two papers (experiment and theory) appeared within few months from one another. In those experiments the lowest photon energy used was approximately $\hbar\omega \sim \Delta/3$ where the coherence peak is not expected. The microwave range of frequency was investigated in some details few years later by J.R. Waldram [194] and M.S. Khaikin [104]. They measured the temperature dependence of the surface resistance and compared their results with the BCS model, in those cases $\hbar\omega \sim \Delta/2$. Subsequent studies by S.L. Lehoczky were based on measurements of the microwave (24 – 70 GHz) transmission and reflection coefficients for thin

superconducting films of Pb [126, 166]: the inferred $\sigma_1(T)$ was interpreted in terms of fluctuation effects. More recently, some new microwave (5 GHz) studies were performed in Germany by Halbritter [75] on the surface resistance of Pb and Nb. The aim was to evaluate more carefully the residual R_s in those materials and study mean-free-path effects. Again the results were in good agreement with the microscopic theory developed by BCS [21]. In the last couple of years, with the apparition of new families of 'unconventional' superconductors, a renewal of interest has flourished for their electrodynamic properties. But between those two periods, the experimental techniques have evolved greatly and the precision of the measurements has been considerably enhanced.

4.1.2 Theoretical models

The microscopic theory of BCS was applied to compute the electrodynamic properties by Mattis and Bardeen [135] and by Abrikosov [2, 3] whereby superconductors are near the weak coupling limit and in small magnetic fields. These theories were developed for type I superconductors (Pb) in the clean limit, where the penetration depth $\lambda(0)$ is small compared with the coherence length $\xi(0)$ but the result applies also for superconductors with a mean-free-path ℓ smaller than $\xi(0)$. In both cases, the quasiparticles life-time τ is not taken into account. In the weak coupling case, numerical computations were performed by P.B. Miller [139] in 1960. Later, Sang-Boo Nam extended the work for impure superconductors near the strong coupling limit [145, 146]. Starting with the Eliashberg theory [56, 57] he extended the BCS model and provided a well tested [40] model of dynamical properties. For Pb [179], one has to take into account the retarded nature of the electron-phonon interaction [173, 60]. In 1964, D.J. Scalapino [174] calculated the density of states for Pb assuming that the phonon spectrum is Lorentzian and used strong coupling effects to fit the data from tunneling experiments [63].

Our results on the Pb and Nb are compared with the Mattis-Bardeen model, with no corrections from finite mean-free-path. The Nb conductivity is calculated from the surface impedance data with a local formalism, while the anomalous regime is used to analyze the Pb. In the later element, some deviations from the BCS result are reported and the differences are explained in terms of strong coupling effects.

4.2 Sensitivity optimization

The results presented in this chapter are restrained to a particular frequency, 60 GHz. It represents our best measurement sensitivity.

4.2.1 60 GHz cavity

One can estimate retrospectively the feasibility of the experiment and the predicted magnitude of the effects. It was shown in chapter 2 that the size of the peak decreases logarithmically as the photon energy increases (Eq. (2.2.6)). The single particle gap value of Pb and Nb is around 20 cm^{-1} from optical measurements [167]. To detect at least a 10% effect, a frequency below 2 cm^{-1} or 60 GHz should be employed. Also, it was shown on page 22 that R_s increases as ω^2 for a BCS superconductor. Therefore the highest frequency is desirable to increase the sensitivity. However as the wavelength decreases it becomes more and more difficult to avoid the formation of a spurious standing-wave. Practically, we cannot measure accurately the frequency of the source above 100 GHz, making our 60 GHz cavity the best compromise. We display in Fig. [4.1] the expected temperature dependence of the measured parameter for Pb. The curves were computed from Mattis-Bardeen both in the local and anomalous regime (cf. Chapter 2). Decreasing the frequency accentuates the drop of $R_s(T)$ around T_c.

The resonator used in this study is a cylindrical copper cavity working in the TE_{011} mode, its height is 4.77 mm and its diameter is 7.15mm. It resonates at 60 GHz or 2 cm^{-1} on the TE_{011} mode.

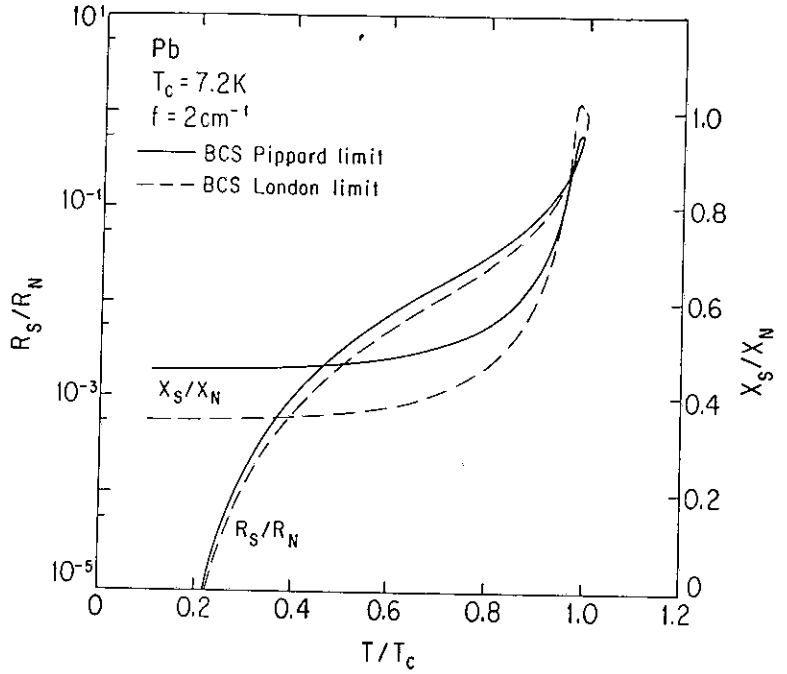

Fig. [4.1]: Calculated temperature dependence of the surface impedance $Z_s = R_s - iX_s$ at 60 GHz in both the Pippard and the London limit, for a BCS superconductor. We have used the parameters of Pb for the simulation (T_c = 7.2K, $\Delta(0)$ = 15.5K).

4.2.2 End-plate technique

The measurement of the surface impedance of the material was done by using an endplate technique, where Z_s is proportional to the variation of the resonator bandwidth Γ and resonance frequency f_o when one of the Cu endplates of the cavity is replaced by the sample. This scheme has the advantage over other possible experimental configurations, that no assumption is needed on the sample size or geometry (no depolarization factor is involved), which simplifies the analysis. We also worked in the most comfortable position, by measuring the largest sample with the sensitivity of a high Q resonator. Our experiments have been performed with a bulk sample of Nb and Pb cut in a flat disk of 10mm diameter and 5 mm height, with a polished face that replaced the copper endplate and form a wall of the cavity. For the TE_{011} mode, the resonator constant is given by the expression:

$$\xi = -i\frac{{c_o}^3\pi^2}{h^3\omega^3} = 0.0458, \tag{4.2.1}$$

where h is the height of the cavity and $f = \omega/2\pi$ the frequency.

4.2.3 Calibration

The frequency of resonance f_o and the half-width Γ are measured as a function of the temperature in two separate runs one before and one after the replacement of the copper (Cu) endplate by the sample (s).

$$\Delta\Gamma = \Gamma_s - \Gamma_{Cu} = \alpha(\frac{1}{\sqrt{A_s}} - \frac{1}{\sqrt{A_{Cu}}}), \tag{4.2.2a}$$

$$\Delta f = f_s - f_{Cu}. \tag{4.2.2b}$$

The difference is related to Z_s, the surface impedance of the sample, through the relation:

$$\frac{\Delta f}{f_o} + i\frac{\Delta\Gamma}{2f_o} = \xi(Z_s - Z_{Cu}), \tag{4.2.3}$$

where ξZ_{Cu} is the loss of the copper endplate only and ξ is the resonator constant.

In order to evaluate the surface impedance of the Cu endplate, we have calculated the ratio of the ohmic losses in the endplate compared with the total losses at all the other surfaces of the resonator. This ratio is independent of the Cu conductivity value. For a cylindrical cavity operating in the TE_{011} mode with a radius of 7.15 mm, 39 % of the wall losses occur on one of the endplate. If the assumption is made that all of the losses in the cavity are ohmic solely, then:

$$\xi Z_{Cu} = 0.39\hat{\omega}_{Cu}, \tag{4.2.4a}$$

$$\hat{\omega}_s - 0.61\hat{\omega}_{Cu} = \xi Z_s. \tag{4.2.4b}$$

This subtraction give a fair agreement with the experimental results (R_s of a superconducting endplate goes almost to zero) but some other phenomena are neglected from the above assumption, for example radiative losses through the coupling hole. Those effects are small and contribute in an additive way. In the analysis, after the subtraction of the Cu impedance, a small offset (less than 5%) is left as a free parameter to account for this additive term such that R_s of the superconductor is adjusted to be zero at the lowest temperature.

Also one cannot make an absolute measurement of Δf, as the endplate must be removed between the runs. Since the frequency is proportional to the volume of the cavity, it is extremely sensitive to the precise position of the walls. Due to the mechanical uncertainties, it is not possible to put the endplate on, in exactly the same position each time, and the frequency shift $f_s - f_{Cu}$ can be measured only up to a numerical additive constant f_a. In other words, while $\Delta\Gamma$ is known (as reassembling does not change the loss), only $f_s - f_{Cu} + f_a$ can be measured with f_a unknown.

Because of the unknown f_a, some assumption had to be made for either the properties of the normal or superconducting state. As will be discussed below, both cases lead to similar results. For example, the zero temperature value of the penetration depth can be used to evaluate f_a. Alternatively, the normal state ratio X_s/R_s is known: for a metal in the local regime $R_s = X_s$, Eq. (2.3.4); if the anomalous regime applies then $X_s = \sqrt{3}R_s$.

4.3 Experimental results

We discuss the results obtained in Nb and in Pb separately. The reason for this is that (as will be shown later) those materials fall to different limits and the electrodynamics is somewhat different.

4.3.1 Nb

The Nb used in this study was a bulk piece of 99.9 % purity. The samples were provided and prepared by B. Alavi at UCLA. The metal piece was etched with nitric acid, in order to remove the oxide layer at the surface. One surface was polished using a diamond polishing cream down to 0.3 μm. When we cooled down the sample we observed an abrupt drop of the bandwidth at 9.3K, defining the transition temperature. The cusp at T_c is sharp and fluctuation effects are not detectable within our temperature accuracy (fluctuations effects smear the transition). We display in Fig. [4.2] the temperature dependence of both R_s and X_s, both normalized to the normal state value (defined as value taken when the temperature of the sample is slightly above T_c, i.e. $\sim$ 10K). For the analysis, we have assumed that the specimen was in the local regime, as supported by earlier measurements of Blaschke in 1982 [27]. In this case, we can use the Hagen-Rubens condition ($R_s = X_s$) to evaluate the frequency offset f_a. In the normal state we find that R_s and X_s have the same temperature dependence, confirming the validity of the latter assumption in the entire measured temperature range.

Using the measured value of the half-width in the normal state, we have calculated the normal state surface resistance $R_n = 0.0538\ \Omega$. This result leads to a resistivity $\sigma_n = 0.85 \times 10^6\ \Omega^{-1}.\mathrm{cm}^{-1}$. The length

	T_c [K]	R_n [Ω]	σ_n [Ω^{-1}cm^{-1}]	δ [$\AA$]	λ [$\AA$]	v_F [cm sec^{-1}]	ℓ [$\AA$]	$\xi(0)$ [$\AA$]	$\Delta(0)$ [K]
Nb	9.3	0.0538	0.85×10^6	2270	440	0.15×10^8	200	380	16.4
Pb	7.2	0.0421	1.40×10^6	1780	380	0.42×10^8	2000	830	15.5

Limiting cases:
Anomalous clean limit: $\lambda \ll \xi(0), \ell$
Local dirty limit: $\ell \ll \xi(0), \lambda$

Table 4.1: Various electrodynamical properties of Nb and Pb measured at 60 GHz, the v_F values are after Ref. [27, 96].

scale for the surface reactance is thus determined by the skin-depth in the normal state $\delta = 2270$ $\AA$. The surface resistance R_s(T) drops rapidly with decreasing temperature, the details are plotted on a logarithmic scale in Fig. [3]. The error bars diverge at low temperature and in this region (below 5K) the scatter of data points fixes an upper bound at 0.05 mΩ for the resolution. We have subtracted a positive offset of 2 mΩ to the R_s data, the difference is attributed to an overestimation of the baseline position when evaluating the loss in the Cu endplate, Z_{Cu}, from the empty cavity measurement. The offset reflects the systematic uncertainty of Eq. (4.2.4a) that neglects radiation leakage through the coupling hole or the contact between the endplate and the cavity body. Careful measurements of the residual surface resistance at this frequency were obtained through a different method: instead of using the endplate technique we have placed a small superconducting sample at the bottom of the same Cu cavity (antinode of the magnetic field). In this configuration Z_{Cu} can be measured directly and it was found that R_s far below T_c was inferior to 0.2 mΩ. There is also an intrinsic uncertainty in the measurement of the absolute value of the loss, originating from the dismantling of the cavity endplate after each run. We estimate also an upper bound of 0.1 mΩ for this effect.

The temperature dependence of the surface reactance, X_s, is directly proportional to the temperature dependence of the penetration depth λ(T). From the graph, we can deduce the zero temperature value of the penetration depth.

$$\frac{X_s(0)}{X_n} = \frac{2\lambda(0)}{\delta}. \tag{4.3.1}$$

On the same figure we can see that X_s(T) saturates at low temperature to a threshold value at 38.5% below the normal state value ($\delta/2$). This result gives a penetration depth $\lambda(0) = 440$ $\AA$, a result in good agreement with the value measured by B.W. Maxfield [136].

Using a fermi velocity value $v_F = 0.15 \times 10^8$ cm sec^{-1} we deduce a mean-free-path $\ell \sim 200$ $\AA$ just above T_c, in agreement with the value that one would extrapolate from R. Blaschke measurements [27], where they were using a sample with a conductivity three times higher than ours. We can also check that the value for the penetration depth $\lambda(0)$ that we obtained is not in disagreement with their value of the London penetration depth $\lambda_L = 330$ $\AA$. In the local limit, we can use the Pippard formula to evaluate the penetration depth:

$$\lambda = \lambda_L \sqrt{\frac{\xi(0)}{\ell}} = 450 \AA, \tag{4.3.2}$$

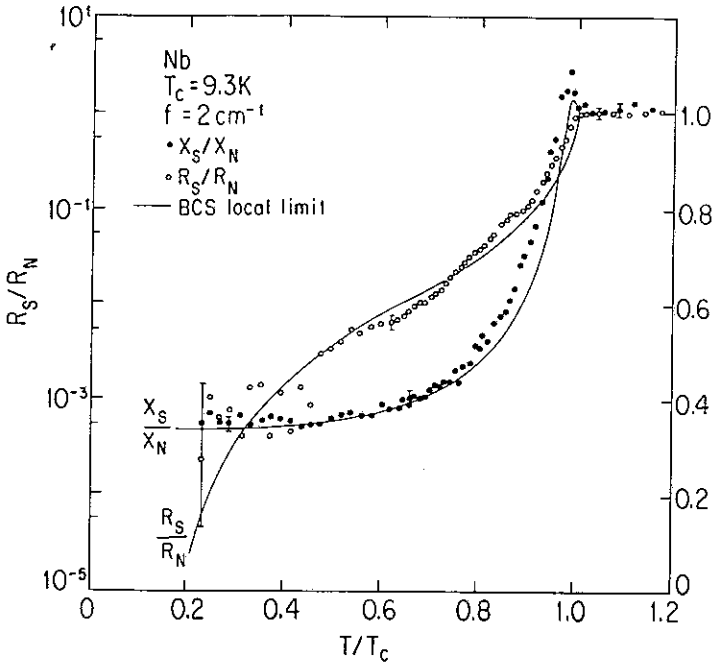

Fig. [4.2]: Temperature dependence of the surface resistance R_s and the surface reactance X_s of Nb. The surface resistance is displayed on a logarithmic scale while the surface reactance is plotted on a linear scale. The solid line is the computed Z_s from the Mattis-Bardeen conductivity [135] assuming that the measurement is in the local limit.

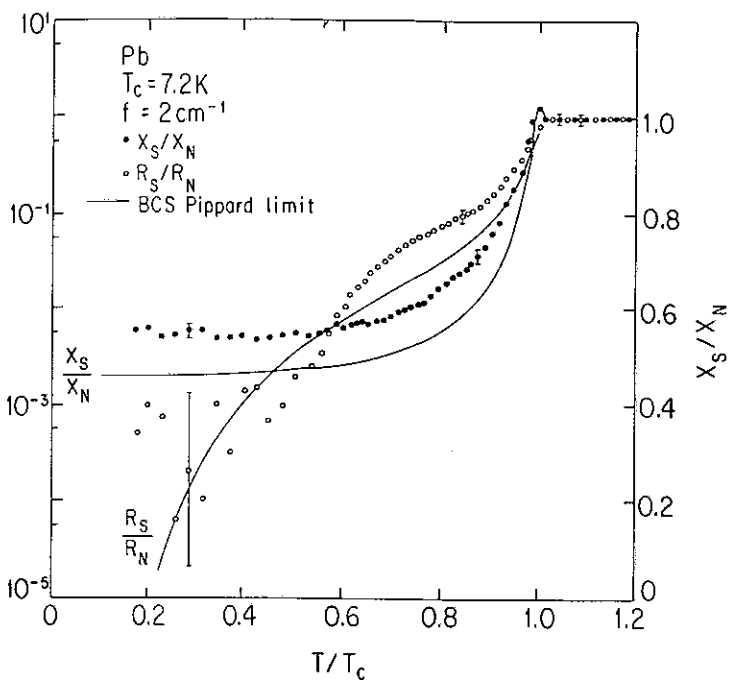

Fig. [4.3]: Temperature dependence of the surface resistance R_s and the surface reactance X_s of Pb. The surface resistance is displayed on a logarithmic scale while the surface reactance is plotted on a linear scale. The solid line is the computed Z_s from the Mattis-Bardeen conductivity [135] assuming that the measurement is in the anomalous and clean limit.

in good agreement with our result. We have used the fermi velocity and the BCS gap $\Delta(0)= 1.57\, k_B T_c$ to evaluate the coherence length $\xi(0) = \hbar v_F/\pi\Delta(0) = 380\mathring{A}$. Now that we have calculated the three relevant length scales in the measurement, we should check for the self-consistency of our assumption (namely, that we are in the local limit) the mean-free-path should be the lowest length scale: $\ell < \lambda < \xi(0)$ and this is indeed the case.

The solid line represents the computation of the temperature dependence of the surface impedance obtained for a superconductor (Nb) in the local limit, whose conductivity follows the Mattis-Bardeen expression. We notice that the agreement between the solid line and the experimental data points is excellent on the whole temperature range.

4.3.2 Pb

Pb is a type I superconductor with $\xi(0) > \lambda(0)$. Critical magnetic field measurements [21] have given a ratio $\xi(0)/\lambda(0) \sim 2$, suggesting that the element is not strongly in the Pippard regime, nevertheless we have used this limit to analyze the results: this approximation was also suggested by S.B. Nam [146]. The analysis in the local limit was published in a previous paper by K. Holczer *et al.* [93]. In the normal state of the anomalous regime $X_n/R_n = \sqrt{3}$.

The Pb used in this study was a bulk piece of 99.99% purity. The acid etched surface used as the wall of the cavity was freshly polished down to 0.05 μm, using an Alumina Permanent Suspension abrasive cream (Pb being very malleable metal). We display on Fig. [3] the measurement of the surface impedance in the superconducting phase. First we note, that the value observed for both the surface resistance and the surface reactance are much higher than the one on the Nb, although the single particle gap and the frequency are roughly similar. Our first step is to compute the normal state surface resistance. Here again the procedure consists of using the measured value $\Delta(1/2Q)$ and converting it to surface resistance via the resonator constant. We find for R_n a value somewhat similar to the one reported previously for the Nb: $R_n(\text{Pb}) = 0.0421\ \Omega$. The index n means again the normal state value, or the value at

temperature slightly above the critical temperature, T = 8K in this particular case. This value of R_n gives an effective conductivity $\sigma_n' = 1.6 \times 10^6\ \Omega^{-1}.\mathrm{cm}^{-1}$, where the term "effective" means the figure that we would have computed for a classical metal (local limit). The real conductivity is larger and is corrected by the anomalous formula:

$$\sigma_n \sim \frac{\ell}{\delta}\sigma_n', \tag{4.3.3}$$

where ℓ is the mean-free-path and δ is the skin-depth, related to the effective conductivity through the local formula:

$$\delta = \frac{c_o}{\sqrt{2\pi\omega\sigma_n'}}. \tag{4.3.4}$$

Using the measured value, we deduce that $\delta = 1780$ Å. The same conclusion that we made on the Nb behavior of $R_s(T)$ applies here. The inherent resolution of our R_s measurement is of the order of 0.1 mΩ. We subtracted a spurious offset of 1.5 mΩ in the baseline.

We cannot evaluate directly the value of the mean-free path ℓ of the Pb in our microwave measurement. We have to refer to some other works done by Tinkham on the infra-red properties [65, 159, 55] to evaluate the ration n_e/m in the normal state conductivity [167]. From those measurements we estimate $\ell \sim 2000$ Å just above T_c. That will indicate that the sample is at the border line of the clean limit $\ell/\ \pi\xi(0) \sim 1$. This will also mean that we are just entering into the anomalous regime and the effective conductivity is approximately equal to the intrinsic one.

The surface reactance $X_s(\mathrm{T})$ is still proportional to the penetration depth $\lambda(\mathrm{T})$ in the Pippard limit, although in the normal state X_s is not simply related to the skin-depth anymore. We can show that the equivalent of Eq. (4.3.1) in the anomalous regime is:

$$\frac{X_s(0)}{X_n} \sim \frac{2.6\lambda(0)}{\delta}. \tag{4.3.5}$$

From the saturation value of the surface reactance at low temperature we estimate the ratio $X_s(0)\ /X_n = 0.55$ and then compute the value for the penetration depth at zero temperature $\lambda(0) = 380$ Å, very similar to the value quoted earlier [51].

We have plotted on the same graph the Mattis-Bardeen prediction in the Pippard limit (solid line). We observe a consistent underestimation of the surface impedance by the theoretical curve. The surface reactance is almost 20% higher, which is equivalent to saying that the penetration depth observed is 20% larger than the one predicted by BCS. This difference has repercussions on the evaluation of the surface resistance too, as the BCS loss is computed on an underestimated thickness. The net effect can be crudely modeled by a 20% translation of the whole curve on the semi-logarithmic scale. The measured values compared well with the reported results of R. Blaschke [27], and a more detailed discussion can be found in the next section.

J.P. Carbotte has computed the correction effects due to strong electron-phonon interaction [40] in the framework of the Eliashberg theory [56]. On page 1125 of his article in *Rev. Mod. Phys.* [40], he predicts a deviation of 20% for a coupling strength $T_c/\ \omega_{ln} = 0.1$, which is the value used for Pb.

4.4 Analysis

4.4.1 Nb

Using the measured value of R_s and X_s, we have evaluated the temperature dependence of the complex conductivity by inverting Eq. (2.3.12a). We display the results in Fig. [4.4]. Several features of the observed behavior are of importance. First the real part of the conductivity $\sigma_1$displays a wide peak that we attribute

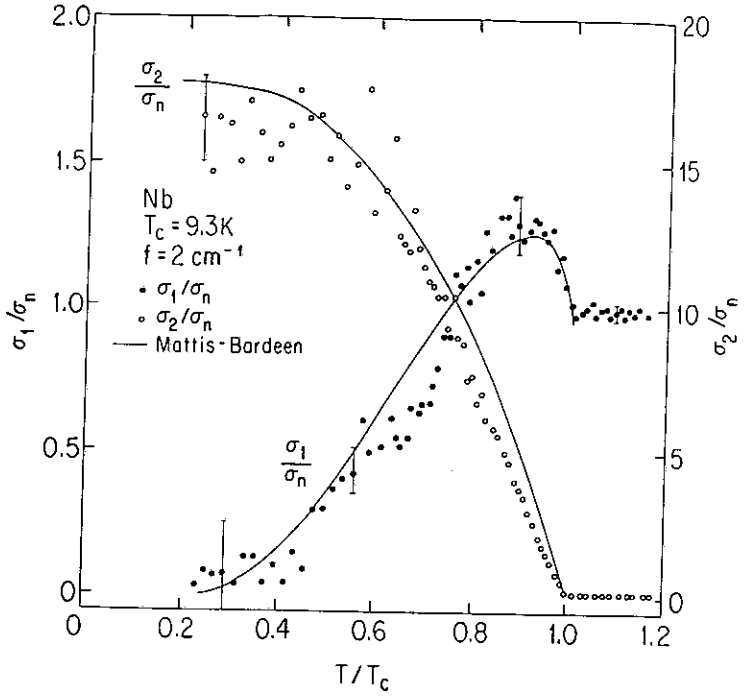

Fig. [4.4]: Temperature dependence of the complex conductivity of Nb evaluated from the surface impedance measurement. The solid line is the Mattis-Bardeen prediction [135].

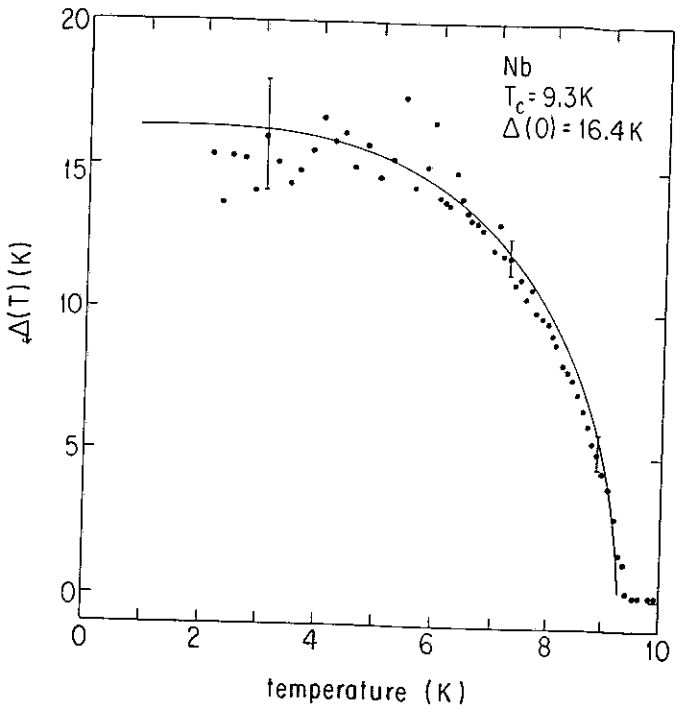

Fig. [4.5]: Temperature dependence of the superconducting gap of Nb as evaluated using Eq. (2.3.21). The full line is the BCS gap obtained from the Eq. (1.1.5).

to coherence effect. The temperature position of the maximum is too low compare to T_c to be fooled by fluctuation effects and this will be in contradiction with the temperature dependence of R_s, where we have seen a sharp drop, R_s is already several orders of magnitude lower than its normal state value at the peak maximum. The width of the peak at the normal state value is a signature of how fast the gap opens, and an indication of the coupling constant. The size of the peak depends on the cut-off energy scale of Eq. (1.2.18). In his original paper, L.C. Hebel [84], was fitting the coherence peak by assuming an anisotropy in the gap distribution. In the extreme dirty limit, the only relevant energy scale for the cut-off energy is the probing frequency. As shown in Chapter 2, the size of the peak is proportional to the logarithm of the ratio of the gap over the photon energy [188]. The size of the peak can thus indicate the value of the gap. The solid curve again represents the Mattis-Bardeen results. As expected from Fig. [4.3], the solid curve fits our data perfectly, which indicates already that the material closely follows the BCS weak coupling approximation.

We have displayed on the same figure the temperature dependence of the imaginary part of the conductivity. From those measurement one can evaluate the temperature dependence of the superconducting gap. By inverting Eq. (2.3.21) derived by S.B. Nam results in the local limit [145], one can thus deduce the temperature dependence of the BCS gap, using the result in Fig. [4.4]. We display the result on Fig. [4.5], and compare it with the BCS self-consistent gap equation (solid line) Eq. (1.1.5): the agreement is excellent.

4.4.2 Pb

In Fig. [4.6] we report the evaluated temperature dependence of the complex conductivity inferred from the surface impedance measurement, still using the Pippard limit:

$$\frac{Z_s}{R_n} = 2\left(-\frac{\hat{\sigma}}{\sigma_n}\right)^{-1/3} . \tag{4.4.1}$$

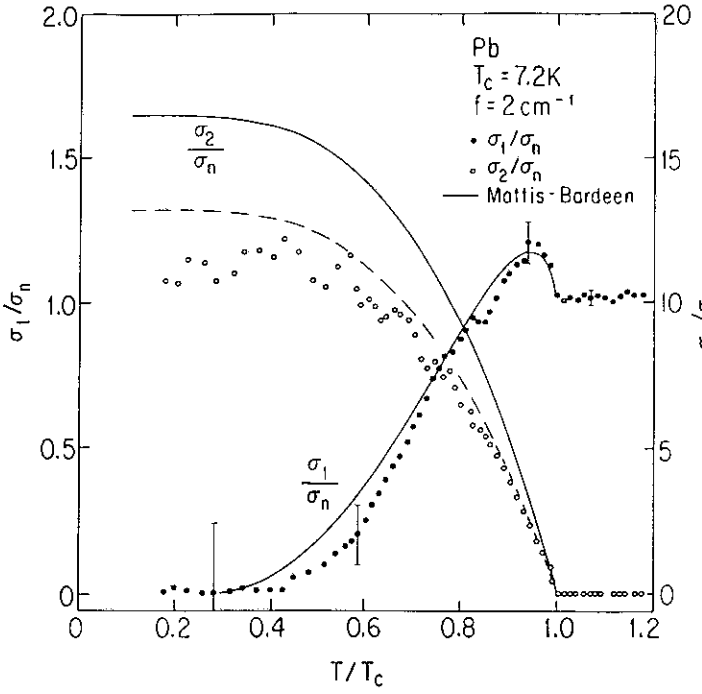

Fig. [4.6]: Temperature dependence of the complex conductivity of Pb evaluated from the surface impedance measurement. The solid line is the Mattis-Bardeen prediction [135]. The dashed line is the strong coupling correction of the BCS simulation.

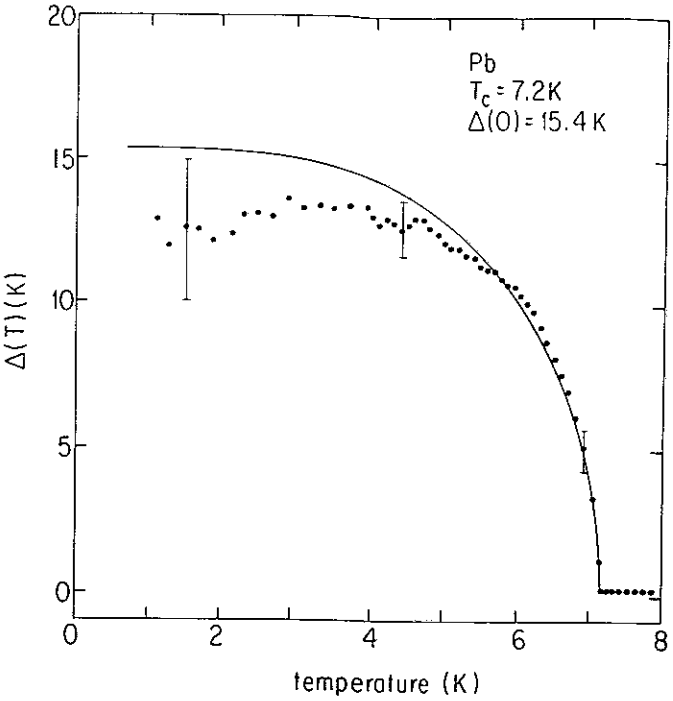

Fig. [4.7]: Temperature dependence of the superconducting gap of Pb as evaluated using Eq. (4.4.3). The full line is the BCS gap obtained from the Eq. (1.1.5).

We clearly observe a peak in the temperature dependence of σ_1 in the superconducting phase. We will use the same argumentation to convince the reader that the effect is intrinsic and not due to fluctuation effects, although fluctuations are expected to be higher in the Pb [55]. The temperature (T_{max}) at the maximum of σ_1 is well below T_c and corresponds to a setpoint where $R_s(T_{max})$ is an order of magnitude lower than R_n. Some studies performed by S.L. Lehoczky [126] on the microwave transmission and reflection coefficients for thin films of superconducting Pb, estimate that at high frequency (2 cm^{-1}) the real part of the conductivity σ_1 at T_c exceeds by 4% the normal state value and the effect is attributed to fluctuations. Those details are within our error bars and much smaller than the height of our peak.

The solid line is the Mattis-Bardeen conductivity computed for the Pb. As expected we observe a big discrepancy between the theoretical value and the measured value of σ_2. More surprising, we observe that the model works pretty well for σ_1(strong coupling effects should decrease the σ_1 value). Although it is not very clear in the literature how much strong-coupling effects would lower the Mattis-Bardeen value of σ_1, one can estimate it for σ_2. Using the expression given by S.B. Nam [146] we calculate that in the Pippard limit:

$$\frac{\lambda_L}{\lambda} = \left[\frac{3\pi^2}{4}\frac{\lambda_L}{\xi(0)}S\right]^{1/3}, \tag{4.4.2}$$

where S is given by the same expression as in Eq. (2.3.19). We know that in the Pippard limit we should recover the local result, nevertheless, in the computation we recover a correction factor due to the strong coupling. In a first approximation we have:

$$\frac{\sigma_2}{\sigma_n} = \frac{\Delta_{BCS}(0)}{\Delta_{Pb}(0)}\frac{\pi\Delta(T)}{\hbar\omega}\tanh\frac{\Delta(T)}{2k_BT}. \tag{4.4.3}$$

We have plotted as the dashed line the temperature dependence of σ_2 in the strong coupling regime.

Using the previous equation, we have calculated the observed temperature dependence of the single

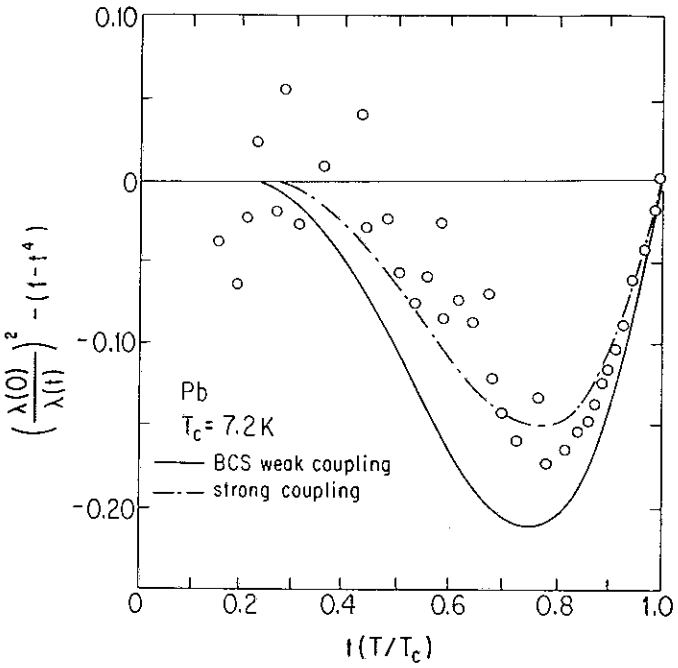

Fig. [4.8]: Temperature dependence of the penetration depth. We have plotted the deviation from the Gorter-Casimir prediction [70]. The solid line is the BCS Yosida function [199]. The dashed line is the correction obtained for strong coupling between electron-phonons.

particle gap for the Pb. We have plotted the result in Fig. [4.7]. The overall agreement is good, but we still observe some discrepancy between the observed data and the theoretical prediction. We attribute it to mean-free-path correction, or in other words that the limiting case used for the analysis might not apply tightly.

Finally we wish to display in Fig. [4.8] the temperature dependence of the penetration depth of Pb inferred from the surface reactance data. We display the result as a deviation from the phenomenological two-fluid [70]. We observe that the experimental data are in disagreement again with the BCS weak-coupling Yosida function, Eq. (2.5.2), and one need to introduce the electron-phonon interaction to account for our findings. This is again an indication that, within the measurement accuracy we can measure the departure from the weak-coupling limit.

We report the first results on the evaluation of the complex conductivity of Pb and Nb in the microwave range (2 cm^{-1}). The conductivity is inferred from the high accuracy measurement of the surface impedance. We describe our result within the framework of the BCS theory and the electrodynamic response calculated by Mattis and Bardeen gives a good description of our experimental results in the case of Nb, when the data are analyzed in the London limit. In particular, within our experimental accuracy we do not need to introduce any mean-free-path correction to account for our findings. In the case of the Pb, we found a good agreement with the BCS prediction for the real part of the conductivity σ_1, when the data are evaluated in the Pippard limit. But we have used the Eliashbergh strong coupling correction to fit the observed temperature dependence of σ_2.

In conclusion, our experiments are in full agreement with the BCS theory and confirm the existence of a peak in the conductivity below T_c. While Nb is in the weak coupling local limit, for Pb strong coupling corrections and nonlocal effects are evident.

Chapter 5

Electrodynamics of the cuprates

Until 1986, the highest T_c known for a superconductor was around 25 K (Nb_3Ge), the compound family were metallic alloys known as the $A15$. The value was regarded as an upper threshold imposed by the magnitude of the Debye temperature in crystals. In 1986 Bednorz and Müller [26] made a breakthrough discovery: a new class of oxide metals (known as charge transfer or mixed valence salts) were superconducting above 30 K. Five years later, the ground state properties of those new materials has not yet been resolved.

5.1 Theoretical models

This section is a short introduction to the current theories of superconductivity in the cuprates. A review was written by P. Lederer [123] and more specific details can be found herein. The focus of our discussion is to look at all the symmetry of the electron pair predicted by those various models. Again the details are left to the references.

5.1.1 The Hubbard hamiltonian

The Hubbard hamiltonian has been selected [14] to model the electron dynamics in the CuO_2 plane:

$$\hat{H} = \sum_{<i,j>,\sigma} t_{ij} \hat{a}^{\dagger}_{i,\sigma} \hat{a}_{j,\sigma} + U \sum_{i} n_{i,\uparrow} n_{i,\downarrow}, \tag{5.1.1}$$

where $n_{i\uparrow} = \hat{a}^{\dagger}_{i\uparrow} \hat{a}_{i\uparrow}$ is the number of electrons with a spin up (down) at site i. The first term sums the indices on the nearest neighbors only. In this representation there are four different states at each site: no occupancy $|0>$, single occupancy with spin up or down $|\uparrow>$ and double occupancy $|\uparrow\downarrow>$. The first term of the hamiltonian models the metallic properties of the crystal: it carries an electron from one site to its adjacent (t is the hoping term proportional to the overlap integral) and thus is responsible for the formation of a band (width $4t$). The second term is the on-site Coulomb repulsion that makes the double occupancy state less desirable, the repulsion range is short and vanishes for neighboring sites. For strongly correlated metals the on-site interaction U tends to infinity, and we are left with a truncated space where the double occupancy state is projected out. As $U \rightarrow \infty$, the hamiltonian transforms to the t-J model:

$$\hat{H}_{tJ} = P \left(t \sum_{<i,j>,\sigma} \hat{a}^{\dagger}_{i,\sigma} \hat{a}_{j,\sigma} + J \sum_{i,j} S_i S_j \right) P, \tag{5.1.2}$$

where $J = t^2/U$, P is the Gutzwiller projector parallel to the doubly occupied site and S_i is the spin operator. In two dimension and at half filling the tJ model has two competing ground states, one is the long range order antiferromagnet, the second is the short range Resonance Valence Bound (RVB) with

a singlet superconductor ground state and a transition temperature on the order of J. In this case the symmetry of the pairing is a 's+id' singlet pairing, (meaning that the ground state is made from Cooper pairs and two gap symmetries are competing: the isotropic 's-wave' and anisotropic 'd-wave' with two lines of nodes in the k-space). A definition of the terms 's- or d-wave' pairing can be found at the end of Chapter 1.

5.1.2 The 'd-wave' pairing

At exactly half doping the 's and d-wave' pairing are degenerate and the later is favored with doping. For 'd-wave' the gap parameter is given by [202]:

$$\Delta_k = \frac{\Delta(T)}{2}(\cos k_x - cosk_y), \tag{5.1.3}$$

$$E_k = \sqrt{\cos^2 k_x + \cos^2 k_y}, \tag{5.1.4}$$

where E_k is the quasiparticle energy. The gap Δ_k vanishes at $k = (\pm\pi/2, \mp\pi/2)$ and the excitation spectrum has two lines of nodes that delimits alternating signs of Δ. The terminology 'd-wave' refers to the spherical harmonics $Y_l^m(k)$ where $l = 2$: an illustration can been found in Fig. [1.8]. Other models, such as the Commensurate Flux Phase (CFP) give similar results. The CFP describes each electron in the strongly correlated medium as the carrier of one flux tube with one flux quantum, so that the electrons of a given spin move in the effective average field due to the electrons of the other spin direction. It has been demonstrated rigorously that there is a total equivalence between the RVB and CFP [5].

5.2 Experimental survey

It is impossible to give a complete review of this subject: the literature is too vast and many essential question are still unresolved today. The main difficulty is that the physical properties are strongly dependent of the compound stoichiometry (the oxygen content) and some early results are now known to be spurious effects. We have preferred to give a succinct chronological account of the knowledge and concentrate on a single compound the $YBa_2Cu_3O_7$.

The memorable steps in the synthesis of those cuprates include the $La_{2-x}Ba_xCuO_4$, discovered by Bednorz and Müller in 1986 with a $T_c = 36$ K ($x = 0.15$), followed by the $YBa_2Cu_3O_7$ with a $T_c = 92$ K: the first material superconducting in liquid nitrogen. Other variants synthesized are the $Bi_2Sr_2CaCu_2O_8$ and $Tl_2Ca_2BaCu_3O_{10}$ with transition temperatures above 100 K. They all share the same crystallographic structure: a perovskite crystal. Their phase diagram is usually rich and varies from one family to the other. They all posses CuO_2 planes that are believed to be responsible for superconductivity, and it appears that the T_c increases with the increased stacking number of those sheets per unit cell.

5.2.1 Crystal structure

The $YBa_2Cu_3O_7$ has at room temperature an orthorhombic unit cell of dimensions $a = 3.82\AA$, $b = 3.89\AA$ and $c = 11.68\AA$ [41]. The crystal undergoes a phase transition from orthorhombic to tetragonal at around 750 K. The orthorhombic structure is shown in Fig. [5.1], it consists of two CuO_2 planes that are parallel to the a, b direction, those planes are the dominant conducting pathways. They are weakly bound together by the CuO_3 linear chain that are along the b-axis. This interaction distorts slightly the CuO_2 planes and the Cu(2) is weakly attracted by the O(4) directly above. The Cu(2) is five-coordinate, the strongly bound being the one with the four neighboring oxygens O(2) and O(3). The plane is thus displaced by $0.27\AA$ in the c direction. Both the Ba and Y atom are linked to their (10 or 8 respectively) oxygen nearest

neighbors. The valences of the chemical formula is such that:

$$Y^{3+}Ba_2^{2+}Cu^{3+}Cu_2^{2+}O_7^{2-}. \tag{5.2.1}$$

Notice the mixed valence state of the Cu, that is in its $3d^8$ or $3d^9$ configuration. Assuming one carrier per unit cell gives a carrier concentration $n = 6 \times 10^{21}$ cm^3. Hall effect measurement have indicated that the transport properties are mediated by the holes and the carrier concentration is $\sim 7 \times 10^{21}$ cm^3 [153]. As mentioned, the physical properties are strongly dependent on the oxygen concentration x in $YBa_2Cu_3O_{7-x}$. The oxygen content can be changed reversibly from $x = 0$ to 1 simply by pumping oxygen in and out of the chains. The superconducting ground state is next to a degenerate anti-ferromagnetic state that appears at lower oxygen concentration (T_c= 0 for $x = .36$). The corresponding phase diagram is shown in Ref. [9]. As the oxygen concentration decreases the unit cell distorts $a \nearrow, b \searrow$ and $c \nearrow$ and becomes tetragonal for $x < 0.4$ (isolating anti-ferromagnetic state).

5.2.2 Electronic properties

The particularity of those layer compound is the anisotropy of their electrical properties: the conductivity is regarded as two dimensional and along the a, b plane. ρ_{ab} is given by the simple functional form:

$$\rho_{ab}(T) = A + BT, \tag{5.2.2}$$

where the zero-temperature intercept A is negligible for the best quality sample ($x = 0$). The proportionality constant B is approximately 1 $\mu\Omega$ cm/K and the resistivity has a value of 100 $\mu\Omega$ cm at 100 K. The large anisotropy makes the measurement of ρ_c difficult as defects can change the homogeneity of the current density: ρ_c is believed to be 100 times larger than ρ_{ab} at 100 K. Evaluation of the coherence length in the superconducting state gives $\xi_{ab}(0) \sim 35\mathring{A}$ and $\xi_c(0) \sim 4\mathring{A}$, as extracted from critical field measurement [195]. The penetration depth is $\lambda_{ab} = 1400\mathring{A}$ and $\lambda_c = 8000\mathring{A}$ from magnetization measurements [183]. The Debye temperature is not well defined, because of the complex electron-phonon spectrum: a common used value is around 500 K. All those numbers are extracted from review papers of B. Batlogg in 1991 [24, 25] and the references cited therein.

5.3 Pairing state

A central aspect of understanding the ground-state properties is knowing its pairing symmetry as it might help to rule out some of the suggested models. There are many experiments that have tried to ascertain the pairing state but none is conclusive. First, we review the few experimental evidence that have shown unambiguously that superconductivity in the cuprates originates from electron-pairing mechanism.

5.3.1 Singlet pairing

The earliest experiments on this subject were the measurement of the flux quantization in a superconducting ring of $YBa_2Cu_3O_7$ [71, 111]. It was found that the flux was quantized in units of $\phi = (0.97 \pm 0.04)h/2e$ consistent with a paired condensate (cf. Chapter 1). Other evidence include measurement of the size of the Shapiro step in the I-V characteristic of a Josephson junction radiated with a rf-signal of frequency ω: the steps are quantized in $\hbar\omega/2e$ [197]. The last evidence is the observation of the Andreev scattering [91], that study the inelastic scattering of an electron at the interface of a metal-superconductor junction: an electron in the metal can be absorbed by the condensate to form a pair (leaving a hole vacant). The process is monitored by a point contact tip. The information extracted is a confirmation that the electrons are formed into pairs with zero net momentum (singlet).

5.3.2 Pairing symmetry

The results above imply that $YBa_2Cu_3O_7$ is a superconductor formed from Cooper pairs and other exotic possibilities (like triplet superconductivity) are ruled out. Now, we turn the discussion to the various experiments that have investigated the nature of the gap symmetry (k-dependence).

A Josephson current between a conventional superconductor (In) and $YBa_2Cu_3O_7$ has been observed [22]. Also, a persistent current was induced in a ring made of a half loop of $YBa_2Cu_3O_7$ and Nb in contact [103]. Those experiments strongly suggest that the ground state is 's-wave', but they are not conclusive as other effects can also cause a non-zero Josephson coupling [59], for example spin-orbit coupling can induce similar results with a 'd-wave' superconductor.

In principle the angular dependence of the upper critical field also probes the symmetry of the order parameter. It is one of the strongest pieces of evidence that the superconductivity is unconventional in the heavy-fermions family (UPt_3) [185]. There are no reliable measurement for the $YBa_2Cu_3O_7$, as the upper critical field is too large.

Electrodynamic properties, theoretical predictions

1. The temperature dependence of the penetration depth at low temperature reflects the form of the quasiparticle-density spectrum: nodes in the gap lead to power law dependence:

$$\frac{\lambda(T)}{\lambda(0)} - 1 \sim \left(\frac{k_B T}{\Delta_{\max}}\right)^{\alpha}, \tag{5.3.1}$$

   where $\Delta_{\max}$ is the maximum value of the gap over the fermi surface and α is an integer. Some calculations were performed by Hirschfeld *et al.* [89, 90] for heavy-fermions. Depending on the value of α, one could distinguish among various pairing symmetries. Supposedly $\alpha = 2$ is a signature of 'd-wave' pairing and if so, the specific heat should give identical result.

2. The shape (height and width) of the coherence peak (NMR relaxation rate or optical conductivity) varies with the pairing states. Some calculations were performed by Hasegawa and Fukuyama [82] for NMR.

3. The conductivity spectra can reveal the presence of low-lying excitations that will indicate a coupling of the electromagnetic radiation with some exotic component of the order parameter (higher order symmetry). Tunneling experiments also should probe the same excitations and confirm the optical results. Theoretical predictions include the recent work of Hirshfeld *et al.* [88] and references herein.

4. Knowledge of anisotropy effects (c-axis transport) is essential for a complete understanding of the electronic states involved and has implication for the theory [118]: this domain has been the least explored because of technical difficulties.

Penetration depth results

The temperature dependence of the penetration depth $\lambda(T)$, has been extensively studied and there are numerous measurements that favored a 's-singlet' [198]. However two recent data by Hardy *et al.* [78] on 'high-quality' single crystal and Lee *et al.* [124], using thin-films, claim a linear term ($\alpha = 1$) at low temperatures. It is then difficult to draw firm conclusions. Also the specific heat should be exponential (for 's-wave') at low temperature, instead it can be fitted by the functional form [184]:

$$C = AT + BT^2. \tag{5.3.2}$$

The linear term was explained by the presence of impurities and grain boundaries.

NMR

A stronger evidence for the unconventional model is the absence of a Hebel-Slichter peak in the nuclear relaxation of both the Cu(2) and O(2,3) [77]. More puzzling, the decay of $1/T_1$ goes as T^3 at low temperature, the same power law found for the UBe_{13} [130]. Furthermore the Knight shift anisotropy ratio is temperature dependent [134] and can be well fitted by a 'd-wave' pairing [36]. The former result might not constitute a conclusive proof as other effects might also decrease the height of the coherence peak, strong coupling for example [149, 133, 7].

Low-lying excitations

There are many data that suggests the presence of low-lying excitation below the single-particle gap. The most often cited are:

- Raman scattering, where various published data showed broad maxima at 350 cm^{-1} and 550 cm^{-1}, but no evidence of a single particle gap. This suggests an anisotropic gap [50] although inconsistent with other tests: for example, the positions of those 'peaks' are invariant with oxygen depletion (decreasing T_c) and alternative explanation have been proposed by Monien and Zawadowski [142].

- Infrared reflectivity data measured by the IBM group [177] have been interpreted in terms of a large gap with many low-energy excitations, but the analysis is till controversial as inconsistencies were pointed out by D.B. Tanner and T. Timusk [187]: the mid-infrared band, that should be associated with single particle excitations, do not shift significantly at the superconducting transition temperature.

- Tunneling experiments by Lee *et al.* [125] also suggests low-lying excitations and an anisotropic gap, although those measurements are usually poorly reproducible as the results are strongly dependent on the surface layer of the contact. The surface contamination problem is more critical than in conventional superconductors because of the shortness of the coherence length ($\xi_{ab} \sim 10\mathring{A}$).

In conclusion, there are two principal candidates for the pairing symmetry, one is a conventional 's-wave' with an isotropic gap, the second is a 'd-wave'. Both have their own set of experimental support, but no observation so far are conclusive. A review of the pairing symmetry of $YBa_2Cu_3O_7$ can be found in the article Annett *et al.* [16] and the references cited therein.

5.3.3 Optical properties

The optical properties of the cuprates is still very controversial, and some recent results contradict earlier findings. The far-infrared spectrum of the cuprates was measured as early as 1988 on oriented powders [30], more precise data were taken on single crystal somewhat later [177, 46, 171]. The main conclusion was the absence of any feature at the expected position of the BCS single-particle gap (100 cm^{-1}), the materials being very good conductor around this frequency range and the reflectivity is almost 100% in the normal state. Several review papers cover the material [154, 193]. Some optical data suggest a large single-particle gap [46] $2\Delta(0)/k_BT_C \sim 8$ and this interpretation is in agreement with other experiments on the $Bi_2Sr_2CaCu_2O_8$ like photoemission [127] or tunneling [131] where people have observed a large gap that opens sharply at T_c. At UCLA, Drabeck *et al.* have performed extensive measurements on the surface resistance of $YBa_2Cu_3O_7$ (thin films) [53] and the temperature dependence of R_s suggests also a large gap value, well exceeding the weak coupling BCS limit.

At the beginning of 1991, our group at UCLA observed for the first time an increase in the conductivity below T_c in the $Bi_2Sr_2CaCu_2O_8$ compound, at frequencies well below the single-particle gap [92]. The peak was sharp, with an extremely narrow width ($\sim$ 6 K): the published data are shown in Fig. [5.2]. We suggested that the effect was the consequence of coherence effects. Two comments written by Olsson *et*

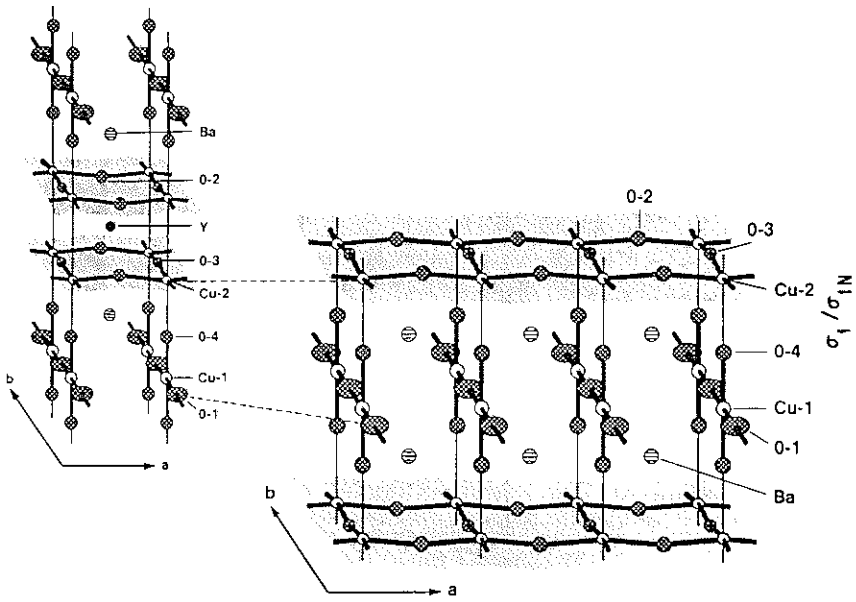

Fig. [5.1]: Orthorombic structure of $YBa_2Cu_3O_7$, with the two CuO_2 plane separated by the fencelike CuO chains. The Figure was obtained after Ref. [58].

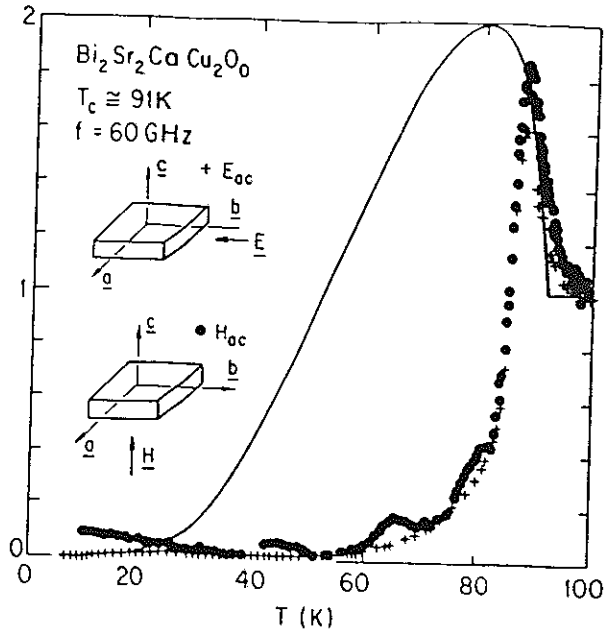

Fig. [5.2]: Temperature dependence of the optical conductivity in the $Bi_2Sr_2CaCu_2O_8$ compound, after Ref. [92]. The measurements were done along the (ab)-plane.

al. [151] and Horbach *et al.* [95, 94] offered alternative explanation and suggested that the increase in $\sigma_1(T)$ was due to fluctuation effects that modify the normal-state conductivity and consequently is not a signature of the superconducting state. In this interpretation the transition temperature would be at the peak maximum. Their explanation remained a possibility, as the phase transition is very broad for the $Bi_2Sr_2CaCu_2O_8$ (strongly two-dimensional) and in the article of Holczer *et al.* [92] the conductivity σ_1 also displayed a strong increase above T_c, that was attributed to fluctuation effects. In $YBa_2Cu_3O_7$ however, two-dimensional fluctuation effects are less important, and fluctuations leading to a peak in σ_1 are most probably suppressed. Indeed it has been found that σ_1 increases below T_c and the observations were interpreted in terms of a marginal fermi liquid [148], the data of Nuss *et al.* are shown in Fig. [5.9]. We have therefore measured the finite frequency conductivity in this material in order to gain further insight in the electrodynamics of the superconducting state: the result is discussed in what follows.

5.4 σ_{ab} at 60 GHz

We have measured both the surface resistance R_s and the surface reactance X_s of a $YBa_2Cu_3O_7$ single crystal at millimeter wave frequencies and have evaluated the conductivity σ_1. All the experiments reported in this Chapter were conducted at 60 GHz.

5.4.1 Introduction

Single crystal samples were provided by G.A. Emelchenko from the Academy of Sciences in Chernogolovka, Moscow. They were prepared in the standard way, and dc-resistivity measurements lead to a sharp transition at 92 K, with a width less than 1 K. Above T_c, the dc-resistivity increases linearly with temperature and has a small zero temperature intercept.

The finite frequency conductivity cannot be measured directly (except on very thin films or powders) due to the finite penetration of the electromagnetic radiation into the specimen investigated. The only parameter experimentally accessible is the surface impedance $Z_s = R_s - iX_s$ where R_s is the surface resistance and X_s the surface reactance. To measure it, we have employed a cavity perturbation technique,

where the sample is placed inside a resonant cavity at either the electric or magnetic field anti-node. We found similar results for both configurations, however the data shown in the figures were all taken with the specimen in the maximum of the **H** field, with the field direction along the crystallographic c-axis (i.e. probing the electrodynamics in the (ab)-plane). Using the power of the source (100 mW) and the Q of the cavity ($\sim 10^4$) we have estimated the magnitude of the ac-magnetic field at the surface of the sample (neglecting all causes of loss from leakage or joule effect). The value found was below the earth magnetic field (0.5 G).

During the experiment both the characteristic frequency f_o (without the specimen) or f_s (with the specimen) and the bandwidth Γ_o (and Γ_s) are monitored during two separate experimental runs, one without and one with the sample. Experimentally one cannot make an absolute measurement of the frequency shift, as the endplate must be removed between the runs with the sample in the cavity and out of the cavity. Because of the unknown f_a, some assumptions have to be made about the properties of the normal or superconducting state. The relevant length scale in the superconducting state is the penetration depth $\lambda(T)$, and we can use the known zero temperature value of $\lambda(0) = 1500 \pm 50$ $\AA$ [79] to evaluate f_a. Alternatively we can assume that in the normal state the so-called Hagen-Rubens limit, $\omega\tau \ll 1$ applies. In this case $\sigma_1 \gg \sigma_2$ and consequently $R_s = X_s$. As will be discussed below, both assumptions lead to similar results for σ_1 below T_c.

5.4.2 Surface Impedance

In the superconducting phase, R_s drops rapidly to zero with decreasing temperature Fig. [5.3], showing a sharp cusp at 92 K, in agreement with the T_c inferred from dc measurement. We have compared on Fig. [5.3] our data below T_c with earlier measurements of $R_s(T)$ on high quality laser ablated films and the surface resistance of both the film and the crystal are identical, giving evidence for the high quality of the crystal we have investigated. The experiments however were conducted at different frequencies ($f = 100$ GHz for the film and $f = 60$ GHz for the crystal), and we have used the well confirmed ω^2 frequency dependence [53] of R_s in the superconducting state to compare both measurements. The values obtained on those films [53, 48] have been reproduced by other groups and the observed temperature dependence is thought to represent the intrinsic surface resistance not influenced by defects or irregularities in the specimen. A word of caution: this ω^2 approximation is only valid well below T_c, both data sets cannot be compared in the narrow temperature range just below the transition (more complex manipulations are needed to account for the response of the normal fluid). At low temperature, R_s saturates around $2m\Omega$, representing the intrinsic resolution of our detection scheme. This value is imposed by the systematic errors of the technique (limited by the mechanical necessity of removing a wall in order to access to the sample) but not the intrinsic resolution. In the superconducting phase, the temperature dependence of R_s is at odds with recently published data of D.A. Bonn, et al. [29] (shown in the same Fig. [5.3]) at 3 GHz. In particular, we do not observe any abnormal feature around 40K. Again we have corrected Bonn's data by ω^2 to compare them on the same graph, the residual surface resistance value (normalized to the same frequency) is almost five times larger. This effect has been observed on thin-films too and we refer to the work of Drabeck *et al.* [53] for a more detailed description. In any case, we will come back to this point in the next section when we compare our findings with other (optical and microwave) measurements.

In Fig. [5.4] we display the temperature dependence of R_s and X_s, both normalized to the surface resistance measured just above the superconducting transition. We have used the Hagen-Rubens condition (R_s=X_s) to evaluate the frequency offset f_a: this approximation is justified by optical data where the measured scattering rate ($1/\tau \sim 200\text{cm}^{-1}$) [170] is much larger than the electromagnetic wave frequency (2 cm^{-1}). If we approximate the sample by an oblate spheroid of semi-major axis $a = 0.03$ cm and semi-minor axis $b = 0.002$ cm we can compute the resonator constant [105]. Using the measured value of the bandwidth $[\Gamma_s - \Gamma_o](T$=100 K) = 3×10^{-6}, we calculate the normal state surface resistance $R_n = 0.5\ \Omega$ using Eq. (2.3.1), this results leads to a resistivity $\rho_n = 100\ \mu\Omega$ cm (the subscript n refers to the normal

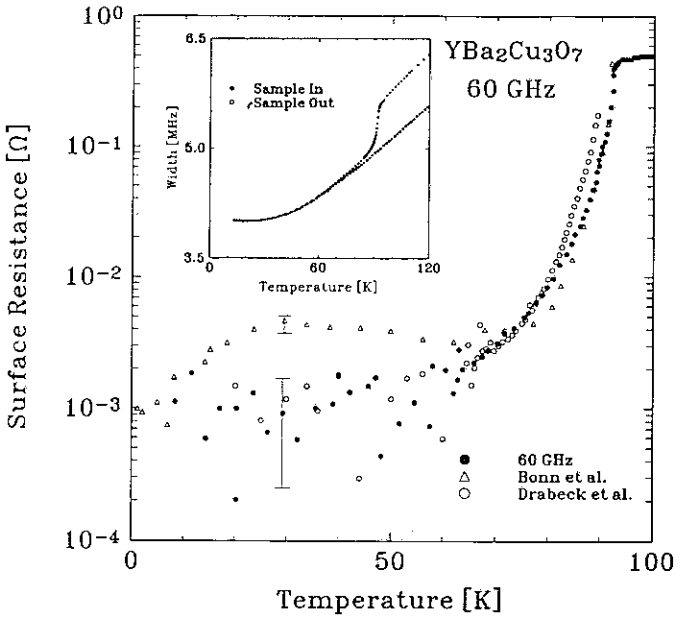

Fig. [5.3]: Temperature dependence of the surface resistance measured along the (ab)-plane. On the same figure is displayed for comparison the measurements of Bonn *et al.* at 3 GHz after Ref. [29] and Drabeck *et al.* after Ref. [53]. We have multiplied those results by ω^2 to take in account the frequency difference. In the inset is shown the actual raw data, the temperature dependence of the cavity bandwidth before and after loading the resonator with a sample in configuration 2 (cf. Fig. [3.1]).

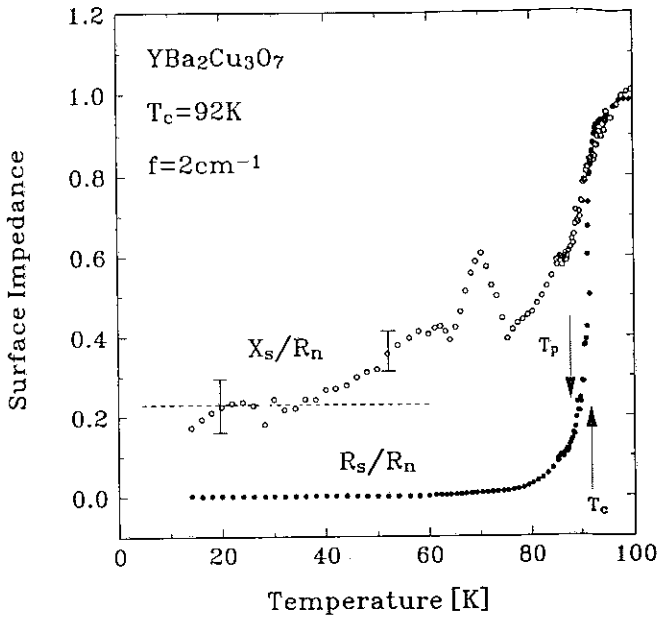

Fig. [5.4]: Temperature dependence of the surface impedance $Z_{s\parallel} = R_s - iX_s$ of the (ab)-plane.

state or T = 100 K value). The length scale is thus determined by the skin-depth in the normal state $\delta = 1.8\ \mu$m. Using the temperature dependence of $X_s(T) = \omega\mu_o\lambda(T)$ we can deduce the penetration depth at zero temperature. On Fig. [5.4] we can see that $X_s(T)$ saturates at low temperature to a value corresponding to a penetration depth $\lambda(T = 0K) = 1500\ \mathring{A}\ \pm\ 10\%$ in agreement with μSR results by Harshman *et al.* [79]. The peak in X_s(T) around 70 K is not reproducible and varies in height with different temperature sweep (the error bars indicate the variations). We attribute the effect to slight gas evaporation (nitrogen) at the cavity walls that changes the dielectric constant of the resonator. As mentioned in Chapter 3 it is difficult to measure the frequency accurately on a wide temperature range. For the analysis, we have chosen to normalized the data at 100 K and the low temperature part fluctuates from one run to the other. The error bars in Fig. [5.4] indicates the typical difference between consecutive measurements and the dashed line is the averaged value. From our data, the penetration depth is on the average temperature independent up to 40 K.

5.4.3 Complex conductivity

Using the R_s and X_s measurements shown in Fig. [5.4] we have evaluated σ_1 and σ_2. Our results are displayed in Figs. [5.5] and [5.6]. We normalized all the values of the conductivity with $\sigma_n = \sigma_1(T = 100K)$. In Fig. [5.5], several features of the observed behavior are of importance:

- First, the rise of σ_1 *above* T_c is small and comparable to the experimental accuracy, in contrast to the behavior found for Bi.

- Second, the conductivity displays a clear sharp peak (width $\sim$ 7K), with the peak temperature T_p = T($\sigma_{1\max}$) well below T_c (difference $\sim$ 3K). We note that at T_p, the surface resistance has dropped

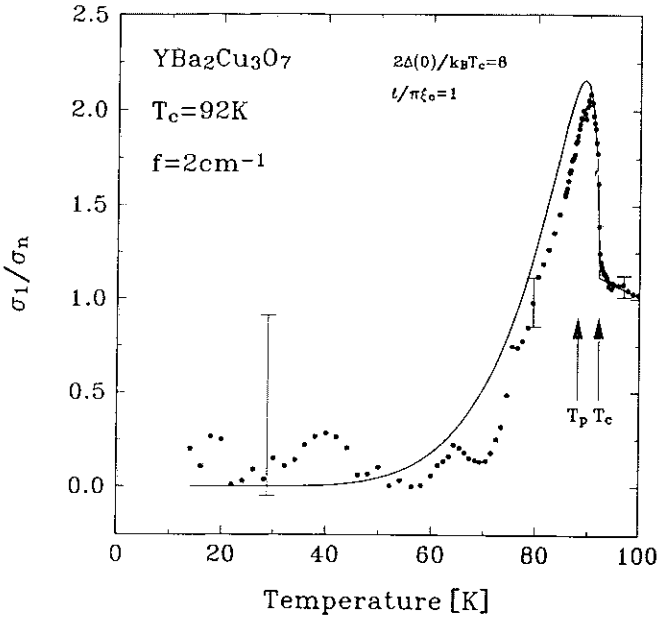

Fig. [5.5]: Temperature dependence of the optical conductivity $\sigma_{1\parallel}$ in the superconducting phase. The data are normalized to the 100 K value $\rho_n = 100\ \mu\Omega$ cm. The solid line is obtained using a BCS ground state formalism with two fit parameters the coupling constant $2\Delta(0)/k_BT_c = 8$ and the mean-free-path $\ell/\pi\xi(0) = 1$

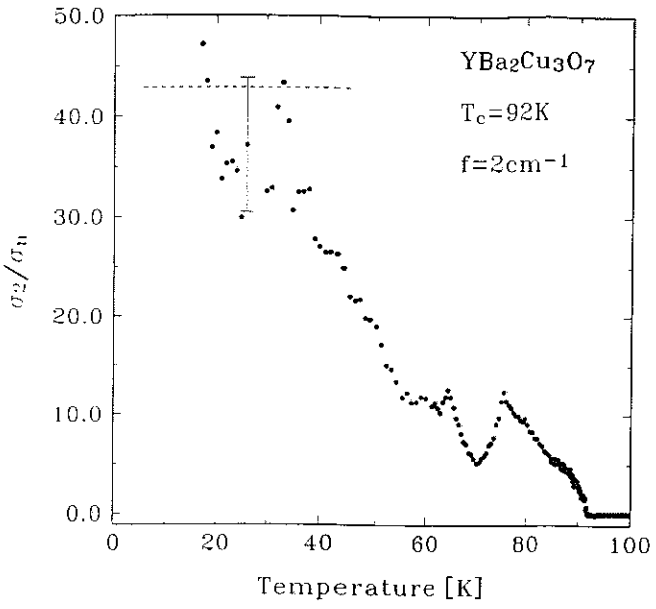

Fig. [5.6]: Temperature dependence of the imaginary part of the complex conductivity $\sigma_{2\parallel}$ in the superconducting phase. The data are normalized to the 100 K value $\rho_n = 100\ \mu\Omega$ cm.

by an order of magnitude from the normal state value, a signature that the material is well into the superconducting state, as one can compare with Fig. [5.4].

Those two observations are at odds with alternative explanations from H.K. Olsson and R.H. Koch [150], that have suggested that the peak in σ_1 can be attributed to a broadening of the resistive transition, where fluctuation effects lead to a peak strictly at T_c. Our measured increase of σ_1 is entirely due to the development of the superconducting state below T_c.

Similarly to what has been observed in the Bi compound, the peak of σ_1 is sharp in clear contrast to what is predicted by Mattis-Bardeen for weak coupling BCS theory [135] (a comparison with Mattis-Bardeen is illustrated in Fig. [2.13]).

We have shown in Fig. [5.6] the temperature dependence of σ_2(T). The strong feature at 70 K reflects the jump in X_s, and we believe it is spurious. The error bars associated with the data are similar to the one drawn for X_s in Fig. [5.4] and the average value of σ_2 is independent of temperature below 40 K. From the low temperature ratio $\sigma_2(0)/\sigma_n$ we have evaluated the gap, using Eq. (2.3.31). We found that the coupling ratio $2\Delta(0)/k_BT_c \sim 6$ for the parallel direction, leading to a single particle gap $2\Delta(0) \sim 380$ cm^{-1}.

5.4.4 Fitting with 's-wave'

Recent calculations [43] using the finite mean-free-path effects ($\ell/\pi\xi_o = 1$ [53]) and the two-dimensionality, lead to σ_1(T) similar to that shown in Eq. (2.1.10). To fit our data we have used the BCS formalism with two adjustable parameters the coupling constant and the mean-free-path. The result of those calculations are shown in Figs. [5.7] and [5.8]. The important point is that both parameters adjust almost independently the width (coupling) or the height (mean-free-path) of the peak. One finds a gradual sharpening of the conductivity peak with increasing $2\Delta(0)/k_BT_c$ as in Fig. [2.13], and a decrease of the height with increasing τ. A large value of the $2\Delta(0)/k_BT_c \sim 8$ and $\ell/\pi\xi_o \sim 1$ gives a good description of our results in the

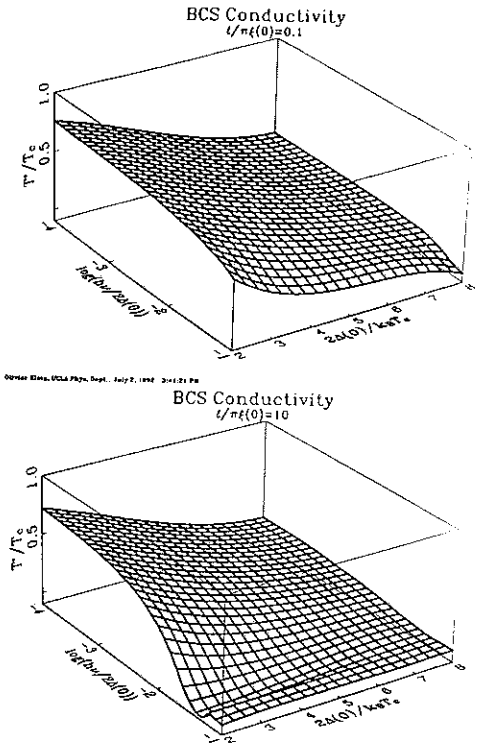

Fig. [5.7]: Variation of the width of the coherence peak for different frequency $h\nu = \hbar\omega$ and different coupling constant but maintaining the BCS formalism. The width is defined as follow $\sigma_1(T^* < T_c) = \sigma_n$. The top figure corresponds to the dirty limit, the bottom to the clean limit.

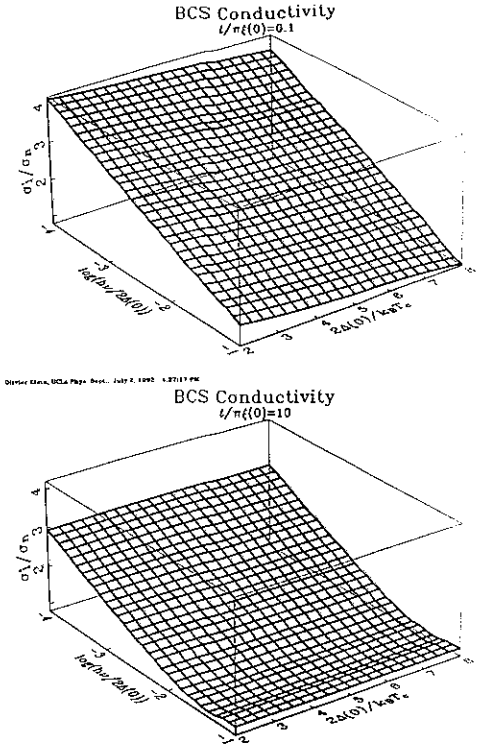

Fig. [5.8]: Variation of the height of the coherence peak for different frequency $h\nu = \hbar\omega$ and different coupling constant but maintaining the BCS formalism. The top figure corresponds to the dirty limit, the bottom to the clean limit.

temperature range near T_c. Thus the sharpness of the coherence peak reflects the rapid increase of the gap below the transition (faster than the BCS model). The mean-free-path value indicates that the sample is at the cross-over between the clean and dirty limit. We have included the temperature dependence of the relaxation rate in the fit by assuming that $\tau \propto 1/T$ following the normal-state behavior. Notice that this type of correction does not drastically change the shape of the peak, as shown in Fig. [2.13].

In summary, we observe a narrow increase in σ_1 below T_c. Whether it is due to coherence effects or to a temperature dependent scattering rate remains to be seen as this information cannot be inferred from conductivity measurements solely. Nevertheless our data can be fit within a BCS formalism adjusting both the mean-free-path and the coupling constant value. The narrow width indicates a rapid opening of the gap and the $\sigma_2(0)/\sigma_n$value suggest strong coupling ~ 6. The height of the peak indicates a sample in the clean limit where $\ell/\pi\xi_o \sim 1$.

5.5 Comparison with other experiments

The suggestion that the peak in $\sigma_1(T)$ arises as a consequence of coherence effects is still a controversial issue in the physics community. We will review briefly the arguments against this interpretation, but note that none of the experiments described below have ever been independently reproduced.

5.5.1 Fluctuation effects

Soon after the publication of the Bi data, Fig. [5.2], two comments suggested that an increase of $\sigma_1(T)$ could be simply due to fluctuations effects: one comment was written by Horbach *et al.* [95] and the other by Olsson *et al.* [151].

The 'fluctuation-effects' interpretation [151] can be ruled out unambiguously for the $YBa_2Cu_3O_7$, because T_p is well in the superconducting state as shown in Fig. [5.4]. The rise of σ_1 is an intrinsic property of the superconducting state and cannot be accounted for by fluctuation effects. In particular, in the case

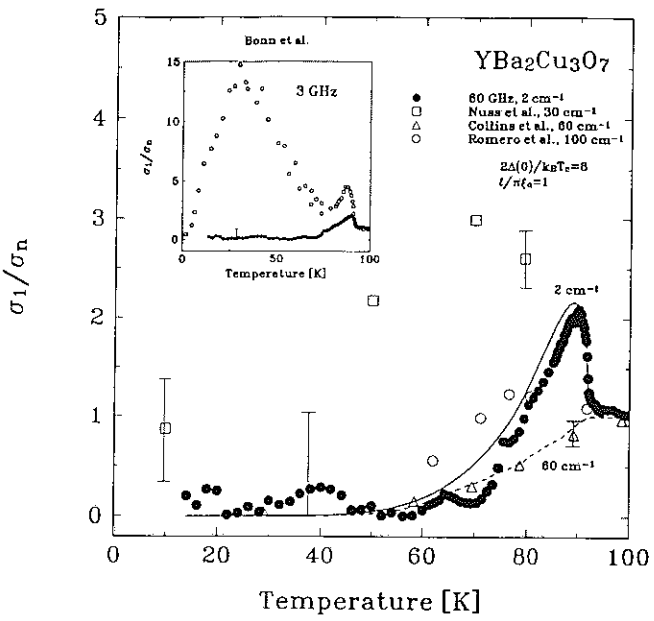

Fig. [5.9]: Comparison of $\sigma_1(T)$ obtained in Fig [5.5] with other optical results at 30, 60 and 100 cm^{-1}, after Refs. [148, 170, 46] respectively. The solid and dashed line is the 's-wave' prediction at 2 cm^{-1} and 60 cm^{-1} (fix parameters). In the inset we compare our results with the data of Bonn *et al.* [29] at 3 GHz.

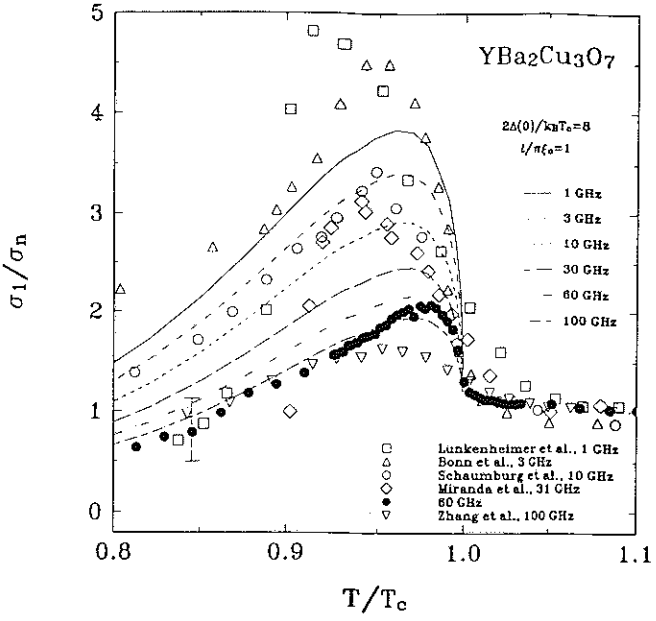

Fig. [5.10]: Comparison of $\sigma_1(T)$ obtained in Fig [5.5] with other microwave results at 1, 3, 10, 30 and 100 GHz, after Refs. [129, 29, 175, 141, 201] respectively. The line is the 's-wave' prediction at various frequencies with fix parameters.

of the $YBa_2Cu_3O_7$, fluctuation effects can only account for a very narrow temperature range (below 1 K) while the peak observed at 60 GHz has a width of 6 K. The experiment of Olsson *et al.* [150] measured an extremely narrow peak ($\sim$ 1 K) at around 100 MHz. Another argument against this interpretation is illustrated in Fig. [5.10], where we show the size of the peak at various frequencies: if the peak was due to fluctuation effects the height would have increased as $1/\omega$ and the low frequency results should have been an order of magnitude higher (if we believe our 60 GHz data). We will come back to this figure later.

5.5.2 Optical experiments

We list in this section all the experiments that have probed $\sigma_1(T)$ in the optical range (above 10 cm^{-1}) and a comparison is illustrated in Fig. [5.9]

Our findings are quantitatively different from the observations of M.C. Nuss et al. [148] as shown in Fig. [5.9]. They reported a broad 'coherence peak' in $\sigma_1(T)$ at frequencies somewhat above our measurement frequency (1 THz). We recall that the coherence peak should increase logarithmically with decreasing frequency but the width should remain the same. The reason for this disagreement is not clear at present. We note that performing the identical experiment with the same analysis to the one described above, led in conventional superconductors to a behavior fully consistent with the BCS theory (Chapter 4). The technique developed by M.C. Nuss is a novel spectroscopic detection scheme based on the analysis of the transient response to an electromagnetic stimuli and it is difficult to ascertain the reliability of the data from only this experiment.

The reported absence of a coherence peak in several optical experiments has been sometimes used as evidence for unconventional pairing. The BCS coherence peak disappears at high frequencies (above 5 cm^{-1} for the $YBa_2Cu_3O_7$ parameters). We compare in Fig. [5.9] our results with experiments conducted at optical frequencies by Collins *et al.* [46] together with the calculated σ_{1BCS} at 2 cm^{-1} (solid line) and 60 cm^{-1} (dashed line) and *both* sets of data are in full agreement with 's-wave' pairing.

Also shown on the figure are the results of Romero *et al.* [170] and both data sets are in crude agreement

on the figure. It is difficult to further compare the meaning of this similarity, as it is unclear to label at which frequency the optical data refers to. The data of Romero are an extrapolation to low frequencies of their results at 100 cm^{-1}. They interpreted the peak as an evidence of a temperature dependent scattering rate and we will comment on it below.

5.5.3 Microwave results

A recent measurement by D. Bonn et al. [29] has found a peak in the conductivity centered around 40 K, in disagreement with all the other results where the peak occurred just below the transition (T_p = 89 K for a T_c= 92 K). A comparison with our data is shown in the inset of Fig. [5.9]. In this analysis, the extraction of the conductivity was done indirectly: they used the temperature dependence of $\lambda(T)$ from another dc-experiment. The results are non conclusive around T_c where the screening of the normal fraction has to be taken into account, and the effect is frequency dependent. Finally, their value of R_s at low temperature is substantially higher than any other reported data on any single crystals (an ω^2 correction factor has to be applied for comparison). They attribute it to the high quality of their sample, R_s increases as one goes to the clean limit.

To our defense, they are many other experiments that have reported a narrow peak ($\sim$ 6 K width) at microwave frequencies. They include the experiments of Lunkenheimer *et al.* at 1 GHz [129], Golubov *et al.* at 3 GHz [68], Cheah *et al.* at 5 GHz [44], Nichols *et al.* at 9 GHz [147], Schaumburg *et al.* at 10 GHz [175, 176], Miranda *et al.* at 35 GHz [141], Kobrin *et al.* at 60 GHz [110, 109] and Zhang *et al.* at 100 GHz [201, 200]. We have plotted a selection of these data on the same Fig. [5.10] for comparison. We have also included on the same graph the 's-wave' calculation extrapolated to lower frequencies but using the same parameters as the one obtained in Fig. [5.5]. The overall agreement is excellent considering the diversity in the techniques.

5.5.4 Temperature dependent scattering rate

Two recent electromagnetic absorption experiments by Romero *et al.* and Bonn *et al.* [29, 170] have recently ascertained that the rate $1/\tau$ at which electrons are scattered in the normal state undergoes a dramatic decrease when superconductivity occurs. Those findings are of extreme importance as they are used to support models based on unconventional pairing states [143]. In this comment, it will be shown that the $1/\tau$ mentioned above is not related to the quasiparticle scattering rate.

To support our argumentation, we use the measurement of the surface impedance of Nb at 60 GHz, shown in Chapter 4. Following the same analysis as Bonn *et al.* [29], we define the superfluid fraction, n_s:

$$n_s(T) = \frac{\lambda^2(0)}{\lambda^2(T)} = \frac{{X_s}^2(0)}{{X_s}^2(T)}, \tag{5.5.1}$$

where $\lambda(T)$ is the penetration depth. As shown in Fig. [2.7] the missing spectral weight in the conductivity spectrum is transferred to the Goldstone mode at zero frequency responsible for the Meisner effect:

$$\frac{\pi}{2} n_s(T) \frac{e^2}{m\omega} = \frac{{c_o}^2}{8\lambda^2(T)}. \tag{5.5.2}$$

The normal fraction, n_n, is determined from the value of the conductivity:

$$\frac{\sigma_1(T)}{\sigma_n} = 2\Im\left[\frac{{R_n}^2}{{Z_s}^2(T)}\right] = n_n(T)\frac{\tau(T)}{\tau_n}\frac{1+\omega^2{\tau_n}^2}{1+\omega^2\tau^2(T)}, \tag{5.5.3}$$

where $f = \omega/2\pi$ is the frequency and the subscript n indicates the value just above T_c. For Nb, it was

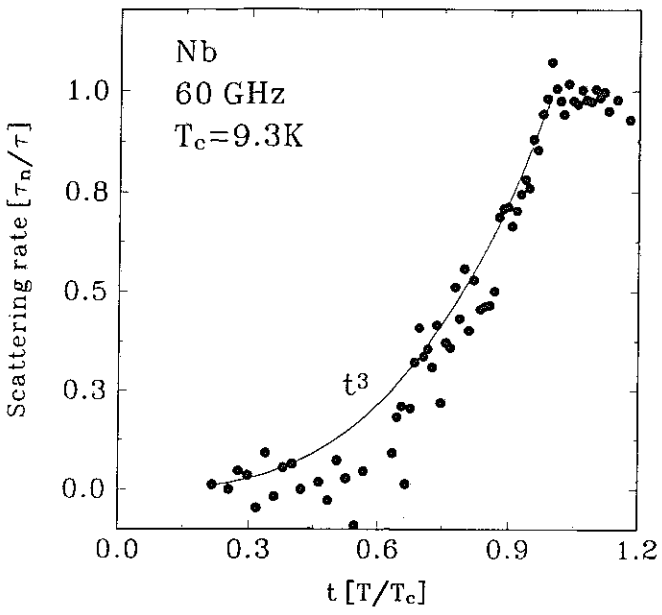

Fig. [5.11]: Temperature of the scattering rate evaluated from the Nb data using the analysis described in the text Eq. (5.5.3).

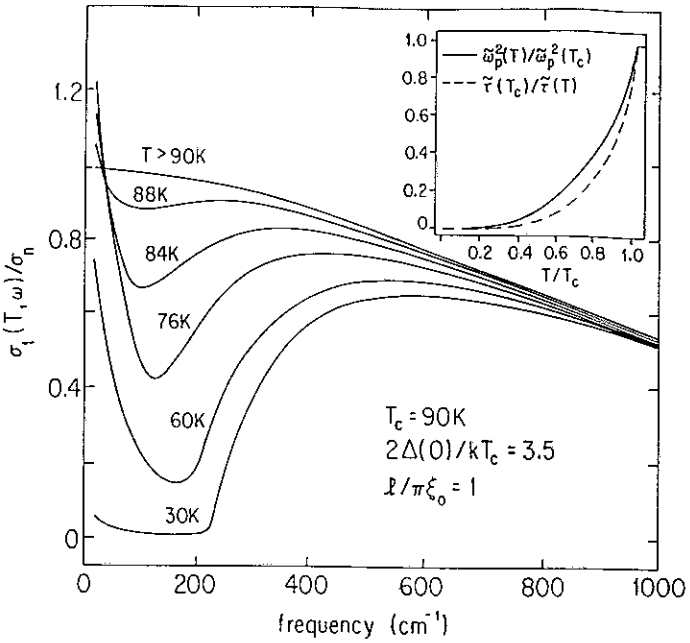

Fig. [5.12]: Frequency dependence of the optical conductivity for a BCS superconductor. In the inset evaluation of the plasma frequency and scattering rate as defined in the text.

found that $1/\tau_n \sim 250$ cm^{-1} (Chapter 4). If one assumes a two-fluid model [178],

$$n_s(T) + n_n(T) = 1, \tag{5.5.4}$$

like in Refs. [29, 170], then one can extract $1/\tau$ from the microwave data and the result is plotted in Fig. [5.11]. Therefore, the same analysis as Bonn *et al.* applied on a *conventional* superconductor leads to a rapid decrease of $1/\tau$ below T_c and the drop follows approximately a $(T/T_c)^3$ power law.

In summary, the quasiparticle scattering rate cannot be inferred from optical absorption experiments solely: the conductivity is a mixture of $n_n(T)$ and $\tau(T)$. Extracting the later parameter necessitates some assumptions on the behavior of the former (two-fluid model of Refs. [29, 170]) and then the $1/\tau$ value has no further significance than its own definition.

As an exercise, we have computed the frequency ($f = \omega/2\pi$) and temperature (T) dependence of the BCS conductivity [135] and the results are shown in Fig. [5.12], where σ_1 is normalized to the dc normal state value $\sigma_n = \sigma_1(\omega = 0, T = T_c^+)$. The parameters chosen for this simulation were a transition temperature $T_c = 90K$, a single particle gap $2\Delta(0) = 3.5k_BT_c$ and a temperature *independent* relaxation rate $1/\tau = \Delta(0)/\hbar$.

Following the analysis described by Romero et al. [170], we define a new variable $\tilde{\sigma_1}(T) = \sigma_1(T) - \sigma_1(T = 30K)$ and fit the low-frequency part ($10\text{cm}^{-1} < f < 1000\text{cm}^{-1}$) of $1/\tilde{\sigma_1}$ versus ω^2 with a straight line using the functional form $y = a + bx$. From the fitting parameters, we define a relaxation rate $1/\tilde{\tau} = \sqrt{a/b}$ and a plasma frequency $\tilde{\omega}_p^2 = 4\pi\sqrt{1/ab}$ at different reduced temperatures T/T_c. The results are plotted in the inset of the figure (the parameters have been normalized to their T_c values) and *both* $1/\tilde{\tau}$ and $\tilde{\omega}_p^2$ drop sharply below T_c in qualitative agreement with the results reported in their paper. Note that due to the particular definition of $\tilde{\sigma_1}$, $\tilde{\tau}(T_c) \neq \tau$.

The comment is then two-fold: a subtraction of the 30 K spectrum to eliminate the MIR contribution just arbitrarily fixes the temperature dependence of the superfluid fraction (it forces n_s to vanish at 30 K) and assuming a two-fluid models forces again a temperature dependence of the scattering rate. We believe that the measurement by Romero et al. [170] does not rule out the interpretation that the observed sharp increase in the microwave conductivity [92, 106, 108] is due to coherence effects.

5.5.5 Absence of peak in NMR

One of the strongest argument against the 'coherence peak' interpretation are the reported results in NMR of the Cu(2) and O(2,3) sites in $YBa_2Cu_3O_7$ [77] where no coherence peak is found. The reasons for this difference are not clear because in principle $1/T_1$ and σ_1 should couple to the same degrees of freedom for a metal. But there are several important distinctions between the information provided by the conductivity and by the nuclear relaxation rate and we would like to enumerate them:

1. The temperature dependence of the NMR relaxation rate is identical to the optical absorption if the dominant term in the hyperfine interaction is the contact term. In the case of the O(2,3) or Cu(2) site, the dipolar term is also non-negligible as the CuO_2 plane is not-symmetric. In the case where the dipolar interaction dominates the relaxation process, $1/T_1$ is a mixture of case 1 and case 2 coherence factors and the drop should be substantially faster.

2. NMR and optics do not probe the same response function in the $\mathbf{q}$ space. Optics measure the average response over several lattice constants, and therefore probes the $\mathbf{q} = 0$. NMR in contrast is a local probe and therefore measure the $\mathbf{q}$-integrated contribution:

$$\frac{1}{T_1} = \frac{T}{N} \sum_{\mathbf{q}} |A(\mathbf{q})|^2 \frac{\Im[\chi(\mathbf{q},\omega)]}{\omega}\bigg|_{\omega=\omega_e}, \tag{5.5.5}$$

   where $|A(\mathbf{q})|^2$ is the hyperfine form factor and its value depends on the chemical constituents and its position in the crystal, numerical estimation were performed by Mila and Rice [138]. This is a non-negligible difference with optics, in particular for the Cu(2) site which is subjected to anti-ferromagnetic fluctuations which gives rise to an enhanced susceptibility at (π,π).

3. In the case of the O(2,3) site, experiments are usually performed in high magnetic field. The dominant absorption process involved in the relaxation of the O nuclear spin, is the *electron* spin flip [178] (the contact term of the hyperfine interaction is dominant) which implies that the quasi-particle spectral density function is probed at the *electronic* Larmor frequency (instead of the nuclear Larmor frequency). This difference is insignificant for a metal, where the density of states $N_s(\omega)$ is constant around the Fermi energy, but not for a superconductor where $N_s(\omega)$ is singular at the gap value. In consequence, high magnetic field NMR (typically 7 Tesla) is probing the BCS response function at higher energy (8 cm^{-1}) than the present conductivity measurement (2 cm^{-1}) and as mentioned earlier, an increase in the probing frequency smears out the height of the coherence peak.

4. NMR is sensitive to the local spin fluctuation while optics measures the charge excitation, and those two degrees of freedom can be, in principle, completely uncorrelated.

Conductivity experiments in high magnetic field are published elsewhere [158].

5.6 Complementary measurements

5.6.1 Conductivity along the *c*-axis

We have measured the electrodynamic properties along the c-axis by placing the sample at the antinode of the electric field, configuration 3 of Fig. [3.2]. The results are shown in Fig. [5.13]. Due to the particular sample shape, geometrical factors (depolarization) do not enhance the signal as much as for the parallel direction and the data are of poorer resolution than those obtained for the (ab)-plane. In the inset the normal state surface resistance is shown and we observe a 'semi-conductor' like behavior below 100 K. These features have also been observed in the dc-resistivity [161, 32] and have been interpreted recently [73] as

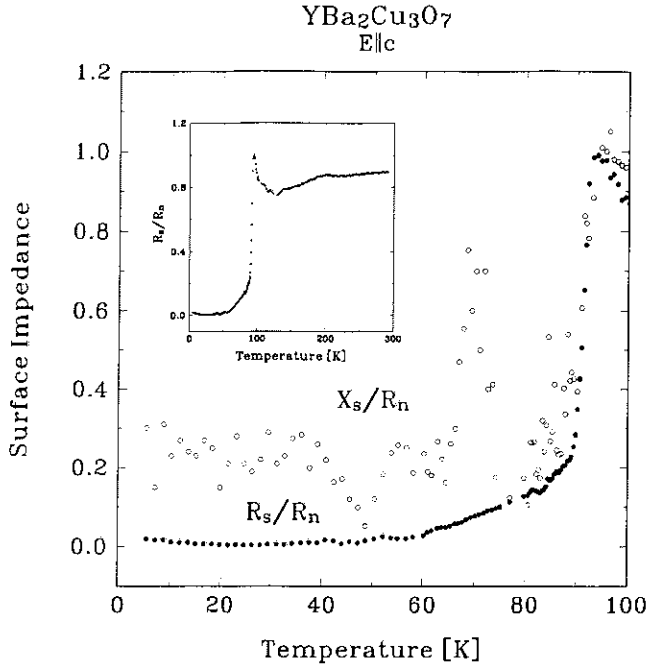

Fig. [5.13]: Temperature dependence of the surface impedance $Z_{s\perp} = R_s - iX_s$ along the c-axis. The data are normalized to the 'normal-state' value just above T_c. The full temperature dependence of the surface resistance along the c-axis is shown in the inset.

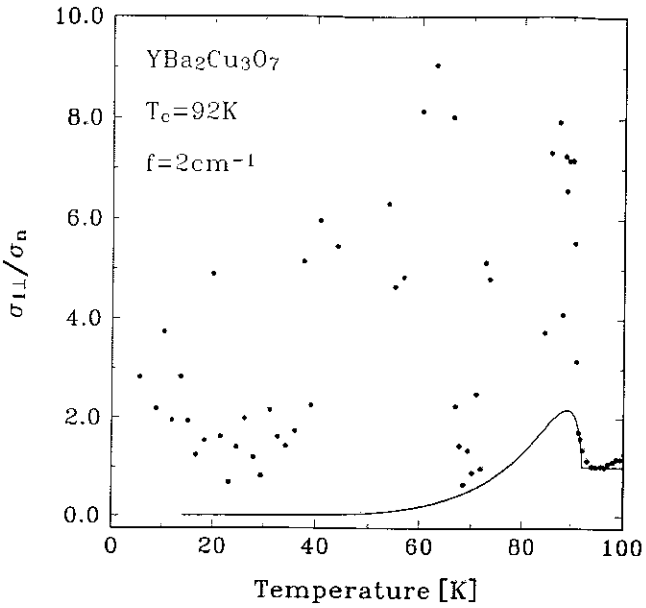

Fig. [5.14]: Temperature dependence of the perpendicular conductivity evaluated form the surface impedance measurement $Z_{s\perp}$ shown in Fig. [5.13], also included as a solid line is the surface impedance of the (ab)-plane.

the signature of a series stack of Josephson tunnel junctions. The model requires in addition unusually large fluctuations to extend the behavior well above T_c.

Approximating the sample as oblate spheroid of semi-major axis $a = 0.036$ cm and semi-minor axis $b = 0.0012$ cm, we have evaluated the resonator constant. From the measured value of the bandwidth $[\Gamma_s - \Gamma_o](T{=}100\text{ K}) = 2 \times 10^{-6}$, we have calculated the normal state surface resistance $R_n = 11.2\ \Omega$ using Eq. (2.3.1), this results leads to a resistivity $\rho_n = 50$ mΩ cm (the subscript n refers to the normal state or T = 100 K value). The anisotropy factor is approximately $\rho_c/\rho_{ab} \sim 500$ just above T_c. With the resistivity value one can estimate the skin-depth of the material in the normal state $\delta = 40\ \mu$m. Using the temperature dependence of $X_s(T) = \omega\mu_o\lambda(T)$ we can deduce the penetration depth at zero temperature. On Fig. [5.13] we can see that $X_s(T)$ saturates at low temperature to a value corresponding to a penetration depth $\lambda(T = 0K) = 3.7\mu$m. From our data, the perpendicular penetration depth is on the average temperature independent up to 40 K.

The temperature dependence of R_s and X_s suggest the presence of a peak. In fact the condition *sanae*

	ρ_n [Ω cm]	δ [Å]	λ [Å]	ℓ [Å]	$\xi(0)$ [Å]	τ [cm^{-1}]	$2\Delta(0)$ [K]
$\parallel$	100×10^{-6}	1.8×10^4	1500	100	35	200	550
$\perp$	50×10^{-3}	4.0×10^5	3.7×10^4	?	4	?	> 550

Table 5.1: Electrodynamics properties of $YBa_2Cu_3O_7$ measured at 60 GHz, with the current flowing whether in the (ab)-plane ($\parallel$ configuration) or along the c-axis ($\perp$).

qua non for a raise in σ_1 below T_c is

$$\left.\frac{d\sigma_1}{dT}\right|_{T_c^-} \leq 0 \Longleftrightarrow -\left.\frac{dX_s}{dT}\right|_{T_c^-} \leq \left.\frac{dR_s}{dT}\right|_{T_c^-} \tag{5.6.1}$$

assuming that $R_s = X_s(T > T_c)$. On the graph, R_s and X_s drops with the same slope at T_c implying that σ_c should display a strong increase below T_c. This simple argument is indeed confirmed in Fig. [5.14] where we display the temperature dependence of σ_c below T_c as evaluated from the impedance data. If the increase of σ_1 is caused by coherence effects for the a-direction then the height of the peak suggests a large gap value, well exceeding the one quoted for the (ab)-plane.

5.6.2 ^{89}Y NMR

In this section we discuss new NMR studies on the ^{89}Y nuclear spin, the experiments were performed in the superconducting state of oriented powders. The Y is a spin-1/2 nucleus and has no electric quadrupole moment. Its isotope is 100% abundant but has a small gyromagnetic ratio. The Y is nested between adjacent CuO_2 plane and its indirect coupling to the superconducting layer has provided many interesting results. The first measurements of the Y NMR were made by Markert *et al.* [132] and Balakrishnan *et al.* [18] but the most extensive study of the normal state has been performed by Alloul *et al.* [10]. He has shown that the Y nucleus follows a fermi-liquid picture and in particular the nuclear spin relaxation rate follows the Korringa relation above T_c, contrary to the Cu(2) site affected by the 2D antiferromagnetic fluctuations [140].

Small crystallites of $YBa_2Cu_3O_7$ were mixed with Stycast and during the hardening period aligned in a magnetic field of 7.5 T. From X-ray scattering, the misorientation is less than 3^o. The data were taken in a double channel setup. The echoes obtained in a $\pi/2$ (10μs) - π pulse sequence were Fourier transformed. The experiments were performed in a field of 7.5 T, and the measuring frequency was ~15.64 MHz. From zero field shielding diamagnetism measurements, the onset of superconductivity is at $T_c(0)$~92 K. In the NMR magnetic field, $T_c(B)$ ~89 K, defined as the onset of the diamagnetism in the rf-coil.

Linewidth

The temperature dependence of the linewidth for $H \parallel c$ and $H \perp c$ is shown in Fig. [5.15]. The narrow linewidth (0.6 kHz) in the normal state is a signature of the good stoichiometry of the compound, $x = 1$. It has been shown recently that below 100 K, underdoped ($x < 1$) samples have a second resonance line [35] (note that the ^{89}Y NMR shift varies also drastically as soon as x departs from unity [8]). Below T_c, the lineshape depends on the flux phase (array or liquid).

The main feature of Fig. [5.15] is that the linewidth broadens only below $T^* \sim 83$ K for the $H \parallel c$ configuration, while for $H \perp c$ the linewidth increases already below 89 K, $T_c(B)$. In the high-T_c compounds there are numerous experiments that have shown the existence of a vortex liquid phase between $T_c(B)$ and T^*, where T^* defines the onset of magnetic irreversibilities in the sample [158] (below which flux pinning occurs) and $T_c(B)$, is the onset of diamagnetism (or the start of the resistivity drop). For $H \parallel c$, the absence of line broadening between $T_c(B)$ and T^* is probably due to motional narrowing as suggested by Brom *et al.* [35]. For $H \perp c$, there is no liquid vortex phase and the start of the line broadening coincides with the apparition of the superfluid fraction in the sample (as expected for conventional superconductors). It has been shown in a previous report that the temperature dependence of the linewidth could be well fit by a two-fluid formula if T is scaled by the melting temperature T^* for the $H \parallel c$ configuration, or $T_c(B)$ for the other configuration, $H \perp c$. This empirical law is the appropriate form of $\lambda(T)$ if the material is governed by strong-coupling effects. The anisotropy of the linewidth is related to the anisotropy of the

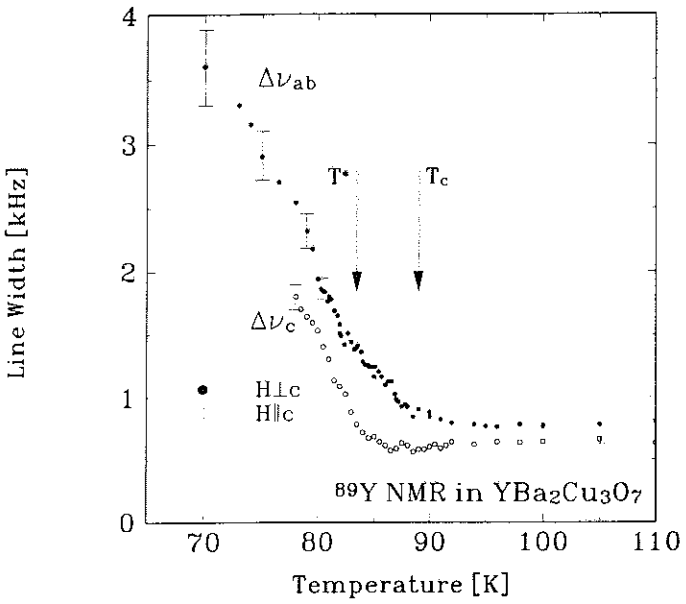

Fig. [5.15]: Temperature dependence of the linewidth of the ^{89}Y in a 7.5 Tesla field perpendicular and parallel to the c-axis.

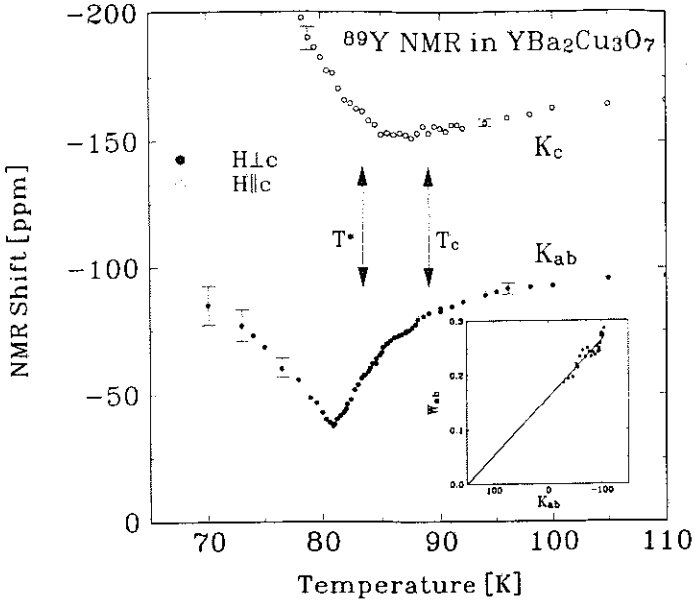

Fig. [5.16]: Temperature dependence of the NMR shift of the ^{89}Y in a 7.5 Tesla field perpendicular and parallel to the c-axis. Inset: K_{ab} between 81 K ¡T¡ 89 K compare to the nuclear relaxation W_{ab}. The solid line is the Korringa relation in the normal state.

penetration depth:

$$\frac{\Delta\nu_{\perp}}{\Delta\nu_{\parallel}} = \left(\frac{\lambda_c}{\lambda_{ab}}\right)^2. \tag{5.6.2}$$

The ratio is ~ 4 from our data, somewhat smaller than the one extracted from conductivity but larger compare to other measurements [163]. It is difficult to ascertain firm conclusion, as the effect might be dominated by misorientations of the grains.

Knight shift

It was shown in Chapter 2, that the NMR shift is related to the magnetic susceptibility at the nucleus site. It can be divided in two distinct parts, the spin susceptibility (Knight shift) and an orbital contribution (chemical shift),

$$K_\nu(T) = {K^L}_\nu + {K^S}_\nu(T), \tag{5.6.3}$$

where K_ν is the total shift, ${K^L}_\nu$ is the T-independent chemical shift and ${K^S}_\nu$ is the T-dependent Knight shift. It was shown by Alloul *et al.* [8] that above T_c the dominant contribution to K^S is the hyperfine coupling with the O2$p\sigma$ orbital of the eight neighbor oxygens. Using the Mila-Rice [138] hyperfine form factors A, K^S is related to the spin susceptibility by the following formula:

$${K^S}_\nu(T) \sim A_\nu \chi_\nu^{(O)}, \tag{5.6.4}$$

where A is negative for the Y site. The normal state anisotropy is shown in Fig. [5.16], the magnitude of the Y shift was evaluated carefully in Ref. [8]: it was found that ${K^L}_{ab} \sim 150$ ppm at room temperature, while ${K^L}_{ab} - {K^L}_c \sim 15$ ppm; for the Knight shift ${K^S}_{ab} \sim -240$ ppm and ${K^S}_{ab} - {K^S}_c \sim 72$ ppm. Above T_c, the anisotropy of the NMR shift is interpreted as an anisotropy of the spin susceptibility at the oxygen

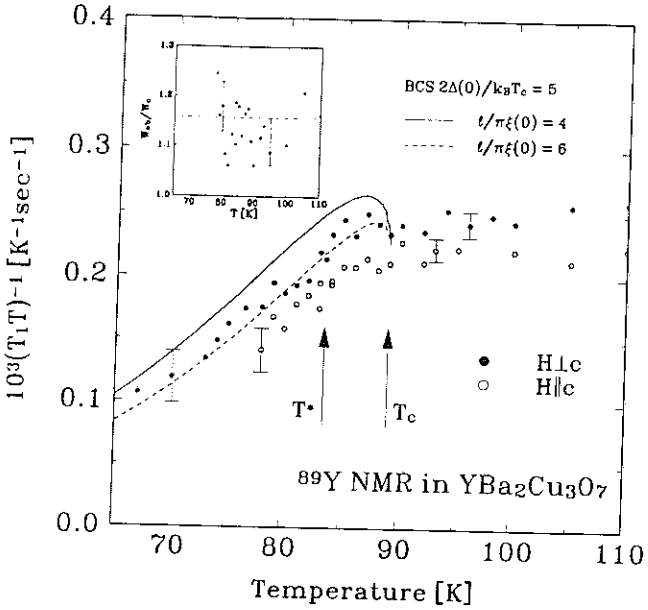

Fig. [5.17]: Temperature dependence of the ^{89}Y nuclear relaxation rate for both the $H \parallel$ and $\perp c$ configuration. Inset: anisotropy of the relaxation rate, the dashed line is the normal state value.

sites $\chi_c^{(O)}/\chi_{ab}^{(O)} \sim 1.2$.

In the superconducting phase, the temperature dependence of K_ν is rather peculiar, as shown in Fig. [5.16]. For the $H \perp c$ configuration, one observe the expected decrease of the spin susceptibility below $T_c(B)$ (the shift increases because the hyperfine coupling is negative). The onset of the drop is not sharp, and seems to scale with the nuclear spin relaxation. This result is in contrast with the temperature dependence of the Yosida function shown in Fig. [2.16]. On the inset of Fig. [5.16], we have compared the NMR shift versus the nuclear spin relaxation rate for the same orientation, the plot is limited to the temperature range $T > 81K$. The significance of this plot will be analyzed later. A sharp cusp is observed at 81 K, and below the NMR shift decreases with increasing temperature. The abruptness suggests a regime change; a possible explanation is that the penetration depth becomes comparable to the dimension of the powder and the increase fraction of the superfluid screens the magnetic field at the Y site. Further work needs to be done before drawing firm conclusion, and in particular a study of the intensity of the signal.

For the $H \parallel c$ configuration the shift seems constant in the same temperature window where K_{ab} increases. Later, below 85 K, K_c decreases with decreasing temperature. The onset of the change is slightly higher than the irreversibility temperature T^*. We note that similar behavior have been observed for the Cu(2) sites in the temperature range T^*-$T_c(B)$ [23].

Nuclear spin relaxation

The temperature dependence of the ^{89}Y nuclear spin relaxation rate W is shown on Fig. [5.17]. Below $T_c(B)$, we observe a shoulder of approximately 3K width that can be interpreted as the remaining of the coherence peak. We recall that the excitation spectrum is probed at Larmor frequency, or 8 cm^{-1} for the 7.5 T NMR magnetic field.

By fitting the observed temperature dependence with the BCS response function where only the q=0 contribution of the susceptibility [10] was included, we find parameters that are very close to the conductivity results: a strong coupling ($2\Delta(0)/k_BT \sim 5$) and a sample in the clean limit ($\ell/\pi\xi(0) \sim 5$). We also observe that the results for the ^{89}Y surprisingly differs from the ^{17}O that decreases substantially faster. This might be an indication that at low temperature the relaxation of the Y is dominated by other pro-

cesses, which then will indicate that the quoted value of the coupling constant represents a lower bound. However, there is a strong argument against the coherence peak interpretation suggested by the inset of Fig. [5.16]. If the plateau in W_{ab} is a remaining of the coherence peak then we should see a strong departure of the ratio W_{ab}/K_{ab}^{S} from the Korringa law below $T_c(B)$. Quite the opposite, we observe that the nuclear spin relaxation rate of the Y follows the same Korringa relation in the superconducting phase up to 81 K (the solid line in the inset is a continuation of the normal state behavior). This observation will then seems to rule out the simple explanation mentioned above. Below 81 K, the NMR shift changes regime and we haven't included the data point in the figures.

For the $H \parallel c$ configuration, we find a behavior that is very similar to the perpendicular direction. It is not very clear from our data wether $T_c(B)$ or T^* should be used as the transition temperature to compare with the BCS formula and thus we haven't attempted to compare the data point with the BCS predictions. A fit similar to the $H \perp c$ configuration (same fitting parameters) could have been obtained if we would have neglected the presence of the flux melting zone.

Finally we show in the inset of Fig. [5.17], the anisotropy of the Y nuclear spin relaxation. The dashed line is the normal state mean value. The anisotropy decreases below 120 K, to recover the former value in the superconducting phase. The change is small and slightly larger than our measurement accuracy. The significance of this anisotropy is not clear but seems a characteristic of the normal state rather than of the superconducting compound. We could not go further lower in temperature due to technical difficulties.

Chapter 6

Organic superconductors

The field of organic superconductivity started a decade ago, long after the prophetic ideas of W.A. Little (1964) [128]. The first superconducting compound was discovered by D. Jérome in 1980, it was the quasi-one dimensional $(TMTSF)_2PF_6$ salt, that has a T_c= 0.9 K under a pressure of 12 kbar [99]. Although the T_c was small, the advance received a lot of attention because the chemistry of those molecules is well controlled and thus is perfectly suited for a systematic study. A tremendous effort has been spent in the past decade, but still very 'little' is known about those materials. The compound that we have studied, is the κ-$(ET)_2Cu(NCS)_2$ salt, it was the first 10-kelvin organic superconductor synthesized in 1988.

6.1 Experimental survey

Like the cuprates, the organic superconductors are charge-transfer salts, where the cation part comes from an organic molecule and the anion is usually an inorganic complex. In our case the organic building block is BEDT-TTF (bis(ethylenedithia)tetrathiafulvalene) which for simplicity is written ET. The anion is $Cu(SCN)_2^-$, but can be replaced by $Cu[N(CN)_2]Br^-$ and $Cu[N(CN)_2]Cl^-$ for an increase of the critical temperature ($\sim$ 13 K). The delocalized electrons that are responsible for the conducting properties of these materials come from the overlap of the π orbitals between the cations (the 3p orbitals of the sulfur atom). The syntheses of the new salts follow from electrolysis. This procedure uses two glass cell connected by a frit, which allows the ion migration but prevents the mixing of the cell's content. The platinum electrodes inject a small current (a few μA) that oxides the ET molecule, and crystals form on the anode through a slow diffusion process. The crystals formed have a characteristic flat hexagonal shape. The solvent is usually an organic polar molecule (trichloroethylene). The samples used in this study were provided by F. Wudl from the Department of Physics at the University of California, Santa Barbara.

6.1.1 Crystal structure

The salts produced split in two distinct phases called the β- and κ-crystals. The κ-phase is made of a combination of dimers couple almost facing each other (dihedral angle between planes is 2.1°, interplanar spacing is 3.3 Å), but that are oriented at nearly right angles with respect to their neighbors (88°); a schematic representation can be found in Fig. [6.1]. In contrast the β-phase is a two-dimensional parallel stacking of those dimers.

The κ-crystals only are superconductors, their space group is $P2_1$ (non centro-symmetric), it has a monoclinic unit cell of dimensions $a = 16.25\AA$, $b = 8.44\AA$ and $c = 13.12\AA$ [192] at room temperature; a drawing of the crystallographic structure can be found in Fig. [6.1]. As mentioned earlier, each organic molecule is linked by inter-dimer sulfur contact (3.51 Å) the bounding forms the two-dimensional conducting layer and the donor sheet lays in the (bc)-plane. The (bc)-plane is usually parallel to the largest crystal surface and has a typical hexagonal boundary. Every conducting layer is sandwiched by the insulating

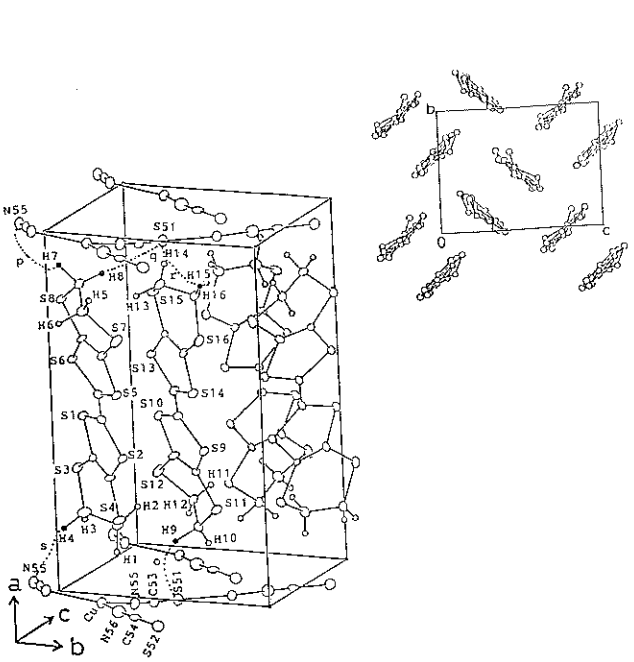

Fig. [6.1]: Top: crystal structure viewed along the molecular long axis (κ-phase). Only the BEDT-TTF molecules are depicted. Bottom: Crystal structure at 104 K and specific cation-anion contacts. Figures are after Ref. [192].

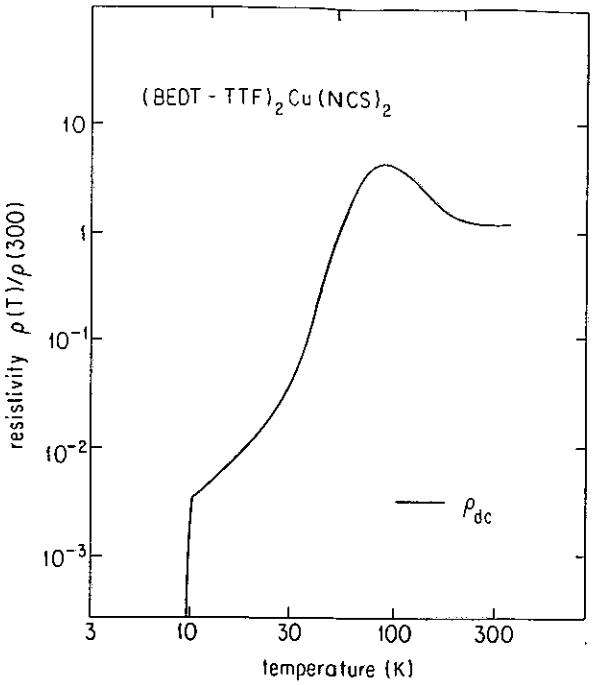

Fig. [6.2]: Temperature dependence of the (bc)-plane dc-resistivity. The curve is normalized to the room temperature resistivity value $\rho_{dc} = 0.05\Omega$ cm, the curve was taken from Buravov *et al.* [38].

$Cu(NCS)_2$ along the a-axis. The anion posses a permanent dipole, that is not screened by the crystal. Notice that there are no distinct structural phase transition which occurs as lowering the temperature.

6.1.2 Electronic properties

The electronic properties of organic superconductors are very similar to the one observed in the cuprates. They are very anisotropic in the normal-state, the highly conducting pathways are parallel to the (bc)-plane and the poorly conducting direction is along the a-axis. We have used different symbols to distinguish the two cases where the currents flow along ($\|$) or perpendicular ($\perp$) to the (bc)-plane. The temperature dependence of the electrical resistivity along the (bc)-plane has an oscillating shape and the result is shown in Fig. [6.2], the curve was reproduced after Ref. [38]. The room temperature dc-resistivity is around $\rho_{\|} = 0.05\Omega$ cm. The temperature dependence goes through a minima at 250 K and then a maxima at 100 K. It drops sharply below 100 K, and in range 10-30 K it can be fitted by the functional form:

$$\rho_{\|} = A + BT^2, \tag{6.1.1}$$

where $A \sim 50\mu\Omega$ cm and $B \sim 2\mu\Omega$ cm K^{-2}. The resistivity at 10 K (slightly above the transition) is $\rho_{\|} = 250\mu\Omega$ cm. The anisotropy is large but has never been estimated accurately: Buravov *et al.* [38] estimated a ratio $\rho_{\perp}/\rho_{\|} = 10^3 - -10^4$ at low temperature, while Urayama*et al.* gave a more conservative figure ~ 600 [192, 156], regarded as a lower limit. The carrier density (holes [112]) is low ($n = 2\times10^{20}$ cm^3) [190], and an order of magnitude smaller than the number $\sim 1.2 \times 10^{21}$ cm^3 expected if one carrier exists per unit formula. Consequently, there is less screening and the dynamics is dominated by the Coulomb repulsion between the carriers, the system is strongly correlated (represented by a large Hubbard U) and the conduction band is narrow ($4t_{\|} \sim 0.5$ eV, where $4t$ is the tight-binding bandwidth), leading to a large renormalized mass of the carriers ($m_{\|}^* = 4m_e$ in the (bc)-plane). Those materials have an important difference with their HTC counterparts, there is no magnetic ground state nearby in the phase diagram: however some of those molecules have a degenerate SDW ordering.

The parameters describing the superconducting state are the coherence lengths $\xi_{\|} \sim 70\AA$ and $\xi_{\perp} \sim 5\AA$,

as extracted from critical field measurement [172]. The penetration depth evaluated from μSR [80] is $\lambda_{||} = 9800\mathring{A}$ and there is no reliable evaluation of $\lambda_{\perp}$ in the literature. A complete review of those electronic properties can be found in the book edited by V. Kresin and W. Litttle [116] and references therein.

Shubnikov de-Haas (SdH) experiments by Toyota *et al.* [190] and Oshima *et al.* [157] gave a value for the scattering time $\tau_{||} \sim 2\text{cm}^{-1}$, the fermi momentum $k_F \sim 1.4 \times 10^7\text{cm}^{-1}$, which implies that the mean-free-path $\ell = \tau \times \hbar k_F/m^* \sim 500\mathring{A}$, placing the compound well into the clean limit $\ell/\pi\xi_o > 1$.

6.1.3 Pairing symmetry

The nature of the pairing state in those materials is still a matter of speculation, and there is no consensus in the community on this matter. Contrary to the cuprates, the investigation was not as diverse and complete (but as confusing): almost all the experiments on the subject are measurements on the temperature dependence of the penetration depth at low temperature [89] and looked if $\lambda(T)$ obeys some power law (cf. Chapter 5). In the last three years, there are been at least five conflicting papers on the subject, where even the same experiment at the same facility, found different results. One μSR experiment claims a conventional 's-wave' pairing [80] while another claims a linear behavior at low temperature and 'd-wave' pairing [122] (a schematic drawing of various gap symmetry was shown in Fig. [1.8]). Shielding diamagnetism measurement in contrast found a T^2 dependence ('p-wave' pairing) [102] and other support the 's-wave' [121] model. The only clear message out of this cacophony, is that measurements of $\lambda(T)$ are not conclusive and there may be some other effects that have to be taken into account: like the sample quality. A hint might be given by the results of Sridhar *et al.* on the rf-penetration depth under various magnetic fields [182]. They suggested that the zero-field state might not simply obey a London relation: the measured λ might turn out to be the flux-flow skin-depth.

Specific-heat experiments [72] have shown good agreement with 's-wave' pairing with a single transition; if nodes would have been present in the gap, some split transition would have been observed like in the heavy fermion compound UPt_3 [61, 83]. The data showed a shallow drop of the specific heat at T_c (width of 1 K) that was interpreted as the signature of a rather broad distribution of T_c's in the sample.

NMR experiments on these materials have displayed some rather strange feature. Measurement of the temperature dependence of the proton relaxation rate by Takahashi *et al.* exhibited a strong peak around 5 K [186]. This enhancement was interpreted as a signature of triplet pairing (all the models mentioned so far were singlet). A more recent study however, done at Orsay, showed that a careful and systematic characterization of the 'peak' features are in full agreement with flux-motion models [98]. The conclusion is: although NMR data show an enhancement of the relaxation rate, there is no direct evidence of 'coherence-peak like' behavior, that could infirm or support any pairing model.

6.1.4 Optical properties

The optical properties of the κ-$(ET)_2Cu(NCS)_2$ [114, 113] share several similarities with the cuprates. The important conclusion is that, like for the oxides, optical experiments were not successful in determining the single-particle gap [115], although the position of the BCS gap is near 20 cm^{-1}, slightly above the threshold of detection sensibility of most FIR spectrometer (but great care was taken to measure the spectrum down to 5 wave-numbers). Those unsuccessful attempts could be well explained by the clean-limit argument sketched in the previous section, where the reflectivity in the normal-state is almost 100 % and thus too high to allow any detectable variation at the gap edge. Also, as for the cuprates, a large temperature-independent feature appears in the mid-infrared region, and certain data are suggestive of states below the gap [113]. No attempt has been made to extract the temperature dependence of quasiparticle life-time, as the data resolution is poor below 20 cm^{-1}.

Excluding our work, there are very few published microwave data on the κ-$(ET)_2Cu(NCS)_2$, in fact we are only aware of a recent preprint of Achkir *et al.* [4] that studied the electrodynamics at 17 GHz. They

measured a broad peak in the temperature dependence of the conductivity $\sigma_1(T)$ that was attributed to a strongly temperature dependent scattering rate. The analysis was identical in the form as the one used in Ref. [29] and thus we refer to the discussion page 81 in Chapter 5 for a critic review of the method: we believe that the temperature dependence of τ is spurious and impeded by the assumptions in the analysis. They claimed also a linear term in the temperature dependence of the penetration depth in good agreement with the one observed by Le *et al.* [122], although inconsistent with their raw data as shown in Fig. [6.5]. Finally, they measured also the normal state properties down to 1.2 K by applying a dc-magnetic field above H_{c2} and later we will use extensively their result to infer $\tau_{\|}(T)$ below T_c.

In conclusion, the nature of the pairing symmetry has not been solved by the previous experiments and there is no agreement on the results. Again, the two principal candidates are a conventional 's-wave' or a 'd-wave' pairing. The following will review the microwave properties of κ-$(ET)_2Cu(NCS)_2$ as evaluated by cavity perturbation technique at 60 GHz.

6.2 In-plane properties

We have measured the surface impedance $Z_s = R_s - iX_s$ of κ-$(ET)_2Cu(NCS)_2$ in the millimeter-wave spectral range at both the magnetic and electric field antinode for various crystallographic orientation. Again, only the data at 60 GHz will be mentioned although we have performed some measurements at other frequencies. We first discuss the in-plane (bc-plane) electrodynamics properties.

In terms of the complex conductivity $\hat{\sigma} = \sigma_1 + i\sigma_2$, the surface impedance is given by Eq. (2.3.1):

$$Z_s = \sqrt{\frac{\omega}{4\pi i\hat{\sigma}}}, \tag{6.2.1}$$

where R_s and X_s are the surface resistance and surface reactance. In the normal state, $\sigma_1 \gg \sigma_2$ and

$$R_s(T) = X_s(T) = \frac{\omega}{c_o}\frac{\delta(T)}{2}, \tag{6.2.2a}$$

where δ is the skin-depth defined as $\delta = c_o/\sqrt{2\pi\omega\sigma_1}$. In the superconducting state, the surface reactance is proportional to the penetration depth (at temperature where $\sigma_2 \gg \sigma_1$)

$$X_s(T) = \frac{\omega}{c_o}\lambda(T) \text{ and } \quad R_s \sim 0, \tag{6.2.2b}$$

and R_s is determined by the losses due to thermally excited carriers within the penetration depth (cf. Chapter 2 for more details).

6.2.1 Normal state

Our experiments were conducted by employing 'cavity perturbation' techniques, where a small specimen is placed inside a resonant cavity at various positions (see below). The signal is detected by the 'amplitude configuration' analogous to the one used in ESR (Chapter 3). The measured parameters are the resonant frequency, f_o and the resonance bandwidth, Γ. The changes due to the specimen normally represent a small perturbation of the resonance, and are linearly related to the changes of the surface impedance of the specimen:

$$\frac{1}{2}\frac{\Delta\Gamma}{f_o} - i\frac{\Delta f}{f_o} = \alpha(R_s - iX_s), \tag{6.2.3}$$

where α, the resonator constant, is a geometrical factor reflecting the dimensions of the sample and cavity, and can be calculated by using Table (3.3).

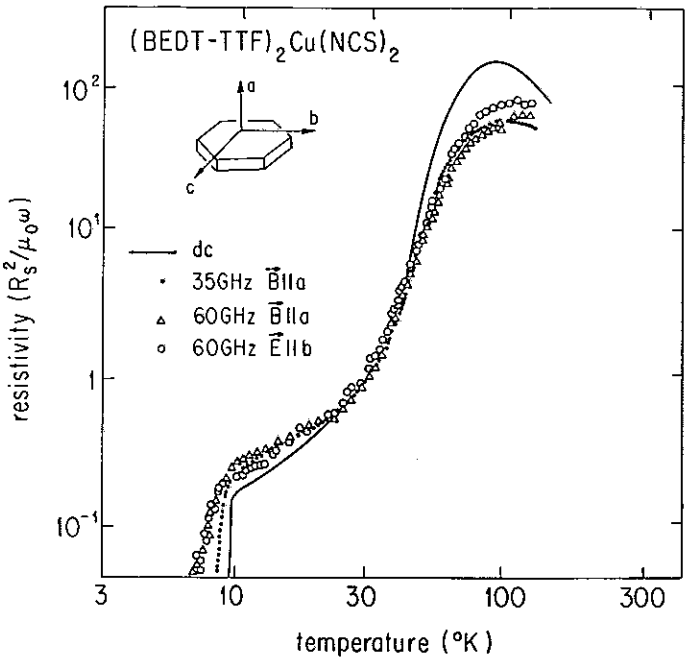

Fig. [6.3]: Temperature dependence of the ac-resistivity $8\pi {R_s}^2/\omega$, the currents are flowing in the (bc)-plane but are induced either by an ac-electric or magnetic field. All quantities are normalized to the $T = 30$ K dc-resistivity value.

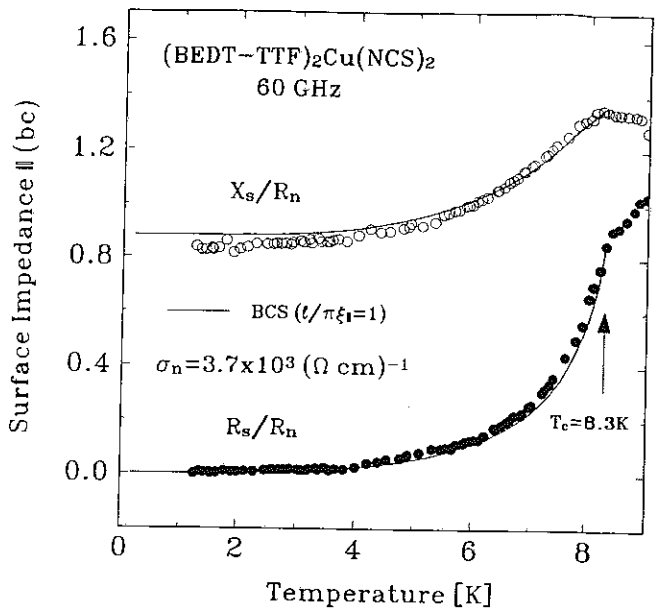

Fig. [6.4]: Temperature dependence of the surface impedance $Z_{s\|} = R_{s\|} - iX_{s\|}$ of the highly conducting plane. The solid line is the BCS prediction convoluted over 1 K, the fit parameter is $\ell/\pi\xi_o$ =1.

For the specimens we have investigated, two different configurations have been implemented to explore the anisotropy of the normal- and superconducting state properties. In one configuration the sample is at the antinode of the ac-magnetic field and the ac-electric field is zero at the surface of the specimen (configuration 2). In the other configuration $\mathbf{E}_{\rm ac}$ is maximum and $\mathbf{H}_{\rm ac}$ is zero at the surface (configuration 3): a schematic diagram of the two positions can found in Figs. [3.1] and [3.2]. In the experiments where $\mathbf{E}_{\rm ac}$ is parallel or $\mathbf{H}_{\rm ac}$ perpendicular to the highly conducting (bc)-plane, the currents flow in the plane and we refer to the surface impedance as $Z_{s\|} = R_{s\|} - iX_{s\|}$.

In our experiments where the specimen is subjected to electromagnetic fields, demagnetization effects and misalignment of the field with respect to the crystallographic axes may play a role. The former may lead to vortex contributions to the electrodynamic response, the latter to a mixture of in-plane and perpendicular to the plane properties. We have obtained identical results for both configurations (electric and magnetic anti-node) where the induced ac-currents flow in the (bc)-plane, and we conclude that demagnetization effects (which could be relevant for configuration 2, but not for configuration 3) do not play a significant role.

Using the measured value for the quality factor, one can estimate the conductivity in the normal state just above T_c. Using cavity perturbation theory in the skin depth regime (cf. Chapter 3) and approximating the sample shape with an oblate spheroid, we obtain a value for σ_n $(T = 9$ K$) = 3.7 \times 10^3\ \Omega^{-1}$ cm $^{-1}$ in good agreement with both the dc [38] [σ_n $(T = 12$ K$) = 5.0 \times 10^3\ \Omega^{-1}$ cm $^{-1}$] and far infrared values [113] [σ_n $(T = 10$ K$) = 2.0 \times 10^3\ \Omega^{-1}$ cm $^{-1}$]. Thus, we conclude that misalignment effects are negligible.

The superconducting transition temperatures observed were typically 8.3 K. Shielding diamagnetism measurements indicate a typical width of the transition $\Delta T = 1$K. Such a significant width is evident from magnetization, dc resistivity, and specific heat [72] studies conducted by other groups.

In Fig. [6.3] we display the dc resistivity together with $8\pi {R_s}^2/\omega$ measured along the conducting (bc)-plane. All quantities are normalized to their $T = 30$ K value. For a metal $\rho_{dc} = 8\pi {R_s}^2/\omega$, for $\omega\tau < 1$ and consequently, Fig. [6.3] suggests that in the normal state κ-$(ET)_2Cu(NCS)_2$ is a simple metal with a relaxation rate which exceeds $\omega/2\pi = 2$ cm^{-1} (60 GHz), in agreement with optical studies which lead to a relaxation time $1/\tau_{\|} = 1000$ cm^{-1} [113]. This figure differs greatly from the quoted value above (SdH

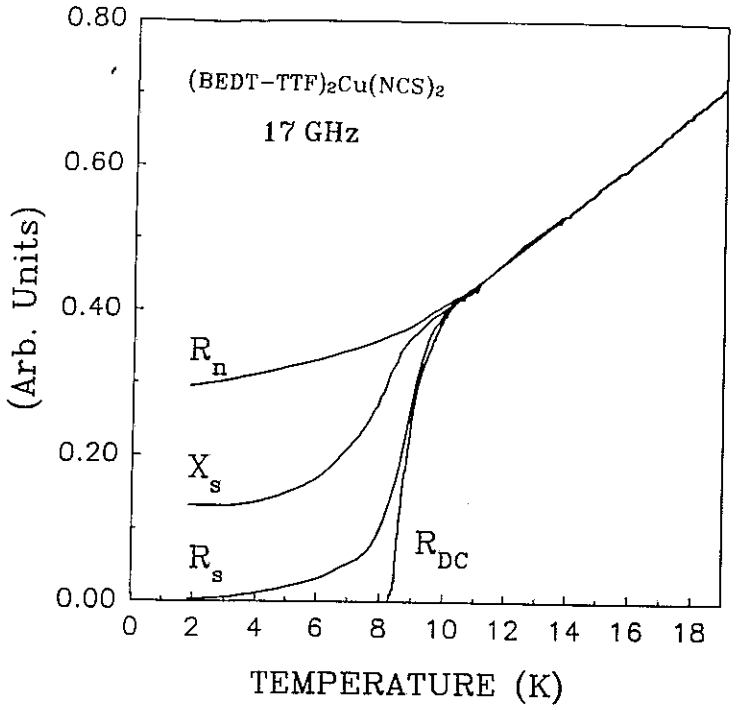

Fig. [6.5]: Temperature dependence of the surface impedance at 17 GHz by Achkir *et al.* [4]. R_n is the surface resistance of the sample under a dc-magnetic field of 10 Tesla (well above H_{c2}).

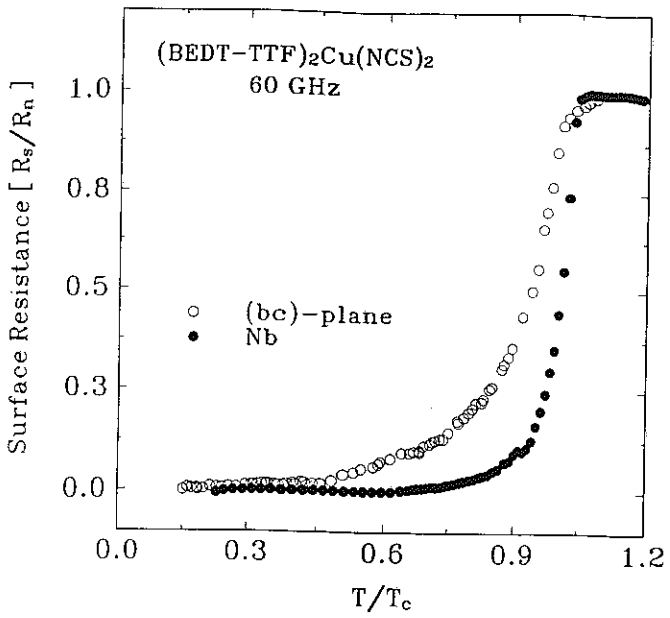

Fig. [6.6]: Temperature dependence of $R_{s\|}$ of κ-$(ET)_2Cu(NCS)_2$ compare to the result obtained for a bulk piece of pure Nb (Chapter 4).

experiments). The reasons for this difference are not clear at the present and several explanations will be suggested below. In this limit, $R_s = X_s = \sqrt{\omega/8\pi\sigma_1}$ and both components of the impedance R_s and X_s have the same value. Just above T_c our high frequency results are somewhat different from σ_{dc} available in the literature. Experiments on several specimen indicate that this is due to the difference in sample quality. We have also observed differences in the transition temperature, as it is also evident from Fig. [6.3].

6.2.2 Superconducting state

The temperature dependence of R_s and X_s below T_c= 8.3 K, obtained from a configuration where the electric field is parallel to the c direction, is shown in Fig. [6.4]. For the data displayed, the electric currents flow within the conducting plane, and consequently $Z_{s\|}$ is measured. All the data shown in Fig. [6.4] are normalized to the value of the surface impedance at 9 K (R_n and X_n). It is important to notice that, in the temperature region below T_c, the 'normal-state' factor is defined by the value of σ_n at a fixed temperature point (9 K) rather than the expected normal state conductivity $\sigma_n(T)$ (and consequently $R_n(T)$ and $X_n(T)$) which would be recovered at the same temperature. Nevertheless, the temperature dependence of $\sigma_n(T)$ below T_c was measured by Achkir *et al.* [4] by applying a magnetic field of 10 Tesla (well above H_{c2}) while performing similar surface impedance measurements at 17 GHz, the results are shown in Fig. [6.5]. It was found that the scattering rate $1/\tau_{\|}(T)$ is temperature dependent and in continuation of the above T_c temperature range, the overall behavior in agreement with the T^2 functional form discussed in Eq. (6.1.1). This temperature dependence has to be taken into account in order to compare with the theoretical models developed in Chapter 2. The result of Achkir *et al.* [4] rules out also models predicting any drastic deviation from a shallow monotonic decrease of $1/\tau_{\|}(T)$ in the region 0-9 K.

Both the surface resistance and surface reactance depend on the parameters which determine the superconducting state. For a BCS superconductor, in the dirty limit the theory worked out by Mattis-Bardeen apply [135]. This limit, however, is not appropriate for κ-$(ET)_2Cu(NCS)_2$. The normal state dc conductivity and optical relaxation time leads to a mean-free-path $\ell \sim 100\text{Å}$. This value differs from the

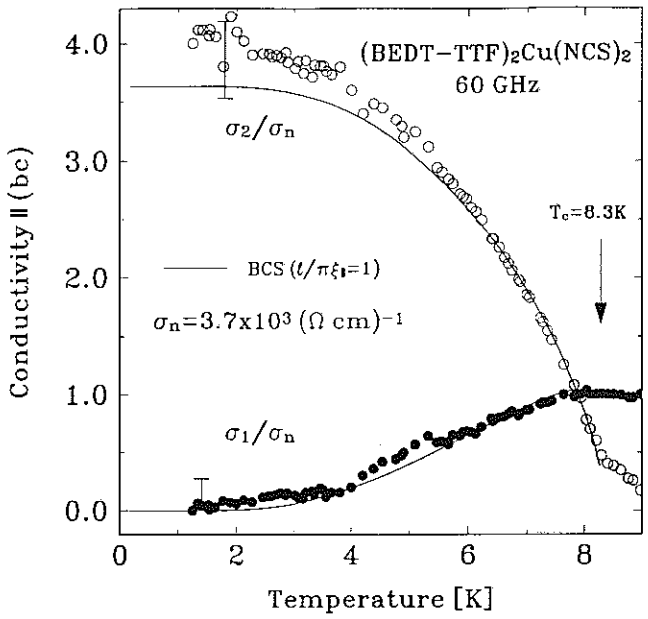

Fig. [6.7]: Temperature dependence of the complex conductivity $\hat{\sigma}_{||} = \sigma_1 + i\sigma_2$. The solid line is obtained using a BCS ground state convoluted over 1 K and a mean-free-path $\ell/\pi\xi(0)$ =1.

quoted figure page 90, it uses a more conservative estimation of the dc-conductivity and provides a lower limit. The coherence length [189] $\xi_{||} = 70\mathring{A}$, and the penetration depth $\lambda_{||} = 1\mu$m, all parameters referring to the in-plane quantities. We have calculated R_s and X_s for various values of $\ell/\pi\xi_o$ (cf. Chapter 2), assuming a two-dimensional BCS ground state [43], with a single particle gap given by the weak-coupling limit $2\Delta(0) = 3.5k_BT_c$. The best fit of our data (Figs. [6.4] and [6.7]) leads to a value of $\ell/\pi\xi_{||} = 1$, and, consequently to $\omega\tau_{||}$ =0.15 at f = 60 GHz, and this leads to a relaxation rate $1/\tau_{||} = 15$ cm^{-1}. This value for the scattering rate is shorter than $1/\tau_{||} = 1000$ cm^{-1} obtained from optical studies and somewhat larger than $1/\tau_{||} = 2$ cm^{-1} which is evaluated using Shubnikov-de-Haas measurements [190]. Some of these differences may reflect a frequency-dependent relaxation time and deviations from a single Drude response in the metallic state. The fit value $\omega\tau_{||}$ was used to calculate the unknown offset that adds to the frequency shift (Chapter 3, page 49). The ratio X_s/R_s of a Drude metal in the relaxation regime depends only on the $\omega\tau_{||}$ value. Using table [2.1] we have obtained a self-consistent number. Again, the 'normal-state' values refer to the 9 K temperature point for $\tau_{||}$. We have included in the fit the temperature dependence of the scattering rate, and the effect was obtained in the following way: we have fit $\rho_n(T)$ the normal-state resistivity above T_c by a second order polynomial, and used this to estimate $\tau_{||}(T)$ in the temperature region below T_c. The validity of this type of analysis is based on the results of Achkir *et al.* displayed in Fig. [6.5]. It is important to note that due to the slow variation of $\tau_{||}(T)$ this analysis is purely formal (cf. Fig. [2.11]) and ignoring the effect due the temperature variation of the relaxation rate will have given equally good fit with very similar parameter values.

The relatively broad transition observed in κ-(ET)$_2$Cu(NCS)$_2$ can crudely be modeled along the lines which have been done for interpreting the specific heat [72] by assuming a distribution of local transition temperatures in the specimen. Such a distribution is expected also to influence the temperature dependence of the electrodynamics response. We have modeled this by assuming that:

$$R_s(T), X_s(T) = \int [R_s(T), X_s(T)]P(T-u)du, \tag{6.2.4}$$

where $R_s(T)$ and $X_s(T)$ are the calculated surface impedance parameters described before and $P(u)$ =1 for $|u| < 0.5$ K and $P(u) = 0$ outside this temperature range. The solid line in Fig. [6.4] are $X_s(T)$ and $R_s(T)$

resulting from such procedure. Although representing the broad transition with a simple distribution of independent local transition temperatures and calculating X_s and R_s using Eq. (6.2.4) is certainly an oversimplification, it is clear from Fig. [6.4] that one can account for the full in-plane electrodynamics with a BCS ground-state and moderate sample quality.

In Fig. [6.6], we compare the drop of the surface resistance of the sample with a measurement on a piece of bulk Nb (cf. Chapter 4). As mentioned, $R_s(T)$ of the organic is much broader than the typical behavior observed for a three dimensional conventional superconductor. In the previous paragraph, we have used a distribution of T_c's to model the experimental findings, but we want to mention also that there exists several fluctuation-based models that can fit the data equally well, fluctuation effects are expected to be particularly dominant near T_c for very anisotropic conductor.

The normal-state skin depth $\delta = c_o/\sqrt{2\pi\omega\sigma_1} = 3.4$ μm at $f = 60$ GHz. With this value of δ, using the temperature dependence of X_s below T_c one gets a parallel penetration depth $\lambda_{||}(0) = 1.4\mu$m in excellent agreement with λ values evaluated from muon-spin-resonance (μSR) studies which lead to $\lambda_{||}(0) = 0.70$ and 0.98 μm, respectively [80, 122]. The agreement with the μSR results also demonstrates again that misalignment effects do not play an important role.

We also note that within experimental error X_s displays only a weak temperature dependence at temperature well below T_c. In this limit $X_s = \omega/c_o\lambda_{||}$ and consequently, our results are in full agreement with $\lambda_{||}(T)$ evaluated from μSR studies, and in clear disagreement with the temperature dependence of $\lambda_{||}(T)$ evaluated from ac-magnetization measurements [102].

6.2.3 Coherence peak

We have also evaluated σ_1 and σ_2 in the superconducting state by using Eq. (6.2.1) and the measured R_s and X_s values. In Fig. [6.7] we display the conductivity σ_1 normalized to the 'normal-state' conductivity σ_n at 9 K. Also displayed in the figure are the calculations based on the BCS model that lead to a broad maximum, reflecting case 2 coherence factors [178]. The solid line includes the temperature dependence effects of $\tau_{||}$(T). It is clear that our results are in full agreement with a BCS ground state. The broad maximum below T_c is a reminiscence of the coherence peak: at 60 GHz the photon energy is large (compare to the relatively modest T_c) and gives a ratio $\hbar\omega/\Delta(0) \sim 0.3$ above the maximum threshold that allows the observation of the coherence peak, as shown in Fig. [2.9].

We note that higher momentum pairing leads to the rapid disappearance of the coherence peak (cf. Chapter 1) and is expected to give σ_1 values significantly below the solid line of Fig. [6.7]. Our experiments, in contrast, lead to a conductivity which lies above the curve calculated for singlet pairing, and, consequently, we regard Fig. [6.7] as important evidence for a singlet ground state.

Unfortunately very little information can be extracted from the zero-temperature value of σ_2. In the relaxation regime $\omega\tau > 1$, the ratio $\sigma_2(0)$ / σ_n tends to $1/\omega\tau$ and not $\hbar\omega/\pi\Delta(0)$, as shown in Eq. (2.3.29). The measured value is then used as a check of the analysis consistency.

In conclusion, the temperature-independent surface reactance for $T \ll T_c$ and the increase of σ_1 somewhat below T_c rule out a superconducting ground state which is significantly different from singlet pairing.

We believe that observations which suggest an unconventional superconducting ground state (cf. previous section) are the consequence of non-ideal sample quality, of the strongly anisotropic nature of the superconducting state and/or demagnetization effects. Spurious power-law temperature dependences of λ for $T \ll T_c$ are also often obtained in oxide superconductors where it is believed that they may arise from the presence of inhomogeneities weak links regions [49, 117].

6.3 Out-of-plane properties

We have also measured the conductivity of the κ-$(ET)_2Cu(NCS)_2$ along the a-axis, i.e. perpendicular to the highly conducting plane that is along the (bc)-directions. Those experiments are extremely important

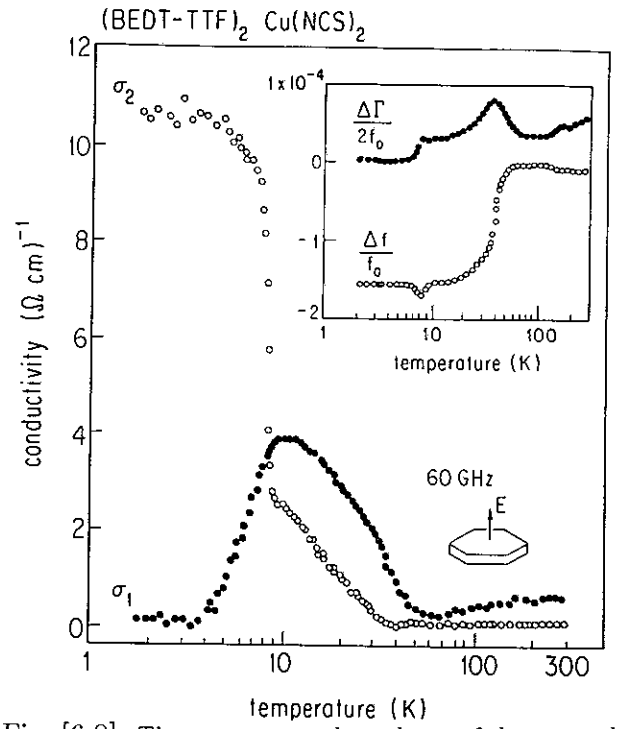

Fig. [6.8]: The temperature dependence of the perpendicular conductivity $\sigma_\perp$ of κ-$(ET)_2Cu(NCS)_2$ calculated from the measurement of $\Delta\hat{\omega}/\omega_0$ at the antinode of the electric field. The raw data $\Delta\Gamma$ and Δf are shown in the inset.

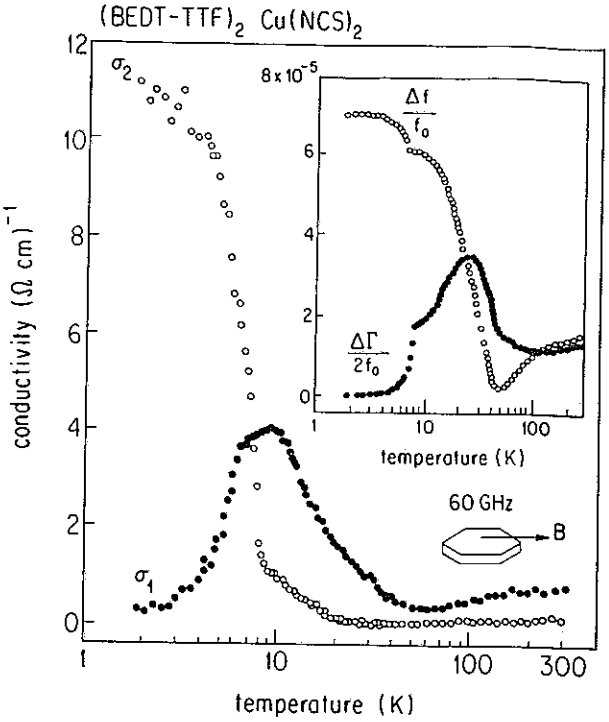

Fig. [6.9]: The temperature dependence of the perpendicular conductivity $\sigma_\perp$ of κ-$(ET)_2Cu(NCS)_2$. The measurement was done in the antinode of the magnetic field with **H** in the highly conducting (bc)-plane. The measured data $\Delta\Gamma$ and Δf are shown in the inset.

as they probe directly the anisotropy of the excitation density of states, and thus can give some important hint on the gap symmetry. Moreover there are no precise measurements of the anisotropy from dc data: the room temperature value $\sigma_{||}/\sigma_\perp$ was estimated to lie around 600 by Urayama *et al.* [192, 156] while Buravov *et al.* [38] estimated it to be between $10^3 - 10^4$. In both cases the accuracy is poor, as the end result is hindered by the exact current density distribution in the sample (expected to be temperature dependent too). In contrast, measurements of the high frequency response can be very precise as the technique is contactless and independent of the current distribution: the only relevant parameter is the total loss, that is dominated by the poorly conducting axis.

6.3.1 Normal state properties

Again, the a-axis conductivity was measured in two different configurations, in one the sample was sitting at the antinode of the electric, while in the other it was at the antinode of the magnetic field. The results are shown in the inset of Figs [6.8] and [6.9] respectively: the striking feature of the normal state properties is that the raw data have a very different temperature behavior between the **E** and **H** field, although they are supposed to probe the same parameters (for example the characteristic frequency f_E drops sharply around 50 K while f_H increases). This difference finds a natural explanation in the cavity perturbation theory (Chapter 3), where a sample can induces a very different response between the **E** or **H** configuration, when the conductivity crosses over from the depolarization to the skin-depth regime. The difficulty is then to evaluate the complex conductivity in a consistent fashion, and it will be shown that the intrinsic properties (the material conductivity) are in astonishing agreement between the two experiments despite the apparent differences in the experimental results.

Electric Field

In the inset of Fig. [6.8], we display the temperature dependence of the experimentally accessible parameters ($\Delta\Gamma$ and Δf), when the (BEDT-TTF)-sample was located at the antinode of the electric field. In this

case, the crystal was placed on top of a tiny quartz rod and the electric field pointed in the direction of the sample a-axis. The remarkable thing about this figure is that the sample response crosses *four* totally different regimes in one temperature scan ranging from 1.2 to 300 K. On the same plot one can see both the insulator and the metallic sides of the depolarization regime (the result of a relatively large anisotropy combined with a modest sample dimension), separated by the depolarization peak visible in the $\Delta\Gamma$-curve, together with the metallic and the superconducting state of the skin-depth regime. The skin effect regime is entered when the skin-depth becomes smaller than the sample radius. From the frequency change at T_c= 8.2 K we see that the superconducting penetration depth $\lambda(0)$ soon gets smaller than the skin-depth δ. Using the methods described in Chapter 3, we can extract both the real and imaginary parts of the conductivity in all those four different regimes. We assume that slightly above the transition temperature we are in the metallic regime. Thus at this temperature the frequency shift $\Delta f/f_0 = -\gamma/n - \xi X_s$. The frequency offset is settled by assuming that in the depolarization regime $\Delta f/f_0 \sim 0$. The sample is approximated by an oblate spheroid of dimensions $a = 30$ μm and $b = 200$ μm. We can then compute $\gamma/n = 1.4 \times 10^{-4}$ using Eq. (3.3.8c). The measured value of $\Delta\Gamma/2f_0$ slightly above the transition is equal to 2.5×10^{-5}. The temperature dependence of $\sigma_\perp$ calculated from the data is shown on the figure. We can see that $\sigma_\perp(T$=9 K) = 4.0 (Ω cm)$^{-1}$. Comparing this number to the published [107] value of $\sigma_{1\|}(T$=9 K) = 3.7×10^3 (Ω cm)$^{-1}$ gives an anisotropy of $\sim 1.1 \times 10^3$. The temperature dependence of $\sigma_{1\perp}$ is very similar to the one observed for the parallel direction, (bc)-plane. For example on the figure, one recognizes the semiconductor-like behavior at high-temperature. Using the data shown in the first section, we have extracted the temperature dependence of the anisotropy coefficient, and the ratio $\sigma_\perp/\sigma_\|$ was found to be almost temperature independent (within 10 %) between room temperature and 9 K.

Magnetic Field

In Fig. 6.9 we present the results for the same material at the antinode of the magnetic field. In this case, the magnetic field was oscillating along the (bc)-plane of the crystal and the measured conductivity was a combination of both the parallel and perpendicular values. However, due to the large anisotropy, we expect that the losses in the perpendicular direction will dominate. Using a similar procedure as described above, we fix the frequency offset by assuming that the minimum of $\Delta f/f_0 \sim 0$. The sample shape is approximated by an oblate spheroid of dimensions $a = 400$ μm and $b = 60$ μm. The value of $-\gamma/(n-1) = 6.5 \times 10^{-6}$ and we use our data to estimate $\Delta\Gamma/2f_0$ slightly above T_c to $\Delta\Gamma/2f_0$(9 K) = 2.2×10^{-5}. Remarkably, we recover the same temperature dependence of the intrinsic conductivity in both configurations, although the raw data are strikingly different.

6.3.2 Penetration depth

We have shown in Chapter 3, that the cavity frequency is determined by the total volume of the cavity which includes the skin-depth or the penetration depth of the materials forming the walls of the resonator. In the normal state the surface reactance is proportional to $\delta/2$ and goes to $\lambda(0)$ in the superconducting phase as in Eq. (6.2.2b). In principle by knowing δ one can then deduce the value of $\lambda(0)$. The normal-state resistance is highly anisotropic with $\rho_\perp/\rho_\| = 10^3$, and this leads to the normal state R_s and X_s which are a factor of $\sqrt{10^3} \sim 30$ times larger than the in-plane quantity. Using the skin-depth $\delta_\perp = \sqrt{c_o/2\pi\omega\sigma_{1\perp}}$ and a procedure analogous to that described above leads to an approximate value for the penetration depth in the superconducting state $\lambda_\perp = 30$ μm. In the configuration where the sample is at the antinode of **H** both the penetration depth along the layers $\lambda_\|$ and perpendicular $\lambda_\perp$ make a contribution to the total frequency shift. The frequency shift due to the specimen is then given by:

$$\frac{\Delta f}{f_o} \propto \frac{S_\| \lambda_\| + S_\perp \lambda_\perp}{V}, \tag{6.3.1}$$

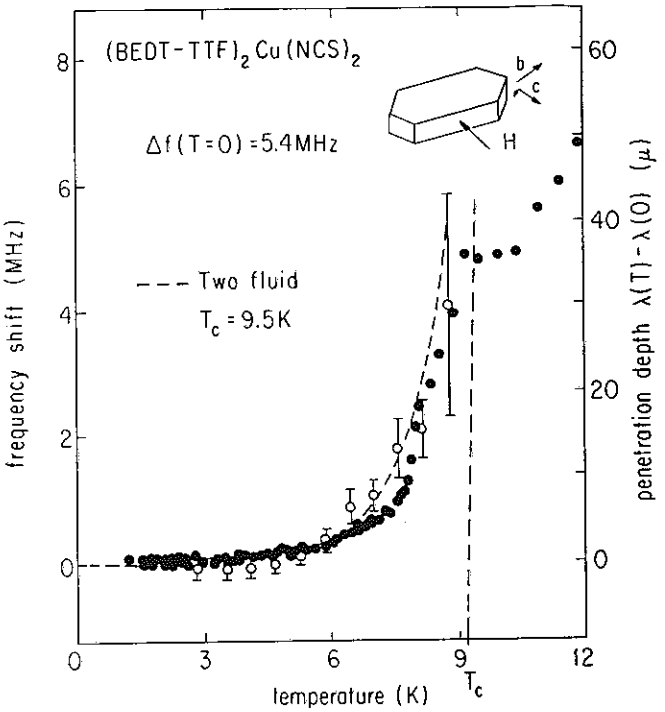

Fig. [6.10]: Temperature dependence of the frequency shift (left scale) and the perpendicular penetration depth $\lambda_\perp - \lambda_\perp(0)$ (open circles). Also shown are the parallel penetration depth results of Harshman *et al.* [80] obtained in μSR (solid circles). In the figure 40 $\times\lambda_{||}$ is plotted in order to scale the behavior of $[\lambda(T) - \lambda(0)]/\lambda(0)$ for both directions.

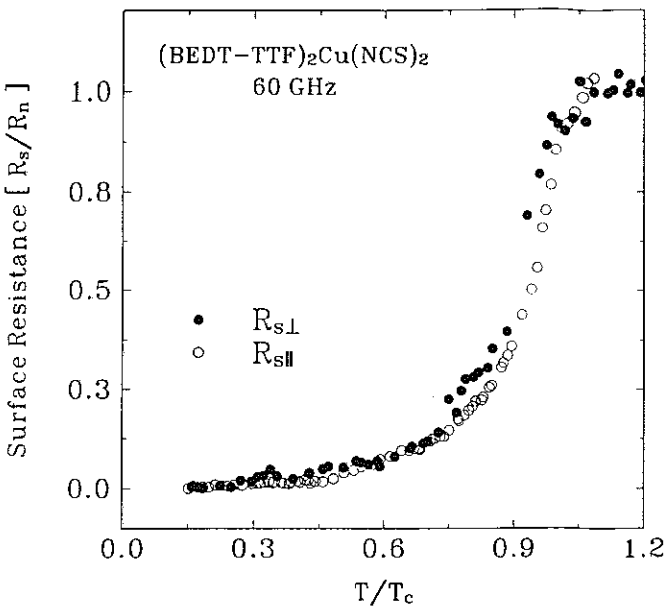

Fig. [6.11]: Comparison of $R_s/R_n(T)$ in the superconducting phase of κ-(ET)$_2$Cu(NCS)$_2$ for the two configurations where an ac-electric field is applied along or perpendicular to the highly conducting plane. All quantities are normalized to their 9 K value.

where S is the surface area of the sample and V is the volume of the cavity. Due to the pronounced anisotropy $\lambda_\perp \gg \lambda_{||}$, the former dominates the frequency shift. Using the calculated value of the resonator constant one can estimate again $\lambda_\perp \sim 35$ μm.

Using this result one can display in Fig. [6.10] the temperature dependence of the penetration depth and compare it with a BCS model: our results again can described well with a model which is based on singlet pairing. Furthermore, the T variation of λ at low temperature does not show any power law dependence and thus are in conflict with the reported results of unconventional pairing. For comparison we have plotted on the same figure our experiment together with μSR experiments which measure $\lambda_{||}$. Both this anisotropy and the magnitude of the penetration depth can be understood in terms of highly anisotropic electronic structure.

Perpendicular to the planes $\xi_\perp < d$, where d is the interplanar separation. Under such circumstances, the situation is close to that of Josephson-coupled planes, with the resulting penetration depth [11]:

$$\lambda_\perp = \sqrt{\frac{hc_o^2\rho_\perp}{8\pi^3\Delta(0)}}, \tag{6.3.2}$$

where $\rho_\perp$ is the resistivity perpendicular to the planes. Our surface resistance measurement gives an approximate value $\rho_\perp = 0.25\ \Omega$ cm just above the transition; this, together with $\Delta(0) = 1.76k_BT_c$ leads to $\lambda_\perp = 32$ μm in excellent agreement with the experimentally obtained value.

6.3.3 Coherence peak

In Fig. [6.11] we compare the temperature dependence of the surface resistance as measured with the **E** field along the a-axis ($R_{s\perp}$) together with the same measurement configuration but an **E** field oriented along the c-axis ($R_{s||}$). Although the normal state values are very different, the two sets of data maps perfectly against one another. Again this observation tends toward an 's-wave' pairing interpretation.

	σ_n [Ω^{-1}cm^{-1}]	δ [Å]	λ [Å]	ℓ [Å]	$\xi(0)$ [Å]	τ [cm^{-1}]	$2\Delta(0)$ [K]
$\parallel$	3.7×10^3	3.4×10^4	1.4×10^4	100	70	15	29.2
$\perp$	4.0	1.0×10^6	3.5×10^5	15	5	7	29.2

Table 6.1: Electrodynamics properties of κ-$(ET)_2Cu(NCS)_2$ measured at 60 GHz, with the current flowing wether the (bc)-plane ($\parallel$ configuration) or along the a-axis ($\perp$).

The temperature dependence of R_s and X_s below T_c= 8.2 K, obtained from a configuration where the electric field is parallel to the a direction, is shown in Fig. [6.12]. As for the parallel direction, all the data shown in Fig. [6.12] are normalized to the value of the surface impedance at 9 K (R_n and X_n). The coherence length [189] $\xi_\perp = 5\AA$, and the penetration depth is $\lambda_\perp = 35\mu$m, all parameters referring to the out-of-plane quantities. We have fit R_s and X_s for various values of $\ell/\pi\xi_o$ (cf. Chapter 2), assuming a two-dimensional BCS ground state [43], with a single particle gap given by the weak-coupling limit $2\Delta(0) = 3.52k_BT_c$. The best fit of our data leads to a value of $\ell/\pi\xi_\perp = 2$, and the mean-free-path is of the order of the distance between the $Cu(NCS)_2$ sheets. We have included in the fit the temperature dependence of the scattering rate, to do so we have fitted $\rho_n(T)$ the normal-state resistivity above T_c by a second order polynomial fit, and used this to estimate $\tau_\perp(T)$ in the temperature region below T_c.

Finally, Fig. [6.13] display an expand view of the temperature dependence of the perpendicular conductivity in the superconducting phase, the measurement was done at the antinode of the electric field. The first striking feature is that the normalized behavior is extremely analogous to the parallel (bc-plane) results shown in Fig. [6.7] despite the fact that the normalization factor (the 'normal-state' values) are several order of magnitude different between the two configurations. Again we can fit very well the data points by using a BCS model that include correction due to finite mean-free-path [43], the best fit is obtained for a value of the mean-free-path $\ell/\pi\xi_\perp = 2$, where $\xi_\perp = 5\AA$ is the perpendicular coherence length. The BCS result is shown on the figure as a solid line, notice that we have kept the weak coupling formalism $2\Delta(0)/k_BT = 3.52$. We have used the same type of analysis as the one mentioned for the parallel direction to account for the temperature dependence of the scattering rate. It is impossible to assert from our data solely what are the electronic variables responsible for the 'normal-state' anisotropy (scattering rate, band-mass etc...), the only experimentally accessible parameter is the conductivity and σ_1 is a mixture of different contributions. However, the agreement between the normalized results for the parallel and perpendicular configurations is a strong evidence that the pairing is isotropic, and the reasoning is as follow: the size of the 'coherence peak' depends on the coherence factor (case 2 for singlet pairing) plus the divergency of the excitation density of state at the gap edge. It is expected that this singularity is removed for 'd-wave' pairing leading to a sharp decrease of the optical conductivity analogous to the Yosida function in Eq. (2.5.2). For 's-wave' pairing, the photon energy smooths out this singularity as shown in Eq. (2.2.6) and is responsible for the reduced height of 'peak' feature for this relatively-small T_c compound (the size of the peak goes as Log[$\hbar\omega/\Delta(0)$]. As a consequence, since we observe the same temperature dependence for $\sigma_1(T)$ we deduce that the divergency in the optical-response of the system is identical at various orientation (as the photon energy is unchanged): we conclude that the ratio $\Delta(0)/\hbar\omega$ is a fundamental constant of the superconducting phase and thus the gap is isotropic. and we believe that this figure constitutes a conclusive evidence that the pairing is 's-wave'.

In conclusion, we have measured the surface impedance in the normal and superconducting state of κ-$(ET)_2Cu(NCS)_2$, and have evaluated the conductivity σ_1 along different crystallographic axes. The temperature-independent X_s from $T \ll T_c$, the weak maximum observed for σ_1 below T_c and the agreement

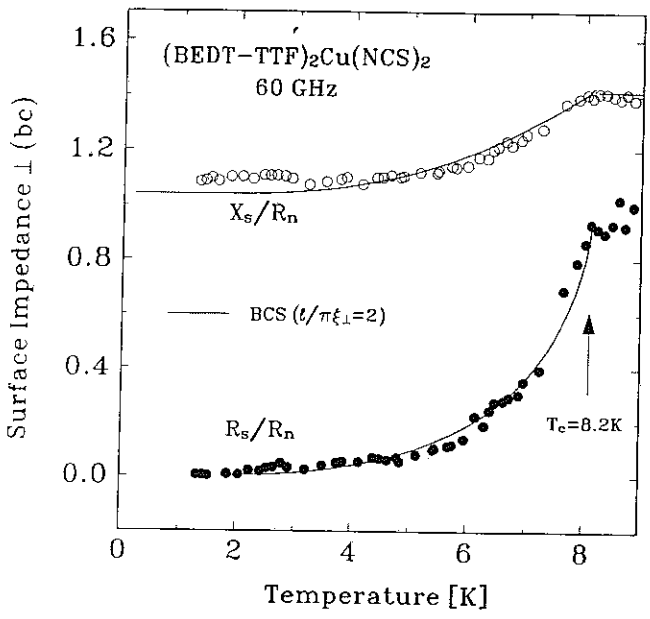

Fig. [6.12]: Temperature dependence of the surface impedance $Z_{s\perp} = R_s - iX_s$ of the a-direction. The solid line is the BCS prediction using $\ell/\pi\xi_o$ =2 as a fit parameter.

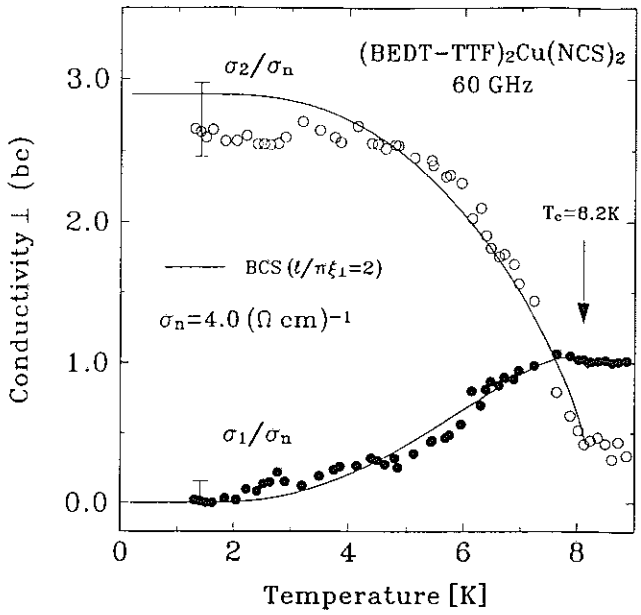

Fig. [6.13]: Temperature dependence of the perpendicular conductivity $\hat{\sigma}_\perp = \sigma_1 + i\sigma_2$. The solid line is obtained using a BCS ground state and a mean-free-path $\ell/\pi\xi_o = 2$.

between the different crystallographic orientation suggest an isotropic pairing. Our results are in good agreement with calculations based on a BCS ground state.

Chapter 7

Conclusion

We have presented in this report the electrodynamics of several family of superconductors. We have emphasized that the qualitative behavior of the response function is governed by the pairing symmetry through the so-called coherence factors (Chapter 1). The response function of the BCS ground state to an electromagnetic excitation displays a characteristic peak whose shape gives some important clues on the gap symmetry, the magnitude of the coupling between electrons, and the elastic scattering of the quasi-particles (Chapter 2).

7.1 Syntheses of the result

The experimental results shown in this report were all taken at 60 GHz as it represented the best compromise signal/sensitivity for the scheme that we have developed.

7.1.1 Conventional superconductors

We have measured for the first time the conductivity coherence peak in a conventional superconductor. Although predicted for 20 years this feature was never measured due to technical difficulties. This peak can only be observed in the millimeter spectral range and a direct evaluation of the optical conductivity at microwave frequencies necessitates the accurate measurement of both the surface resistance and surface reactance of the sample as both parameters are interrelated to σ_1. We have developed a new detection scheme which allows for an evaluation of σ_1 and the principle of the set-up is closely related to an ESR spectrometer (Chapter 3). The results on conventional superconductors, Nb and Pb are in good agreement with the simplest model developed by Mattis-Bardeen (Chapter 4) and despite the fact that no new striking features were observed, it represents an important confirmation of the BCS model.

7.1.2 Oxides and organic

We have measured the electrodynamics of new materials with unexpectedly high transition temperatures, the cuprates (Chapter 5) and the organic superconductors (Chapter 6). The motivation was to measure the gap symmetry as many other experiments were inconclusive or conflicting on this question. We have used 'cavity perturbation' techniques to investigate their electromagnetic response. We have made an extensive study of those two-dimensional materials and we have probed the different crystallographic axes by using various orientations of the sample with respect to the field. Also we have used both the electric and magnetic field antinode of the cavity to get a complete mapping of the electronic properties. The main conclusion of our study are summarized below.

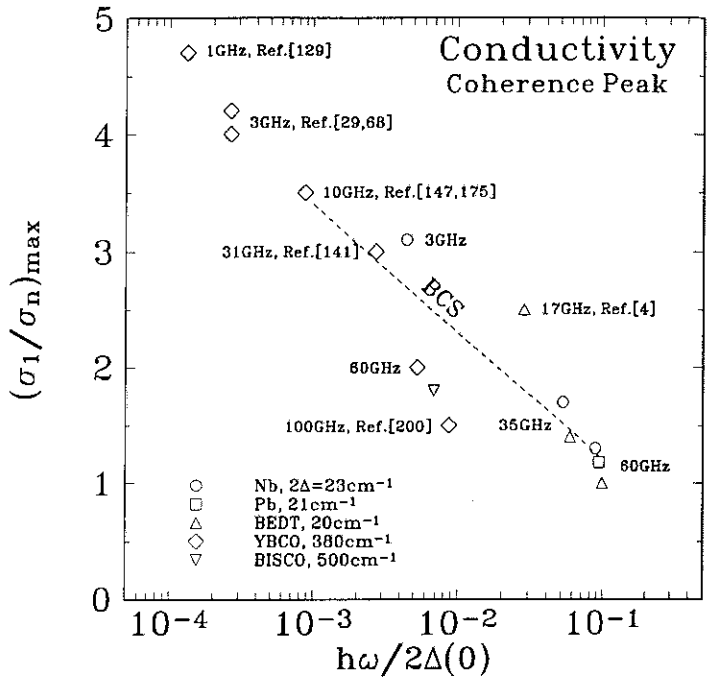

Fig. [7.1]: In this figure we have plotted the frequency dependence of the width and height of the conductivity peak, at various frequencies as extracted from various references.

High T_c superconductors

We have observe a sharp increase below T_c in the optical conductivity of the highly conducting plane. The peak shape is at odds with weak-coupling models as the width is much smaller than the one expected for a conventional BCS superconductor. The experimental results have been fit within the BCS formalism using two free parameters, the coupling constant $2\Delta(0)/k_BT_c$ and the elastic scattering rate. The fitting results suggest a strong coupling with a rapid opening of the single particle gap. The inferred scattering rate indicates that the sample is in the clean limit $\ell/\pi\xi_o > 1$ which would explain why the FIR optical measurements were unsuccessful in determining the single-particle gap.

Organic superconductors

We have repeated the same measurements for the organic superconductors where conflicting results have also been reported on the gap symmetry. In this particular case we have found that the experimental results could be fit with a weak coupling BCS formalism allowing only one free parameter, the mean-free-path. Again our results are suggestive that the material is in the clean-limit. The measurement of the anisotropic properties in the superconducting phase were astonishing: despite the fact that the normal-state properties differ by several order of magnitudes depending on whether the eddy-currents flow parallel or perpendicular to the highly conducting planes, the normalized result show a nearly identical temperature dependence. We regard this as a conclusive evidence that the gap is isotropic in those materials and thus that the pairing symmetry is 's-wave'.

7.2 Future work

Those preliminary results were very promising but it will be still important to continue further the investigation at other frequencies. The next paragraph review the importance of this unachieved part of the work.

7.2.1 Frequency dependence of σ_1

In spite of the wealth of data so far collected, there remains several important shady points in the study. In particular we have been unsuccessful in determining the temperature dependence of the scattering rate solely from conductivity measurements, as $\sigma_1(T)$ is a combination of several parameters, and no independent extraction can be made without assuming a model that will then imped the result. One way to circumvent this difficulty would be to measure the complete spectrum of σ_1. The task will be tedious and many experimental difficulties need still to be solved. But this study can be crucial in many respects: first it will give a clear hint if the temperature dependent scattering rate models are valid, as the predicted frequency dependence of the height of the coherence peak differs between theories. We have collected the various data already measured and plotted them in Fig. [7.1]. The results suggest so far that the height of the conductivity coherence peak follows a logarithmic law as predicted by the BCS model, and the width is frequency independent. A second important aspect of a complete spectrum investigation will be to look at other collective mode excitation at sub-millimeter ($2 - 20$ cm^{-1}) wave frequencies. Any anomalous absorption feature below the gap edge might indicate a coupling of some exotic components of the order parameter (Goldstone mode) with the electromagnetic radiation.

Chapter 8

Appendix

A Depolarization factors

Depolarization factor of simple degenerate ellipsoid:

1. A sphere ($a = b = c$): $n_x = n_y = n_z = 1/3$.
2. A cylinder in the x-direction ($a \to \infty, b = c$): $n_x = 0, n_y = n_z = 1/2$.
3. A flat plate ($a\&b \to \infty$): $n_x = n_y = 0, n_z = 1$.
4. A prolate spheroid ($a \geq b = c$) of eccentricity $e = \sqrt{1 - (b/a)^2}$:

$$n_x = \frac{1 - e^2}{2e^3}\left(\ln\frac{1+e}{1-e} - 2e\right), \quad n_y = n_z = \tfrac{1}{2}(1 - n_x). \tag{A1}$$

5. An oblate spheroid ($a = b > c$) with $e = \sqrt{(a/c)^2 - 1}$:

$$n_z = \frac{1 + e^2}{e^3}(e - \arctan e), \quad n_x = n_y = \tfrac{1}{2}(1 - n_z). \tag{A2}$$

B The TE_{011} mode

For a cavity of radius $d/2$ and height h, resonating at the TE_{011} mode, the fields inside the cavity varies as follow:

$$H_r(r,z) = \frac{H_o J_o'(kr)\cos\left(\frac{\pi z}{h}\right)}{\sqrt{1+\left(\frac{2\alpha_{01}h}{\pi d}\right)^2}}, \tag{B1}$$

$$H_z(r,z) = \frac{H_o J_o(kr)\sin\left(\frac{\pi z}{h}\right)}{\sqrt{1+\left(\frac{\pi d}{2\alpha_{01}h}\right)^2}}, \tag{B2}$$

$$E_\phi(r,z) = -\sqrt{\frac{\mu}{\epsilon}} H_o J_o'(kr)\sin\left(\frac{\pi z}{h}\right), \tag{B3}$$

$$E_r(r,z) = H_\phi = E_z = 0, \tag{B4}$$

where J_o', represents the derivative of the zeroth order cylindrical Bessel function, and

$$k = 2\alpha_{01}/d, \quad \text{with} \quad \alpha_{01} = 3.83171. \tag{B5}$$

The frequency of the cavity is given by

$$\omega_o = c_o\sqrt{\left(\frac{2\alpha_{01}}{d}\right)^2 + \left(\frac{\pi}{h}\right)^2} = 2\pi f_o. \tag{B6}$$

The average of the electric field is

$$<|\mathcal{E}|^2> = 0.0832982\frac{\mu}{\epsilon}H_o^2. \tag{B7}$$

The electric field anti-node is at

$$r = 0.480512a. \tag{B8}$$

For a cavity of dimension $d/h = 3/2$, the mode constant is:

$$\frac{V_c}{V_s}\gamma = \begin{cases} 2.03226 & \text{at } r = 0.48\frac{d}{2} \text{ and } z = h/2, \\ 0.67494 & \text{at } r = 0.48\frac{d}{2} \text{ and } z = 0, \\ 4.17731 & \text{at } r = 0 \text{ and } z = h/2 \end{cases} . \tag{B9}$$

(The first position is the electric field antinode, the last two are different possibilities for the magnetic field antinode).

C The spherical solution

The measured parameters are related to the sample polarizability:

$$\frac{f_s - f_e}{f_e} - \frac{i}{2}\left(\frac{1}{Q_s} - \frac{1}{Q_e}\right) = -4\pi\gamma\hat{\alpha}, \tag{C1}$$

where $\hat{\alpha}$ is the sample polarizability and γ is the mode constant (cf. P. 43). The polarizability is:

$$\hat{\alpha}_e = \frac{1}{4\pi n}\frac{\hat{\beta}\hat{\epsilon} - 1}{n(\hat{\beta}\hat{\epsilon} - 1) + 1}, \tag{C2}$$

$$\hat{\alpha}_m = \frac{1}{4\pi n}\frac{\hat{\beta} - 1}{n(\hat{\beta} - 1) + 1}, \tag{C3}$$

where n is the depolarization factor, $\hat{\epsilon} = \epsilon_\infty + 4\pi i\hat{\sigma}/\hat{\omega}$ is the permitivity and $\hat{\beta}$ defined by:

$$\hat{\beta} = -2\left(\frac{-(\hat{k}a)\cos(\hat{k}a) + \sin(\hat{k}a)}{-(\hat{k}a)\cos(\hat{k}a) + \sin(\hat{k}a) - (\hat{k}a)^2\sin(\hat{k}a)}\right), \tag{C4}$$

with $\hat{k} = \sqrt{\hat{\epsilon}}\omega/c_o$.

D Resonator constant of a prolate spheroid in H

If the sample is in the magnetic field maximum, the total power dissipated in the sample is given by [97]

$$L = \frac{1}{2\sigma_1\delta}\int_S |\vec{K}|^2 dS, \tag{D1}$$

with

$$\frac{1}{\sigma_1\delta} = \frac{4\pi}{c_o}R_s. \tag{D2}$$

The integral in Eq. (D1) is over the surface of the spheroid and $\vec{K}$ is the effective surface current given by

$$\vec{K} = \int_0^\infty \vec{J}d\zeta = \frac{c_o}{4\pi}(\hat{n}\times\mathbf{H}). \tag{D3}$$

where ζ is in the direction of the outward normal vector $\hat{n}$ to the surface and $\mathbf{H}$ is the magnetic field at the surface of the spheroid. In the skin-depth regime, we have seen Eq. (3.4.7b) that the magnetic field is related to the external applied field through the relation

$$\mathbf{H} = -\frac{\mathcal{H}_o}{n-1}. \tag{D4}$$

The simplest way to solve this problem is to make use of prolate spheroidal coordinates [17]. In this coordinate system the three independent coordinates are given by u, v, and ϕ and the usual cartesian coordinates are related to these through the transformation

$$x = \sqrt{a^2-b^2}\sinh u \sin v \cos\phi, \tag{D5}$$
$$y = \sqrt{a^2-b^2}\sinh u \sin v \sin\phi, \tag{D6}$$
$$z = \sqrt{a^2-b^2}\cosh u \cos\phi, \tag{D7}$$

where a and b are the semi-major and semi-minor axes respectively. The three components of the metric are given by

$$h_u = \sqrt{a^2-b^2}\sqrt{\cosh^2 u - \cos^2 v}, \tag{D8}$$
$$h_v = \sqrt{a^2-b^2}\sqrt{\cosh^2 u - \cos^2 v}, \tag{D9}$$
$$h_\phi = \sqrt{a^2-b^2}\sinh u \sin v. \tag{D10}$$

The unit normal vector $\hat{u}$ is given by

$$\hat{n} = \hat{u} = \frac{1}{h_u}\frac{\partial\vec{r}}{\partial u} = \frac{\cosh u \sin v \cos\phi}{\sqrt{\cosh^2 u - \cos^2 v}}\hat{x} + \frac{\cosh u \sin v \sin\phi}{\sqrt{\cosh^2 u - \cos^2 v}}\hat{y} + \frac{\sinh u \cos v}{\sqrt{\cosh^2 u - \cos^2 v}}\hat{z}. \tag{D11}$$

Assuming the external field is in the $\hat{z}$ direction leads to

$$|\vec{K}|^2 = \frac{c^2|\mathcal{H}_o|^2}{16\pi^2(n-1)^2}\left(\frac{\cosh^2 u \sin^2 v}{\cosh^2 u - \cos^2 v}\right). \tag{D12}$$

Inserting Eq. (D12) into Eq. (D1) and using the fact that $dS = h_v h_\phi dv d\phi$ gives

$$L = \frac{c^2|\mathcal{H}_o|^2 \cosh^2 u_o \sinh u_o d^2}{32\pi^2\sigma_1\delta(n-1)^2}\int_0^{2\pi} d\phi \int_0^{\pi} dv \frac{\sin^3 v}{\sqrt{\cosh^2 u_o - \cos^2 v}}, \tag{D13}$$

where $\cosh u_o = a/\sqrt{a^2-b^2}$, $\sinh u_o = b/\sqrt{a^2-b^2}$, and $d = \sqrt{a^2-b^2}$. From Eqs. (3.1.2) and (3.3.15a) appropriate for the magnetic field, one finds

$$Im\frac{\Delta\hat{\omega}}{\omega_o} = \frac{8\pi\gamma L}{|\mathcal{H}_o|^2 V_s \omega}. \tag{D14}$$

The integral in Eq. (D13) can be easily solved, and the resulting expression is in Eq. (D14) is proportional to the real part of the surface impedance. By analogy with Eq. (3.3.27) the resonator constant is given by

$$\begin{aligned}\xi &= \frac{-3ic_o\gamma d^2 \cosh^2 u_o \sinh u_o}{2b^2 a\omega(n-1)^2} \\ &\quad \times \left\{\sinh u_o + (2-\cosh^2 u_o)\arcsin\left|\frac{1}{\cosh u_o}\right|\right\}.\end{aligned} \tag{D15}$$

Bibliography

[1] A.A. Abrikosov and L.P. Gorkov, *J. Exptl. Theoret. Phys.* (Engl. Trans.), **15**, 752, (1962).

[2] A.A. Abrikosov, L.P. Gor'kov, and I.M. Khalatnikov, *J. Exptl. Theoret. Phys.* (Engl. Trans.), **35**, 182, (1959).

[3] A.A. Abrikosov, L.P. Gor'kov, and I.M. Khalatnikov, *J. Exptl. Theoret. Phys.* (Engl. Trans.), **37**, 132, (1960).

[4] D. Achkir, M. Poirier, C. Bourbonnais, G. Quirion, C. Lenoir, P. Batail, and D. Jérome, (1993), submitted to *Phys. Rev. Lett.*

[5] I. Affleck, Z. Zou, T. Hsu, and P.W. Anderson, *Phys. Rev. B*, **38**, 745, (1988).

[6] P.B. Allen and R.C. Dynes, *Phys. Rev. B*, **12**, 905, (1975).

[7] P.B. Allen and D. Rainer, *Nature*, **349**, 396, (1991).

[8] H. Alloul, A. Mahajan, H. Casalta, and O. Klein, *Phys. Rev. Lett.*, **70**, 1171, (1993).

[9] H. Alloul, P. Mendels, H. Casalta, J.F. Marucco, and J. Arabski, *Phys. Rev. Lett.*, **67**, 3140, (1991).

[10] H. Alloul, T. Ohno, and P. Mendels, *Phys. Rev. Lett.*, **63**, 1700, (1989).

[11] V. Ambegakoar and A. Baratoff, *Phys. Rev. Lett.*, **10**, 486, (1963).

[12] P.W. Anderson, *Physics Chem. Solids*, **11**, 26, (1959).

[13] P.W. Anderson, *Phys. Rev.*, **112**, 1900, (1963).

[14] P.W. Anderson, *Science*, **235**, 1196, (1987).

[15] P.W. Anderson and J.M. Rowell, *Phys. Rev. Lett.*, **10**, 230, (1963).

[16] J.F. Annett, N. Goldenfeld, and S.R. Renn, in *Physical Properties of High-Temperature Superconductors II*, Ed. D.M. Ginsberg, (World Scientific, New York, 1990).

[17] G. Arfken, *Mathematical Methods for Physicists*, (Academic Press, New York, 1970).

[18] G. Balakrishnan, R. Dupree, I. Farnan, D. McKPaul, and M.E. Smith, *J. Phys. C*, **21**, L847, (1988).

[19] J. Bardeen, L.N. Cooper, and J.R. Schrieffer, *Phys. Rev.*, **106**, 162, (1957).

[20] J. Bardeen, L.N. Cooper, and J.R. Schrieffer, *Phys. Rev.*, **108**, 1175, (1957).

[21] J. Bardeen and J.R. Schrieffer, in *Progress in Low Temperature Physics* (Vol. 2), page 170, Ed. C.J. Gorter, (North-Holland, Amsterdam 1961).

[22] A. Barone, *Physica C*, **153-155**, 1072, (1988).

[23] S.E. Barrett, D.J. Durand, C.H. Pennington, C.P. Slichter, T.A. Friedmann, J.P. Rice, and D.M. Ginsberg, *Phys. Rev. B*, **41**, 6283, (1990).

[24] B. Batlogg, *Physica B*, **169**, 7, (1991).

[25] B. Batlogg, in *Physics of High-Temperature Superconductors*, Eds. S. Maekawa and M. Sato, (Springer-Verlag, New York, 1991).

[26] J.G. Bednorz and K.A. Müller, *Z. Phys. B*, **64**, 189, (1986).

[27] R. Blaschke and R. Blocksdorf, *Z. Phys. B*, **49**, 99, (1982).

[28] N.N. Bogoliubov, *Nuevo Cimento*, **7**, 794, (1958).

[29] D.A. Bonn, P. Dosanjh, R. Liang, and W.N. Hardy, *Phys. Rev. Lett.*, **68**, 2390, (1992).

[30] D.A. Bonn, A.H. O'Reilly, J.E. Greedan, C.V. Stager, T. Timusk, K. Kamaràs, and D.B. Tanner, *Phys. Rev. B*, **37**, 1574, (1988).

[31] J.J. Bowman, T.B.A. Senior, and P.L.E. Uslenghi, *Electromagnetic and Acoustic Scattering by Simple Shapes*, (Hemisphere, New York, 1987).

[32] G. Briceño, M.F. Crommie, and A. Zettl, *Phys. Rev. Lett.*, **66**, 2164, (1991).

[33] L. Brillouin, *Les Tenseurs*, page 183, (Dover, New York, 1946).

[34] M.E. Brodwin and M.K. Parsons, *J. Appl. Phys.*, **36**, 494, (1965).

[35] H.B. Brom and H. Alloul, *Physica C*, **117**, 297, (1991).

[36] N. Bulut and D.J. Scalapino, *Phys. Rev. Lett.*, **68**, 706, (1992).

[37] L.I. Buranov and I.F. Shchegolev, *Pribory i Tekhnika Eksper.* (Instr. Exp. Techn.), **2**, 171, (1971).

[38] L.I. Buravov, A.V. Zvarykina, N.D. Kushch, V.N. Laukhin, V.A. Merzhanov, A.G. Khomenko, and E.B. Yagubskii, *Sov. Phys. JETP* (Engl. Trans.), **68**, 182, (1989).

[39] J. Butterworth and D.E. Mac Laughlin, *Phys. Rev. Lett.*, **20**, 265, (1968).

[40] J.P. Carbotte, *Rev. Mod. Phys.*, **62**, 1027, (1990).

[41] R.J. Cava, B. Batlogg, R.B. van Dover, D.W. Murphy, S. Sunshine, T. Siegrist, J.P. Remeika, E.A. Rietman, S. Zahurak, and G.P. Espinosa, *Phys. Rev. Lett.*, **58**, 1676, (1987).

[42] K.S. Champlin and R.R. Krongard, *IRE Trans. Microwave Theory Techn.*, **MIT-9**, 545, (1961).

[43] J.J. Chang and D.J. Scalapino, *Phys. Rev. B*, **40**, 4299, (1989).

[44] H.-M. Cheah, A. Porch, and J.R. Waldram, *Physica B*, **165-166**, 1195, (1990).

[45] M. Cohen, S.K. Khanna, W.J. Gunning, A.F. Garito, and A.J. Heeger, *Solid State Comm.*, **17**, 367, (1975).

[46] R.T. Collins, Z. Schlesinger, F. Holtzberg, C. Feild, U. Welp, G.W. Crabtree, J.Z. Liu, and Y. Fang, *Phys. Rev. B*, **43**, 8701, (1991).

[47] R. Comes, B. Renker, L. Pintschovius, R. Currat, W. Glaser, and G. Scheiber, *Phys. Stat. Sol. B*, **71**, 171, (1975).

[48] D.W. Cooke, E.R. Gray, H.H.S. Javadi, R.J. Houlton, N. Klein, G. Müller, S. Orbach, H. Piel, L. Drabeck, G. Grüner, J.Y. Josefowicz, D.B. Rensch, and F. Krajenbrink, *Solid State Comm.*, **73**, 297, (1989).

[49] J.R. Cooper, C.T. Chu, L.W. Zhou, B. Dunn, and G. Grüner, *Phys. Rev. B*, **37**, 638, (1988).

[50] S.L. Cooper, F. Slakey, M.V. Klein, J.P. Rice, E.D. Bukowski, and D.M. Ginsberg, *Phys. Rev. B*, **38**, 11934, (1988).

[51] P.G. de Gennes, *Superconductivity of Metals and Alloys*, (Adison-Wesley, New York, 1989).

[52] B.S. Deaver and W.M. Fairbank, *Phys. Rev. Lett.*, **7**, 43, (1961).

[53] L. Drabeck, K. Holczer, G. Grüner, J.J. Chang, D.J. Scalapino, A. Inam, X.D. Wu, L. Nazar, and T. Venkatesan, *Phys. Rev. B*, **42**, 10020, (1990).

[54] L. Drabeck, K. Holczer, G. Grüner, and D.J. Scalapino, *J. Appl. Phys.*, **68**, 892 (1990).

[55] H.D. Drew and A.J. Sievers, *Phys. Rev. Lett.*, **19**, 697, (1967).

[56] G.M. Eliashberg, *J. Exptl. Theoret. Phys.* (Engl. Trans.), **11**, 696, (1960).

[57] G.M. Eliashberg, *Z. Eksp. Teor. Fiz.*, **38**, 966, (1960).

[58] M.A. Beno *et al. Appl. Phys. Lett.*, **51**, 57, (1987).

[59] E.W. Fenton, *Solid State Comm.*, **54**, 709, (1985).

[60] M. Fibich, *Phys. Rev. Lett.*, **14**, 561, (1965).

[61] R.A. Ficher, S. Kim, B.F. Woodfield, N.E. Phillips, L. Taillefer, K. Hasselbach, J. Flouquet, A.L. Giorgi, and J.L. Smith, *Phys. Rev. Lett.*, **62**, 1411, (1989).

[62] S. Fujimoto, *J. Phys. Soc. Japan*, **61**, 765, (1992).

[63] I. Giaever, H.R. Hart Jr., and K. Megerle, *Phys. Rev.*, **126**, 941, (1962).

[64] D.M. Ginsberg, P.L. Richards, and M. Tinkham, *Phys. Rev. Lett.*, **3**, 337, (1959).

[65] D.M. Ginsberg and M. Tinkham, *Phys. Rev.*, **118**, 990, (1960).

[66] J. Goldstone, *Proc. Roy. Soc.* (London), **A239**, 267, (1957).

[67] J. Goldstone and K. Gottfried, *Nuevo Cimento Ser.*, **X13**, 849, (1959).

[68] A.A. Golubov, M.R. Trunin, S.V. Shulga, D. Wehler, J. Dreibholz, G. Müller, and H. Piel, (1993), submitted to *Phys. Rev. Lett.*

[69] L.P. Gor'kov, *J. Exptl. Theoret. Phys.* (Engl. Trans.), **9**, 1364, (1959).

[70] C.J. Gorter and H.B.G. Casimir, *Z. Physik*, **35**, 963, (1934).

[71] C.E. Gough, M.S. Colclough, E.M. Forgan, R.G. Jordan, M. Keene, C.M. Muirhead, A.I.M. Rae, N. Thomas, J.S. Abell, and S. Sutton, *Nature*, **326**, 855, (1987).

[72] J.E. Graebner, *Phys. Rev. B*, **41**, 4808, (1990).

[73] K.E. gray and D.H. Kim, *Phys. Rev. Lett.*, **70**, 1693, (1993).

[74] G. Grüner, *Rev. Mod. Phys.*, **60**, 1129 (1988).

[75] J. Halbritter, *Z. Physik*, **266**, 209, (1974).

[76] C.A. Hamilton, *Phys. Rev. B*, **5**, 912, (1972).

[77] P.C. Hammel, M. Takigawa, R.H. Heffner, Z. Fisk, and K.C. Ott, *Phys. Rev. Lett.*, **63**, 1992, (1989).

[78] W.N. Hardy, D.A. Bonn, D.C. Morgan, R. Liang, and K. Zhang, Jan. (1993), submitted to *Phys. Rev. Lett.*

[79] D.R. Harshman, G. Aeppli, E.J. Ansaldo, B. Batlogg, J.H. Brewer, J.F. Carolan, R.J. Cava, and M. Celio, *Phys. Rev. B*, **36**, 2386, (1987).

[80] D.R. Harshman, R.N. Kleiman, R.C. Haddon, S.V. Chichester-Hicks, M.L. Kaplan, L.W. Rupp, T. Pfiz, D. Ll. Williams, and D.B. Mitzi, *Phys. Rev. Lett.*, **64**, 1293, (1990).

[81] Y. Hasegawa and H. Fukuyama, *J. of the Phys. Soc. of Japan* (Letters)., **56**, 877, (1987).

[82] Y. Hasegawa and H. Fukuyama, *J. of the Phys. Soc. of Japan (Letters).*, **56**, 2619, (1987).

[83] K. Hasselbach, L. Taillefer, and J. Floquet, *Phys. Rev. Lett.*, **63**, 93, (1989).

[84] L.C. Hebel, *Phys. Rev.*, **116**, 79, (1959).

[85] L.C. Hebel and C.P. Slichter, *Phys. Rev.*, **113**, 1504, (1959).

[86] P.W. Higgs, *Phys. Lett.*, **12**, 132, (1964).

[87] D.S. Hirashima and H. Namaizawa, *J. Low Temp. Phys.*, **73**, 137, (1988).

[88] P.J. Hirschfeld, W.O. Putikka, and P. Wölfle, *Phys. Rev. Lett.*, **69**, 1447, (1992).

[89] P.J. Hirschfeld, P. Wölfle, and D. Einzel, *Phys. Rev. B*, **37**, 83, (1988).

[90] P.J. Hirschfeld, P. Wölfle, J.A. Sauls, D. Einzel, and W.O. Putikka, *Phys. Rev. B*, **40**, 6695, (1989).

[91] H.F.C. Hoevers, P.J.M. van Bentum, L.E.C. van der Leemput, H. van Kempen, A.J.G. Schellingerhout, and D. van der Marel, *Physica C*, **152**, 105, (1988).

[92] K. Holczer, L. Forro, L. Mihály, and G. Grüner, *Phys. Rev. Lett.*, **67**, 152, (1991).

[93] K. Holczer, O. Klein, and G. Grüner, *Solid State Comm.*, **78**, 875, (1991).

[94] M.L. Horbach and W. van Saarloos, *Phys. Rev. B*, **46**, 432, (1992).

[95] M.L. Horbach, W. van Saarloos, and D.A. Huse, *Phys. Rev. Lett.*, **67**, 3464, (1991).

[96] R.E. Glover III and M. Tinkham, *Phys. Rev.*, **108**, 243, (1957).

[97] J.D. Jackson, *Classical Electrodynamics*, (John Wiley & Sons, New York, 1975).

[98] D. Jérome, (1993), Private communication.

[99] D. Jérome, A. Mazaud, M. Ribault, and K. Bechgaard, *J. de Phys. I* (Paris), **41**, 95, (1980).

[100] R.I. Joseph and E. Schlömann, *J. Appl. Phys.*, **36**, 1579, (1965).

[101] B.D. Josephson, *Phys. Lett.*, **1**, 251, (1962).

[102] K. Kanoda, K. Akiba, K. Suzuki, T. Takahashi, and G. Saito, *Phys. Rev. Lett.*, **65** , 1271, (1990).

[103] M.N. Keene, T.J. Jackson, and C.G. Cough, *Nature*, **340**, 210, (1989).

[104] M.S. Khaikin, *J. Exptl. Theoret. Phys.* (Engl. Trans.), **34**, 961, (1958).

[105] O. Klein, S. Donovan, M. Dressel, K. Holczer, and G. Grüner, to be published in *J. Appl. Phys.*

[106] O. Klein, K. Holczer, and G. Grüner, *Phys. Rev. Lett.*, **68**, 2407, (1992).

[107] O. Klein, K. Holczer, G. Grüner, J.J. Chang, and F. Wudl, *Phys. Rev. Lett.*, **66**, 655, (1991).

[108] O. Klein, K. Holczer, G. Grüner, and G.A. Emelchenko, *J. de Phys. I* (Paris), **2**, 517, (1992).

[109] P.H. Kobrin, J.T. Cheung, W.W. Ho, N. Glass, J. Lopez, I.S. Gergis, R.E. De Wames, and W.F. Hall, *Physica C*, **176**, 121, (1991).

[110] P.H. Kobrin, W. Ho, W.F. Hall, P.J. Hood, I.S. Gergis, and A.B. Harker, *Phys. Rev. B*, **42**, 6259, (1990).

[111] R.H. Koch, C.P. Umbach, G.J. Clark, P. Chaudhari, and R.B. Laibowitz, *Appl. Phys. Lett.*, **51**, 200, (1987).

[112] B. Korin-Hamzić, L. Forró, and J.R. Cooper, *Phys. Rev. B*, 41, 11646, (1990).

[113] K. Kornelsen, J.E. Eldridge, C.C. Homes, H.H. Wang, and J.M. Williams, *Solid State Comm.*, **72**, 475, (1989).

[114] K. Kornelsen, J.E. Eldridge, H.H. Wang, and J.M. Williams, *Solid State Comm.*, **74**, 501, (1990).

[115] K. Kornelsen, J.E. Eldridge, H.H. Wang, and J.M. Williams, *Phys. Rev. B*, **44**, 5235, (1991).

[116] V.Z. Kresin and W.A. Little, in *Organic Superconductors*, (Plenum, New York, 1991).

[117] L. Krusin-Elbaum, R.L. Greene, F. Holtzberg, A.P. Malozemoff, and Y. Yeshurun, *Phys. Rev. Lett.*, **62**, 217, (1989).

[118] N. Kumar and A.M. Jayannavar, *Phys. Rev. B*, **45**, 5001, (1992).

[119] L.D. Landau and E.M. Lifschitz, *Electrodynamics of Continuous Media*, (Pergamon, Oxford, 1984).

[120] L.D. Landau and E.M. Lifschitz, *Stastical Physics*, page 446, (Pergamon, Oxford, 1984).

[121] M. Lang, N. Toyota, T. Sasaki, and H. Sato, *Phys. Rev. Lett.*, **69**, 1443, (1992).

[122] L.P. Le, G.M. Luke, B.J. Sternlieb, W.D. Wu, Y.J. Uemura, J.H. Brewer, T.M. Riseman, C.E. Stronach, G. Saito, H. Yamochi, H.H. Wang, A.M. Kini, K.D. Carlson, and J.M. Williams, *Phys. Rev. Lett.*, **68**, 1923, (1992).

[123] P. Lederer, *Lecture Notes* (Orsay), Dec. (1989).

[124] J.Y. Lee and T.R. Lemberger, Nov. (1992), submitted to *Appl. Phys. Lett.*

[125] M. Lee, A. Kapitulnik, and M.R. Beasley, in *Mechanisms of High Temperature Superconductivity*, Eds. H. Kamimura and A. Oshiyama, (Springer-Verlag, New York, 1991).

[126] S.L. Lehoczky and C.V. Briscoe, *Phys. Rev. B*, **4**, 3938, (1971).

[127] Y. Li, J.L. Huang, and C.M. Lieber, *Phys. Rev. Lett.*, **68**, 3240, (1992).

[128] W.A. Little, *Phys. Rev. A*, **134**, 1416, (1964).

[129] P. Lunkenheimer, A. Loidl, C. Tomé-Rosa, and H. Adrian, *Physica C*, **201**, 13, (1992).

[130] D.E. MacLaughlin, C. Tien, W.G. Clark, M.D. Lan, Z. Fisk, J.L. Smith, and H.R. Ott, *Phys. Rev. Lett.*, **53**, 1833, (1984).

[131] D. Mandrus, L. Forro, D. Koller, and L. Mihály, *Nature*, **351**, 460, (1991).

[132] J.T. Markert, T.W. Noh, S.E. Russek, and R.M. Cotts, *Solid State Comm.*, **63**, 847, (1987).

[133] F. Marsiglio, *Physica C*, **185-189**, 1675, (1991).

[134] J.A. Martindale, S.E. Barrett, C.A. Klug, K.E. O'Hara, S.M. DeSoto, C.P. Slichter, T.A. Friedmann, and D.M. Ginsberg, *Phys. Rev. Lett.*, **68**, 702, (1992).

[135] D.C. Mattis and J. Bardeen, *Phys. Rev.*, **111**, 412, (1958).

[136] B.W. Maxfield and W.L. Mc Lean, *Phys. Rev.*, **139**, A1515, (1965).

[137] J.-L. Miane, R. Chastanet, A. Ben Salah, and D. Daoud, *phys. stat. sol. (a)*, **88**, 325, (1985).

[138] F. Mila and T.M. Rice, *Physica C*, **157**, 561, (1989).

[139] P.B. Miller, *Phys. Rev.*, **118**, 928, (1960).

[140] A.J. Millis, H. Monien, and D. Pines, *Phys. Rev. B*, **42**, 167, (1990).

[141] F.A. Miranda, W.L. Gordon, K.B. Bhasin, V.O. Heinen, and J.D. Warner, *J. Appl. Phys.*, **70**, 5450, (1991).

[142] H. Monien and A. Zawadowski, *Phys. Rev. Lett.*, **63**, 911, (1989).

[143] P. Monthoux and D. Pines, *Phys. Rev. Lett.*, **69**, 961, (1992).

[144] R.W. Morse and H.V. Bohm, *Phys. Rev.*, **108**, 1094, (1957).

[145] S.B. Nam, *Phys. Rev.*, **156**, 470, (1967).

[146] S.B. Nam, *Phys. Rev.*, **156**, 487, (1967).

[147] C.S. Nichols, N.S. Shiren, R.B. Laibowitz, and T.G. Kazyaka, *Phys. Rev. B*, **38**, 11970, (1988).

[148] M.C. Nuss, P.M. Mankiewich, M.L. O´Malley, E.H. Westerwick, and P.B. Littlewood, *Phys. Rev. Lett.*, **66**, 3305, (1991).

[149] S. Ohsugi, Y. Kitaoka, M. Kyogaku, and K. Ishida, *J. Phys. Soc. Japan*, **61**, 3054, (1992).

[150] H.K. Olsson and R.H. Koch, *Physica C*, **185**, 1847, (1991).

[151] H.K. Olsson and R.H. Koch, *Phys. Rev. Lett.*, **68**, 2406, (1992).

[152] N.P. Ong, *J. Appl. Phys.*, **48**, 2935, (1977).

[153] N.P. Ong, in *Physics of High-Temperature Superconductors*, Eds. S. Maekawa and M. Sato, (Springer-Verlag, New York, 1991).

[154] J. Orenstein, G.A. Thomas, A.J. Millis, S.L. Cooper, D.H. Rapkine, T. Timusk, L.F. Schneemeyer, and J.V. Waszczak, *Phys. Rev. B*, **42**, 6342, (1990).

[155] J.A. Osborn, *Phys. Rev.*, **67**, 351, (1945).

[156] K. Oshima, H. Urayama, H. Yamochi, and G. Saito, *J. Phys. Soc. Japan*, **57**, 730, (1988).

[157] K. Oshima, H. Urayama, H. Yamochi, and G. Saito, *Physica C*, **153-155**, 1148, (1988).

[158] J. Owliaei, S. Sridhar, and J. Talvacchio, *Phys. Rev. Lett.*, **69**, 3366, (1992).

[159] L.H. Palmer and M. Tinkham, *Phys. Rev.*, **165**, 588, (1968).

[160] C.H. Papas, *J. Appl. Phys.*, **25**, 1552, (1954).

[161] T. Penney, S. von Molnar, and D. Kaiser *et al. Phys. Rev. B*, **38**, 2918, (1988).

[162] A.B. Pippard, *Proc. Roy. Soc.* (London), **A216**, 547, (1953).

[163] B. Pümpin, H. Keller, W. Kündig, W. Odermatt, I.M. Savié, J.W. Schneider, H. Simmler, P. Zimmermann, E. Kaldis, S. Rusiecki, Y. Maeno, and C. Rossel, *Phys. Rev. B*, **42**, 8019, (1990).

[164] G.E.H. Reuter and E.H. Sondheimer, *Proc. Roy. Soc.* (London), **A195**, 336, (1948).

[165] C.A. Reynolds, B. Serin, W.H. Wright, and L.B. Nesbitt, *Phys. Rev.*, **78**, 487, (1950).

[166] N.M. Rhugheimer, A. Lehoczky, and C.V. Briscoe, *Phys. Rev.*, **154**, 414, (1967).

[167] P.L. Richards and M. Tinkham, *Phys. Rev.*, **119**, 575, (1960).

[168] G. Rickayzen, *Phys. Rev.*, **111**, 817, (1958).

[169] G. Rickayzen, *Theory of Superconductivity*, (Interscience, New York, 1965).

[170] D.B. Romero, C.D. Porter, D.B. Taner, L. Forro, D. Mandrus, L. Mihàly, G.L. Carr, and G.P. Williams, *Phys. Rev. Lett.*, **68**, 1590, (1992).

[171] L.D. Rotter, Z. Schlesinger, R.T. Collins, F. Holzberg, C. Field, U.W. Welp, G.W. Crabtree, J.Z. Liu, Y. Fang, K.G. Vandervoort, and S. Fleshler, *Phys. Rev. Lett.*, **67**, 2741, (1991).

[172] G. Saito, *Physica C*, **162-164**, 577, (1989).

[173] D.J. Scalapino and P.W. Anderson, *Phys. Rev.*, **133**, A921, (1964).

[174] D.J. Scalapino, J.R. Schrieffer, and J.W. Wilkins, *Phys. Rev.*, **148**, 263, (1966).

[175] G. Schaumburg, H.W. Helberg, P. Berberich, and H. Kinder, (1993), accepted in *Ann. Physik.*

[176] G.W. Schaumburg, *Mikrowellenimpedanz der Hochtemperatur-Supraleiter* (Ph.D. Thesis), (Göttigen, Germany, 1992).

[177] Z. Schlesinger, R.T. Collins, F. Holtzberg, C. Feild, S.H. Blanton, U. Welp, G.W. Crabtree, and Y. Fang, *Phys. Rev. Lett.*, **65**, 801, (1990).

[178] J.R. Schrieffer, *Theory of Superconductivity*, (Addison-Wesley, New York, 1988).

[179] J.R. Schrieffer, D.J. Scalapino, and J.W. Wilkins, *Phys. Rev. Lett.*, **10**, 336, (1963).

[180] M. Sigrist and K. Ueda, *Rev. Mod. Phys.*, **63**, 239, (1991).

[181] C.P. Slichter, *Principles of magnetic resonances*, (Springer-Verlag, New York, 1978).

[182] S. Sridhar, B. Maheswaran, B.A. Willemsen, D.H. Wu, and R.C. Haddon, *Phys. Rev. Lett.*, **68**, 2220, (1992).

[183] S. Sridhar, D.H. Wu, and W. Kennedy, *Phys. Rev. Lett.*, **63**, 1873, (1989).

[184] S.E. Stupp and D.M. Ginsberg, *Physica C*, **158**, 299, (1989).

[185] L. Taillefer, *Physica B*, **163**, 278, (1990).

[186] T. Takahashi, T. Tokiwa, K. Kanoda, H. Urayama, H. Yamochi, and G. Saito, *Synthetic Metals*, **27**, A319, (1988).

[187] D.B. Tanner and T. Timusk, *Mod. Phys. Lett. B*, **3**, 189, (1989).

[188] M. Tinkham, *Introduction to Superconductivity*, (Mc Graw-Hill, New York, 1975).

[189] M. Tokumoto, H. Anzai, K. Takahashi, K. Murata, N. Kinoshita, and T. Ishiguro, *Synth. Met.*, **24**, A305, (1988).

[190] N. Toyota, T. Sasaki, K. Murata, Y. Honda, M. Tokumoto, H. Bando, N. Kinoshita, H. Anzai, T. Ishiguro, and Y. Muto, *J. Phys. Soc. Japan*, **57**, 2616, (1988).

[191] M.T. Tuominen, J.M. Hergenrother, T.S. Tighe, and M. Tinkham, *Phys. Rev. Lett.*, **69**, 1997, (1992).

[192] H. Urayama, H. Yamochi, G. Saito, K. Nozawa, T. Sugano, M. Kinoshita, S. Sato, K. Oshima, A. Kawamoto, and J. Tanaka, *Chem. Lett.*, page 55, (1988).

[193] D. van der Marel, H.-U. Habermeier, D. Heitmann, W. König, and A. Wittlin, *Physica C*, **176**, 1, (1991).

[194] J.R. Waldram, *Adv. in Phys.*, **13**, 1, (1964).

[195] U. Welp, W.K. Kwok, G.W. Crabtree, K.G. Vandervoort, and J.Z. Liu, *Phys. Rev. Lett.*, **62**, 1908, (1989).

[196] J.M. Winter, *Magnetic resonance in metals*, (Oxford, London, 1971).

[197] T.J. Witt, *Phys. Rev. Lett.*, **61**, 1423, (1988).

[198] D.H. Wu, J. Mao, S.N. Mao, J.L. Peng, X.X. Xi, T. Venkatesan, R.L. Greene, and S.M. Anlage, *Phys. Rev. Lett.*, **70**, 85, (1993).

[199] K. Yosida, *Phys. Rev.*, **110**, 769, (1958).

[200] D. Zhang, *Quasi-Optical millimiter-wave characterization and application of HTC superconducting thin films* (Ph.D. Thesis), UCLA, (Los Angeles, 1992).

[201] D. Zhang, D.V. Plant, H.R. Fetterman, N.E. Glass, J.T. Cheung, and P.H. Kobrin, (1993), submitted to *Phys. Rev. Lett.*

[202] F.C. Zhang, G. Gros, T.M. Rice, and H. Shiba, *Supercond. Sci. Technol.*, **1**, 36, (1988).